High energy resolution X-ray spectroscopy of f-electron systems

Evgeny Gerber

Université Grenoble Alpes

THÈSE

Pour obtenir le grade de

DOCTEUR DE L'UNIVERSITE GRENOBLE ALPES

Spécialité : **Physique des materiaux**

Arrêté ministériel : 25 mai 2016

Présentée par

Evgeny GERBER

Thèse dirigée par **Kristina KVASHNINA, Professeur, European Synchrotron Radiation Facility (ESRF)**
préparée au sein du **European Synchrotron Radiation Facility (ESRF)**
dans **l'École Doctorale de physique**

Spectroscopie à rayons X à haute résolution d'énergie des systèmes d'électrons f

Thèse soutenue publiquement le **10 Septembre 2021**,
devant le jury composé de :

M. Clemens WALTHER
Prof., Leibniz University, Hannover Institute of Radioecology and Radiation Protection, Rapporteur
M. Horst GECKEIS
Prof., Karlsruhe Institute of Technology (KIT), Institute for Nuclear Waste Disposal, Rapporteur
Mme Valérie VALLET
D.R. Univ. Lille, CNRS, Rapportrice
Mme Annie KERSTING
Dr., Lawrence Livermore National Laboratory, Examinatrice
M. Daniel BRAITHWAITE
Ing. HDR, CEA, Grenoble, Examinateur
Mme Teodora RETEGAN
Prof. Chalmers University of Technology, Examinatrice
M. Laurent CHARLET
Prof. Université Grenoble Alpes, Président

Acknowledgements

First and foremost I would like to thank my supervisor, Prof. Dr. Kristina Kvashnina. She gave me an excellent opportunity to join her freshly formed group and the guidance she provided during the whole PhD is invaluable. Her experience in HERFD-XANES technique at the beamline and just general things in life might have shaped my experiences in Grenoble the most. Her energy and purposefulness inspired me to do my best not only during the experiments, but also at conferences and schools, resulting in me persuing awards I would have not dared to contest otherwise. I also appreciate the amount of possibilities, which I have been given in terms of methods, research objects and many other things.

My appreciation for postdoctoral researchers from Kristina's team, Dr. Lucia Amidani and Dr. Stephen Bauters and their constant willingness to help cannot be understated. It was a pleasure to be a full member of that group. Lucia always gives gentle advice how to improve my work and cheers me up. Stephen was a perfect companion for night shifts and explained many practical things about beamline. Both were eager to answer my questions and share their knowledge with me. I am grateful for their support during the toughest moments of my PhD.

I also thank the welcoming ROBL team, for making me feel like a proper member, not to mention their help in the obtaining experimental data and the discussion of results. The guidance of Dr. Habil. Andreas Scheinost and Dr. André Rossberg have shaped my experience in many ways. Dr. Christoph Hennig and Dr. Manuel Feig deserve many thanks for the insights they have given me into XRD. Of course, the help and early-morning optimism of Jörg Exner always gave me strength, not a single piece of the ROBL's equipment went off thanks to him.

I am deeply indebted to Stephan Weiss who made me feel welcome during my visits to Rossendorf and who overcame any issue standing in the way of flawless sample packing. It is thanks to him that I became more skillful and confident in my work.

It is my honor to mention the much appreciated support of my Russian colleagues. I thank Dr. Anna Romanchuk, Dr. Alexander Trigub, Dr. Tatiana Plakhova and Prof. Stepan Kalmykov for the expertize they eagerly shared with me. The support and advice they gave during the experiments is greatly appreciated. Anna taught me all of in-depth practical things I know in the laboratory.

This PhD would have never been possible without the support from all my collaborators and beamline stuff from all over Europe, allowing me to continue my work during the shutdown.

I am also grateful to my parents and friends, who supported my decision to complete my PhD in Grenoble and were constantly reassuring me despite the distance. I am happy to thank Dr Yurii Nevolin and Dr. Petr Matveev for our endless scientific calls. Of course, Mikhail Kalinin (he will definitely become a Doctor one day!) and Daria Golovnina, who came in person to cheer me up and forced me to visit more French cities.

This work was supported by European Commission Council under ERC [grant N759696].

Contents

Abbreviations

AIM **A**nderson **I**mpurity **M**odel

APD **A**valanche **P**hoto**D**iode

BM **B**ending **M**agnet

CBC **C**ylindrically **B**ent **C**rystal

CTR **C**rystal **T**runcation **R**od

DCM **D**ouble-**C**rystal **M**onochromator

DMM **D**ouble-**M**ultilayer **M**onochromator

DOS **D**ensity **O**f **S**tates

DW **D**ebye-**W**aller

EBS **E**xtremely **B**rilliant **S**ource

ED **El**ectron **D**iffraction

ESRF **E**uropean **S**ynchrotron **R**adiation **F**acility

EXAFS **E**xtended **X**-ray **A**bsorption **F**ine **S**tructure

FWHM **F**ull **W**idth at **H**alf **M**aximum

HERFD **H**igh-**E**nergy-**R**esolution **F**luorescence **D**etection

HEXS **H**igh-**E**nergy **X**-ray **S**cattering

ID **I**nsertion **D**evice

ITFA **I**terative **T**ransformation **F**actor **A**nalysis

KARA **KA**rlsruhe **R**esearch **A**ccelerator

NP **N**ano**P**article

PDF **P**air **D**istribution **F**unction

PXRD **P**owder **X**-**r**ay **D**iffraction

RAXR **R**esonant **A**nomalous **X**-ray **R**eflectivity

RCSS **R**adio**C**hemical **S**ignal **S**ystem

RIXS **R**esonant **I**nelastic **X**-ray **S**cattering

ROBL **RO**ssendorf **B**eam**L**ine

RXES **R**esonant Inelastic **X**-ray **E**mission **S**pectroscopy

SAXS **S**mall-**A**ngle **X**-ray **S**cattering

SCXRD **S**ingle **C**rystal **X**-**r**ay **D**iffraction

SLS **S**wiss **L**ight **S**ource

WL **W**hite **L**ine

XAFS **X**-ray **A**bsorption **F**ine **S**tructure

XANES **X**-ray **A**bsorption **N**ear-**E**dge **S**tructure

XAS **X**-ray **A**bsorption **S**pectroscopy

XES **X**-ray **E**mission **S**pectroscopy

XFEL **X**-ray **F**ree **E**lectron **L**aser

Abstract

X-rays emitted by synchrotrons are great for studying the atomic structure of materials due to their penetrative nature, as well as their sensitivity to the local and electronic structures of the selected element. It is significantly important for f-elements, precisely actinides since synchrotron-based methods are non-distractive. Actinides such as uranium and plutonium are essential due to their use as a nuclear fuel in commercial nuclear reactors worldwide. Therefore the release of uranium, plutonium and the products of their fission in the environment is of significant concern. The chemical complexity of these elements as well as low concentrations in the samples and/or high radioactivity demand advanced physical methods to reveal fundamental and complicated properties of f-elements, which are needed to predict long-term release from underground repositories of nuclear waste and contaminated sites. In this PhD thesis, the application of various synchrotron-based methods, especially high energy resolution X-ray spectroscopy, on systems containing f-elements is shown.

The first part is devoted to synchrotron physics. Beamline setup is discussed in detail using the example of the Rossendorf Beamline II (ROBL-II) at ESRF. General information about the beamline as well as peculiarities associated with the study of radioactive materials are explained in details. Hutch arrangement and full descriptions of experimental stations including experimental equipment are covered.

The second part is dedicated to a detailed description of various synchrotron methods such as X-ray diffraction, X-ray absorption near edge structure (XANES) spectroscopy, high energy resolution fluorescence detection (HERFD) XANES, extended X-ray absorption fine structure (EXAFS) spectroscopy and high-energy X-ray scattering (HEXS). The theoretical basis for these methods and their underlying fundamental physics principles are considered. Special attention is given to the HERFD method for this study. The experimental setup used in each method and the most important characteristics are described. All methods will be applied to actinide systems, and a real application of each method will be presented.

In particular, the formation processes of MeO_2 (Me = Ce, Th, U, Pu) nanoparticles (NPs) and their characterization are discussed. The following parameters of the synthesis are varied: initial oxidation state of the element in which it is taken for the experiment, its concentration, pH, temperature. The structural stability of NPs in terms of time, as well as redox transformation, and thermal sensitivity are also investigated. Pu containing NPs obtained from plutonium solutions of different oxidation states and at various pH are probed for their structural and electronic properties. The presence of oxidation state impurities is investigated. The intermediate phase of Pu(V) in the course of the PuO_2 NPs synthesis is described, local structure and the oxidation state of this compound are examined. Besides PuO_2 NPs, their analogs – UO_2, CeO_2 and ThO_2 – have been investigated, the results are compared to PuO_2. The most important peculiarities for each system have been highlighted. The formation of UO_2 NPs under inert conditions is observed, and their oxidation after time under an X-ray beam is remarked. It is found that the properties of CeO_2 NPs are affected by their size and their surface is modified by drying at different temperatures. The formation of ThO_2 NPs is studied, nanoparticle size was extracted from the HEXS data. HEXS data are fitted by semi-empirical methods and fits based on real NP structures and reveal the presence of small and medium NPs depending on the synthesis conditions. The size effect of ThO_2 NPs is also determined.

Resumé

Les rayons X dégagés par les synchrotrons sont utiles dans l'étude de la structure atomique des matériaux de par leur sensibilité aux structures locales et électroniques d'un élément donné. Ces caractéristiques sont particulièrement significatives dans le cas des éléments du bloc f, notamment les actinides puisque les méthodes basées sur le synchrotron ne sont pas distractives. Les actinides comme l'uranium et le plutonium sont essentiels parce qu'ils sont utilisés comme combustible dans des réacteurs nucléaires commerciaux dans le monde entier. Donc, le rejet d'uranium, plutonium et de leurs produits de fission dans l'environnement pose un problème important. La complexité chimique des ces éléments ainsi que leur concentration minimale dans les échantillons et/ou radio-activité forte exigent les méthodes physiques avancées pour révéler les propriétés fondementale et complexes des éléments du bloc-f, dont la compréhension est nécessaire nécessaire afin de pouvoir prédire le rejet à long-terme des profonds dépôts souterrains de déchets nucléaires et des sites contaminés. Dans cette thèse est montrée l'utilisation de différentes méthodes propres au synchrotron, notamment la spectroscopie de la haute résolution de l'énergie par les rayons X sur des systèmes comportant des éléments du bloc f.

La première partie de cette thèse est consacrée à la physique pratiquée au synchrotron. L'installation de la ligne est décrite en détails en prenant pour exemple la Rossendorf Beamline (ROBL-II) à l'ESRF. Les informations générales sur la beamline ainsi que les particularités associées avec l'étude des matériaux radioactifs sont mentionnées. La disposition de hutch et la description complète des stations d'expérimentation ainsi que leurs équipements sont abbordés.

La deuxième partie est dédiée à la description de méthodes synchrotron variées, comme la cristallographie aux rayons X, la spectroscopie de structure près du front d'absorption de rayons X (XANES), détection de fluorescence à haute résolution d'énergie (HERFD) XANES, la spectroscopie EXAFS (EXAFS) et la diffusion de rayons X à haute énergie (HEXS). Le fondement théorique de ces méthodes et sous-jacent principes de la physique fondamentale sont considérés. La méthode HERFD fait l'objet d'une attention particulière en tant que méthode principale de cette thèse. La configuration expérimentale utilisée dans chaque méthode et les caractéristiques les plus importantes sont décrites. Toutes les méthodes seront appliquées aux systèmes des actinides. L'application de chaque méthode à des cas scientifiques réels sera présentée.

Les procédures de formation de nanoparticules (NPs) MeO_2 (Me = Ce, Th, U, Pu) et leurs caractéristiques sont traités. Les paramètres suivants de la synthèse sont variés: l'état d'oxydation du précurseur, sa concentration, pH et la tempereature. La stabilité des NPs en termes de temps ainsi que l'oxydation et la sensibilité thermique sont également analysés. Pu NPs reçues de précurseurs différents de plutonium de pH varié, leurs caractéristiques structurelles et électroniques sont sondées. La présence d' impuretés de l'état d'oxydation est analysée. Outre les NPs PuO_2, leurs analogues – UO_2, CeO_2 et ThO_2 – ont été étudiés, les résultats sont comparés à PuO_2. Les particularités les plus importantes de chaque système ont été mises en évidence. La formation des NPs de UO_2 sous les conditions inertes est observée. On a découvert que les NPs de CeO_2 sont affectées par leur taille et que leur surface est modifiée par le séchage à différentes températures. La formation de NPs de ThO_2 sont analysés, la taille des nanoparticules a été extraite des données HEXS. Les données HEXS sont adaptées par des

méthodes semi-empiriques et des ajustements basés sur des structures réelles de NP et révèlent la présence de petites et moyennes NP en fonction des conditions de synthèse. L'effet de taille des NPs de ThO_2 est aussi déterminé.

Introduction

The development of physical methods opened the way for the investigation of slight and precise though important properties of materials and substances. A significant role in modern science is played by large-scale facilities such as different particle accelerators be it betatrons, colliders or synchrotrons. The variety of their methods, based on X-rays, allows implementing of synchrotrons in numerous research areas, including hard-condensed matter science, chemistry, earth sciences, medicine, life sciences, environmental studies and many others. An extremely bright X-ray source is capable of measuring hard-to-detect quantities or properties and observing exceedingly rapid processes. Sensitive and delicate objects of cultural heritage as well as drugs and proteins are objects of paramount importance. To fully profit from a synchrotron radiation source, besides properly performed experiments, careful data evaluation with implementation of specialized software is required.

X-rays emitted by synchrotrons can be used to study the atomic structure of materials because of their penetrative behaviour and their sensitivity to the local and electronic structure of the selected element. It is significantly important for f-elements, as the differences even for different elements may be subtle, and precisely for actinides since due to their radiotoxicity it is preferable to measure low concentrations of these elements. Actinides such as uranium and plutonium are essential due to their application as fuel in commercial nuclear reactors worldwide, although the release of uranium, plutonium and their fission products in the environment is of significant concern. It is still an open question - what will happen to actinides present in the environment or nuclear waste over the years. The way to answer this question is to explore the fundamental understanding of actinide properties with a special focus on the species they can take in different conditions. Chemical complexity of these elements as well as low concentrations in the probes and/or high radioactivity demand advanced physical methods to reveal fundamental and complicated properties of f-elements, which is needed to predict long-term release from deep underground repositories of nuclear waste and contaminated sites.

Although synchrotrons are highly useful in actinide studies, several issues appear. Due to the radiotoxicity of actinides, special radiochemical labs are compulsory to work with this type of materials and they are mostly set aside from synchrotrons. Thus problem of sample transportation arises. Special transport has to be organized for safe and secure transfer. To prevent release of the radioactive materials special sample holders must be designed. If all these hurdles are overcome and samples successfully reached synchrotron, the great amount of useful information can be obtained and in this thesis some highlights in this field will be reported and discussed in details.

Organisation of the thesis

The thesis is organized as follows:

Chapter 1 contains an overview of synchrotron physics. The principal components of synchrotron and the most important parameters are discussed. The beamline setup is described on the example of the Rossendorf Beamline at ESRF (ROBL-II), with the description of the optics and experimental stations.

Chapter 2 is devoted to the methods implemented for the investigation of f-elements. XRD, XANES, HERFD, EXAFS and HEXS techniques are analysed in details. The experimental stations where the measurements for the current work have been performed are presented. Special attention is given to the illustration of the above-mentioned methods. The formation of PuO_2, UO_2, CeO_2 and ThO_2 NPs and their characterization are discussed in details. The influence of different parameters such as the oxidation state and concentration of the actinide, pH, and the temperature of post-synthesis treatment is discussed in details.

Chapter 3 shows, how the combination of several synchrotron methods can be applied to solve the complicated scientific tasks. PuO_2 NPs case is chosen to demonstrate how additional information can be extracted from the complementary approach. The importance of this approach is discussed.

Finally, general conclusions and perspectives of this work is outlined.

1. Synchrotron physics

1.1. Synchrotrons

Synchrotron is a cyclic particle accelerator, in which a particle beam, being accelerated to relativistic velocities, generates electromagnetic radiation from 0.01 eV to more than 100 keV. One of the most popular type of synchrotron machine is a synchrotron light source. Electrons are generated with an electron gun by thermionic emission from a hot filament and then are accelerated in a linear accelerator (linac) to about 100 MeV. A regular supply of electrons is needed due to their loss after collisions with gas particles in the storage ring. Afterwards electrons are additionally accelerated in the booster ring after ejecting from the linac and then they are magnetically injected in the storage ring, where they circulate at highly relativistic velocities. The storage ring contains bending magnets (BMs), which are used to deflect the electrons round the curved sections and to gain bending-magnet radiation. Besides BM, the storage ring also includes insertion devices (IDs) – straight sections, generating the most intense synchrotron radiation. Eventually electrons are lost due to the collisions decreasing the current. To overcome this effect, either new set of electrons is injected (in that case beam has to be interrupted) or frequent mini-injections are used. The last case is called top-up mode, allowing user operation without interruption, and enhancing stable operations. A scheme of a modern synchrotron facility is shown in Fig. 1.

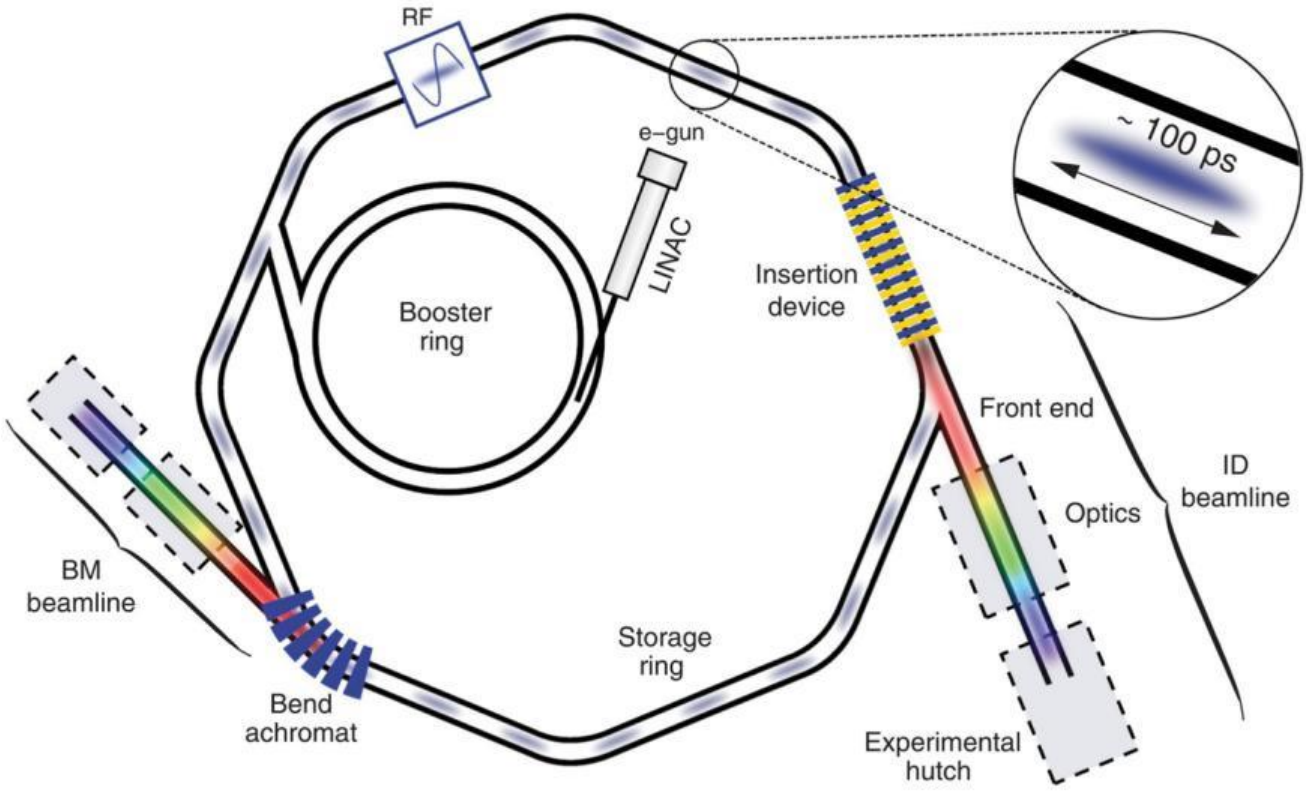

Fig. 1. Illustration of the main components of synchrotron.[1]

The electron beam is characterized by current (mA) and kinetic energies of electrons (GeV), the velocity of electrons is close to the speed of light. Synchrotron radiation produced by an electron beam in turn is described with flux and brilliance. Flux is the number of photons per second per

unit bandwidth (normally 0.1%) passing through a defined area, while brilliance is the flux per unit source area and unit solid angle and defined by the formula:

$$Brilliance = \frac{photons/second}{(mrad)^2(mm^2\ source\ area)(0.1\%\ bandwidth)} \quad (1)$$

Brilliance shows, how flux is distributed in space and angular range. The higher the brilliance, the more precise the information that can be obtained from the X-ray.

There are several dozens synchrotrons all over the world with different electron beam energies, flux and brilliance, however, only a small amount of them are allowed to deal with radioactive samples. Synchrotrons used to produce data for this thesis are listed in Table 1.

Table 1. The list of synchrotron radiation facilities, where radioactive materials from these studies have been measured.[1]

Synchrotron	Location	Energy, GeV	Current, mA	Brilliance, ph/s/mrad^2/mm^2/0.1% BW	Methods used
European Synchrotron Radiation Facility (ESRF)	Grenoble, France	6	200	$8 \cdot 10^{20}$	XRD, HERFD, EXAFS, HEXS
SOLEIL	Paris, France	2.75	500	$1 \cdot 10^{20}$	HERFD
Swiss Light Source (SLS)	Villigen, Switzerland	2.4	400	$4 \cdot 10^{19}$	HERFD
Karlsruhe Research Accelerator (KARA)	Karlsruhe, Germany	2.5	150	10^{18}	HERFD
Kurchatov Synchrotron Radiation Source	Moscow, Russia	2.5	300	10^{15}	XANES

1.2. *Beamlines*

Synchrotron radiation, generated with BMs or IDs, is afterwards channelled down beamlines, located tangentially at BMs and along the axes of IDs, but in any case tangentially to the storage ring. A beamline starts from it's «front end» and has several essential functions: it sets apart the storage ring and the beamline vacuum; tracks the position of the photon beam; prevents x-ray and Bremsstrahlung radiation in further sections of beamline; it also defines the angular acceptance of the synchrotron radiation via the aperture. Afterwards in the optic hutch the beam focuses and monochromates and then goes to the experimental hutch where X-ray radiation is used for the conducting the experiments. Besides X-rays, gamma-radiation and high-energy neutrons may be generated during the measurement, therefore, all experiments should be carried out remotely and lead shielding is absolutely required to eliminate the risks.

Depending on the perfectness of the X-ray optics at the beamline, the brilliance at the experimental station will fall short of theory (equation 1). Table 2 gives a brief overview of some dedicated radionuclide beamtimes.[2]

Beamline setup will be discussed in details on the example of Rossendorf Beamline II (ROBL-II) at ESRF.

Table 2. Overview of the dedicated radionuclide beamlines.

Beamline	ROBL-II (ESRF)	INE (KARA)	ACT (KARA)	Mars (SOLEIL)	microXAS-SLS	STM (Kurchatov Synchrotron)
Reference	[2]	[3]	[4]	[5,6]	[7]	STM page
Photon flux, ph/s	$6 \cdot 10^{12}$ at 20 keV and 200 mA	$2 \cdot 10^{10}$ at 18 keV	10^{11} at 20 keV and 100 mA	$1 \cdot 10^{12}$ at 12 keV and 430 mA	$3 \cdot 10^{12}$ at 12 keV	$3 \cdot 10^{8}$ at 100 mA
Energy range, keV	3.5-35	2.1-25	3.4-55	3.5-35	4-23	4.9-35
Spot size, (h × v) (μm)	21 × 69 (focused) 10000 × 2000 (unfocused)	500 × 500	1000 × 1000 (focused)	300 × 300 15 × 15 (with additional KB optics)	1.0 × 1.0 with 10^{11} ph/s dynamic focusing	10 × 10 2000×3000
Activity	185 MBq	Exemption limit 10^6 for non-fissile isotopes, 200 mg for fissile ^{235}U and ^{239}Pu		185 GBq, 18.5 GBq per sample	100 × LL per sample (Swiss clearance limit) maximum 10 samples	

1.2.1. Rossendorf Beamline II (ROBL-II) at ESRF[2]

ROBL-II is a beamline embedded within the Helmholtz Association's program on nuclear safety and dedicated to the study of actinides and other redionuclides. The full description of the beamline is shown at Scheinost et al.,[2] in this thesis the summary is given. The beamline consists of an optics hutch, two experimental hutches (RCH-1 and RCH-2) and a control room, from where synchrotron X-ray experiments are remotely conducted. Four experimental stations are installed at the experimental hutches:

1. XAFS station with fluorescence and transmission detection for X-ray absorption fine-structure (XAFS) spectroscopy, including (conventional) X-ray absorption near-edge structure (XANES) and extended X-ray absorption fine structure (EXAFS) spectroscopies.
2. XES station with a five-crystal Johann-type spectrometers for high-energy-resolution fluorescence-detection X-ray absorption near-edge spectroscopy (HERFD-XANES), X-ray emission spectroscopy (XES) and resonant inelastic X-ray scattering (RIXS) measurements.
3. XRD-1 station with a heavy-duty, Eulerian cradle, sixcircle goniometer for (high-resolution) powder X-ray diffraction (PXRD), surface-sensitive crystal truncation rod (CTR) and resonant anomalous X-ray reflectivity (RAXR) measurements.
4. XRD-2 station with a Pilatus3 x2M detector stage for single crystal X-ray diffraction (SCXRD) and in situ/ in operando PXRD measurements.

The scheme of the ROBL-II beamline is presented at Fig. 2.

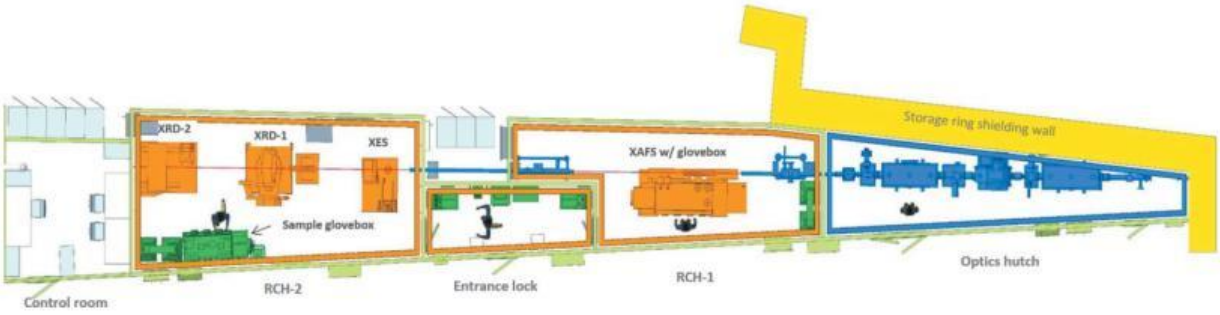

Fig. 2. Layout of ROBL-II, showing from right to left the X-ray Optics hutch (blue), the two experimental hutches (RCH-1 and RCH-2) connected by a common entrance lock room (orange), and the control room. The X-ray beam marked by the red line enters from the right through a port in the shielding wall. RCH-1 houses the XAFS experiment, RCH-2 a five-crystal spectrometer (XES), a six-circle goniometer for powder and surface diffraction (XRD-1), and a Pilatus3 2M diffractometer (XRD-2). Hutch walls are shown in light green, radiation protection equipment in green. Figure from Scheinost et al.[2]

There is a combined double-crystal monochromator (DCM) and a double-multilayer monochromator (DMM). DCM or DMM are used whichever parameter is more crucial: energy resolution or flux. DCM allows to have monochromatic X-rays within 3 to 35 keV with energy resolution of a few eV, while DMM gives only 100 eV resolution, though flux is about 100 times higher. A mirror located before the monochromator collimates the beam, while mirror after the monochromator focuses the beam and suppress higher harmonics.

A monochromator is a combination of double-crystal setups with three laterally mounted sets of crystals with a double-multilayer setup with two laterally mounted sets of multilayers, DCM to t DMM setups are switched by moving the monochromator upward till the multilayer crystals do not reach the beam. Upward-bouncing first crystals are cooled by liquid nitrogen while upward-bouncing multilayer crystals are cooled by water. The DCM setup comprises two Si(111) pairs, oriented at 30-degree difference towards the incoming beam to deal with so-called glitches. The third crystal pair uses the improved energy resolution of the Si(311) plane. Two multilayers from the DMM setup cover the energy range 8.5 to 12.6 keV for the first (with the optimum of 10 keV) and from 12.6 to 18.7 keV for the second multilayer (with the optimum of 15 keV). Optics for the diffraction includes silicon substrate coated with Mo/B_4C multilayers of two different period thicknesses plus a ~4 nm Si cover layer for protection, rotating wihin an angle of 0.76 to 1.13°. It yields energy resolution $\Delta E/E < 1\%$.

The first water-cooled mirror is 1.3 m long and is set at an upward reflecting angle of 2.5 mrad. To collimate the white beam vertically, it is bent to ~20 km in longitude. The silicon body is coated with two Rh and Pt 37 mm-wide stripes and with bare Si surface in between. Rh, Si and Pt surfaces reflect differently, allowing maximize the flux across the working energy range (3-35 keV) and minimizing the contribution of higher-order harmonics. Surface roughness for the 700 Å Rh and Pt coatings is 0.4 nm and 0.6 nm for the bare Si surface. Slope errors depend on stripe and bending radius and vary between 0.7 and 1.1 µrad.

The second downward-reflecting mirror from monocrystalline silicon is 1.2 m long. It has two toroidal grooves (one coated with Rh and the other with Pt) each radius is 61.8 mm to focus the beam both vertically and horizontally for the last two experimental stations, the spot size of the

beam is about 20 µm × 70 µm (h × v).[2] For the third station (XES) is about 100 µm x 900 µm and for the fourth station (XAFS) beam is purposely out of focus to minimize the beam damage of samples, the beam size is up to 10 mm × 2 mm. There is a Si surface without coating between toroidal grooves used to provide a collimated beam of <14 keV for diffraction experiments, demanding minimized divergence. Surface roughness for the 600 Å Rh and Si surface is 0.3 nm while for 600 Å Pt surface it is 1.3 nm. Slope errors are 0.5, 1.0 and 1.3 µrad fof Rh, Si and Pt surfaces respectively.

It is essentially required to have a radiochemical safety system to investigate radioactive samples. Radioprotection design is optimized generally for alpha- and beta-emittting radioisotopes, therefore radioisotopes with the longest half-lifes have priority. Exposure levels outside of the glovebox are limited to <0.5 µSv h^{-1}, in contact with the sample enclosure <15 mSv h^{-1}.

All samples which can be measured at ROBL-II are divided in three groups:

1. Non-active samples, radioprotection treatment is not required.
2. Active samples with activities lower that 3.7 MBq for a group 1 radionuclide on solid form, less for liquids or powders. This limit is an established for ESRF beamlines without dedicated radiochemistry equipment. (https://www.esrf.eu/Infrastructure/Safety/Experiments/RadioactiveSamples).
3. Highly-radioactive samples with the upper activity limit of 185MBq established for the ROBL beamline.

All samples are inside an underpressurized glovebox with ventilation, filter and radiation monitoring in place has an upper activity limit of 185 MBq. Samples from third group must be constantly maintained there during the measurement.

The radiation shielding is carried out through lead shielding, covering walls, doors and roof of two research hutches. These hutches fulfil specific requirements (tightness and ease of decontamination) and therefore may be considered as alpha-radionuclide laboratories. Two hutches are connected by a common entrance lock room (Fig. 2). Hand-foot monitor and body decontamination equipment provide safety and ease of sample transfer between experimental stations of two hutches.

The protection from accidental release of radionuclides from sample holders redundant ventilation and filter system are installed in both hutches. It establishes a pressure gradient from the outside ESRF experimental hall to the hutches and then to gloveboxes.

Last but not least a multistep radiation monitoring system is installed and a radiochemical signal system (RCSS). All information from radiation monitors and ventilation, such as air flux, pressure and temperature are registered by RCSS and warnings or alarms automatically activate in case of any parameter deviations. Alpha/beta gamma values are presented in various places at the beamline itself as well as at the main control room of ESRF.

Hitherto highly radioactive samples from the third group can be investigated only at the XAFS experimental station, also equipped with gamma-spectrometer and contamination monitors in the glovebox. For others experimental stations (XES, XRD-1 and XRD-2) due to the focused beam the amounts of radioactive material needed is usually small enough to fulfil the activity limits of the second group.

There are three types of experiments in terms of radioactive safety: green, yellow and red. A green experiment is an experiment is without any radiation risk, yellow experiments involve samples with moderate activity (like Th, U and Tc) and red ones – for samples with substantial radioactivity (mostly transuranium elements). A red experiment requires the 24h presence of one user at the beamline. After the end of each radioactive experiment ESRF Radioprotection group checks samples and experimental stations.. The RCSS informs about the correct functioning of all radioprotection systems, and warns about any alarms or contaminations. More detail information about beamline and dedicated stations can be found in the article of Scheinost et al.[2]

2. Methods and its applications

2.1. XRD

X-ray diffraction is a coherent elastic scattering of X-rays with the interference of the secondary waves, constructive in a few specific directions, determined by the Bragg's law:

$$2d\sin\theta = n\lambda$$

Where θ is a scattering angle, d - the interplanar distance of the crystal, n is the order of reflection and λ- is the wavelength of the X-ray photons. λ is the same order of magnitude as d, i.e. from about 0.1 to 2 Å (or from 100 keV to 5keV in energy). XRD is a well-established method so here I will concentrate mostly on possibilities granted by modern synchrotron radiation facilities.

1) The availability of high X-ray energies with a low absorption coefficient gives possibility to deeply probe samples (several centimetres), which is crucial for stress measurements. ID15A beamline at ESRF, which will be discussed in 2.5.2 is capable of doing experiments with an X-ray energy of 500 keV.
2) Complex structure refinement tasks demand low beam-divergence simultaneously with high flux values that generally can be achieved only at synchrotrons. Moreover, the determination of protein structure usually employs the phenomenon of anomalous scattering due to the possibility of tuning X-ray energy close to the atom's absorption edge.
3) The high intensity of X-rays allows us to investigate even tiny amounts of samples, which is especially important for nanomaterials, ultra-thin films and radioactive materials
4) Experiments at synchrotrons allow us to conduct time-resolved experiments and experiments with special conditions (in-situ, high pressure or temperatures, cryocooling etc.)

2.1.1. Pilatus diffractometer

At ROBL-II there is a diffractometer station with a Pilatus 2M detector installed together with the sample goniometer on a common granite table.(Fig. 3). It was desgined by Instrument Design Technology Ltd together with SNBL/ESRF.[8] Diffractometer is equipped with aPilatus3 X 2M detector (Dectris Ltd), with a photon-sensitive layer of 450 µm-thick Si of an area of 253.7 mm × 288.8 mm (width × height), and a pixel size of 172 µm × 172 µm. The diffractometer has a fixed position without motorized movements, therefore only the sample-detector distance could be varied, which is still sufficient to make a precise positioning and alignment relative to synchrotron

beam. The sample-detector distances can be varied between 140 and 600 mm. More details can be found at Scheinost et al.[2] The setup also includes a cryocooler 800 series (Oxford Cryosystems Ltd) which controls a temperaturerange of 80–400 K. The diffractometer is operated with the GUI-based software Pylatus.[8] It is possible to conduct in-situ PXRD varying temperature (both heating and cooling) or/and under certain gas atmosphere. The furnace allows to heat up to 1000 ◦C in air, O_2, N_2, Ar, He or vacumm (≥10^{-4} mbar). The measurements in transmission geometry is possible with a capillary spinner, which is crucial for air-sensitive samples and samples with a strong anisotropy.

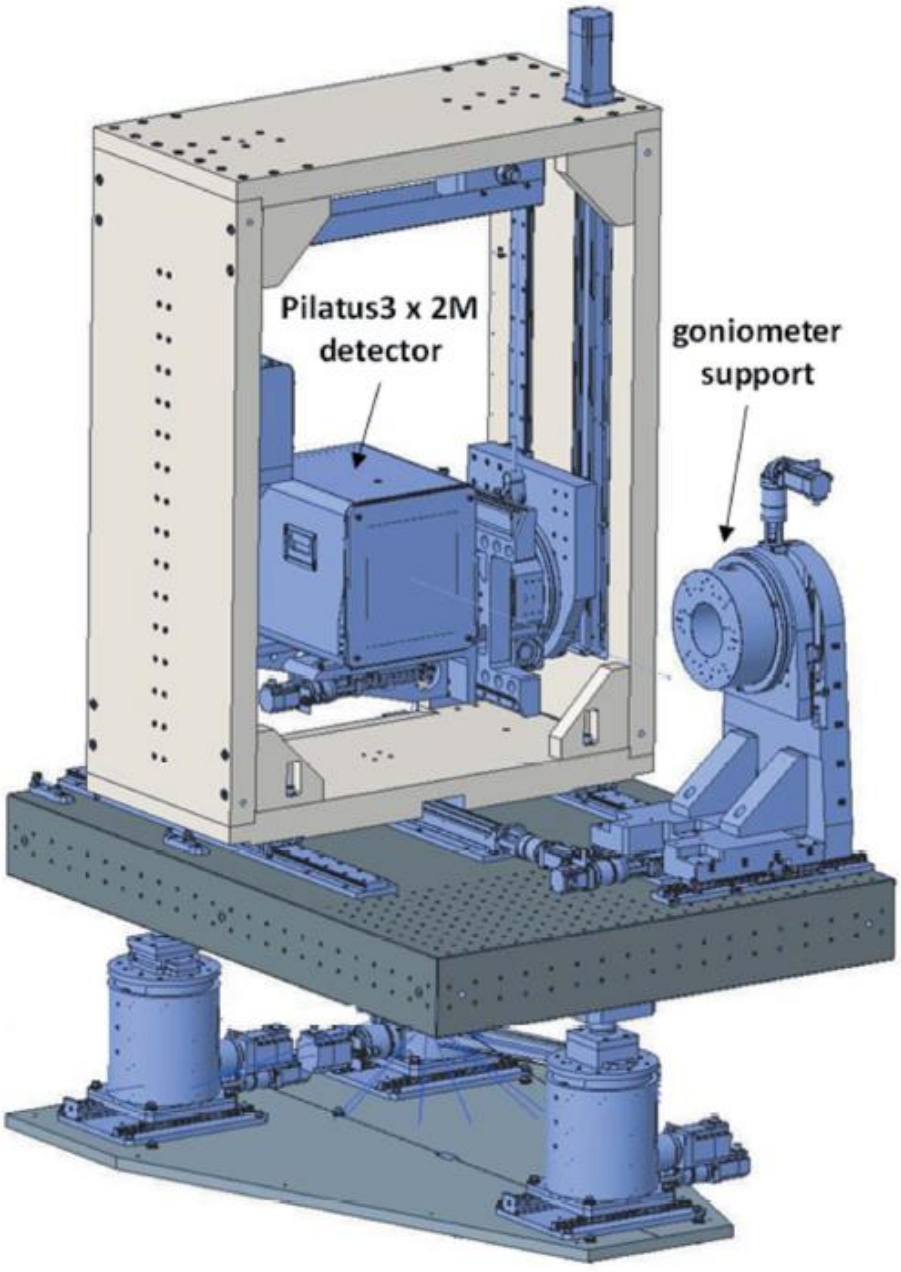

Fig. 3. Pilatus diffractometer station (XRD-2).[2]

2.1.2. Crystal structure verification of PuO_2 NPs

Powder X-ray diffraction (PXRD) is used to characterise PuO_2 nanoparticles, obtained from different initial precursors (Pu(III), Pu(IV) and Pu(V) aqueous solutions) and pH. Data were collected at room temperature at ROBL (λ=0.72756 Å, $2\theta_{max}$=59°). The measured samples were

in a form of wet paste, and belong to the highly-radioactive samples according to ESRF rules since they contain plutonium. Therefore, according to safety rules, all samples were enclosed in the three Kapton capillaries (triple confinement) with outer diameters of 0.81, 1.0, and 1.3 mm respectively. A diffractogram from an empty Kapton capillary was used in the background subtraction procedure for the samples, the obtained diffraction patterns are shown in Fig. 4.

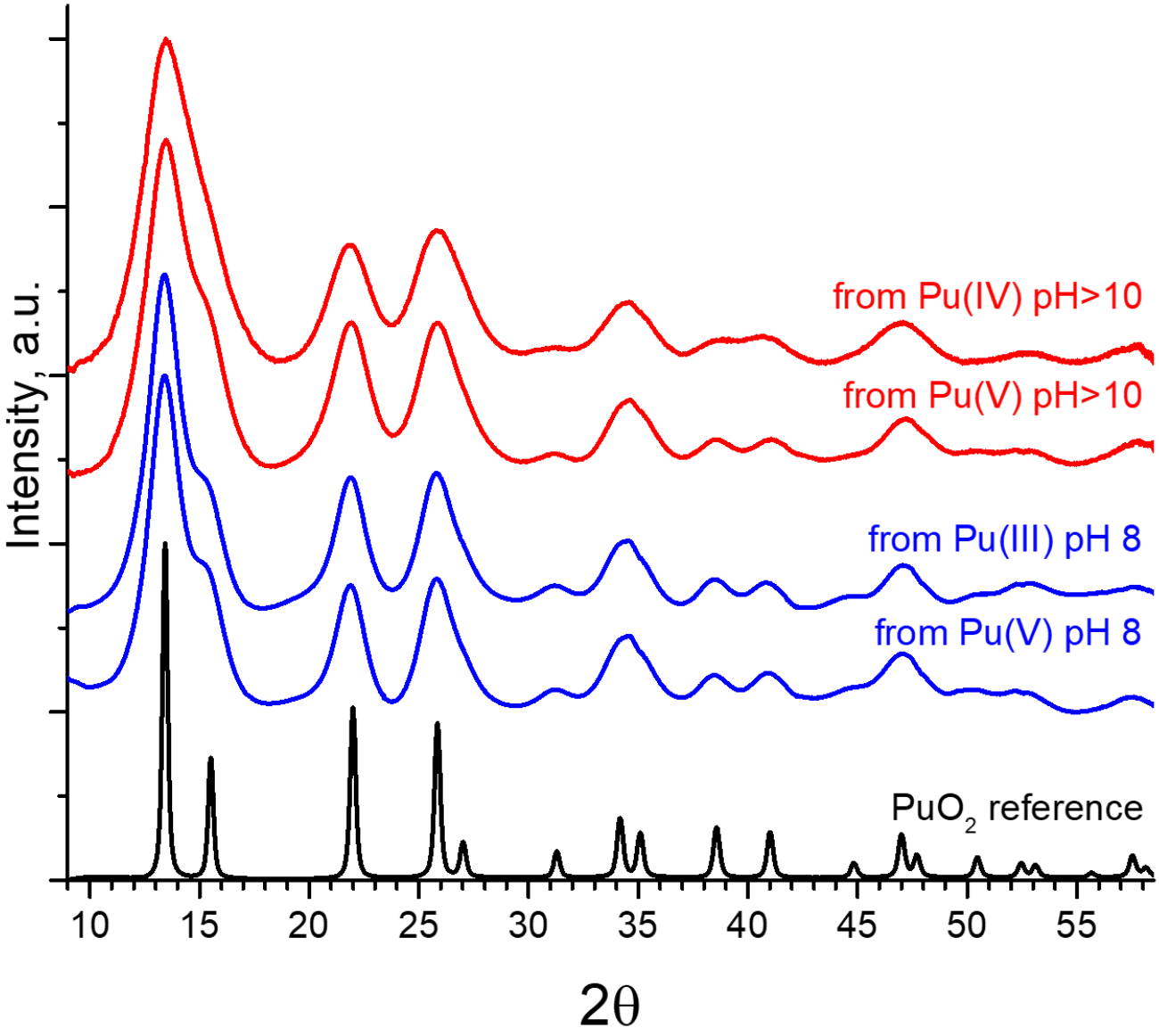

Fig. 4. Diffraction patterns of the precipitates from Pu (III), (IV), (V) in different pH and microcrystalline PuO_2 reference. All samples were measured at ROBL. (Figure from Gerber et al., see)

All peaks observed in the PuO_2 reference diffractogram are present in the patterns of the samples. However, these peaks are much broader due to the nanoscale size of the crystallites. To determine the average particle size, the line broadening at half the maximum intensity (FWHM) β and positions of the peak were determined with TOPAS software[9] and then used in Scherrer's equation:

$$d = \frac{K\lambda}{\beta cos\theta}$$

where d is the mean size of the ordered domains, K– the dimensionless shape factor (Scherrer's constant) – 0.9 for spherical NPs, λ – the X-ray wavelength, and θ is the Bragg angle. The calculation of crystallite size was based on the FWHM of the selected peaks, for each sample, at least six selected peaks were used. Other factors besides crystallite size (*e.g.* microstrain) may cause peak broadening, however, they were not taken into account in this approximation. The results are listed in Table 3. Structural parameters obtained from XRD.

Table 3. Structural parameters obtained from XRD.

Sample	**Mean diameter, nm**	**a, Å**
from Pu(III) pH >10	2.3(2)	-
from Pu(IV) pH >10	1.6(2)	5.399(3)
from Pu(V) pH >10	2.1(2)	5.398(5)
from Pu(III) pH 8	2.2(3)	5.404(4)
from Pu(V) pH 8	2.4(2)	5.407(6)
PuO_2 reference	-	5.4014(3)

The PuO_2 nanocrystals obtained from the different starting solutions are in a narrow size range of 1.6-2.4 nm according to calculations with Scherrer's equation. Besides information about NP size lattice parameters also were refined with WinCSD[10] by least-squares fitting, results are also listed in Table 3.Despite of the small size of the nanoparticles, reported lattice parameter only differs slightly from PuO_2 bulk. It means that the plutonium from the initial aqueous solutions transfers to a PuO_2-like structure. However, there is an equilibrium between several oxidation states in the aqueous solution for the intrinsic colloid formation. One can suppose that the PuO_2 forming from Pu(IV) in solution may cause redox reactions leading to an additional Pu(IV) formation and finally lead to PuO_2 as the dominating product in the solid phase. Moreover, as there is no significant difference between XRD data, one can conclude that neither the initial oxidation state of the actinide nor pH affect the PuO_2 structure, however, it is still possible that other oxidation state might be present. The verification of solely Pu(IV) in NPs will be done in 2.3.3.1.

2.2. XAS

The basic principle of the X-ray absorption spectroscopy is the absorption of X-rays by the sample, leading to electron excitation (generally to the unfilled valence state) and the creation of a core-hole. The relaxation of the system may be achieved in different ways: by emission of photons, ejection of photoelectrons or Auger electrons or secondary electrons with lower energies. The basic physical quantity that is measured in XAFS is the X-ray absorption coefficient μ(E), which describes how strongly X-rays are absorbed as a function of X-ray energy E. There are several factors which may influence the value of μ(E), such as chemical sample composition, sample distribution, chemical bonding, magnetism, light polarization and the wavelength of the X-rays. In the simplest case, μ(E) is quantified by comparing the intensity of the incident beam to that of the transmitted beam from a sample of known thickness d, in accordance to the Beer-Lambert law:

$$I/I_0 = e^{-\mu d}$$

To obtain an absorption spectrum, the scan is going through a range of energies with a slight energy change after each point and absorption is determined at every point. An example of XAS spectrum is shown in Fig. 5.

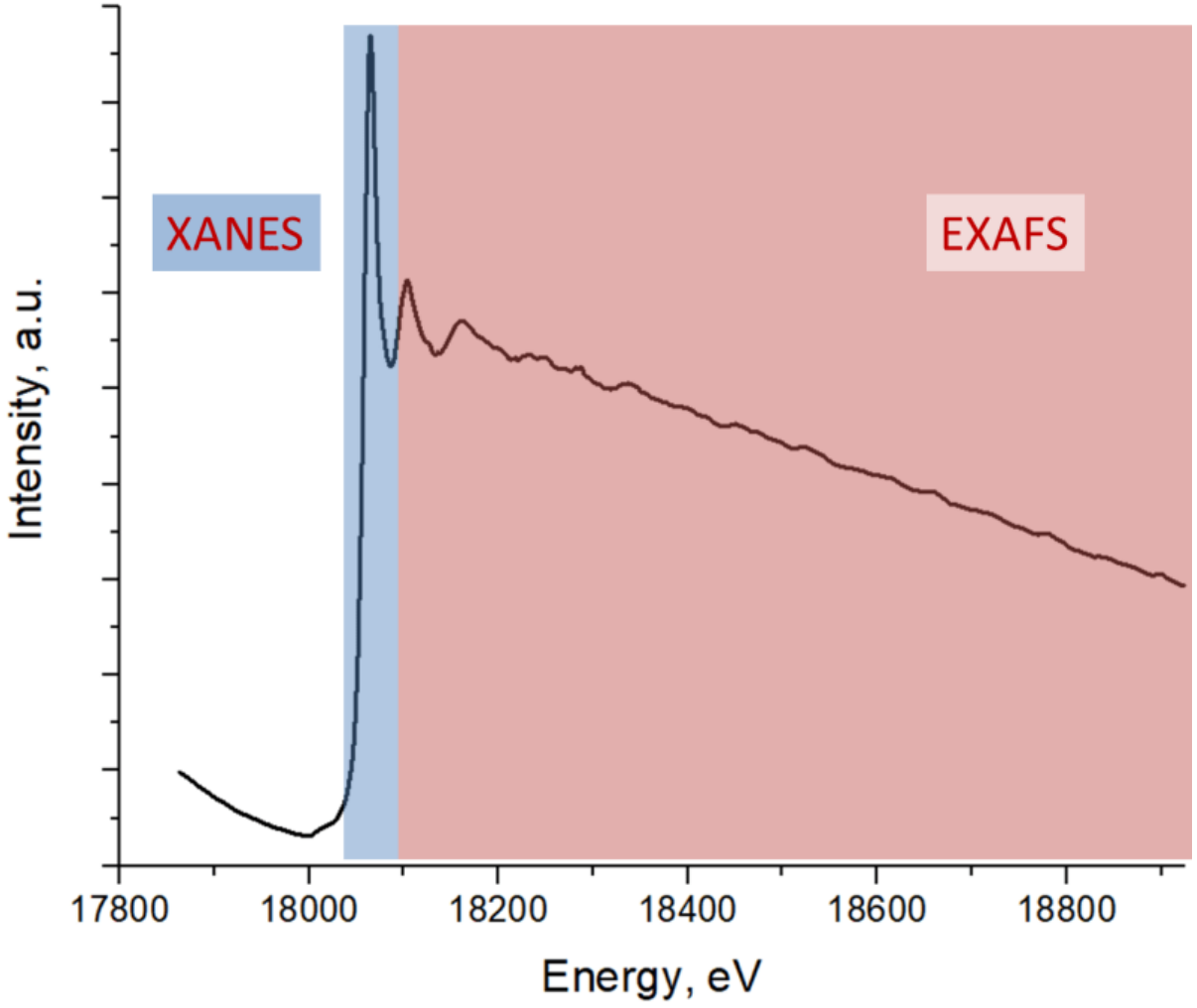

Fig. 5. XAS-spectrum of PuO_2, measured at Rossendorf Beamline, ESRF.

One may pick out four different parts of the spectrum:

- A gradual trend toward lower absorption with energy. It is observed due to the decreasing of μ(E) with energy increasing. Normally this contribution to the spectrum is considered as background.
- A sharp rise in absorption above incident energies. It is called “white line” or absorption edge and it occurs when an electron receives enough energy from X-rays to vacate its bound state in the atom. This energy is specific for each chemical element and each energy state. For Pu L_3 edge this energy is 18057 eV.
- Small peaks or shoulders near the white line are referred to as “pre- and post- edge features”. One can see post-edge at L_3-edge spectrum of $UO_2(NO_3)_2 \cdot 6H_2O$(Fig. 6). There are no pre-edge features at L_3-edge spectrum of $UO_2(NO_3)_2\ 6H_2O$ in that case “pre-edge” is referred to the featureless part of the spectrum before the edge.

- Oscillations spreading from the energy range after the white line till the end of the spectrum, decreasing in the amplitude and increasing in width. This is called the “EXAFS part” of the spectrum.

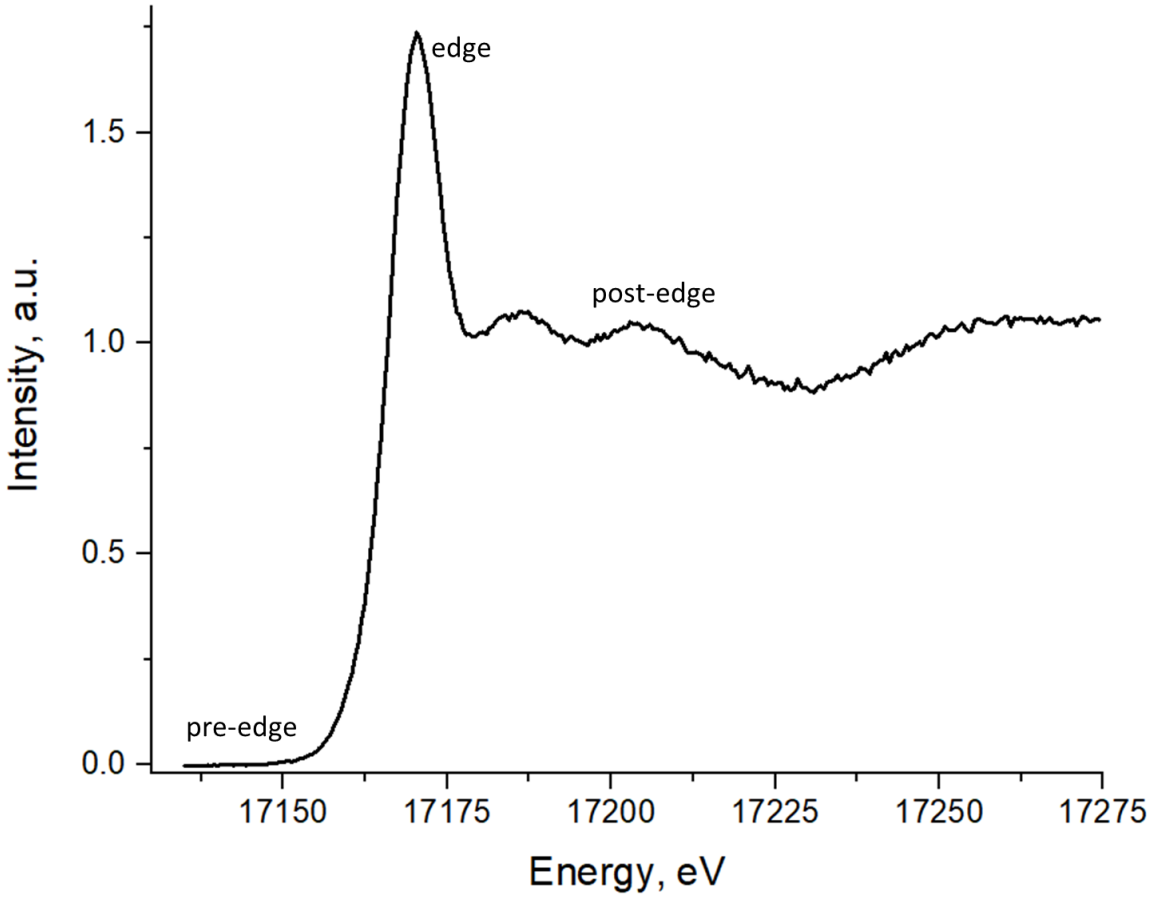

Fig. 6. XANES spectrum of $UO_2(NO_3)_2 \cdot 6H_2O$ measured at Rossendorf Beamline, ESRF.

The whole XAS spectrum is often divided into several parts: Pre-edge, XANES (X-ray absorption near-edge structure) and EXAFS (extended X-ray absorption fine structure). Pre-edge is either featureless or “featureful” part of the spectrum before the white line. It is suggested to consider that XANES region extends to ~50 eV above the absorption edge while EXAFS region extends from ~50 eV above the edge (IUCr Dictionary CXAFS Contribution).

2.2.1. XANES — Theoretical background

In X-ray absorption near-edge structure (XANES) spectroscopy, an X-ray is absorbed by an atom with the ejection of an electron from the core-state to an empty state (Fig. 7). The core hole which is formed after the electron excitation is eventually filled by the electron from the outer shells, followed by either a fluorescent (characteristic for each element) photon or a secondary electron release (Auger electron). Either inelastically scattered photoelectron or the products, emitted after the filling of core-hole are recorded in XANES experiment.

The selection rules determine that, in the dipole approximation, the dipole matrix element is non-zero if the orbital quantum number difference between the final and initial states is one ($\Delta L = \pm 1$ e.g. s→p, p→s/d, etc.) and the spin does not change ($\Delta S=0$).The shape of the absorption spectrum should reproduce the partial density of the ($\Delta L = \pm 1$) empty states projected onto the absorbing site and convoluted with a Lorentzian due to experimental energy broadening. The

selection rule for quadrupole transitions is ΔL = ± 2. However, a quadrupole transition is more than 100 times less intense than a dipole transition. The energy of the X-ray should be at least equal to the binding energy of the corresponding core-level. At this energy a sharp line in the absorption appears, which is called an absorption edge or white line. Fluorescence detected XAS is a photon-in/photon-out process. The incident photon excites a core-electron into an empty state and the subsequent relaxation of the core-hole emits an X-ray photon.

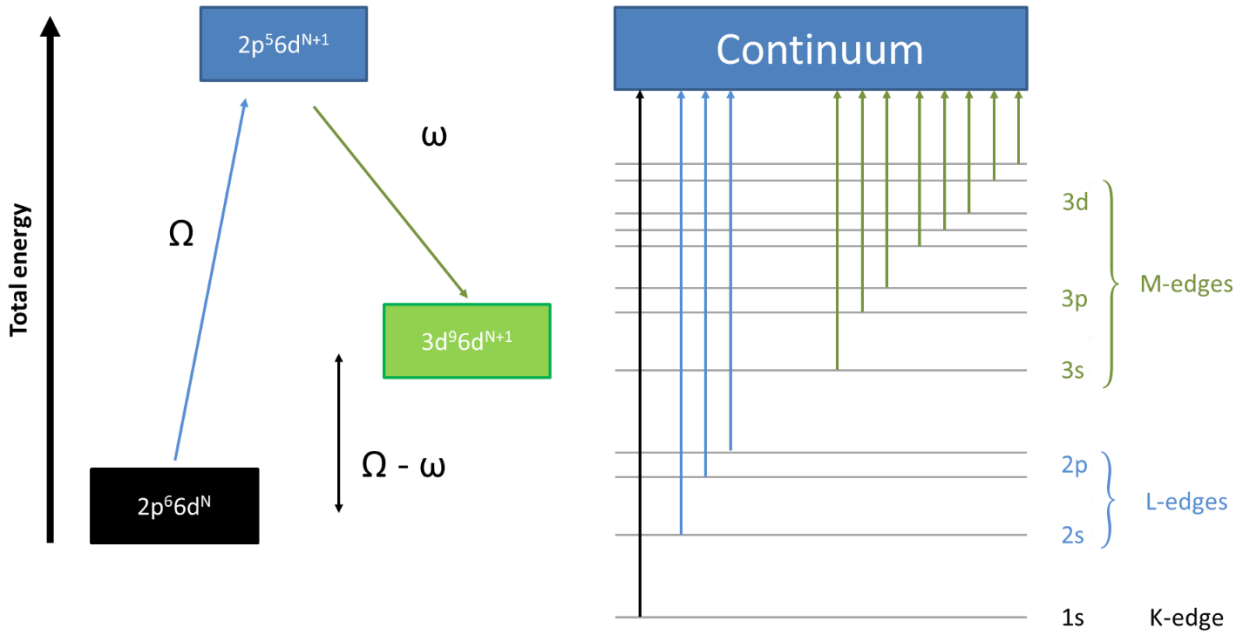

Fig. 7. Total energy diagram and classification of the absorption transitions resulting from the excitation of a core electron.

In accordance with conservation of energy, if the X-ray photon's energy is higher than the binding energy, the electron receives the energy difference as a kinetic energy (so called photoelectron). Due to the wave–particle duality of the electron, electron waves can scatter off of nearby atoms, returning to the absorbing atom and interfere either constructively or destructively. In the case of constructive interference the probability of X-ray absorption is higher.

Aside from scattering elastically off of nearby atoms, photoelectrons may also scatter inelastically off of nearby atoms and excite a valence electron or a phonon. All these processes reduce photoelectron energy. The farther the electron path, the more likely something other than elastic scattering will take place. The mean free path of the photoelectron is the average distance travelled by the photoelectron before the signal is removed from the main channel.

The mean free path of photoelectrons in condensed matter depends strongly on the electron's kinetic energy. For XANES, where photoelectron energies are low, the mean free path is significantly larger then for EXAFS, therefore, a variety of different absorber-scatterer distances are available, *i.e.*, different multiple scattering paths for the photoelectron. It makes theoretical modelling of XANES much more complicated compared to EXAFS. XANES spectra are therefore mostly interpreted and not quantitatively analysed, although there have been recently some positive changes in this direction.[11,12]

2.3. HERFD-XANES

2.3.1. HERFD — Basics and principles

In the high-energy resolution fluorescence detection (HERFD) approach, a spectrometer consisting of several spherically bent crystals is used and positioned to selectively detect a specific emission line. As the experimental broadening of the spectra depends on the lifetime of the final state core-hole, the reduced broadening and the element selectivity in absorption and emission lines makes HERFD XAS a powerful technique to resolve additional features and improve the accuracy in the determination of the electronic structure.

To make a HERFD measurement, one of the two main approaches can be used. First is the scanning approach with a point-to-point focus strategy, where source of the emission, wavelength, dispersive element and X-ray detector are all located in the Rowland circle with radius R_c. Both the wavelength dispersive element (crystal analyzer) and the detector are moved while the emitted energy is scanned.[13] This scheme can result in Johann[14] and Johansson[15] geometries, depending on how crystal analyzers are bent. Besides that, these geometries are almost identical. The common problem is that Johann/Johansson geometry still suffers from the beam size energy resolution dependence at low Bragg angles.

Johansson crystals are bent to $2R_c$, and the inner surface is then ground away to match the radius equal to R_c. This results in an exact focus (Fig. 8) with a high diffraction intensity as the incident and reflected angles are equal with a constant Bragg angle over the entire surface of the crystal.[16] Therefore, a Johansson crystal gives a better resolution over the entire spectrometer range than the Johann crystals.[17] The main drawback of Johansson crystals is that it is difficult and expensive to produce them, therefore the use of Johansson XES spectrometers is scarce.[16,18]

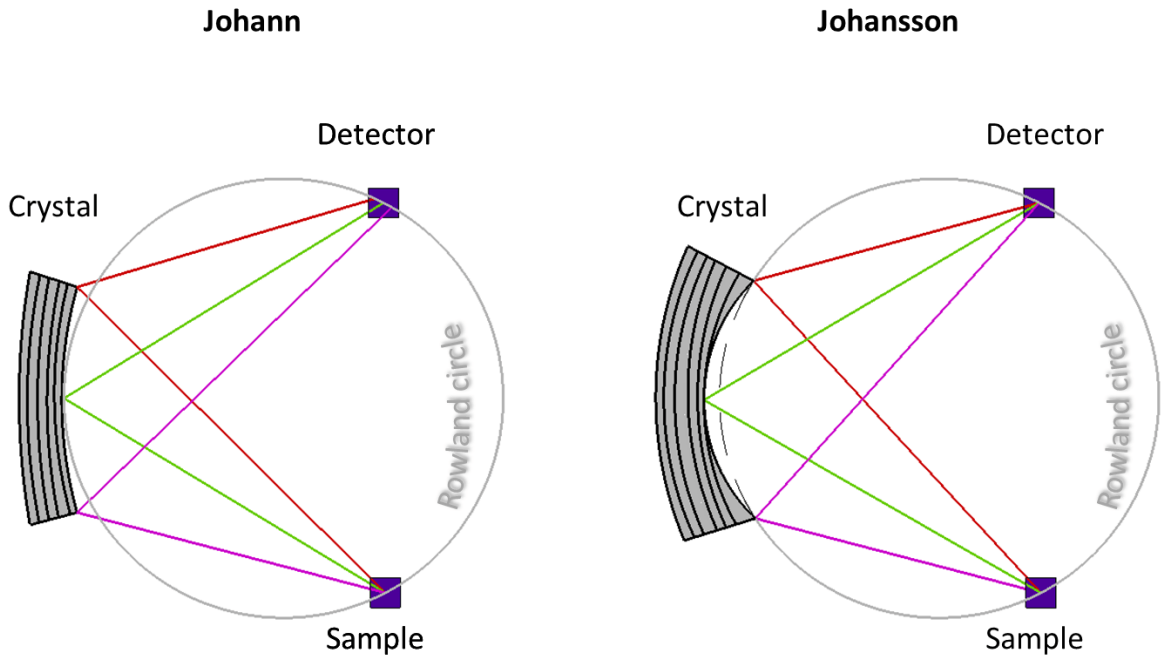

Fig. 8. Principal schemes of Johann and Johansson geometries. Johansson crystal, being not only bent, but also ground to the radius of the Rowland circle, eliminates geometrical aberrations.

Johann crystals are just bent (and not ground), making their manufacturing cheaper and easier. However, for this type of crystals geometrical abberations appear due to the slight variation in

the Bragg angles (Fig. 8). This leads to a contribution to the overall energy resolution. Nevertheless, in most cases, using small crystal analyzers (with diameters of 10–15 cm) posed in a big Rowland circle (R_c = 1m) manages to obtain an overall energy resolution lower than 1 eV.[19] The detailed description of a Johann-type sprectrometer will later be shown in 2.3.2, and in 2.3.3*HERFD — Examples* some illustrations of measurements in this geometry.

The main advantage of the point-to-point scheme is a larger solid angle at a selected energy when using a multi-analyzer system, resulting in a higher detection signal compared to other type of spectrometers.

Nevertheless, for some scientific cases (such as time resolved measurements) dispersive geometry is pivotal. It was first shown by Von Hamos[20] and based on a cylindrically bent crystal (CBC) and two-dimensional pixel detector (Fig. 9).[21–23] The analyzer focuses the photons in one dimension and spatially separates the different energies in the other. The different X-ray energies are detected by a 2D detector, and by appropriate calibration, the spatial dimension can be converted to an emitted energy scale. Besides time resolved experiments, the capability of a simultaneous detection of a large range of emitted X-ray energies is also crucial for radiation-sensitive samples, such as proteins .[24–27] In this geometry none of the components move, i.e. the whole spectrum is acquired at once, significantly decreasing time needed to record one spectrum. It also simplifies the procedure of normalization to the incoming X-ray flux, which is especially beneficial, if XFEL is used as an X-ray source.[22,28,29] Moreover, von a Hamos setup can be installed in a compacted manner if short curvature radiuses are used, energy resolution won't suffer in this case.

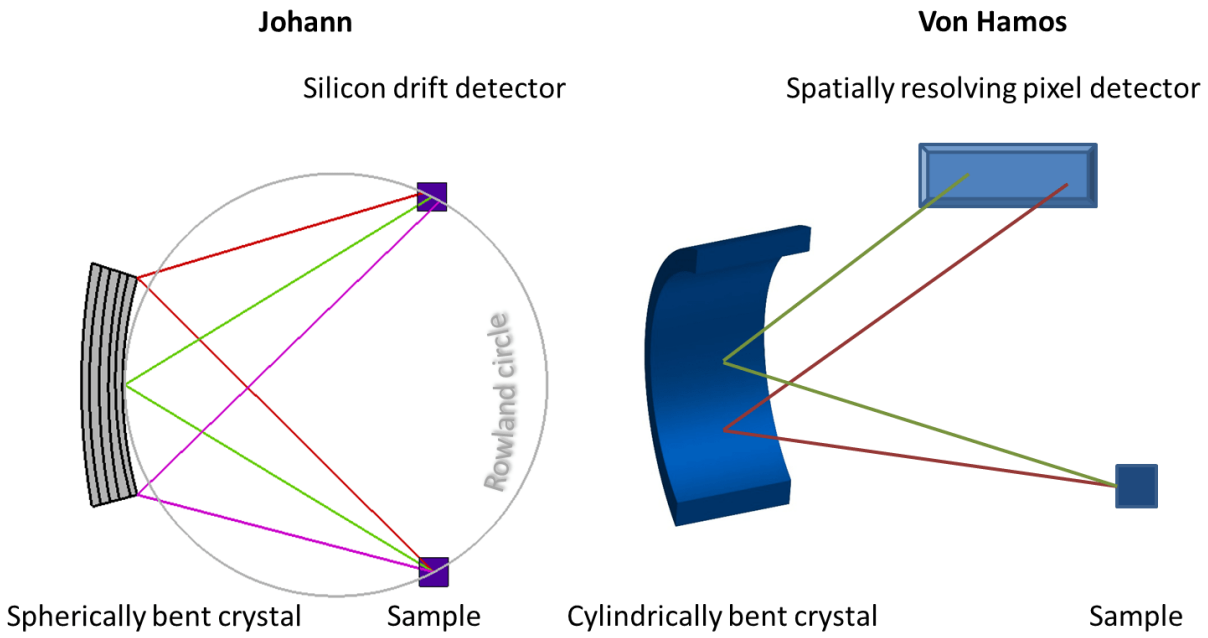

Fig. 9. Principal schemes of Johann and von Hamos geometries.

A typical disadvantage of von Hamos spectrometers is a lower energy resolution,[23] however, with a decent setup optimization even in von Hamos geometry yielding energy resolution below 1 eV at high Bragg angles is possible.[21] In addition, the detected photon flux per energy unit is very small,[22] resulting in lower signal to background ratio compared to the scanning spectrometers.

As a final conclusion, both von Hamos and the Johann/Johansson geometries are capable to achieve an absolute energy resolution below the lifetime of the characteristic emission lines, making a precise analysis of spectral features possible.[21] In terms of efficiency, the detected photon flux per energy unit is very small for von Hamos spectrometers, resulting in a lower signal-to-background ratio when compared with scanning spectrometers, though a von Hamos scheme has better acquisition time as it does not require the scanning of the spatially dispersed spectrum. Another practical aspect is that a Johann/Johansson spectrometer works fine with a quite high beam size of approximately 0.5-1 mm width slits used to tune the fine resolution of the spectrometer, while a von Hamos setup demands a tightly focused beam in the dispersion direction (~50 µm).[30]

2.3.2. The setup of Johann-type spectrometer

In general there are several types of XES spectrometers. In a Johann-type spectrometer energy is scanning along the Bragg angle and Bragg crystal (typically a spherically bent crystal) is used to increase the efficiency of the spectrometer in terms of fluorescence signals from the sample with the same Bragg angle. In that case, sample, detector and crystal need to be in Rowland geometry. The scheme of the spectrometer in this geometry is shown in Fig. 10.

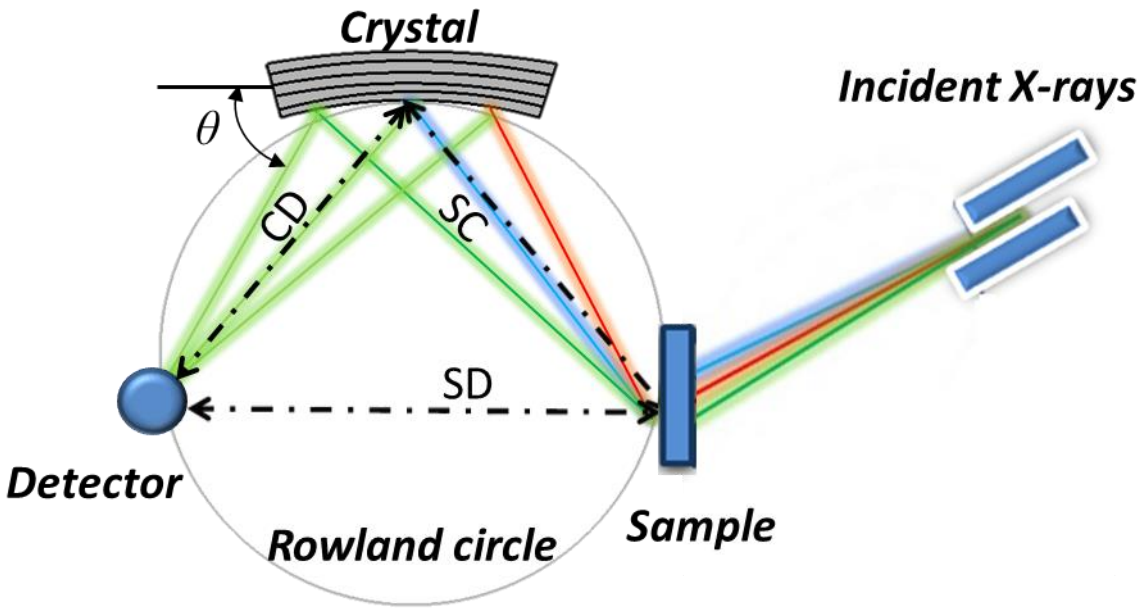

Fig. 10. Schematic drawing of the 1-crystal Johann-type X-ray emission spectrometer.

In HERFD measurements the incident energy is scanning across the absorption edge of the selected element at the maximum of the X-ray emission line. In XES measurements the emitted energy is scanning with a fixed incident energy. The energy of the emitted fluorescence is selected by the Bragg reflection of the crystal analyzer. The fluorescence transmitted through the sample falls on the surface of the monochromator crystal and then part of the beam is reflected at the same angle in accordance with Bragg's law:

$$2d\sin\theta = n\lambda$$

Where θ is a scattering angle, d - the interplanar distance of the crystal, n is the order of reflection and λ- is the wavelength of the X-ray photons. Interplanar distance d can be calculated from the

Miller indices of the crystallographic planes (*h, k, l*) of the crystalline lattice and lattice parameter *a*. For crystals with a cubic symmetry:

$$d=\frac{a^2}{\sqrt{(h^2+k^2+l^2)}}$$

The interplanar distance for the most common Si and Ge crystals is 5.4309 Å and 5.6574 Å respectively. To find the Bragg angle for any energy value (in keV) the equation can be transformed:

$$\theta=arcsin\frac{6.19926n}{dE}$$

The sample, spherically bent crystal analyzer and X-ray detector located on the Rowland circle with R_c radius (Fig. 10). The spherically bent ($2R_c$) crystal analyzer reflects the fluorescence from sample to the detector. For each energy point (i.e. new Bragg angle) the detector should be shifted accordingly along the Rowland circle, the angle of the crystal analyzer also has to be changed. To do this the positions of each component need to be calculated. If sample has a fixed position during the measurements, then the distance between sample and the center of crystal (*SC*) and between centers of crystal and detector (*CD*) must be equal:

$$SC=CD=2R_c sin\theta$$

To keep focusing geometry the detector has to be maintained at an angle of 2θ. At ROBL-II beamline the detector is equipped with a goniometer and two linear stages, that allow moving in two orthogonal directions, DX and DZ. The positions of DX and DZ are calculated as follows:

$$DZ = 2 \times SC \times \sin\frac{(90-\theta)\pi}{180} \times \cos\frac{(90-\theta)\pi}{180}$$

$$DX = 2 \times SC \times sin^2\frac{(90-\theta)\pi}{180}$$

The crystal analyser also has its own goniometer and another two linear stages, AX and AY. The goniometer adjusts crystal position at an angle of 2θ, AX stage moves crystal in SC direction, the value of AX is calculated as:

$$AX = 2 \times R_c \times \sin(\frac{\theta \times \pi}{180})$$

AY linear stage might be substituted with goniometer its function is to direct the reflected X-rays from the crystal to the detector's center.

In order to increase the efficiency of the photons additional crystals can be used. Many beamlines, including ROBL-II, are now equipped with five-element Johann-type X-ray emission spectrometers.[2,31,32] As in a previous example, all parts of the scheme are located at the Rowland circle, however, the exact focusing requirement is met only for the central crystal, and therefore, this optical scheme /includes aberrations (Fig. 11). There are more parameters that need to be calculated for this scheme, namely the positions of each crystal (x_i, y_i, z_i), the azimuthal angle of the crystal surface normal ϕ_i and its polar angle β_i. They can be found with following formulae:[32]

$$x_i = 2 \times R \times \sin\theta \times cos^2\theta + xp_i \times \sin\theta$$

$$y_i = 2 \times R \times \cos\theta \times sin^2\theta - xp_i \times \cos\theta$$

$$z_i = (i - 3) \times dz$$

$$\varphi_i = \pi - \arctan(z_i/(xp_i \times \sin\theta)$$

$$\beta_i = \arctan\frac{\sqrt{z_i^2 + xp_i^2 \times sin^2\theta}}{xp_i \times \cos\theta}$$

$$xp_i = \sqrt{SC^2 \times sin^2\theta - z_i^2}$$

dz is the distance between the crystals along z.

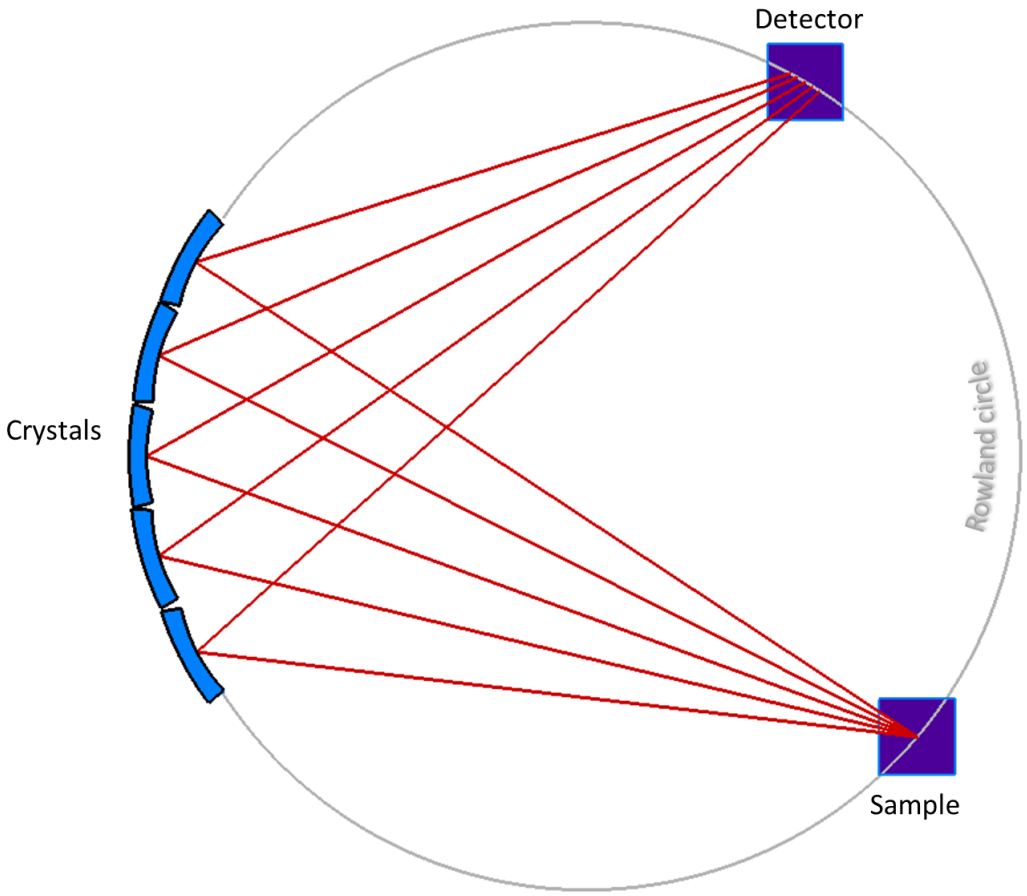

Fig. 11. Schematic drawing of the 5-crystal Johann-type X-ray emission spectrometer.

Detector position and its orientation relative to the sample can be found as follows:

$$x_d = 4 \times R \times \sin\theta \times cos^2\theta$$

$$y_d = 4 \times R \times \cos\theta \times sin^2\theta$$

$$z_d = 0$$

$$\varphi_d = \pi$$

$$\beta_d = \frac{3}{2}\pi - 2\theta$$

The XES station at ROBL-II is able to not only conduct X-ray emission spectroscopy experiments, but also high-energy resolution fluorescence-detection X-ray absorption near-edge structure spectroscopy (HERFD-XANES), resonant inelastic X-ray scattering (RIXS) and/or resonant inelastic X-ray emission spectroscopy (RXES).[33–35] There are two X-ray emission spectrometers at the station, with one and five crystal analysers respectively, though the first one is used only for specific experimental arrangements, requiring X-ray detection in particular scattering geometries.[13] The five-crystal X-ray spectrometer is used for all above-mentioned techniques (Fig. 12). All principal components of the scheme are as follows: spherically bent crystal analyzers, the sample and the detector are arranged in the geometry of Rowland circle. The fluorescence signal emitted from the samples falls on the crystals where it monochromatizes (according to Bragg's law) and then reflected, the monochromatised signal focuses into the detector.

The final resolution is influenced by the selected Bragg angle of the analyzer i.e. by the selected energy, reaching maximum in the backscattering geometry, where Bragg's angle is approaching 90° due to the properties of the Johann geometry.[32] Resolution can be improved by a motorized slit in front of the detector and it has been implemented at ROBL-II as well. The range of Bragg angles is 65-89° for the XES experimental station at ROBL. There are two instruments used for signal detection: an avalanche photodiode (APD) with an area of 10 mm × 10 mm for the samples with high concentration and a Ketek detector with 10 mm diameter and 450 µm Si thickness for the diluted samples.

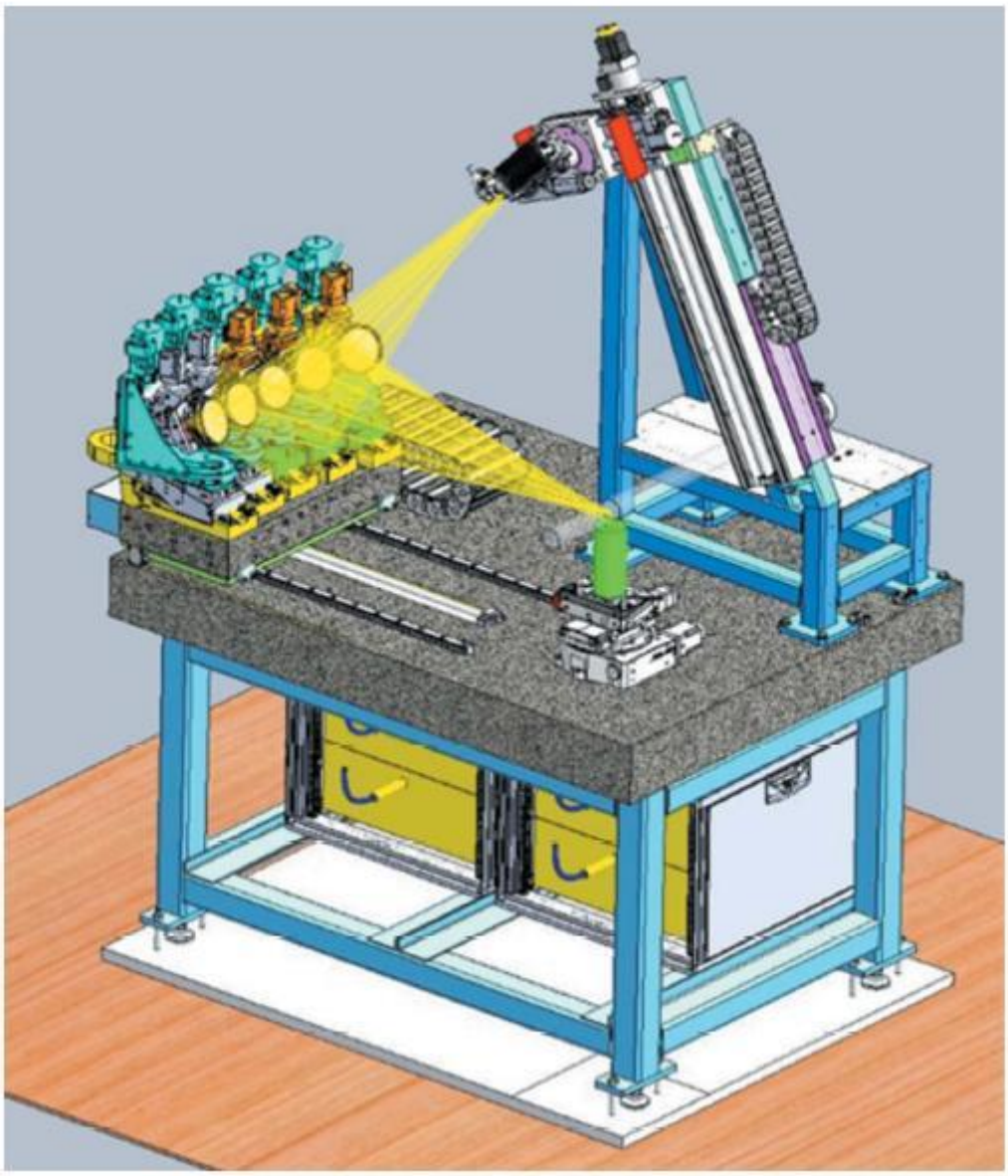

Fig. 12. Schematic drawing of the five-crystal X-ray emission spectrometer.

The bending radius of crystal analyzers is either 0.5 m or 1 m, the diameter is ~100 mm),[36] and the material is Ge or Si. The available stripped crystal analyzers cover an energy range of 3-20 keV and nearly all elements of the periodic table in this range. To obtain more signal at low energies the whole spectrometer can be placed into a He-filled bag in order to reduce fluorescence dissipation at the air.

To conduct a successful energy scan, at each point the positions of sample, crystal analyzers and detector should be according to the Rowland circle geometry.[13] To fulfil these conditions, several motors for crystal analyzers and detector are used. Each crystal analyzer has two linear stages for the vertical and horizontal shifts, a goniometer to focus fluorescence on to the detector and a cradle to select the Bragg angle. The detector is mounted on two linear stages, set up perpendicularly to move vertically and horizontally and the goniometer is used to follow the Bragg angle reflections and to use different detector angles.

The alignment procedure consists of several steps. First of all, the calculations of crystal, sample and detector positions must have been done. It is better to programm these positions according to the formulae to recalculate them automatically if the energy/Bragg angle changed. The next step is the pre-alignment with laser. Laser is used to find a position, where the laser beam will be backscattered, then the correct definition of 90 degrees is possible. Afterwards one need to define bending radius in back scattering geometry to obtain the beam at crystals. Finally the process of 5-crystals alignment on the detector is fulfilled, it is finished when the laser-signal from each crystal is reflected to the detector's window. When laser alignment is finished, the similar procedure is repeated with X-rays. Average time to align the beamline and spectrometer is about 6h, and may vary depending on the Bragg angle, sample type and some other things.

The peculiarities of each technique available at the experimental station are listed in Table 4. Special PyXES software has been developed to simplify the procedure of technique changing and the general operating of the spectrometer by users (Fig. 13). The user chooses the chemical element, the absorption edge (K, L, M), the emission line and the crystal analyzer set, and the software automatically calculates positions of the motors and moves them to these positions. Current motor positions are displayed in a separate window. It also proposes the energy ranges for all methods, though they can be manually adjusted by the user afterwards. The software also allows one to write scripts and macros to set the program up for automatic measuring of several samples and/or techniques.

Table 4. The measurement parameters of the different XES techniques.

	HERFD-XANES	XES	RXES/RIXS
Energy scan	Incident	Emitted	Incident/Emitted
Incident edge position	Across the absorption edge	Above	Below and across the absorption edge
Commentary	Scanning at the maximum of the X-ray emission line	Incident energy is fixed	Incident and emitted energies are scanned

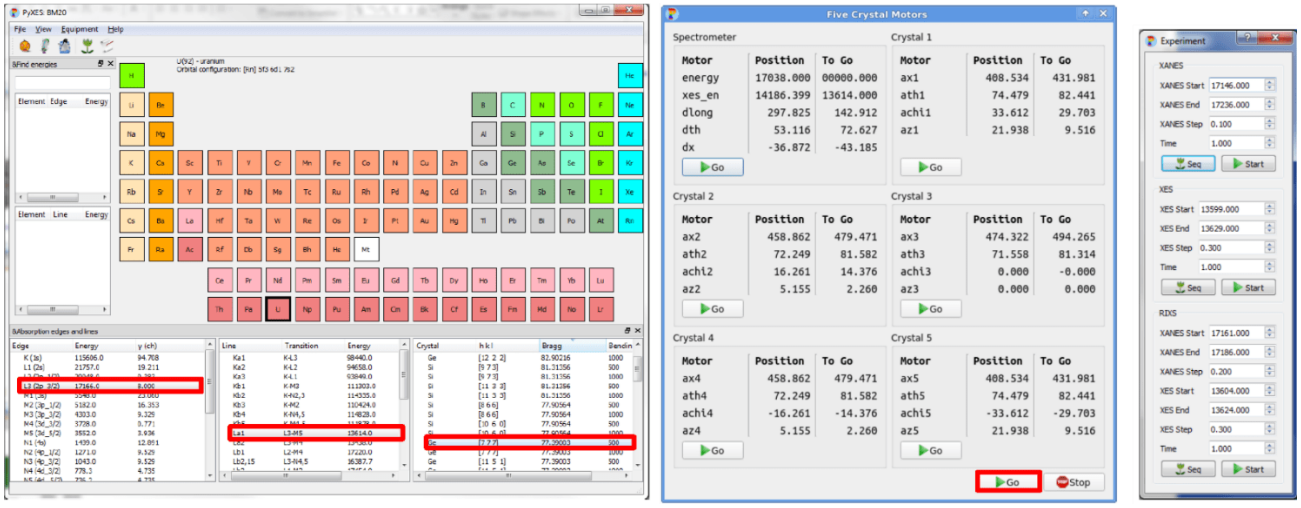

Fig. 13. Screenshot of the custom-designed PyXES software. Left: Periodic table of the elements. After selection of the element and its absorption edge, the corresponding fluorescence lines and the appropriate analyzer crystal is given (all mentioned things are red-bolded). Center:

Calculation of motor positions corresponding to the previously chosen settings. Right: scan settings for XANES, XES, and/or RIXS measurements.

2.3.3. HERFD — Examples

2.3.3.1. The confirmation of solely Pu(IV) in PuO_2 NPs

The plutonium system mentioned earlier in 2.1.2 is also investigated with HERFD method two times with a time delay of three months. The purpose of the second measurement is to investigate the possible presence of the other oxidation states in the structures of PuO_2 NPs obtained from different Pu solutions as well as structural stability of NPs through the time. The experiments were performed at ROBL, Pu L_3 spectra were collected by recording the intensity of the Pu $L_{\alpha 1}$ emission line (~ 14282 eV) as a function of the incident energy. The emission energy was selected using the [777] reflection of spherically bent Si crystal analysers (one for the first experiment and five for the second) (with 0.5 m bending radius[36]) aligned at 75.7° Bragg angle. The intensity was normalised to the incident flux. A combined (incident convoluted with emitted) energy resolution of 2.8 eV was obtained as determined by measuring the full width at half maximum (FWHM) of the elastic peak. The results are shown in Fig. 14. The normalized HERFD-XANES experimental spectra at the Pu L3 edge of Pu NPs samples and PuO2 reference measured at ROBL: a) in January with one crystal b) in April with five crystals.

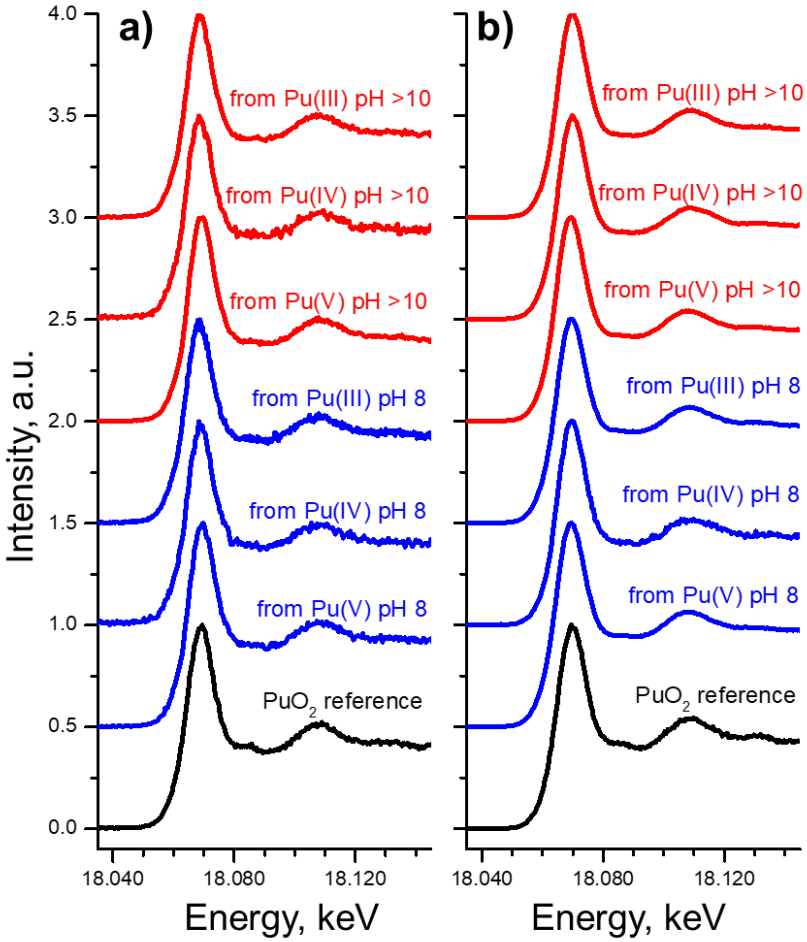

Fig. 14. The normalized HERFD-XANES experimental spectra at the Pu L_3 edge of Pu NPs samples and PuO_2 reference measured at ROBL: a) in January with one crystal b) in April with five crystals.

The Pu L_3 absorption edge refers to the minimum energy needed to excite a core 2*p* electron to the empty Pu 6*d* states.[37] The position and shape of the white line (WL) gives information about the formal valence. One can see that the WL (shape and position) is the same for all samples and the PuO_2 reference as well as pre-edge and post-edge features. It means that the dominating oxidation state for all samples is Pu(IV). A minor WL energy shift among the samples is observed (within 0.2-0.4 eV), which prevents exclusion of tiny amounts of other oxidation states being present. Nevertheless, all other spectral features (pre- and post-edge) are corresponding to those of the PuO_2 reference thus one can conclude the local environment of all samples is similar to PuO_2 and Pu(IV) is the dominating oxidation state. This is also proven with the comparison of the parameters of the WL such as the area under it and FWHM, as seen in Table 5.

Table 5. Gauss fit results of the WL for the samples.

Sample	**Area, (± 1)**	**FWHM, eV**
from Pu(III) pH >10	14	13.0
from Pu(IV) pH >10	13	12.7
from Pu(V) pH >10	13	12.6
from Pu(III) pH 8	14	12.7
from Pu(IV) pH 8	13	13.0
from Pu(V) pH 8	13	12.7
PuO_2 reference	14	13.0

There is a slight difference between all the samples and the reference at an incident energy of ~18090 eV (first post-edge feature). The reason is that the first post-edge feature responsive to the changing in the local environment it was also found and explained for ThO_2 nanoparticles in.[38]

After 3 months, the experiment was conducted again, and this time five crystal analysers were used instead of one. First of all, one can see that signal to noise ratio increased (Fig. 14b) though no changes in the spectral shape were observed, also confirming the stability of PuO_2 NPs over time.

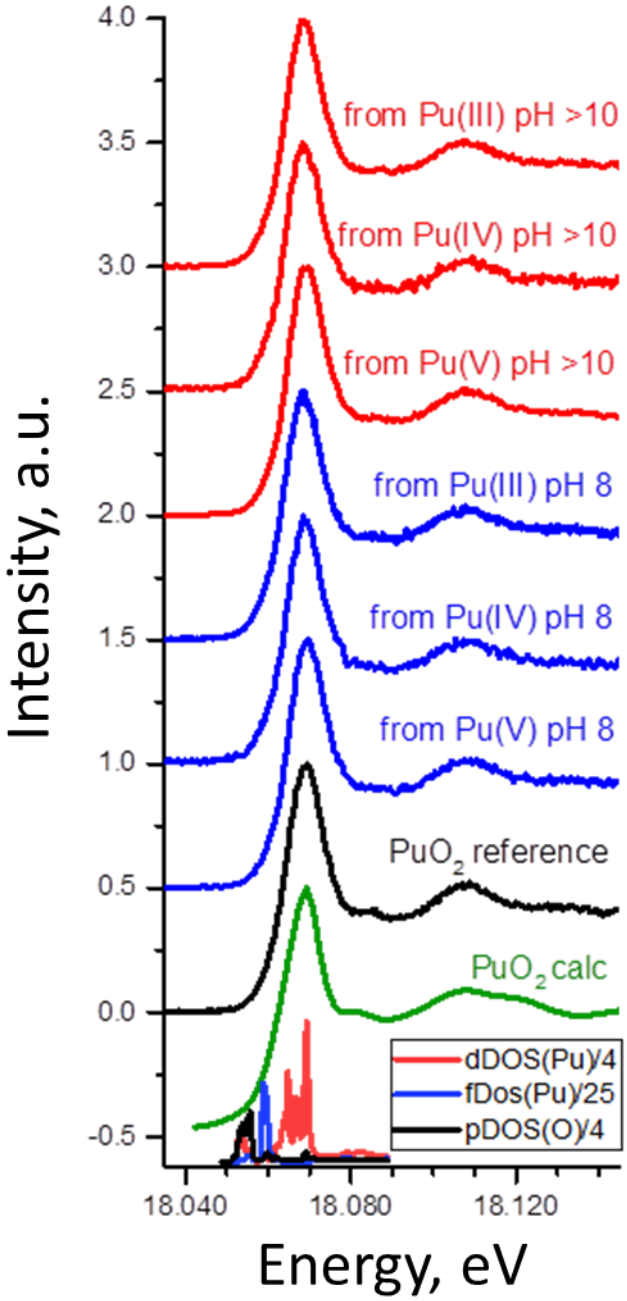

Fig. 15. Pu L_3 HERFD experimental data. Data recorded for six PuO_2 NPs samples and compared with a PuO_2 reference and theoretical calculations, using FEFF9.6. code.[39] The density of states is plotted at the bottom for clarity.

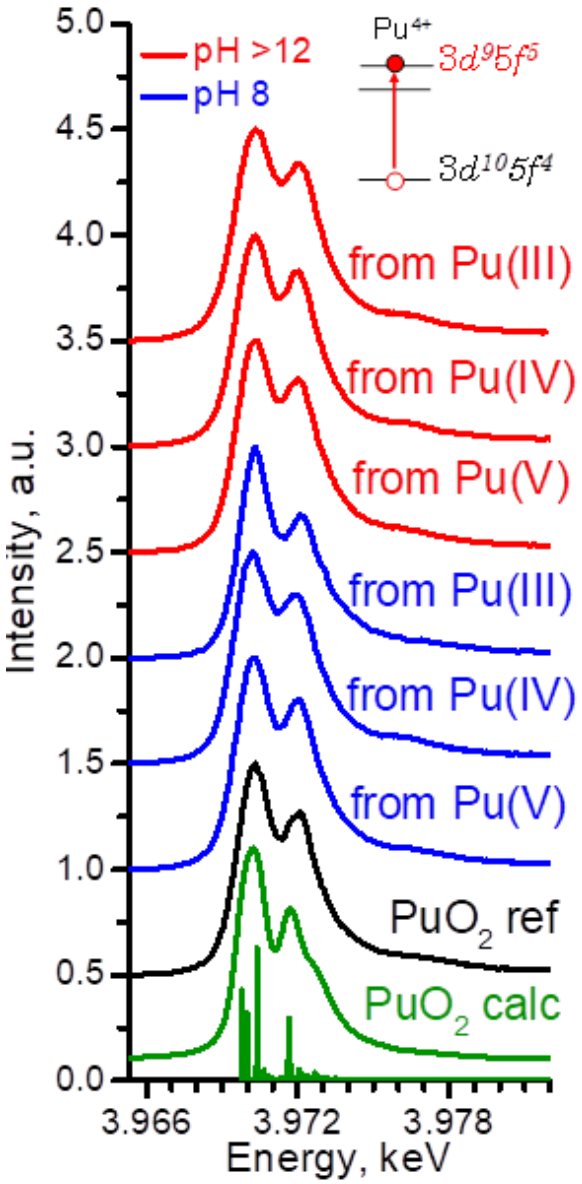

Fig. 16. Pu M_4 HERFD experimental data. Data recorded for six PuO_2 NPs samples and compared with a PuO_2 reference and theoretical calculations, using Anderson impurity model (AIM) approximation.[40]

To reproduce spectral features of PuO_2 the calculations of the PuO_2 L_3 edge spectra and density of states (DOS) were performed using the FEFF9.6. code[39] (Fig. 15). One can see that 6d electronic DOS determines the spectrum in the near-edge region, however, 5f DOS is much closer to the Fermi level and therefore probing that DOS gives more electronic structure information about system. HERFD measurements at the An M_4 edge, characterized by the An 3d-5f electronic transitions, are very powerful for oxidation state identification.[37,41] Reported in Fig. 16 the M_4 edge spectra were measured at ID26 beamline, ESRF.[42] The incident energy was selected using the [111] reflection from a double Si crystal monochromator. Rejection of higher harmonics was achieved by three Si mirrors at angles of 3.0, 3.5, and 4.0 mrad relative to the incident beam. The Pu HERFD spectra at the M_4 edge were obtained by recording the maximum intensity of the Pu M_β emission line (~3534 eV) as a function of the incident energy. The emission energy was selected using the [220] reflection of five spherically bent Si crystal analysers (with 1m bending

radius) aligned at 66.0° Bragg angle. The paths of the incident and emitted X-rays through the air were minimized by employing a He filled bag to avoid losses in intensity due to absorption. An estimated energy resolution (incident convoluted with emitted) found to be an order of 0.4 eV.

Pu M_4 edge spectra for NP samples and PuO_2 reference, as well as calculated with Anderson impurity model (AIM) spectrum of PuO_2 are shown at Fig. 16. AIM fully accounts for electron correlations and treats the inter-atomic interactions as a perturbation. This approach was already shown to be the best for analysis of the HERFD data at the An M_4 edge.[37,41,43] The shape and the position of the spectral features in sample spectra are similar to those in the spectrum of the PuO_2 reference. The HERFD spectrum of PuO_2 shows a sharp peak at ~3970 eV due to the transitions from the $3d_{3/2}$ core level to the unoccupied $5f_{5/2}$ level and a shoulder at higher energy. This splitting of the Pu M_4 main edge transitions is reproduced very well by theoretical calculations and relates to the multiplet splitting of the Pu 5f states.[37] All in all, these results confirm PuO_2-like structure of NPs and show presence of solely Pu(IV).

2.3.3.2. Intermediate Pu(V) solid phase in the course of the PuO_2 synthesis

Another example is devoted to the different oxidation state identification. The investigated system was a Pu(VI) aqueous solution that was neutralized by ammonia addition. Two products were formed during the chemical reaction that lasts longer, than in case of samples from previous examples (several weeks and minutes respectively). During the first weeks, yellow residue precipitated but then dissolved and green precipitation was formed after 5-6 weeks. Both phases were investigated with HERFD method. The L_3 edge measurements were conducted at ROBL and M_4 edge measurements at ID26, while the spectrometer characteristics were the same.

The substantial advantage of HERFD is that it is possible to do qualitative and semi quantitative analysis of oxidation states. Both L_3 (Fig. 17) and M_4 edge (Fig. 18) spectra unequivocally indicates that the intermediate and final phases have plutonium in different oxidation states according to the position of WL. Surprisingly, the intermediate phase contain Pu(V) rather than Pu(VI) which was expected. The only component of the final phase is Pu(IV). FDMNES[44,45] calculations for L_3 edge and AIM calculations for M_4 edge allow specifying the structure of the intermediate phase and explain spectral peculiarities. It is found that intermediate phase is $NH_4Pu(V)O_2CO_3$, and it is first time it has been identified - thanks to the HERFD measurements and theoretical simulations. More details can be found at *Appendix D: Article 4. A novel meta-stable pentavalent plutonium solid phase on the pathway from aqueous Pu(VI) to PuO_2 nanoparticles*

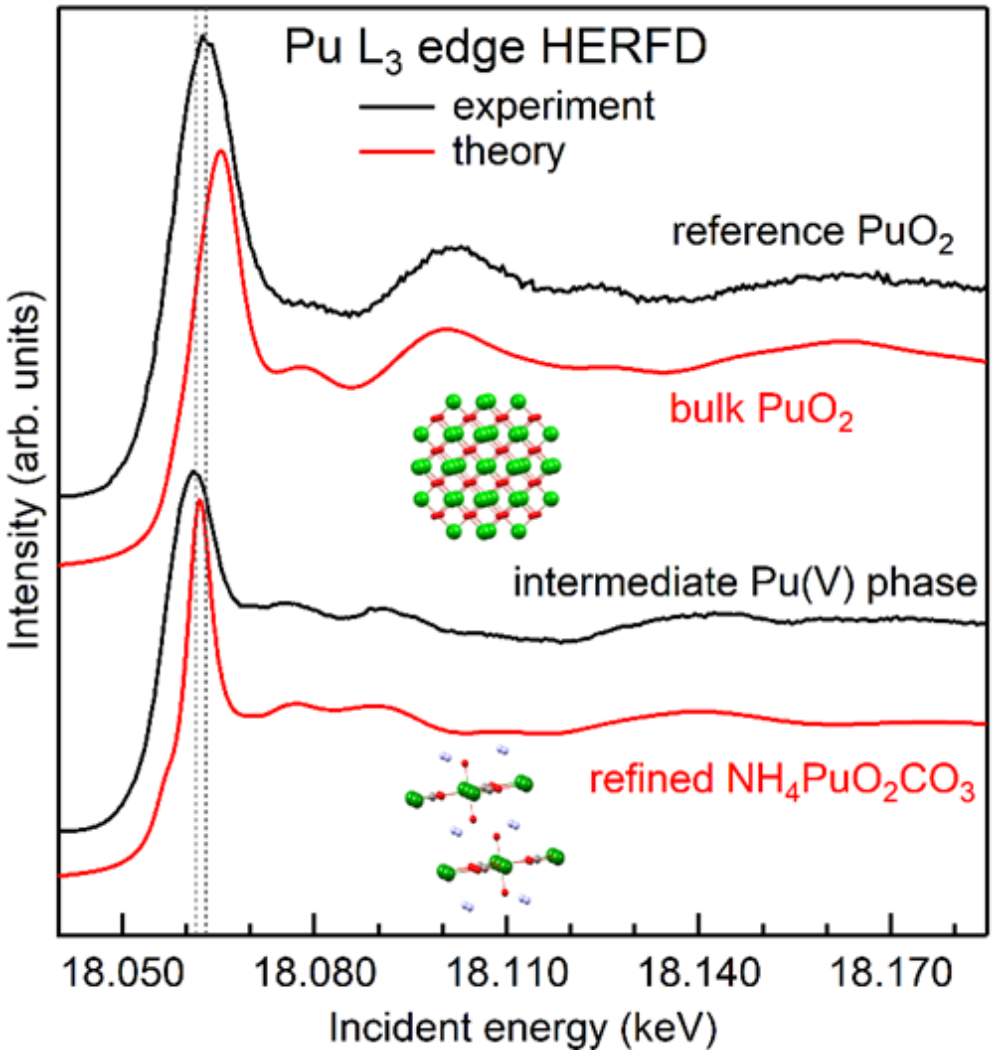

Fig. 17. Pu L_3 HERFD spectra of PuO_2 and the Pu(V) intermediate phase formed during the synthesis of PuO_2 nanoparticles from Pu(VI) precursors at pH 11. Experimental data (black lines) are compared with FDMNES calculations for bulk PuO_2 and $NH_4PuO_2CO_3$ (red lines).

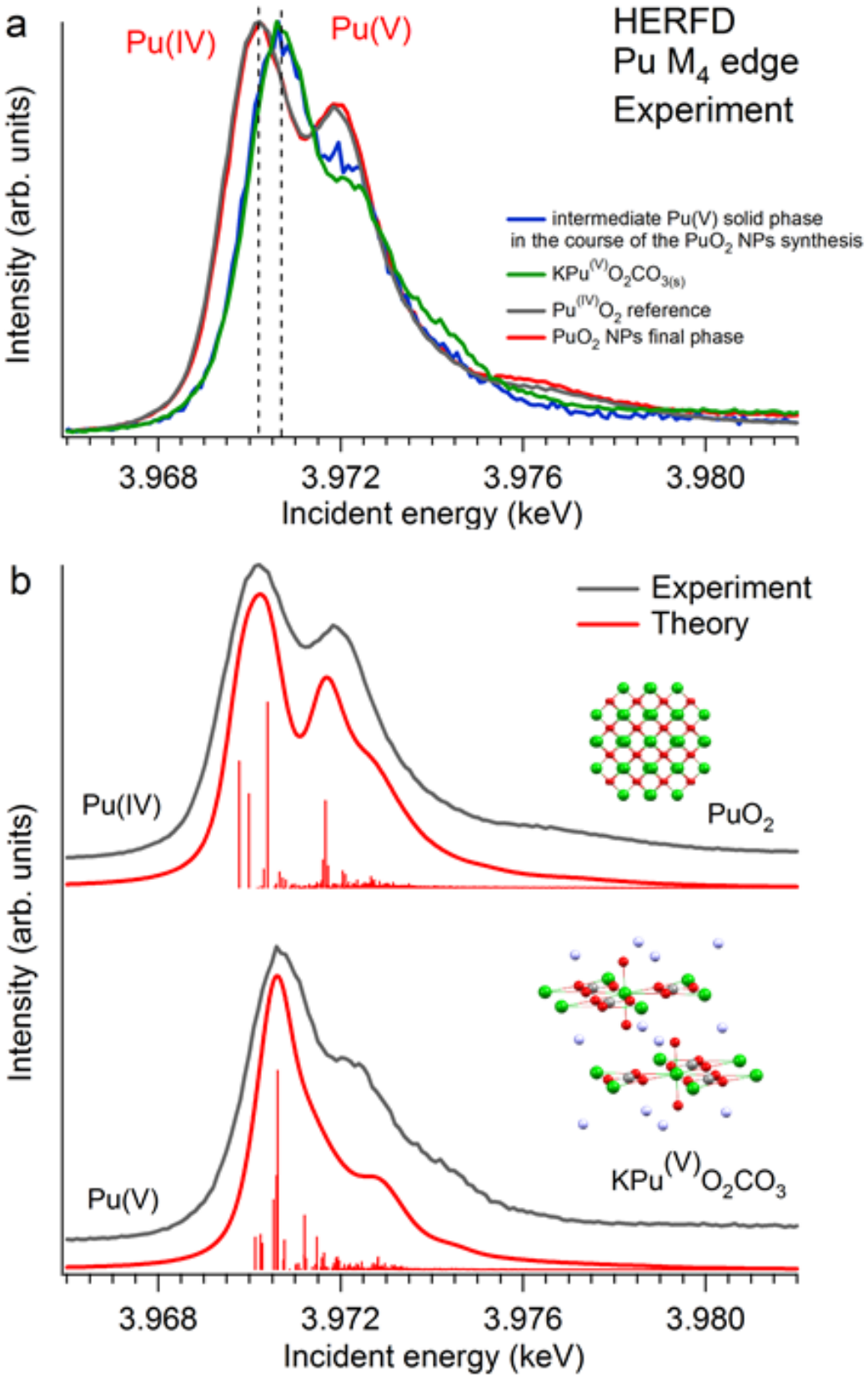

Fig. 18. a) Experimental HERFD data at the Pu M_4 edge from two plutonium phases. Blue curve: spectrum of the intermediate Pu(V) solid phase appearing during the synthesis of the PuO_2 NPs; red curve: spectrum of the final phase of PuO_2 NPs. The spectra of a PuO_2 bulk sample (grey curve) and of $KPuO_2CO_3$(s) (green curve) are also shown as references for Pu(IV) and Pu(V) oxidation states, respectively. b) Experimental HERFD spectra of PuO_2 and $KPuO_2CO_3$(s) compared with the results of AIM calculations.

2.3.3.3. Highlights of the structure–property relationship of UO_2 NPs

The UO_2 NPs were obtained from the U(IV) solution by adding aqueous ammonia solutions in the glovebox under a nitrogen atmosphere, the synthesis factors varied were pH and concentration of the uranium. Special care was taken to maintain the inert conditions during the synthesis, transport and characterisation procedures. Bulk UO_{2+x}, x=0.001 was used as a reference. It was confirmed by HRTEM, XRD and ED that in all cases disregarding pH and uranium concentration small (2-3 nm) crystalline NPs were formed, and crystal structure is UO_2-like. However, due to the existence of various uranium oxides with mixed oxidation states, similarity of their diffraction patterns and the capability of UO_2 to accommodate a large amount of excess oxygen makes diffraction methods unreliable in terms of determination of a partial oxidation of UO_2. It is especially complicated for UO_2 in the form of NPs due to the peak broadening. On the contrary, HERFD at M_4 edge is sensitive to small impurities of different oxidation states, even if they do not deviate the crystal structure.

The HERFD spectra at the U M_4 edge were collected at the CAT-ACT beamline of the KARA facility in Karlsruhe, Germany.[46] Estimated flux at the sample position was in the order of 10^9 ph/sec at an incident energy of 3.8 keV.[4] Sample transport was done in a special argon-filled container in order to avoid oxidation through the kapton foil during the transportation. The spectrometer with one Si crystal analyser (bending radius is 1 m) was used. It was expected that samples might be sensitive to the beam damage, therefore, they were tested for short-term beam damage, making fast HERFD scan too, which was later compared with all HERFD data collected for each sample. Experimental results are shown in Fig. 19.

Due to the similar spectral profile for UO_2 NPs and bulk UO_2 the structural similarity was confirmed. As described in literature, the white line of the UO_2 is an asymmetric peak, though for NP spectra it is even more asymmetric with a pronounced shoulder at higher energy. There are two possible explanations for this effect: partial oxidation or structural distortion. According to theoretical calculations (more details can be found in the published article[47]) distortion or/and change of the coordination numbers greatly affects the intensity of this shoulder. Nevertheless, even if a shoulder appears due to the presence of oxidized uranium species, it is evident that U(IV) is the dominating oxidation state for UO_2 NPs. It is quite surprising as it is assumed that UO_2 is prone to oxidation even in the bulk form, not to mention nanoscale due to the increase of surface-to-value ratio. Nevertheless, these results demonstrate that structural and electronic properties of UO_2 NPs are similar to bulk UO_2 providing the maintenance of reducing or at least inert conditions. Thereby, the properties of UO_2 NPs show the same pattern as PuO_2 NPs (they were discussed in 2.3.3.1). It was shown[48] that no other oxidation states are present in PuO_2 NPs though it could be expected due to the stability of Pu(IV) under these conditions.

The analogy of UO_2 and PuO_2 NPs is important for environmental chemistry as both U(IV) and Pu(IV) are mobile in their colloid forms.[5,75,76]. U(IV) could act as a reference for Pu(IV) not only because of the proximity of ionic radii and crystallochemical properties, but also because at the deep geological repositories the reduced conditions will sustain uranium in the form of U(IV).

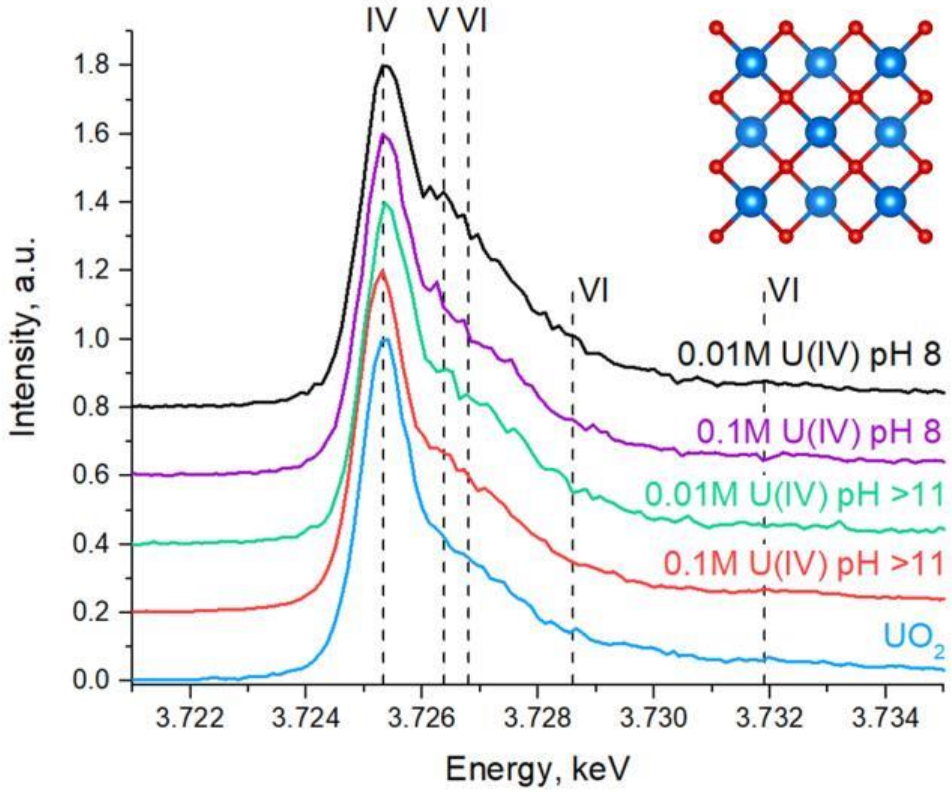

Fig. 19. U M_4 HERFD experimental data recorded for the four UO_2 NPs samples and bulk UO_2 used for comparison. Inset: crystal structure of UO_2

However, the comparison of NPs structural stability shows significant differences between PuO_2 and UO_2 NPs. As was shown in 2.3.3.1, PuO_2 NPs remain intact after at least three months. Time stability of UO_2 NPs has been investigated and it was found that size of NPs increases to 6 nm (calcuted from XRD and HRTEM data) and samples become partially oxidized (Fig. 20b) with time even if samples were kept under inert conditions. The contribution of U(V) considerably increased, though it is evident that the conversion to U_4O_9 has not been completed and the substantial amount of U(IV) is still retained in the aged samples.

The effect of X-ray beam exposure on the fresh samples have also been investigated. To validate that it is indeed the X-ray beam that is responsible for the sample damage, several scans were done at the exact position of the sample, the average of the several scans at the beginning and in the end of exposure were compared (Fig. 20a). The later the scan was done, the more pronounced high-energy shoulder became, resulting in the end in an individual component illustrating the partial oxidation to U(V) and U(VI). More information about UO_2 stability investigations are described in the paper.[47] (*Appendix B: Article 2. Insight into the structure-property relation of UO2 nanoparticles*)

All in all, it was proven that UO_2 NPs are more reactive compared to PuO_2 NPs and it is compulsory to take special care to avoid sample damage. It is needed to maintain inert conditions at any stage of the experiment if it is possible. It is also crucial to do fast scans or/and changing data acquiring position to limit beam exposure. The implementation of cryo conditions may also be a solution, though it has not been checked yet on the UO_2 NPs.

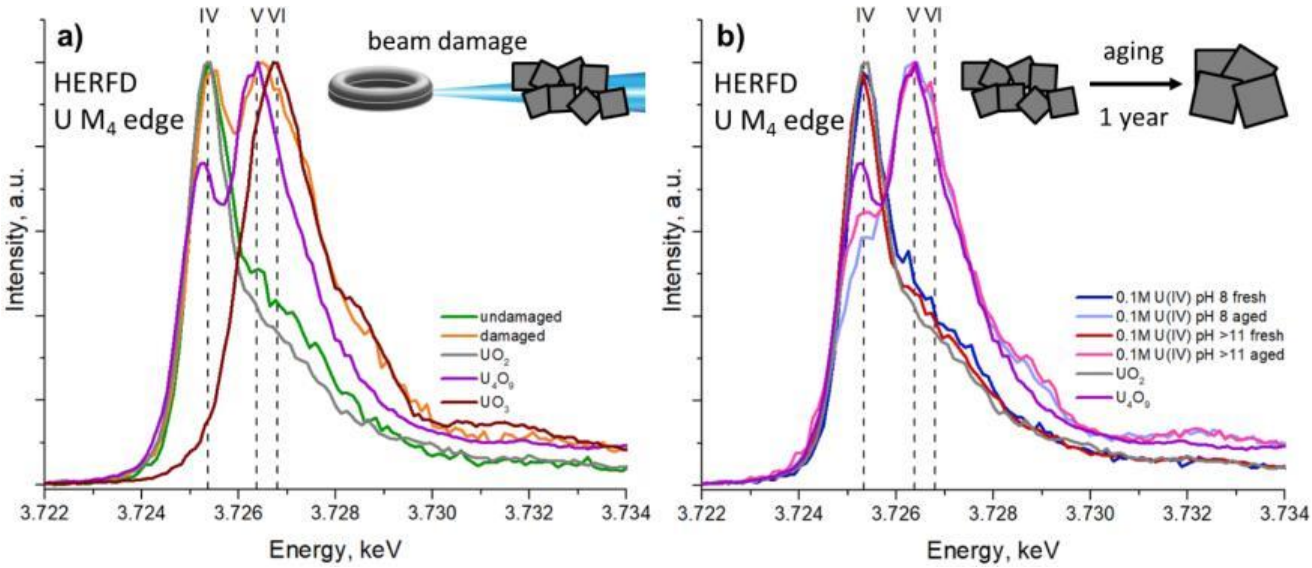

Fig. 20. **HERFD M_4 edge spectra:** a) for 0.01M U(IV) pH >11 before and after beam damage with U(IV), U(IV,V) and U(VI) references. b) for fresh and 1-year-aged 0.1M samples with U(IV) and U(IV,V) references. UO_3 and U_4O_9 reference spectra have been reproduced from Leinders et al.[49]

2.3.3.4. Surface hydroxyl species in CeO_2 NPs

Ce is an analogue of Pu under reducing conditions due to the comparable Ce(III)/Ce(IV) and Pu(III)/Pu(IV) redox transitions and the resemblance of their ionic radii and crystal structure of their dioxides. Besides that, CeO_2 is prominent for its antioxidant and catalytic properties. It is known that at a nanoscale these properties are enhanced due to the increased surface-to-volume ratio and changes in oxygen non-stoichiometry. These changes in turn determine the Ce(IV)/Ce(III) ratio and therefore are perspective for the HERFD studies.

The synthetic route of CeO_2 NPs preparation was similar to those ones for PuO_2 and UO_2 NPs.[47,48] Ce(III) aqueous solution was used as a precursor and mixed with ammonia aqueous solutions. The initial precursor concentration and pH were varied. The obtained yellow precipitation afterwards was washed and dried at different temperatures (more information in the paper[50]) and characterized with XRD, HRTEM and SAXS to determine structural properties, size, shape and spatial organization. In all cases, small crystalline particles were formed with a structure of CeO_2. It was also found that there is a direct correlation between initial concentration of the precursor and the size of obtained NPs (Table 6).

Table 6. Concentration of the precursor and size of obtained CeO_2 NPs.

$Ce(NO_3)_3$ concentration, M	NP size, nm
0.001	2
0.1	5
0.8	8

To find out if CeO_2 NPs contain Ce(III) impurities HERFD measurement was performed. Both L_3 and M_5 edges were probed, L_3 edge measurement was carried out at ROBL by recording the maximum intensity of the Ce Lα1 emission line (4839 eV) as a function of the incident energy. M_5 edge spectra were registered at the PHOENIX beamline at Swiss Light Source (SLS) in Villigen, Switzerland. The incoming flux (I_0) was measured from the total electron yield taken from a polyester foil (0.5 μm thickness), which was coated with 50 nm of nickel. Both total fluorescence

and total electron yield were measured on the sample, though only total electon yield is high enough to be used. The scheme of this measurement mode is shown in Fig. 21. More experimental details one can find in our paper.[50] (*Appendix E: Article 5. Towards the surface hydroxyl species in CeO_2 nanoparticles*)

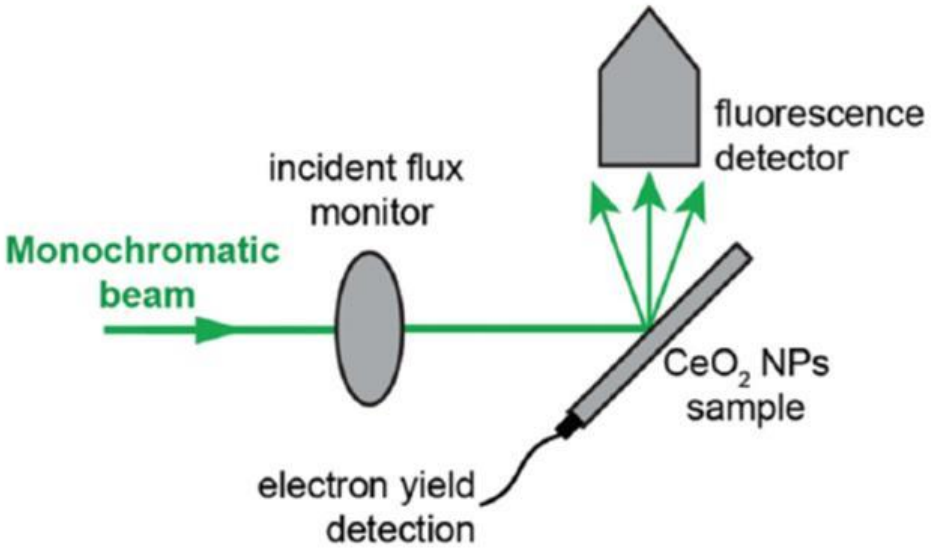

Fig. 21. The scheme of the cerium M_5 edge measurement.

The L_3 edge HERFD spectra show the absence of Ce(III) even for the smallest 2 nm NPs (without any post-synthesis treatment) due to the exceptional presence of Ce(IV) pre-edge. In contrary, the main edge profile varies for NPs of different size. For 8 nm and even 5 nm CeO_2 NPs spectral features reproduce the ones for bulk CeO_2 (for which relatively big 25 nm CeO_2 NPs were chosen), however, 2 nm NPs show different pattern. Main-edge are broader and the intensity of the first one is significantly lower compared to other CeO_2 NPs spectra. As 5d electronic states are responsible for these peaks, the explanation for this effect is an electron delocalization at the surface of NPs and consequently, the decrease of the probability of 2p-5d electron transfer. Besides that, 5d orbitals are active from chemical point of view and capable to form additional bonds with precursor or surfactant materials, most likely, hydroxyl groups. The formation of oxo- or hydroxo-bridged species as intermediate products in the course of the formation of $CatO_2$ NPs (Cat = U, Pu, Ce, Th) is an essential question for f-element chemistry and will be discussed in *Conclusions* later. Nevertheless, Cat(IV) in aqueous solutions is always hydrolyzed, therefore hydroxo groups may exist on the surface of the non-dried samples.

The influence of the surface hydroxyl groups is investigated with ab initio calculations by changing the cluster size of the original CeO_2 model (results are shown at *Appendix E: Article 5. Towards the surface hydroxyl species in CeO2 nanoparticles*).

To further investigate the effects of the surface-to-volume ratio alteration, XAS measurements at Ce M_5 edge were carried out, the results are shown in Fig. 22. The first result was the confirmation of an absence of Ce(III) at the surface of NPs as spectral features are the same for all NPs and they are reproduced in the calculated Ce(IV) system spectrum. Nevertheless, the surface component of the spectrum increases with NP size decreasing. The small post-edge peak at ~889 eV is related to a Ce 4f–O 2p charge-transfer, as a result of strong Ce 4f–O 2p hybridization and configurational mixing. In conclusion, it was shown that soft and hard XAS

results about NPs electronic properties are in a perfect agreement providing the measurements are performed at identical conditions.

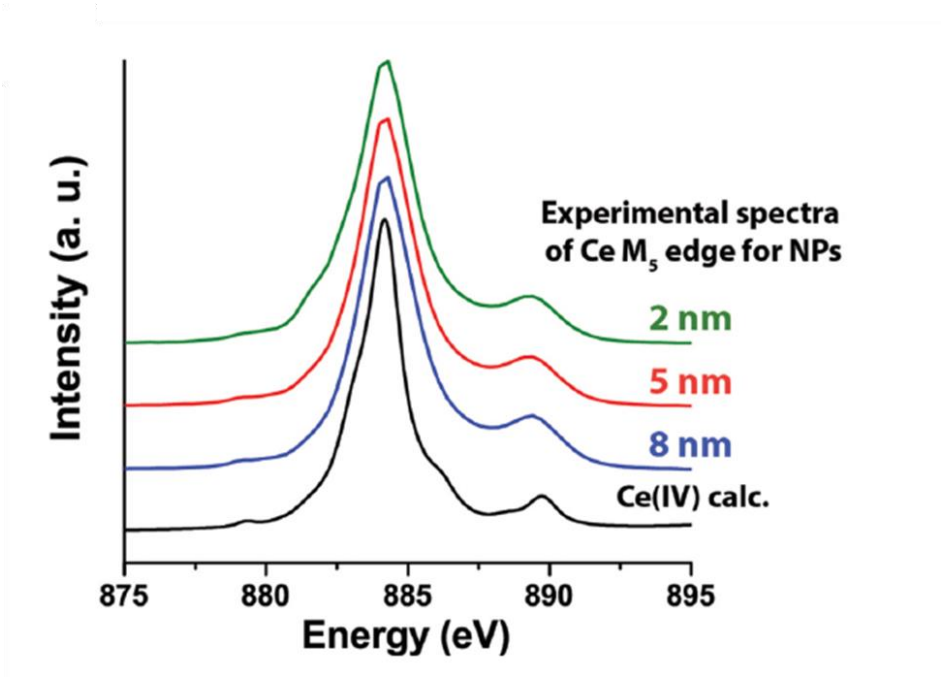

Fig. 22. Ce M_5 edge spectra of CeO_2 NPs compared with calculations.

To investigate how thermal treatment affects surface hydroxylation and accordingly, electronic structure of the NPs 24 h sample heating at 40 °C and 150 °C in air was carried out. Then characterization of structure and electronic properties was executed. It was proven by XRD and HRTEM that neither morphology, nor crystallinity/size distribution were altered. At the same time, the change of Ce L_3 edge spectra was observed (Fig. 23), indicating an electronic structure modification. It is shown that the intensity of the main-edge peaks, their broadening decreasing and this phenomenon are more pronounced in case of 2 nm NPs, though for 5 nm NPs this effect is also observable. No effect of the thermal treatment for 8 nm NPs was detected. It is clear, that dehydroxylation of the NP surface is responsible for the electronic structure changes. Heating leads to the elimination of the OH groups from the surface and this process is more drastic for small NPs as surface contribution is inversely proportional to size. The dehydroxylation process already actively starts at 40 °C causing significant changes in the HERFD spectra of CeO_2 NPs. These results are crucial for the application of CeO_2 NPs as a catalyst as they demonstrate, that OH groups and water on CeO_2 surface possess a long-range effect on the O_2 adsorption, rather then Ce(IV)/Ce(III) transition. It was also proven by chemiluminescent method, that the antioxidant activity of CeO_2 NPs is directly related to the OH groups concentration at the surface and is higher for 2 nm NPs compared to 8 nm NPs.

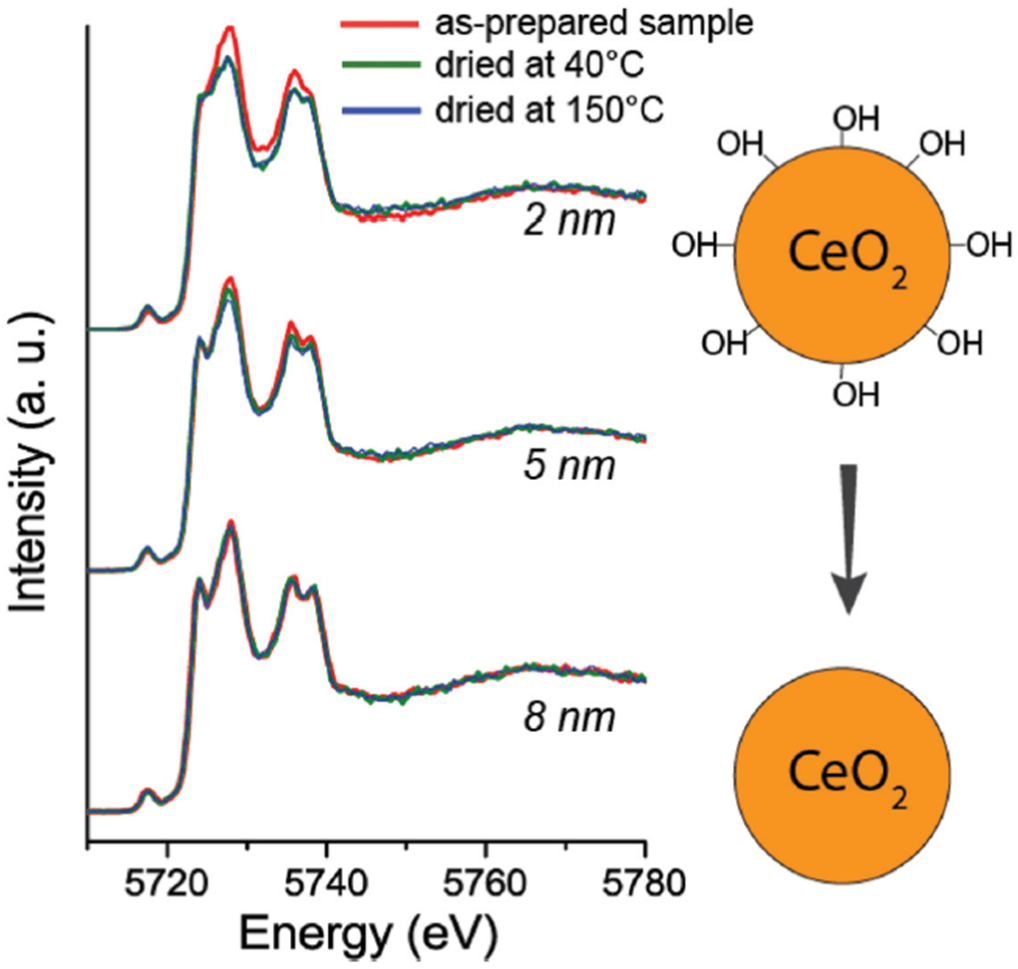

Fig. 23. Ce L_3 edge HERFD spectra before and after thermal treatment.

2.3.3.5. The influence of ThO_2 NPs size on their electronic properties

Another analogue of the PuO_2 is the ThO_2. Th being redox inactive is the simplest of the plutonium analogs. However, it does not make this element and its compounds ordinary or featureless. The exclusion of redox transitions allows us to concentrate on the influence of other parameters, such as size, precursor concentration or thermal treatment on the properties of ThO_2 NPs. Some of these investigations have been already completed and published,[38] some highlights are shown here.

ThO_2 NPs were obtained in a similar manner as previous NPs, by adding a base to a Th(IV) solution, the concentration of the precursor and the temperature of thermal treatment (from 40 to 800 °C) were varied. As usual, XRD and HRTEM were used to obtain information about NP size and crystals structure. The mean particle size and synthesis conditions are listed in Table 7

Table 7. Size of ThO_2 NPs, obtained from XRD data and synthetic conditions.

Th(IV) concentration, M	Temperature of treatment, °C	Mean particle size, nm
0.1	40	2.5
0.1	150	3.8
1	400	5.8
1	800	33.8

Electronic properties of ThO_2 NPs have been investigated with HERFD at Th L_3 edge. The measurements were conducted at ROBL and ID20, ESRF,[51] the experimental data are shown in Fig. 24. 33.8 nm ThO_2 NPs were used as a reference due to the identity of the spectral features with bulk ThO_2. There are three post-edge features where changes were examined marked as A (~16320 eV), B (~16342 eV) and C (~16363 eV). The spectral profile of 5.8 nm NPs was found to be identical, but for 3.8 nm NP feature A is less pronounced and the two others are broader. In the spectrum of 2.5 nm NPs features B and C are even broader while feature A disappears. FDMNES simulations have been done in order to reproduce these features and their transformation with size change, the results are shown in the inset of Fig. 24. One can see that all features, including WL are perfectly reproduced for the calculated spectrum of bulk ThO_2, in terms of the shape, energy position and intensity. Nevertheless, there are two shoulder at the left part of the WL, which are not resolved in the experimental spectra.

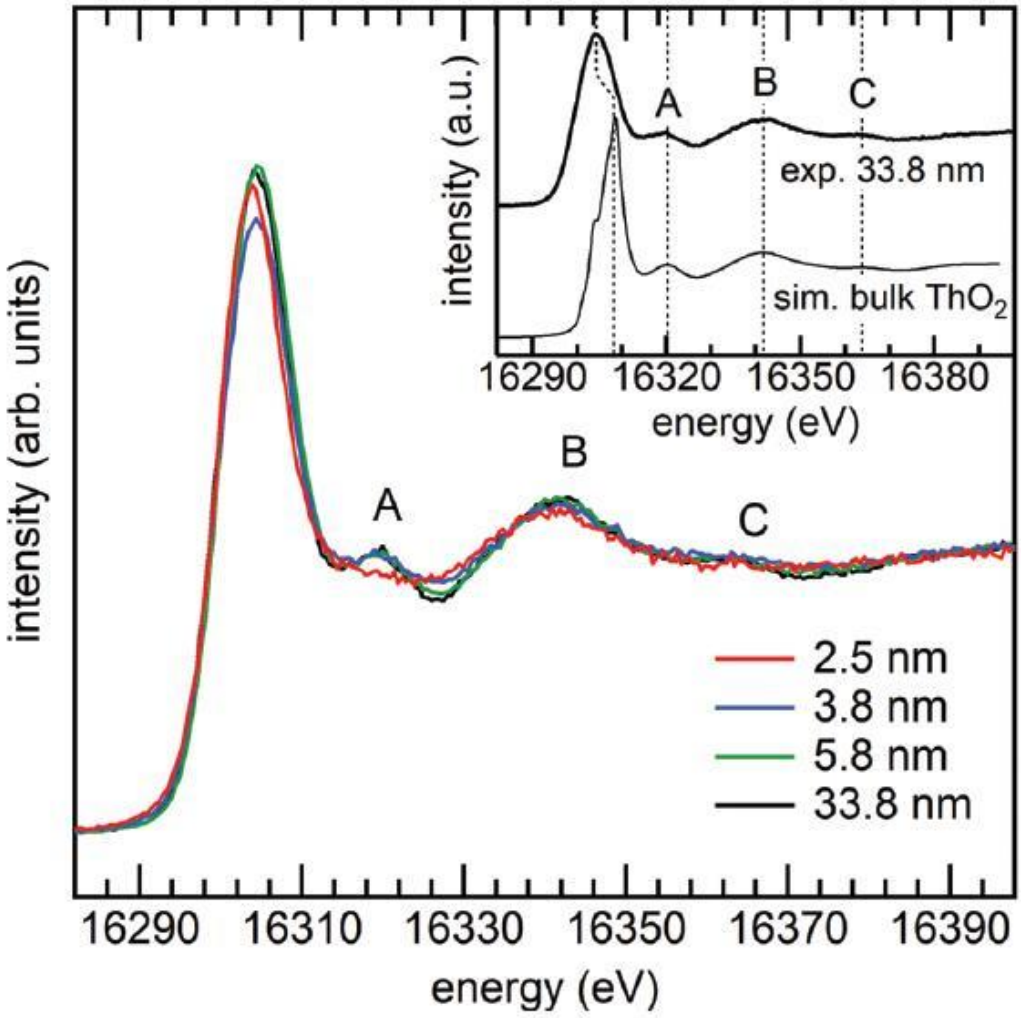

Fig. 24. Th L_3 edge HERFD spectrum on ThO_2 NPs. Inset: HERFD on 33.8 nm NPs and XANES simulation of bulk ThO_2 obtained with FDMNES. Vertical lines mark the main spectral features.

However, it has become possible to observe them in the experimental spectrum when the resolution of 0.5 eV has been achieved, as Fig. 25 proves. To understand the origins of the features, DOS was obtained from FDMNES. It was found that it is mostlyTh d-DOS responsible for the WL post-edge features appearance though O p-DOS also contributes to some features at WL. It also contributes to post-edge features in a similar way with Th d-DOS, which is an indicator of hybridization. More details about simulations can be found in our published work.[38]

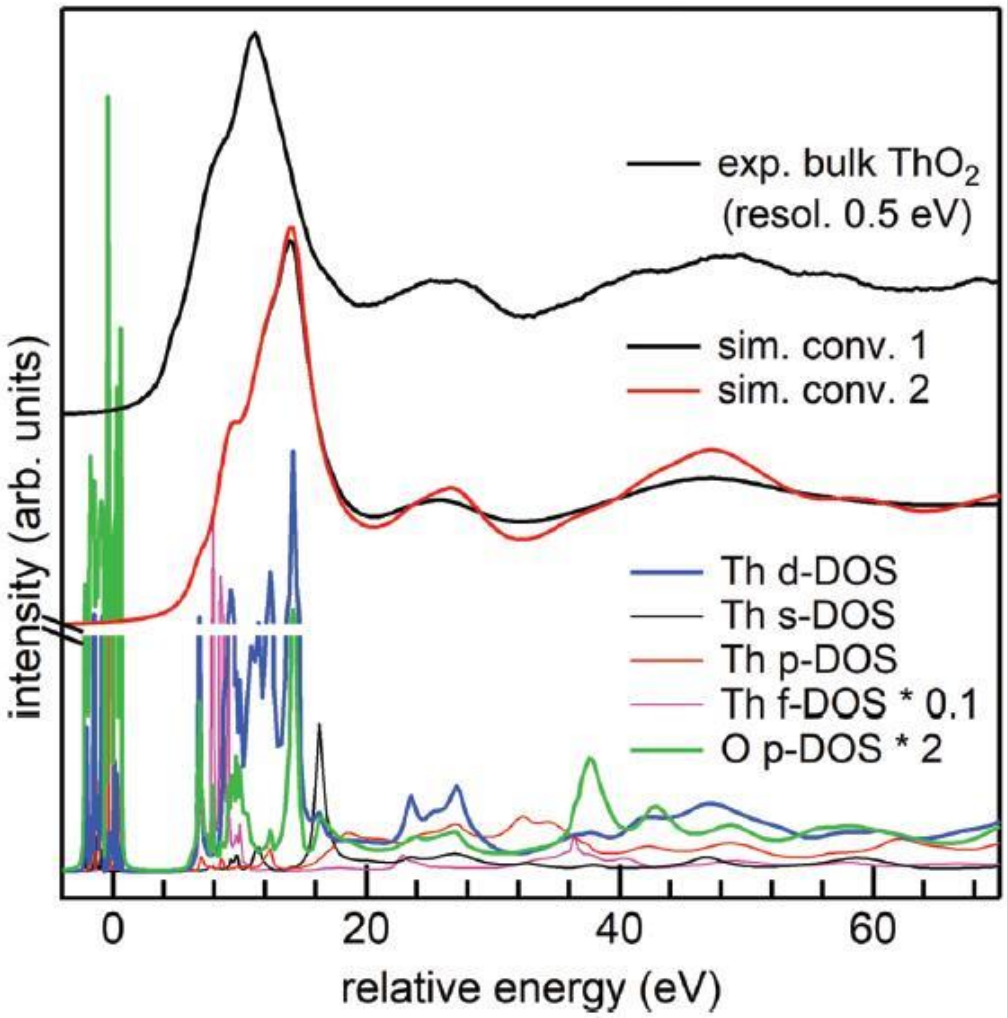

Fig. 25. HERFD spectrum collected with a 0.5 eV resolution (top, black line) compared with two simulations of the L_3 edge XANES of Th in bulk ThO_2 obtained with different convolution parameters. At the bottom the partial DOSs of the Th absorber and of the neighbouring O atoms are shown.

To verify, how surface atoms may affect the XANES spectra three models have been used: spherical, tetrahedral and octahedral clusters of ThO_2. The size of each cluster was chosen to be close to 2.5 nm. Then they were used to simulate with FDMNES the resulting XANES. The details about FDMNES calculations are shown in *Appendix F: Article 6. Understanding the size effects on the electronic structure of ThO2 nanoparticles*. All models reproduce experimental data, and for tetrahedral and octahedral this reproduction is almost quantitative. The reason is the reducing of the coordination numbers compared to the bulk values and the specific collection of Th local environments. Both are strongly correlated with the size and the shape of the NP. Therefore HERFD is a valuable method to study surface interactions for ThO_2 NPs as well as other dioxide NPs.

2.4. EXAFS

2.4.1. EXAFS in a Nutshell

The post-edge oscillations refer to the resulting photoelectron scattering and contain information about local structure: bond distances, number of and type of the neighbours. This region is associated with Extended X-ray Absorption Fine Structure (EXAFS) regime. EXAFS

originates from the photoelectron, being ejecting from the atom after the latter absorbs X-rays. Photoelectron scatters from surrounding atoms, the scattered waves interfere with the original spherical photoelectron wave. The theory of EXAFS is more developed compared to XANES, although not in the last turn because multiple scattering in XANES (in contrast to EXAFS) is more significant. EXAFS can be modelled with the EXAFS equation: (IUCr Dictionary CXAFS Contribution)

$$\chi(k) = \sum_j \frac{N_j S_0^2}{kR_j^2} F_j(k) e^{\frac{-2R_j}{\lambda_j(k)}} e^{-2k^2\sigma_j^2} \sin[2kR_j + \Phi_j(k)]$$

The photoelectron wavenumber k can be defined as:

$$k = \frac{2\pi}{\lambda} = \sqrt{\frac{2m_e(E - E_0)}{\hbar^2}}$$

where E is the X-ray energy, E_0 is the energy of the Absorption Edge, and m_e is the electron mass.

EXAFS equation can be deciphered through the physical process underlying EXAFS. The $F_j(k)$ is the probability that photoelectron scatters (single or multiple) elastically off of a nearby atom *j* at a distance $2R_j$ from the absorber. The degeneracy (i.e. the amount of atoms of the same type) is noted by N_j. The phase shift $\Phi_j(k)$ appears from phase changing of the photoelectron wave after scattering, and constructive interference is taken into account by the expression $\sin[2kR_j + \Phi_j(k)]$. Being a spherical wave, it spreads out isotropically, while the scattering probability decreases as the square of the distance R_j^2. S_0^2 is the amplitude reduction factor, taking into consideration that initial and final states of the absorbing atoms are different. The amplitude reduction factor is a constant, that depends on the element and normally takes values from 0.7 to 1. The factor $e^{\frac{-2R_j}{\lambda_j(k)}}$ is responsible for $\chi(k)$ suppression due to the inelastic photoelectron scattering and due to decay of the core hole. $\lambda_j(k)$ is a mean free path of the photoelectron. The factor $e^{-2k^2\sigma_j^2}$ takes into account local differences in the environment of the absorbing atom, caused by the thermal vibration and static disorder. The σ_j^2 is the mean square radial displacement also known as Debye–Waller factor.

Since the mean free path $\lambda_j(k)$ is of the order of several Angstroms, EXAFS probes the local environment of the absorbing atom, giving us information about short-range structure of materials.

The great advantage of EXAFS is that it can give quantitative information about local environment of the scattering atom: the radial distance and the number of atoms, neighbouring scattering atom. However, in the vast majorities of cases it demands careful data treatment. Starting from the raw data (Fig. 5), the first step is to separate the EXAFS signal from a slow trend towards lower absorption referred to as background. With a background subtraction procedure the normalization of the spectrum is usually done. Normalized spectrum has an edge-jump of unity and this rescaling is done to facilitate the comparison between different samples and theory. The normalized spectrum of PuO_2 is shown in Fig. 26.

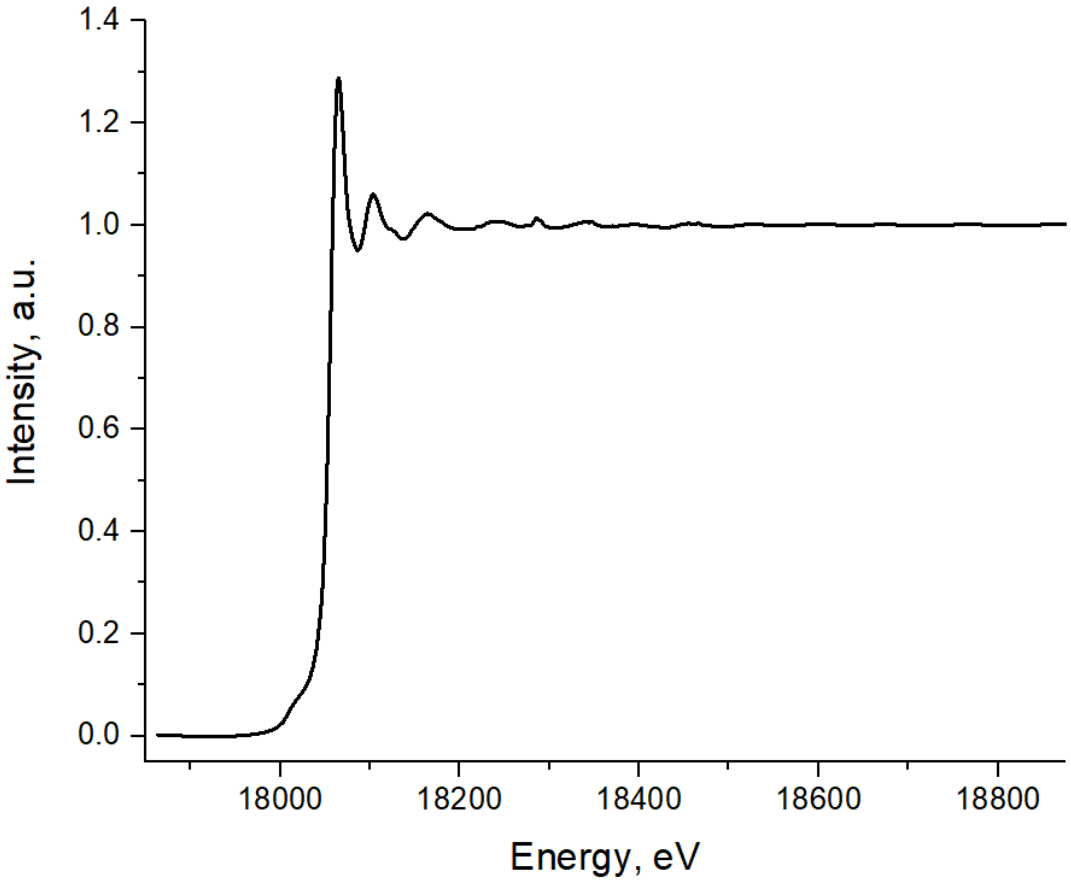

Fig. 26. Normalized spectrum of PuO_2 with subtracted background.

After the spectrum has been normalized, one should convert χ(E) to χ(k) using the correlation between energy and wavenumber. According to the EXAFS equation, the amplitude goes down with k, therefore χ(k) is often multiplied by k, k^2 and k^3 (k-weighting). For heavy elements such as actinides k^2 and k^3 are usually used, as a result the signal at high k becomes more distinct, the undesirable effect of k-weighting is the increase of noise at higher k. One can see the difference between unweighted (Fig. 27a) and weighted spectra (Fig. 27b for k, Fig. 27c for k^3).

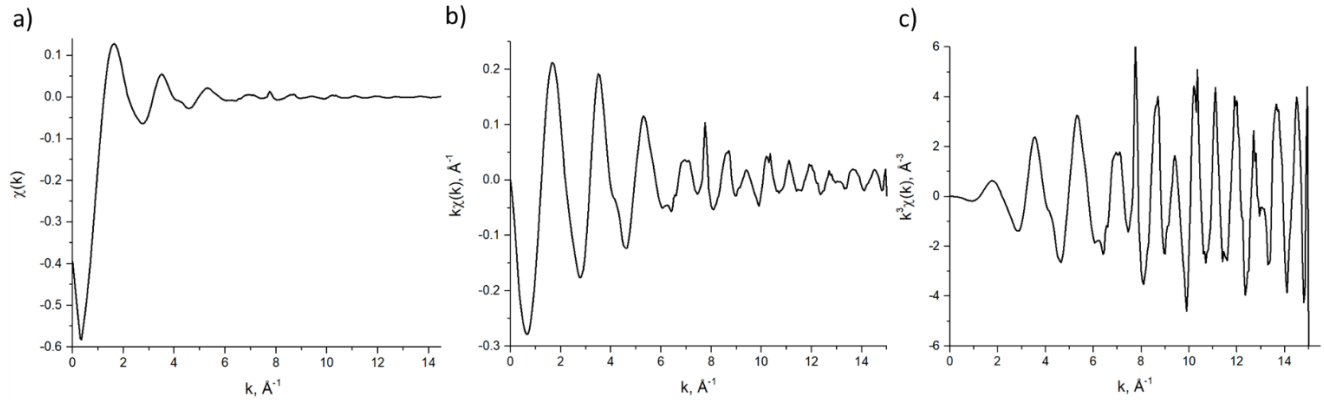

Fig. 27. The χ(k) of PuO_2: a)unweighted, b) weighted by k, c) weighted by k^3.

Further data treatment demands the decomposition of a function into constituent sine waves, it involves Fourier transforms of χ(k). As a result, Fourier transform (FT) magnitudes of experimental EXAFS data are obtained (Fig. 28). Although the procedure of EXAFS analysis, including most common curve fitting to a theoretical standard, can be done both in k-space and

R-space, data representation in R-space form is more clear as one can obtain an important information about sample directly due to the similarity between magnitude of the Fourier transforms and a radial distribution function.

There are three common methods of EXAFS measurement: transmission, fluorescence and electron yield. The measurement in transmission geometry is straightforward: the intensity before and after the sample is recorded and then one is divided by the other. The last two methods are based on the processes taking place after the absorption of the X-ray by the atom. The hole, formed after the electron was ejected from the atom, can be filled by an electron from a higher level. In that case, a characteristic photon is emitted with an energy equal to the difference between two orbitals. This emission is called fluorescent and fluorescence can be measured and compared with intensity upstream of the sample. However, instead of photon emittance, core-hole filling may be accompanied by the emission of a high-energy electron, this is called the Auger effect. In the electron yield, measurement mode the amount of emitted electrons is compared to the initial intensity. Auger effect and fluorescence are competing processes, the probability of characteristic X-ray emission is increases with the atomic number of the element.

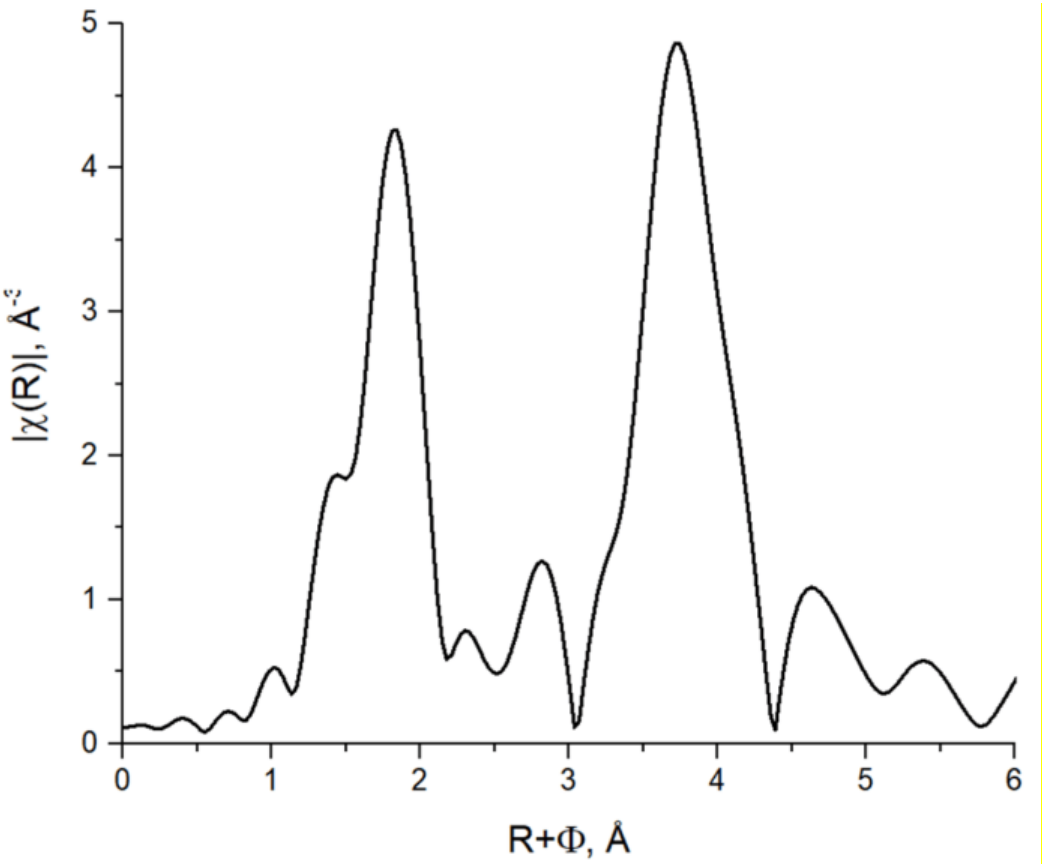

Fig. 28. Fourier transform (FT) magnitude of experimental EXAFS data from PuO_2.

2.4.2. XAFS experimental station at ROBL-II

AT ROBL-II the XAFS experimental station is the one closest to the initial synchrotron source. It operates with an unfocused (2 mm × 10 mm) beam achieved by locating the station out of focus of the toroidal mirror. The beam passes through a back-side extension with Kapton windows, samples are exposed through the glovebox, but ionization and fluorescence detectors are outside (Fig. 29). The glovebox is equipped with two multisampling stages, one for room-temperature

measurements (up to 8 samples) and the other one used for measurements at cryogenic conditions (up to 6 samples). Both stages are automated, i.e., can be moved vertically by motors to expose the current sample to the incident beam. Switching modes between measurement and sample loading is done manually by a tray system, also in the glovebox. For cryogenic measurements, closed-cycle He cryostat (CryoVac) is used.[2]

There are two detectors with electrical cooling used to collect XAFS spectra: Ge and Si multi-element solid state detectors. For the EXAFS measurement discussed in 2.4.3, 12-element germanium detector (Canberra) was used, the experimental details are shown at *Appendix A: Article 1. The missing pieces of the PuO_2 nanoparticle puzzle*)

There are many inhouse data analysis tools, that can be used to derive as much information as possible from XAFS data, such as a wavelet plot analysis, iterative transformation factor analysis (ITFA),[52,53] Monte-Carlo simulations,[48,53] Landweber iteration for the direct derivation of the radial pair distiribution function[48,54] and artificial intelligence approaches.[55]

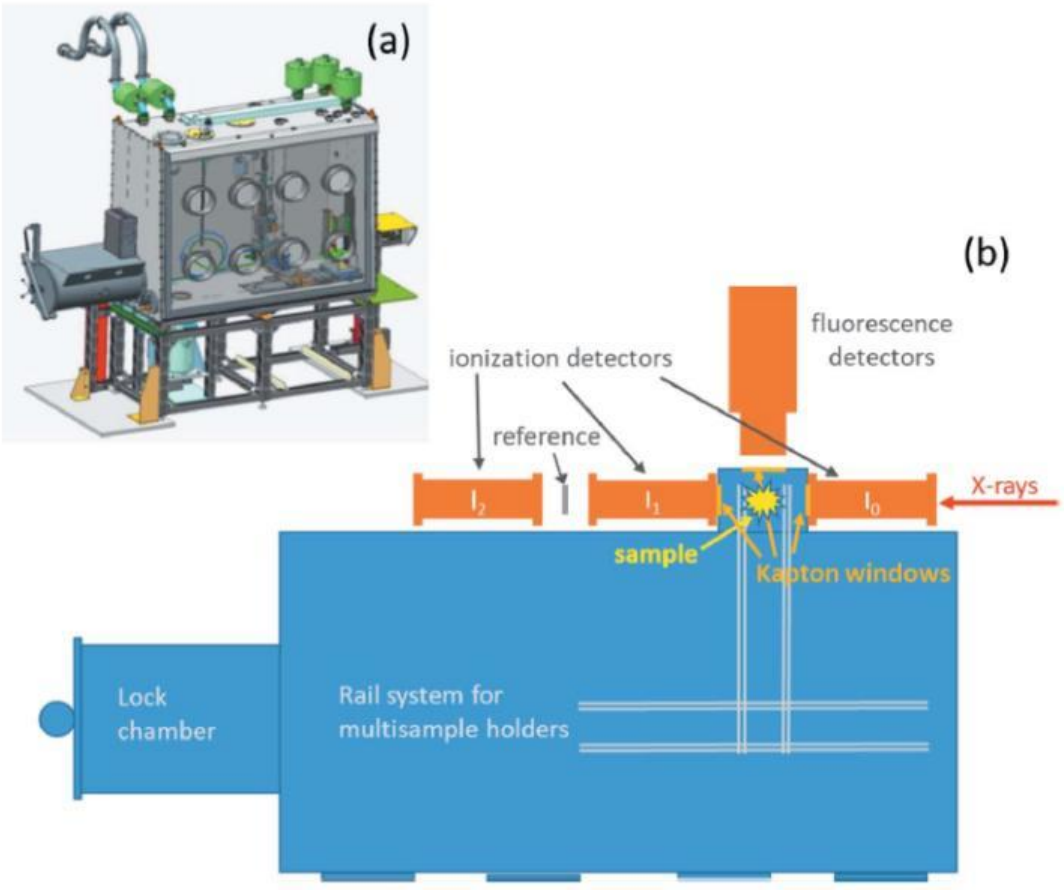

Fig. 29. XAFS glovebox of ROBL-II XAFS experimental section: a) design, b) conceptual drawing.

2.4.3. Investigation of the Pu-O coordination sphere in PuO_2 NPs

The Pu NP system, already discussed in 2.1.2*Crystal structure verification of PuO2 NPs* and 2.3.3.1 was investigated with EXAFS technique to verify the local coordination of Pu. Measurement was conducted at ROBL in transmission mode using ion chambers. Spectra were collected at room temperature. Energy calibration was performed using the zero crossing of the second derivative

of the K-edge of metallic Zr (~17998 eV) and measured in parallel to the sample scans for each sample. Energy calibration and the averaging of the individual scans were performed with the software package SIXpack.[56]

EXAFS data analysis was based on curve fitting to a theoretical standard using the ATHENA[57] and the WinXAS[58] program packages. The EXAFS was extracted from the spectra by using a polynomial spline function to approximate the smooth atomic absorption. E_0, the origin for calculating the EXAFS χ(k)-function is fixed at the white line - peak maximum in the XAFS spectra at ~ 18062 eV. Metric parameters (neighbouring atomic distances R_i, EXAFS Debye-Waller factors σ^2_i and coordination numbers N_i for the different coordination shells i) are determined using the FEFFIT code. All shell fits were carried out in R-space of k^3 - weighted spectra (Fourier transformed (FT) over a k-range of ~2.0 – 14 $Å^{-1}$) using theoretical backscattering amplitudes and phase shifts calculated with FEFF 8.2[59,60] on clusters (R_{max} = 8 Å) derived from the structure of PuO_2.[61] The amplitude reduction factor S_0^2 was fixed at 0.95. Debye-Waller (DW) factors were restricted to float between 0.001 and 0.010 $Å^2$. The experimental EXAFS spectra and shell fits are shown in Fig. 30a.

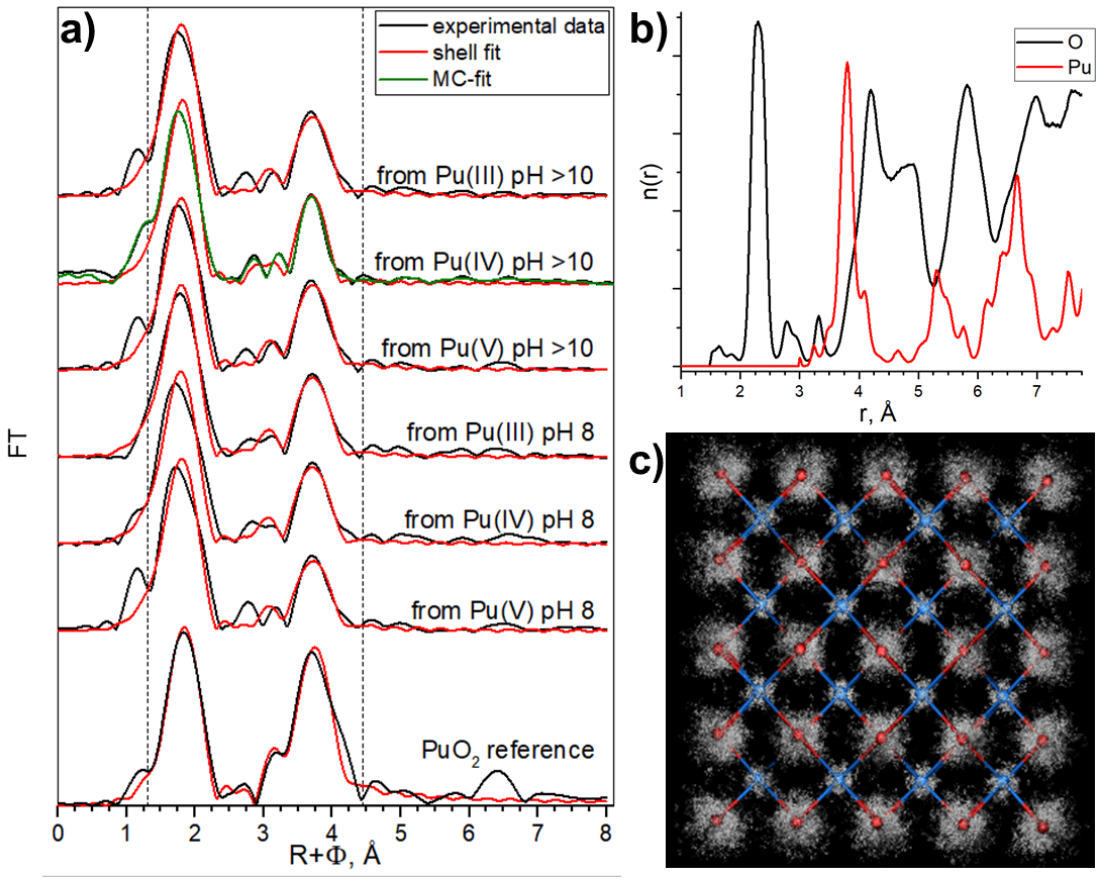

Fig. 30. **Pu L_3-EXAFS results.** a) Pu L_3-EXAFS spectra χ(R) fit results, Fourier transform (FT) magnitude of experimental EXAFS data (black) and a one Pu-O, one Pu-Pu shell fit (red), Monte-Carlo simulations fit (green). Two dashed lines specify the area of the shell fit, b) MC simulation output: radial particle distribution function (n(r)) for Pu-O and Pu-Pu, c) 3D structural refinement based on bulk PuO_2 starting structure. The details about Monte-Carlo simulations are in Gerber et al.[48] (*Appendix A: Article 1. The missing pieces of the PuO_2 nanoparticle puzzle*)

There are several approaches can be potentially implemented to this system and they will be discussed in detail.[48] Here, one oxygen-shell fit is considered as an example of EXAFS data

treatment. This fit is based on the assumption of a PuO_2-like structure of the samples and includes one Pu-O and one Pu-Pu interaction. Therefore only two single scattering paths are taken into account during the fit. This approach turned to be successful for NPs systems, confirming the PuO_2 like structure for samples. The parameters of the best fit are shown in Table 8.

Table 8. Metric parameters extracted by least-squares fit analysis of Pu L_3 EXAFS spectra with one Pu-O and one Pu-Pu paths (k range of 2.0-11.5 $Å^{-1}$)*.

Sample	First coordination shell			Further shells			ΔE_0 [eV]	$\chi^2_{res\,\%}$
	CN	R [Å]	σ^2 [$Å^2$]	CN	R [Å]	σ^2 [$Å^2$]		
from Pu(III) pH >10	7.5 O	2.31	0.0100	3.6 Pu	3.80	0.0045	5.1	14.0
from Pu(IV) pH >10	7.5 O	2.30	0.0100	4.3 Pu	3.79	0.0071	4.9	14.8
from Pu(V) pH >10	7.8 O	2.31	0.0100	3.8 Pu	3.81	0.0041	5.1	12.3
from Pu(III) pH 8	7.5 O	2.31	0.0100	4.5 Pu	3.81	0.0060	4.7	12.9
from Pu(IV) pH 8	7.2 O	2.30	0.0100	4.5 Pu	3.80	0.0065	4.9	15.5
from Pu(V) pH 8	7.7 O	2.32	0.0100	3.2 Pu	3.81	0.0043	5.2	16.5
PuO_2 reference	8.7 O	2.33	0.0068	6.7 Pu	3.82 Pu	0.0011	7.3	9.0
PuO_2 structure	8 O	2.337		12 Pu	3.817 Pu			

*CN: Coordination number with error ± 25 %, R: Radial distance with error ± 0.01 Å, σ^2: Debye-Waller factor with error ±0.0005 $Å^2$.

Both Pu-Pu and Pu-O radial distances are in a good agreement with the corresponding distances of bulk PuO_2, and the number of neighboring oxygens in the first coordination shell is also comparable for NPs and reference structure. However, other fit parameters of the NPs show significant differences compared to PuO_2 reference. DW factor for the Pu-O shell is higher while Pu-Pu CN is lower compared to bulk PuO_2, indicating to a higher static disorder and to a larger fraction of under-coordinated Pu atoms, which are clearly size effects of the samples. However, the parameters of NPs samples do not significantly differ among each other.

EXAFS analysis of NPs is crucial, as the information about type and number of atoms as well as the characteristic distances not only gives an idea about NP structure, but also elucidate the mechanism of their formation – one of the most complicated chemical questions.

2.5. HEXS

High-energy X-ray scattering was used for investigation of PuO_2 NPs. To conduct Pu measurements with this method, an energy of 120 keV is needed. ROBL-II does not have the opportunity to output this energy, therefore, these experiments were carried out at ID15A beamline, also located at ESRF.

2.5.1. HEXS — Basics

High-energy X-ray scattering or pair distribution function (PDF) analysis is based on the Debye scattering equation[62] and the relationship between real-space atomic pair density and the Q-space total scattering intensity.[63] Q is the scattering vector, and its magnitude can be calculated as:

$$Q = \frac{4\pi}{\lambda} sin\theta,$$

where 2θ is the scattering angle λ- is the wavelength of the incident X-ray photons. Unlike ordinary X-ray diffraction technique, giving average structural information of crystalline materials in a long range, high-energy X-ray scattering is capable to directly measure local and intermediate range, i.e. gives information about disordered and nanoscale structures.[64] To obtain atomic bond lengths and coordination numbers, the total structure factor S(Q) is Fourier transformed to a real space function, i.e. reduced pair distribution function G(r) as follows:

$$G(r) = 1 + \frac{1}{2\pi^2 \rho r} \int_{Q_{min}}^{Q_{max}} Q[S(Q) - 1] \sin(Qr) dQ$$

Atomic form factor and atomic displacement parameters, (including thermal vibration and static uncertainties) may cause drop in intensity at high Q, leading to the decrease of data quality. Therefore, to obtain real space information with a sufficient resolution it is necessary to measure S(Q) with high-flux up to the higher Q region since higher resolution in real space is achieved with larger Q_{max}. Since Q is inversely proportional to λ, to obtain larger Q_{max}, short wavelength (hence – high-energy) is required. Therefore, development of HEXS methods became possible with the advancement of X-ray synchrotron facilities, providing extremely high photon flux at the short wavelength.[65]

The pair distribution function $g(r)$ has a strict physical definition and defined as follows:

$$g(r) = \frac{1}{4\pi \rho_o r^2 N} \sum_i \sum_{j \neq i} \delta(r - r_{ij}),$$

Where ρ_0 is the average number density of atoms, N is the total amount of atoms, r_{ij} is the distance between atoms r and j, and $\delta(r\text{-}r_{ij})$ is the Dirac delta function.

However, it is more convenient to use the reduced atomic pair distribution function $G(r)$ for computations:

$$G(r) = 4\pi r \rho_0 [g(r) - 1],$$

as it can be directly calculated from the total structure factor $S(Q)$ through the formula decribed above. S(Q) by definition is calculated by measured coherent scattering intensity $I^{coh}(Q)$:

$$S(Q) = 1 + \frac{I^{coh}(Q) - \sum c_i |f^i(Q)|^2}{|\sum c_i f^i(Q)|^2}$$

c_i is the atomic concentration of the element i, $f^i(Q)$ is its X-ray scattering factor. To acquire $I^{coh}(Q)$ total intensity $I(Q)$ needs to be measured and corrected for background, incoherent intensity, efficiency of the detector and other factors. Therefore, from the total scattering intensity $I(Q)$ measurements pair distribution function $g(r)$ can be determined, however, there

is a closely-related radial distribution function $R(r)$ which can be derived from $g(r)$ and gives some intuitive understanding:

$$R(r) = 4\pi r^2 \rho_0 g(r)$$

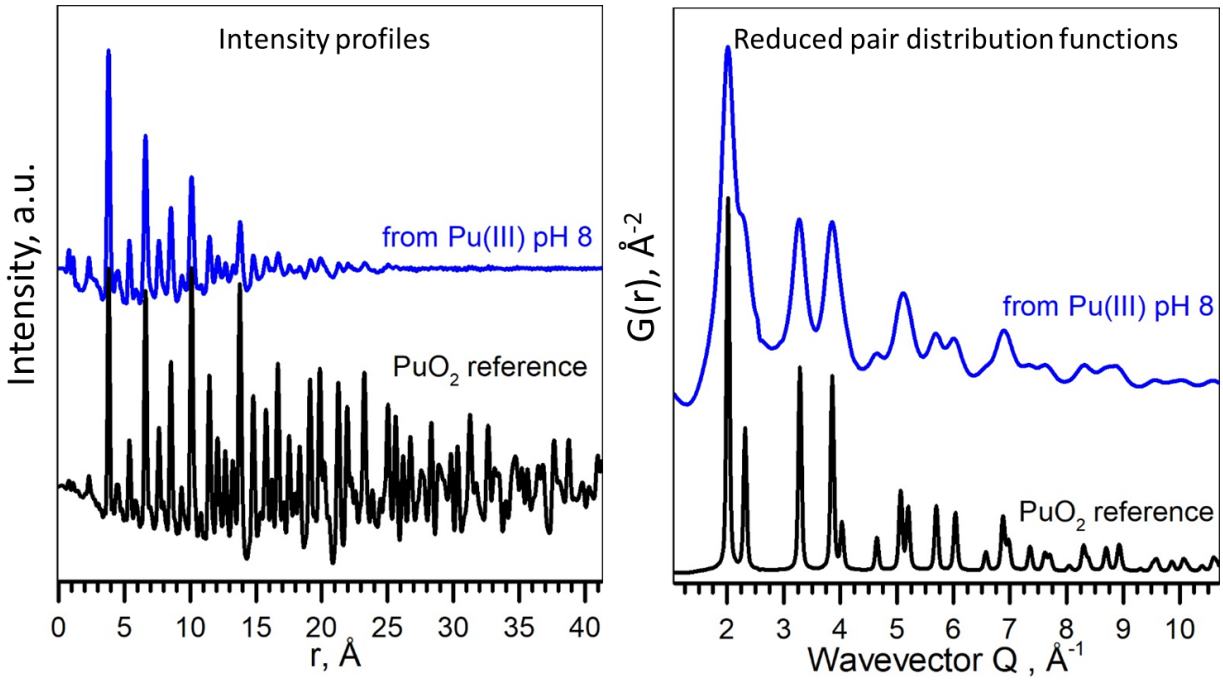

Fig. 31. Left: Intensity profiles of the 2D diffraction of Pu sample and PuO_2 reference, obtained by HEXS, right: the corresponding reduced pair distribution functions G(r) obtained by Fourier transformation (FT) of the data with Q_{max} = 26.0 $Å^{-1}$. Samples were measured at ID15A, ESRF.

Reduced pair distribution functions from Pu samples are shown in Fig. 31(right) and plenty of information about structure can be obtained directly. The peak position shows the distance of atomic pairs, the width of peaks gives information about the short-range order and random atomic displacements. The area of peaks is related to the coordination numbers. The coherence length of the sample can be estimated by the maximum distance of the oscillations.[66,67]

The difference between convenient XRD and HEXS is that in XRD information from diffuse scattering is lost during background subtraction procedures, while in HEXS this information plays an important role. To obtain information from diffuse scattering, besides sample, empty sample holder and air (or other media of the sample) should be measured. The received background pattern must be subtracted from the total scattering pattern, the resulting pattern gives information exclusively about the sample and consist of Bragg, diffuse and inelastic scattering parts. Then the latter part is removed from the data in a dedicated program software PDFgetX3.[68]

The experimental system for HEXS measurements will be discussed in 2.5.3. To collect the scattering data a 2D pixel detector is used with the following correction for detector geometry, response and transparency. Integration of 2D-diffraction with special software pyFAI[69] reveals 1D total scattering function data S(Q), shown in Fig. 31 Left, which subsequently allow to calculate G(r) through Fourier transformation, using modules from DIFFPY-CMI[70] and locally developed cleaning algorithms.

There are several advantages of HEXS method that should be noted:

1) HEXS provides data in high Q-range with small scattering angles, giving higher real space resolution
2) HEXS is a highly penetrative method, thus relatively thick containers can be used for transmission geometry
3) High flux and collimation of X-rays, provided with modern synchrotrons make it possible to conduct measurements in severe heating or pressure; time-resolved diffraction experiments are also achievable
4) With HEXS a rigorous test of atomistic models from theoretical simulations can be provided.

The main drawback of HEXS is its element insensitivity and therefore information on low dopant ions (<1%) cannot be obtained.[71]

2.5.2. ID15A beamline setup[72]

The experiments with total scattering technique have been conducted at ID15A beamline, ESRF. Thanks to the 2m-long undulator with period λ_u = 22 mm and maximum magnetic field of 0.82T, ID15A is perfectly suited to exploit high-energy X-ray scattering (HEXS), capable to characterize the atomic-level structure of polycristalline, nanocrystalline and even amorphous samples. After the extremely brilliant source (EBS) shutdown of ESRF a 1.5 m-long in-vacuum cryogenic permanent-magnet undulator is installed, with an increased maximum deflection parameter and λ_u = 18 mm, given 20-40 times increased flux with harmonics significantly sharpened and symmetrized, especially at high-energy. Besides that, a seven-pole wiggler with period λ_u = 76 mm is used for very high energy applications up to several hundred keV. Wiggler produces high flux and either white or monochromatic unfocused beam above 150 keV.

It is essential to have a long range of q-space available for measurements, normally to 30 $Å^{-1}$ or higher to get a higher real-space resolution. A recently developed DECTRIS Pilatus3 X CdTe 2M detector with high detection efficiency up to 100 keV allows to acquire a perfect signal in second, as well as to conduct time-resolved experiments (operando and in-situ measurements). Some operational parameters for the experimental configurations used in EH3 are listed in Table 9.

Table 9. Operational parameters for the experimental configurations used in EH3.

	XRD-/PDF-/SAXS CT	High-precision total scattering
Energy, keV	20-140	60-140
Primary optics	LLM/DMLM	LLM/DMLM
Secondary optics	TF/CRL/KB	TF
Beam size		
Vertical, µm	0.3-20	100-200
Horizontal, µm	0.3-50	100-200
Spatial resolution		
Vertical, µm	>0.3 µm	-
Horizontal, µm	>0.3 µm	-
Detector	Pilatus/Maxipix	Pilatus
Goniometer	HR	HR/HL

The layout of the experimental hutch is shown at Fig. 32.

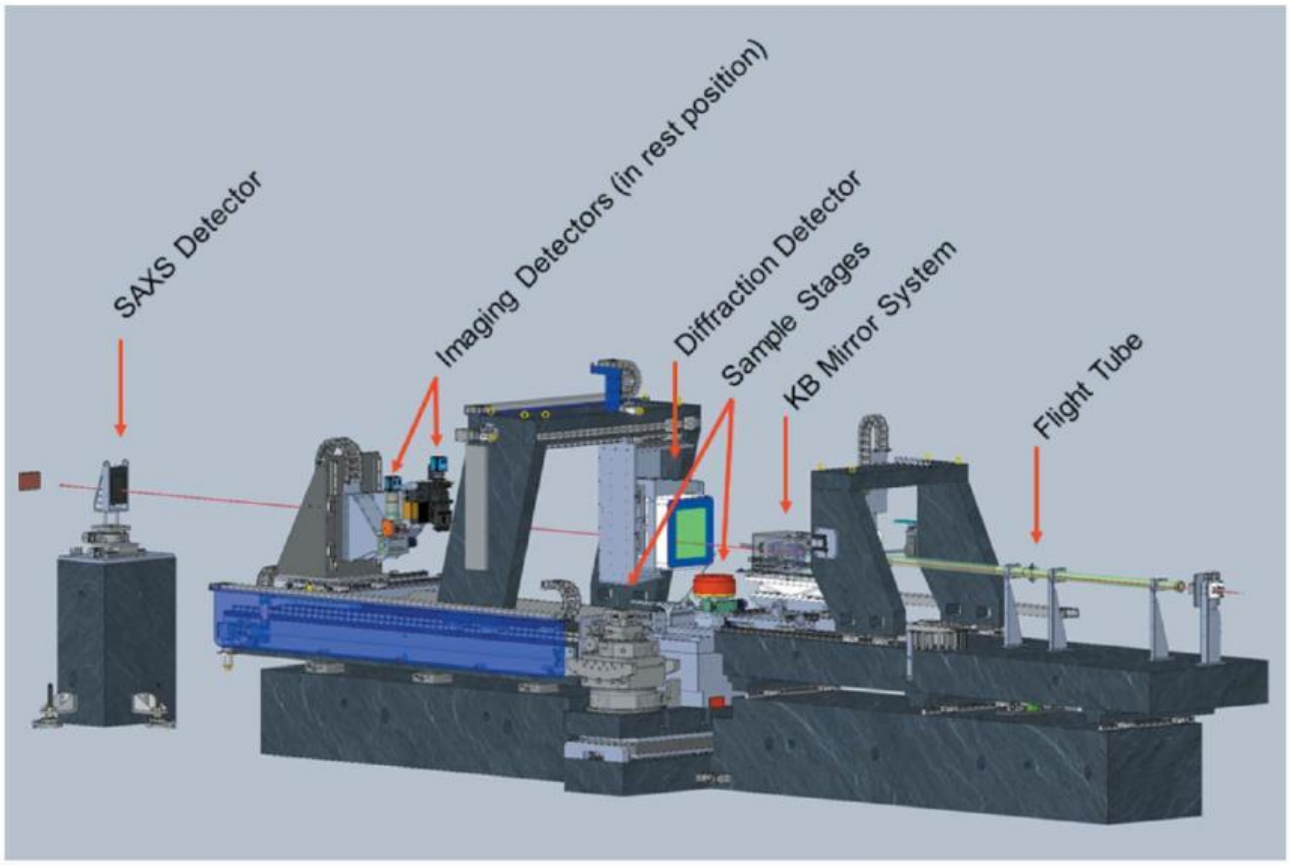

Fig. 32. Experimental hutch overview (Figure from Vaughan et al.[72])

2.5.3. HEXS — Examples

2.5.3.1. The local structure and coherent size domains of PuO_2 NPs.

There will be two examples dedicated to HEXS measurements, one is again devoted to the PuO_2 NPs system, already investigated with XRD, HERFD and EXAFS and second one is about ThO_2 NP NPs.

PuO_2 NPs High energy X-ray scattering data were collected at room temperature at the ID15A beamline of the ESRF, Grenoble.[72] An incident energy of 120000 eV was selected in order to be below the Pu K-edge at 121791 eV and to minimize absorption. Data were collected up to 30 $Å^{-1}$ using a Dectris Pilatus 2M CdTe pixel detector. Patterns were corrected for detector geometry, response and transparency, and integrated using a locally modified version of pyFAI[69] with outlier filtering. F(q) and G(r) were calculated from the resulting powder diffraction patterns using modules from DIFFPY-CMI[70] and locally developed cleaning algorithms. The full profile real-space refinement of crystal structures based on the pair distribution function G(r) was made using PDFgui software.[73] PDFgui performs a least-squares refinement of the structural model to the G(r). The parameters refined for the NPs series were lattice parameter *a*, particle diameter for the G(r) shape damping function (spdiameter), the data scale factor, and factor which accounts for low-r sharpening in G(r) due to nearest-neighbour correlations (delta2). Parameters such as the G(r) Gaussian dampening envelope due to limited Q-resolution and isotropic atomic

displacement parameters (ADPs) were obtained from the fit of the experimental data of the PuO_2 reference and fixed at these values for the refinements of the NPs experimental sets, in order to minimize the number of refinable parameters and to obtain the most robust values for the coherent domain size. Free water was also included in the model in order to reproduce the contribution of water at the short-range order. All samples were fitted in the range from 1.7 to 20 Å and the maximum wave vector Q of the data used for the generation of G(r) was settled to 26 $Å^{-1}$. The R_w value is a goodness of fit measure to show the agreement between calculated and experimental data. Intensity profiles and corresponding reduced pair distribution function G(r) are shown at Fig. 31.

Intensity profiles of the 2D diffraction are very similar for all NP samples and bulk PuO_2, meaning long-range structure is the same, though HEXS is capable to detect local structural deviations from the bulk if they present in nanosized materials. There are some deviations from the bulk in this case: peak broadening, which is typical for objects of this size, and peak at Q~2.40 $Å^{-1}$, that is also present in the intensity profile of an empty kapton capillary and therefore considered as a background peak. For most samples this peak was successfully subtracted. The sharpness of peaks in G(r), being similar for all samples and reference, leads to the conclusion that the short-range order is also identical. The full profile real-space refinement of crystal structures was made using PDFgui software.[73] PDFgui performs a least-squares refinement of the structural model to the G(r). The parameters refined for the NPs series are shown in Table 10. G(r) Gaussian dampening envelope due to limited Q-resolution and isotropic atomic displacement parameters (ADPs) were obtained from the fit of the experimental data of the PuO_2 reference and fixed at these values for the refinements of the NPs experimental sets, to reduce the amount of parameters to be refined and to obtain the most robust values for the coherent domain size. Free water was also included in the model in order to reproduce the contribution of water at the short-range order. All samples were fitted in the range from 1.7 to 20 Å and the maximum wave vector Q of the data used for the generation of G(r) was settled to 26 $Å^{-1}$. The R_w value is a goodness of fit measure to show the agreement between calculated and experimental data.

Table 10. The refined parameter values obtained from HEXS.

Sample	**Diameter, nm**	**a, Å**	**R_w**
from Pu(III) pH >10	1.33 (5)	5.384(6)	0.20
from Pu(IV) pH >10	1.3(2)	5.38(2)	0.29
from Pu(V) pH >10	1.75(8)	5.388(5)	0.23
from Pu(III) pH 8	2.07(8)	5.402(4)	0.18
from Pu(IV) pH 8	1.5(2)	5.39(2)	0.32
from Pu(V) pH 8	1.7(2)	5.39(1)	0.25
PuO_2 reference	-	5.4032(3)	0.11

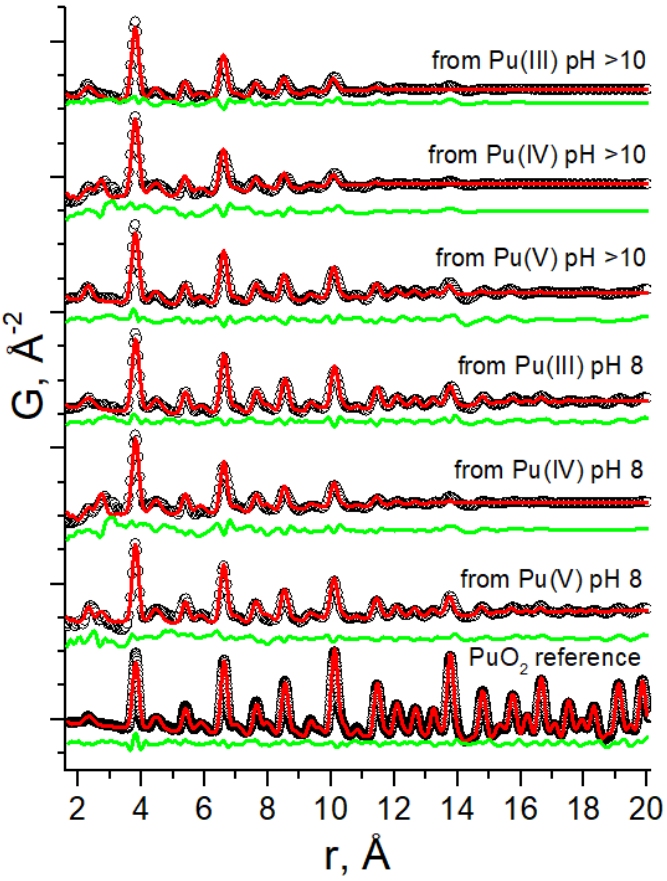

Fig. 33. **The results of the pair distribution functions (PDFs) fits from all samples and PuO_2 reference.** The experimental reduced (PDFs) G(r) obtained by Fourier transformation (FT) of the data with Q_{max} = 26.0 $Å^{-1}$ (black dots), calculated PDFs from the refined structural model (red line) and the difference curve (green line).

The damping of G(r) giving a visual indication of the coherence length of the PuO_2 NPs, can be refined to obtain the average particle size, confirming the direct observation that the NPs diameters are in the range of 1.3 - 2.6 nm. Strictly speaking, HEXS (and also XRD) provide information about coherent scattering domain size and sometimes it may differ from particle size and therefore the real particle size may be underestimated by these methods. Lattice parameter refinement also proves similarities to the bulk PuO_2.

2.5.3.2. The application of HEXS for the structural characterisation of ThO_2 NPs.

PuO_2 NPs were comparatively simple systems to analyse with HEXS. The ThO_2 NPs turned to be much more complicated. To obtain NPs, thorium nitrate pentahydrate and 3M sodium hydroxide were mixed, precipitates were either dried in air at 40 °C (sample 1) or 150 °C (sample 2). Samples were also measured at ID15A, measurement conditions and the process of data treatment were the same as for Pu samples. The G(r) obtained after Fourier transform for ThO_2 NPs and bulk ThO_2 are shown in Fig. 34.

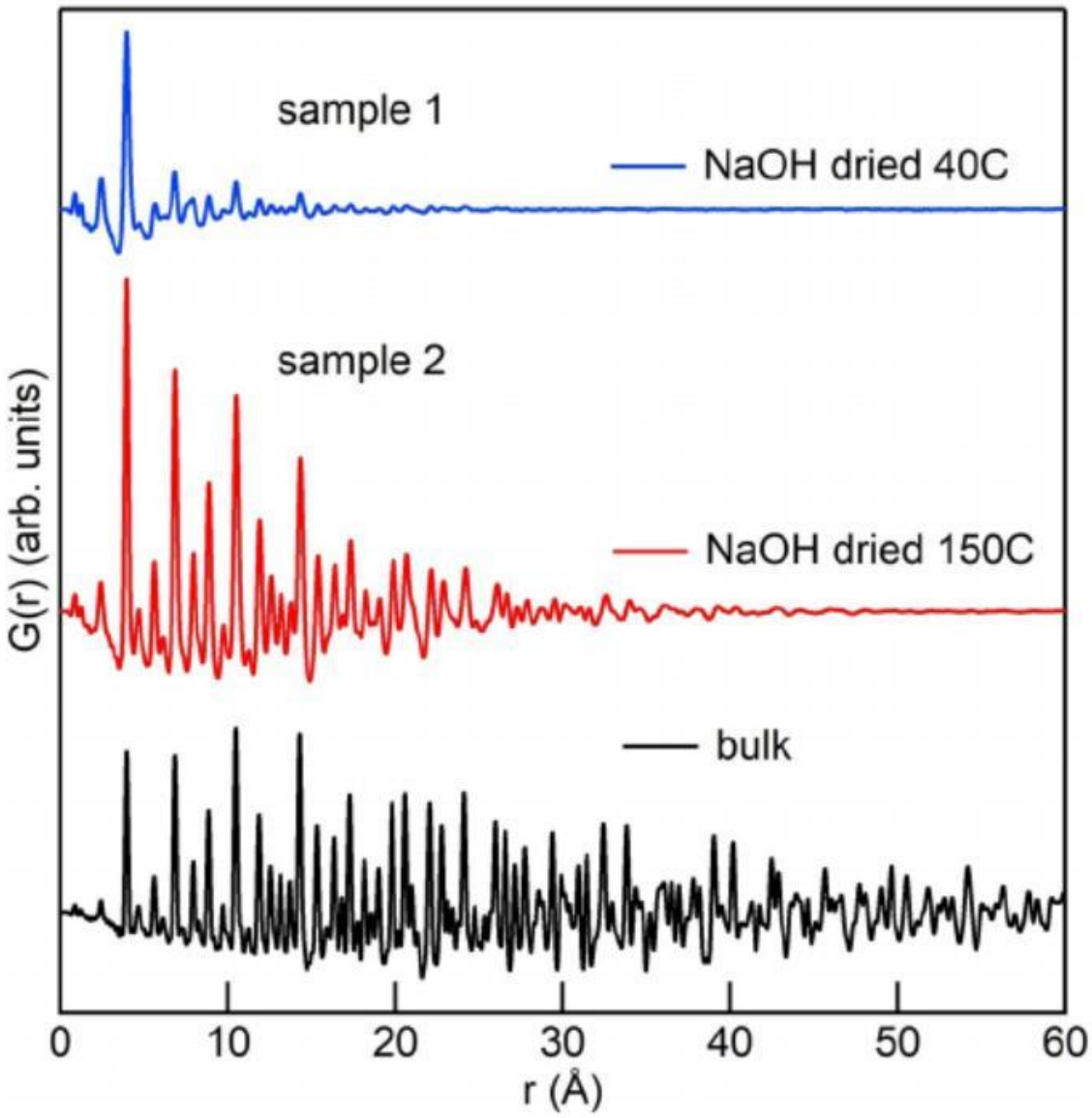

Fig. 34. Unscaled G(r) for ThO_2 samples and bulk ThO_2.

All reference peaks from bulk ThO_2 are present in the G(r) of the samples, though the peaks are broader. The behaviour of sample 1 is more complex, with specific Th–Th peaks showing bigger deviations than the rest. Sample 1 presents an abrupt drop in intensity after the second peak, corresponding to the first Th–Th distance, and remains low for the rest of the signals. This is not the case for sample 2, for which the peak intensities decrease smoothly as r increases. According to the oscillations damping, the upper size limit of NPs is about 4 nm for sample 1 and 6 nm for sample 2. It is clear evidence of the nanoscale nature of the samples and it was also observed for PuO_2 NPs. By direct observation one may see that PuO_2 and ThO_2 have close structural properties such as lattice parameters, ionic radius of actinide(IV) cation and same fcc structural type of fluorite. Therefore, one may expect that ThO_2 NPs will have similar behaviour compared to PuO_2 analogs. However, the first refinement based on the Pu model was unsuccessful; more parameters needed to be included, such as isotropic displacement parameters (U_{iso}) for thorium and oxygen. In addition, two models were used: the single sphere model, which considers the sample as an ensemble of identical spherical NPs, and the lognormal distribution of spherical NPs model. The single sphere model fits the average diameter of the NPs (P_{size}) and the lognormal

model the mean diameter (P_{size}) and the variance (P_{sig2}) of the distribution. All results are listed in Table 11 and fits with data are shown in Fig. 35.

Table 11. Fit results of the ThO_2 samples obtained with the semi-empirical models.*

	Model	Scale	a, Å	Th U_{iso}, Å^2	O U_{iso}, Å^2	P_{size}, nm	P_{sig}^2, nm	R_w
Sample 1	1 sph	1.49	5.610	0.011	0.0075	0.93	-	0.30
Sample 1	1 logn	1.80	5.607	0.010	0.080	0.5	0.2	0.28
Sample 1	2 sph	0.13	5.616	0.009	0.293	3.1	-	0.29
Sample 1	2 logn	0.18	5.616	0.008	0.060	1.5	0.7	0.31
Sample 2	sph	0.96	5.619	0.008	0.059	3.6	-	0.17
Sample 2	logn	1.13	5.619	0.008	0.063	0.8	0.6	0.12
bulk	-	0.57	5.600	0.004	0.036	-	-	0.11

* P_{size} is the NP size from the spherical model or the mean value of the lognormal distribution. P_{sig}^2 is the variance of the lognormal distribution.

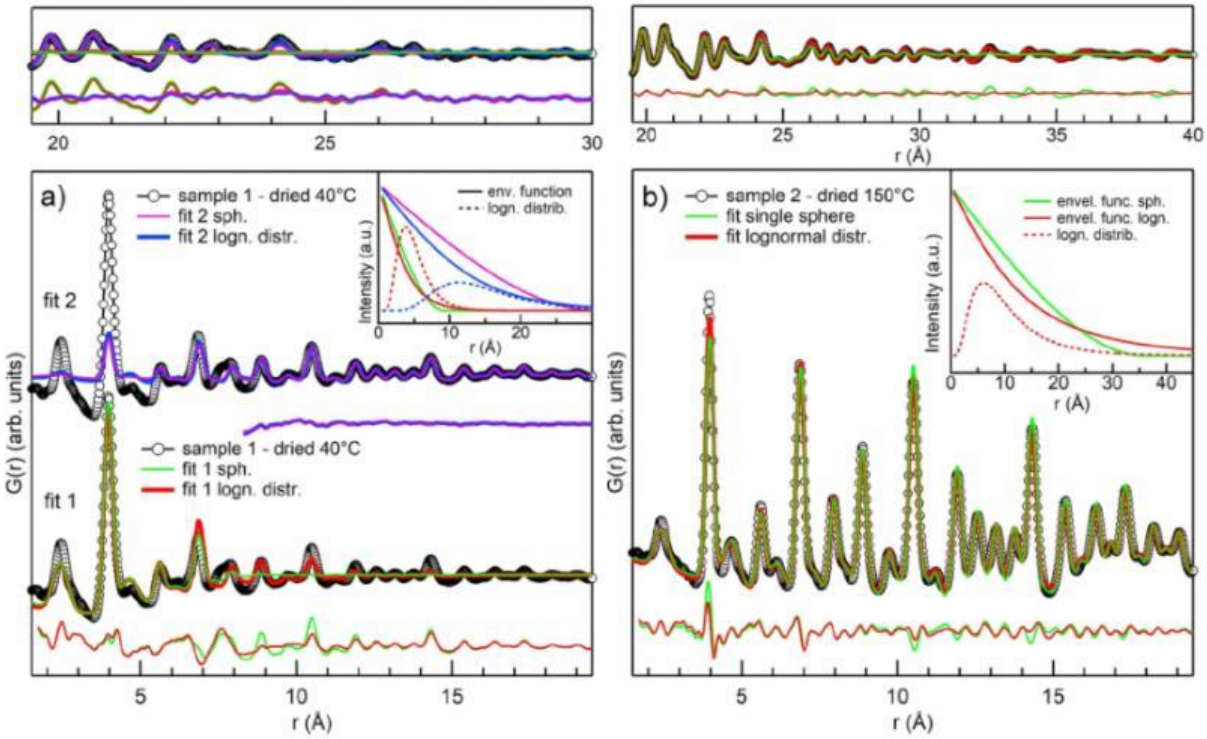

Fig. 35. Data for the samples (black circles) and fit results (coloured lines). Residuals are shown below the corresponding fits: a) for the sample 1, fit 1 is on the range 1.5-30 Å and fit 2 – 8.3-30 Å with an extrapolation to 1.5 Å (residual is not extrapolated), b) for the sample 2, fit results with the single sphere (green) and lognormal (red) models. Insets: the envelope functions (solid lines) for all the fits and lognormal distributions (dashed lines). Top panels show are zooming the high r range.

Both models are applicable for sample 2 (Fig. 35b), though the results show some differences. The average size of the NPs according to the single sphere model is 3.6 nm, while for the second model the mean size is only 0.8 nm and a variance of 0.6 nm with a wide size distribution (shown at the inset). The envelope functions (also present at the inset) are used to modulate the signal of the bulk and one can see that for the single sphere model there is no signal after 3.6 nm, while for the lognormal distribution there are oscillations at the whole r range. These results in slightly

better correspondence between fit and experimental data compared to the single sphere model not only at low r, but also at high r.

Two fits were made for sample 1, fit 1 – for the full range (1.5 – 30 Å) and fit 2 – for the shortened range (8.3-30 Å). Fit 1 (Fig. 35a, bottom) gives unsatisfactory correspondence with data at r higher that 10 Å for both models, though the lognormal fit 1 is slightly better (see R_w values in Table 11). Fit 2 provides a satisfying similarity to data above 10 Å, but an extrapolation to low r leads to a significant underestimation of the signal below 5 Å and R_w is slightly better for the single sphere model. The first conclusion is that neither single NP size nor single distribution can be used to describe obtained data from sample 1. At low r once characteristic size dominates the signal and is detected by the fit 1, considering the whole range. Each model is applicable and the average size is below 1 nm. The presence of the larger particles (determined by the residual above 10 Å) is taken into account by fit 2, where only the signal at high r is considered. To count the contribution of small NPs another fit model was implemented. It is based on a minimal set of NPs cut from the bulk ThO_2. More details in the work of Amidani and coworkers.[74] (*Appendix G: Article 7. The Application of HEXS and HERFD XANES for Accurate Structural Characterisation of Actinide Nanomaterials: The Case of ThO_2*)

As a conclusion, new fits describe data better for both samples. It is confirmed that in sample 1 most NPs are small with admixture of larges ones, while sample 2 has a more homogeneous distribution of sizes. The small octahedral unit cut from bulk ThO_2 used for the fit is similar to thorium hexamer clusters, reported earlier in literature.[75–78] The high flexibility of this method may help to achieve even more detailed structural information, which could be exploited in studies on larger data sets.

3. Combinations of methods

Although each of the methods described above can give important results about the investigated system, in reality, the advantageous approach is to use a combination of methods to obtain a complementary information. Methods, being combined in different ways may unravel scientific puzzles and illuminate the most complex chemical cases. Some of them will be discussed in details in the next subchapters.

3.1. The puzzle of PuO_2 NPs

Actinide nanoparticles are the excellent systems to show the power of each method indepentendtly and the power of the method combination. The nanoscience domain often produces results more extraordinary than any other field. The peculiarities of nanoscale objects affect their properties.[79] It is well-known that nanoparticles can exhibit significantly different physical and chemical properties to their larger material counterparts.There are three parameters, characterising each nanosystem: size distribution (or at least mean size), composition (elements and their chemical species) and morphology (including crystallinity) of NPs. The overview of method possibilities is listed in Table 12. Each method, described here, gives information about one or several parameters of this classification. PuO_2 NPs are the perfect example when the combination of several methods exploiting synchrotron radiation give complementary information about structural and electronic properties. It has been found, that so called “colloidal Pu(IV) polymers”, playing an important role in the plutonium migration processes, are in fact aggregates of PuO_2 nanoparticles with diameters ~ 2 nm. The exact

stoichiometry and structure of such nanoparticles remain questionable, especially with respect to surface hydration and hydroxylation, as well as the purity of the tetravalent oxidation state, considering the existence of four different oxidation states (with relatively small energy barriers III, IV, V, and VI) under environmental conditions. Therefore, a variety of methods was used to characterize PuO_2 NPs obtained from different precursors and at various pH.

Table 12. A brief summary of methods used for PuO_2 NPs characterization. Reproduced from Gerber et al.[48]

Method	Information obtained	Comments
HRTEM	Information about morphology, particle size, elemental composition, and crystal structure with nano-resolution	Local method, which hives statistics only for a relatively small amount of particles; sample state can deviate during measurements due to the high vacuum and possible damage by the electron beam
XRD	Information about crystal structure and coherent scattering domains; statistically reliable; the ability to analyze mixed phases	Fast measurements (from seconds to minutes per sample); cannot easily distinguish between elements with similar Z; atomic level structure of amorphous substances can not be determined; nanoparticle peak broadening complicates the analysis
HEXS	Information about the local structure and coherent size domains; statistically reliable;	Fast measurements (from seconds to minutes per sample); possibility to discriminate between short-range disorder and random thermal displacements; to distinguish amorphous, structurally disordered, and nanocrystalline materials;
HERFD	Element selective method, which gives information about local site symmetry, oxidation state, and orbital occupancy;	Fast measurements (from seconds to minutes per sample); any size of objects can be studied (from nm to cm); allows determination of low An concentrations; provides fingerprint information; quantitative information can be obtained;
EXAFS	Information about local structure (bond distances, number and type of neighbours), sensitive to the type of absorbing element, local disorder and size effects	Time consuming measurements (from minutes to hours per sample); time consuming post- data collection analysis; provides only semi-quantitative estimations of oxidation state impurities; the results are severely dependent on the data quality and may be misinterpreted;

The most straightforward reason to use two (or more) independent methods is the verification of the results. For example, both HRTEM and XRD can obtain information about size. However, due to the possible state deviation caused by the electron beam, an agreement between these methods might be a proof of PuO_2 NPs immutability during the measurement. Besides that, HRTEM is a local method, while XRD is statistically reliable therefore one may extend the local information from HRTEM due to the similarity of the results obtained from local and “global” methods. It also should be emphasized that HRTEM determines the size of the particles while XRD gives information about crystallite size. Therefore, similar results lead to a conclusion, that coherent diffracting crystalline domains and particle size are very close in that case.

HEXS is another powerful method, complementary to XRD and HRTEM. Like XRD, it gives statistically reliable information about coherent crystallite size, but its advantage is the discrimination between short-range order and random thermal displacements. Thus, the confirmation of bulk PuO_2 structure for NPs not only in the long range (given from XRD) but also in the short range (given from HEXS) leads to the conclusion, that there are no local structural deviations from the bulk.

However, structural information is not researchers only element of concern, especially in case of actinide studies. The variety of Pu oxidation states and the ease of their mutual transitions explain the necessity to probe electronic structure properties. Therefore, several methods should be used when different types of information is required for a full characterization of the system. HERFD is capable to detect the impurities of other oxidation states and reveal the information of the local site symmetry. Pu M_4 edge measurements on PuO_2 NPs confirm that regardless of initial precursor oxidation state and pH, Pu(IV) is the only oxidation state present. This put an end to the controversial debates around the presence of other oxidation states of the NPs. Besides that, the spectrum profile of PuO_2 NPs with bulk PuO_2 and calculated spectrum confirm that the local environment of all PuO_2 is similar to the bulk. In other words, there is no size effect, leading to the alterations of electronic structure, which was previously observed for CeO_2 NPs and ThO_2 NPs (more information can be found in chapters 2.3.3.4 for CeO_2 and 2.3.3.5 for ThO_2 and in the works [38,50,80]). Thus it turns out that for $CatO_2$ NPs HERFD must be combined with methods, giving information about structure and size, in order to validate and explain the results with one another.

Finally, last but not least EXAFS was also used in this study. As HERFD, it is sensitive to the type of the absorbing element and the local environment, and as HEXS it gives information about local structure. The information about bond distances, number and type of neighbours, which can be extracted from EXAFS, is crucial in the case of PuO_2 NPs. Several groups have investigated PuO_2 NPs with EXAFS[81–87] but results are questionable and in disagreement. The key problem is the first coordination sphere, referring to Pu-O interaction. There are three principal approaches:

1) A single Pu-O interaction, the same as in the PuO_2
2) Several Pu-O interactions, where coordination of O is varied
3) Several Pu-O interactions, where coordination of O and Pu oxidation state are varied

The first approach is the simplest and based on the fact that PuO_2 NPs have a structure similar to the bulk PuO_2. In the second approach it is assumed that the first shell is splinted due to the different Pu-O contributions and therefore several Pu-O paths must be used. The last approach suggests that Pu(V) (or even Pu(VI)) contributions might be involved in the first coordination sphere. All models were used in the current study. It is possible to obtain a reasonable fit with each approach, however, it is evident that some approaches result in misinterpretation. The fit where Pu(V)-O interaction was added gives 15% of Pu(V), therefore, it can be easily discarded thanks to the HERFD results, because this amount of Pu(V) would definitely appear in HERFD spectra. It was much more difficult to choose between other two approaches. To make a right decision, EXAFS data were analysed with the Landweber Iteration and Monte-Carlo EXAFS simulations. The main concept of these simulations is to derive the radial particle distribution functions directly from EXAFS without shell fit performing. It was found that one Pu-O contribution is enough to describe the coordination of the first sphere due to the symmetric shape of the Pu-O shell. The radial particle distribution functions were compared with HEXS

results and allow us to unequivocally indicate the approach that should be used to define the local environment of Pu. The full description of simulations as well as shell fit results with different approaches are described in Gerber et al.[48] (*Appendix A: Article 1. The missing pieces of the PuO2 nanoparticle puzzle*)

As a final conclusion, it should be emphasized that an application of different methods makes it possible to obtain reliable information about complex chemical systems. In case of PuO_2 NPs the use of various techniques shed light on the mechanisms of the PuO_2 NPs formation, one of the fundamental problem of plutonium chemistry. The significance of these results will be discussed in the last chapter.

3.2. PuO_2 NPs at low pH

The most recent of our investigations also dedicated to the PuO_2 NPs, however, in this case it is acidic and not alkaline media. The solubility of Pu under acidic conditions is significantly higher, therefore, it was necessary to use higher concentration of Pu (compared to the previous studies). In all other respects the procedure of synthesis was similar: ammonia aqueous solution was added to Pu(IV) precursor until pH 1, 2 or 4 was reached. We managed to obtain NPs at these conditions, though according to available solubility data precipitate cannot form at these conditions. Most likely, the reason of discrepancy is that NPs stabilize in the solution and may result in the solubility overstatement, especially if the process of separation was insufficient. Nevertheless, the results reproduce the trend of pH-solubility dependence, though it is still remarkable that NPs may form even at pH 1. The obtained NPs were characterised with HRTEM and HERFD techniques.

HRTEM results proved that pH does not influence significantly on the morphology, size or crystallinity of NPs. As in 3.1, 2-nm crystalline particles were observed, the crystal structure is similar to bulk PuO_2. Slight differences were found only for PuO_2 NPs formed at pH 1 – they were less agglomerated.

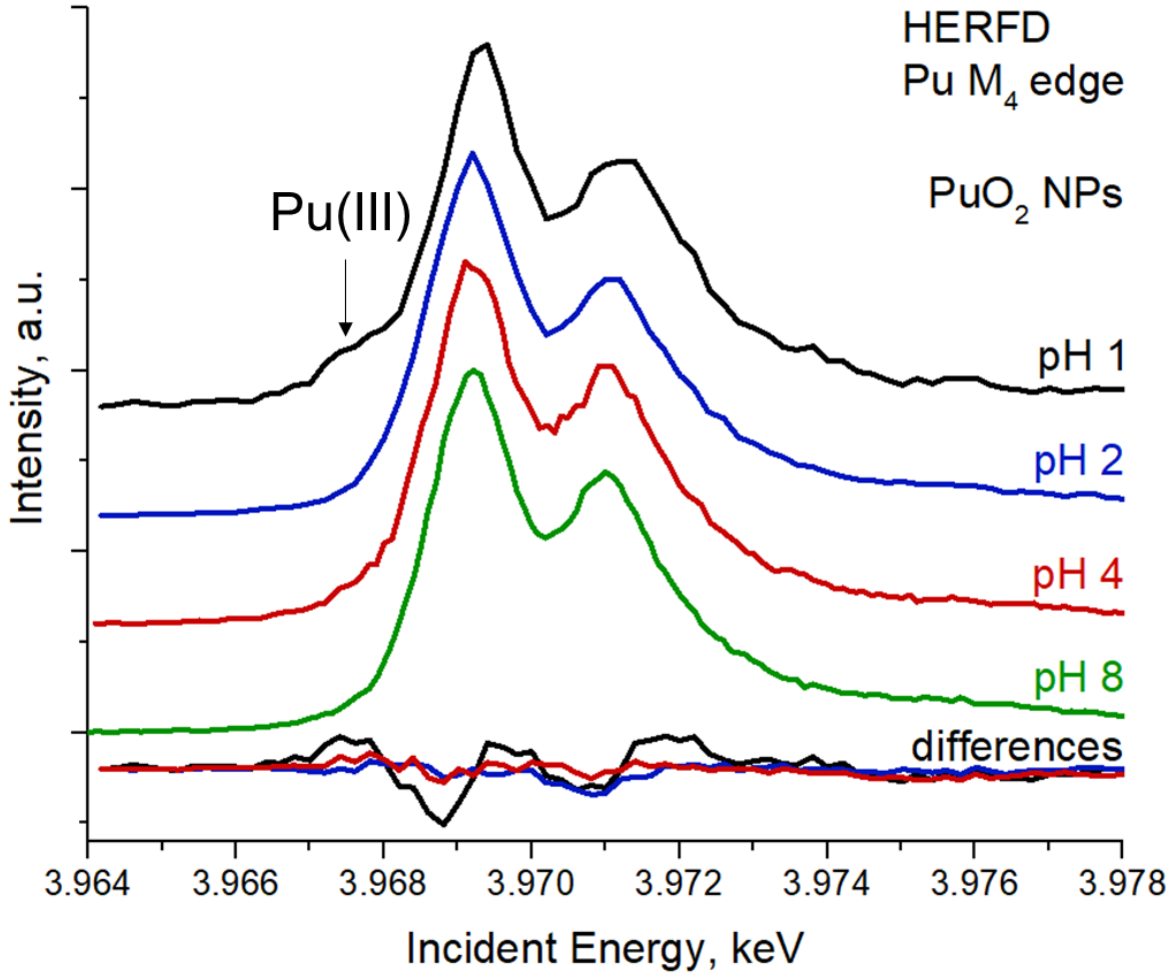

Fig. 36. Pu M_4 HERFD experimental data from NPs samples. Difference curves between samples and reference "Pu (IV) from pH 8" are shown below.

HERFD spectra at the Pu M_4 edge were collected ath the MARS Beamline at SOLEIL, the results are shown at Fig. 36. First of all, one should notice that spectral profiles among each sample from pH 1 to 8 are very similar, indicating that Pu(IV) is the dominating oxidation state not only under alkaline, but also under acidic conditions. It was also confirmed, that NPs has PuO_2-like structure. However, for the sample made at pH 1 peak broadening was detected and even more importantly, there is a shoulder in the left of the WL at 3.967 keV. The peak broadening is a singal of higher oxidation states, likely, Pu(VI) and the shoulder signifies, that Pu(III) might be present. The problem is that this conclusion is made, because such shoulders are generally attributed to the change to lower oxidation state, though even well-known Pu(III) have not been studied with HERFD at the Pu M_4 edge. Therefore we have registered HERFD spectrum of PuF_3 reference at the Pu M_4 edge to find out, how Pu(III) features will look like. The main edge of PuF_3 is consisted of two peaks at 3.967 keV and 3.969 keV respectively, and one may suppose that indicates, that we have a mixture of Pu(III) and Pu(IV). However, the theoretical simulations reassured that both peaks are associated with Pu(III) oxidation state. Therefore one may conclude that PuO_2 NPs formed at pH 1 has Pu(IV) as a dominating oxidation state with Pu(III) and Pu(VI) as impurities. It is possible to estimate the exact contribution of each oxidation state with the ITFA package,[52,88] it was found that there is around 80% of Pu(IV) and 10% for Pu(III) and Pu(VI).

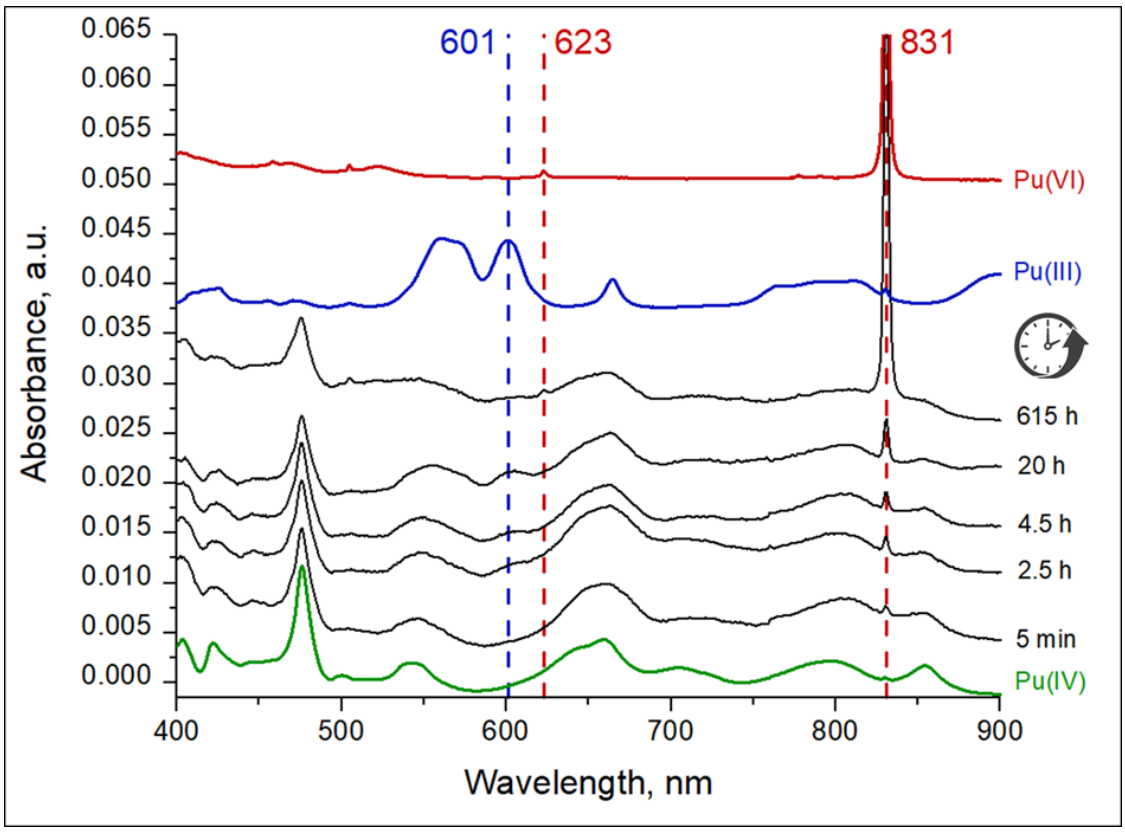

Fig. 37. UV-vis spectra of Pu (IV) pH 1 sample solutions after different times of reactions and reference solutions with wavelengths of the characteristic peaks.

It is evident, that the unusual properties of PuO_2 NPs at pH 1 must be somehow connected with solubility. The contradiction of HRTEM and HERFD results as well in addition to the peculiarity of only one sample are other evidences of that. As already mentioned, the complete particle separation at these conditions might be a problem. In our case, mother liquid solution is used to transfer solid phase samples for HERFD measurements due to the lack of solid sample. Therefore it is obligatory to study the evolution of the initial Pu solution over time, this was done with UV-vis spectroscopy, the results are shown at Fig. 37.

One can see that contribution of Pu(VI) in solution is constanly increasing with time while Pu(IV) is decreasing, indicating that redox reactions occur. However, it is not simple oxidation of Pu(IV) to Pu(VI), as one can observe, that after the beginning of the reaction Pu(III) contribution first increases but then decreases. It should be noted, that total Pu concentration in solution does not change with time, therefore, all concentration changes linked with solution rather than equilibrium between precipitation and solution. One can compare results from HERFD and UV-vis. There are characteristic peaks for each plutonium oxidation state in UV-vis spectra, so their contirbutions may be estimated with the Beer-Lambert law. 20 hours of interaction is the time, corresponding to the period needed to prepare sample for HERFD. It was calculated, that after 20 h of reaction there is about 75% of Pu(IV), 20% of Pu(III) and 5% of Pu(VI) which is in a good agreement with the ITFA results from HERFD data. Therefore, PuO_2 NPs from pH 1 themselves does not contain other oxidation states of Pu but Pu(IV), and therefore similar to other NPs. The additional oxidanion states observed in HERFD data come directly from the solution, as samples were prepared as the wet pastes and some mother solution was caught during sample preparation. Due to the high sensibility of HERFD, tiny amounts of other oxidation states of Pu were detected.

Therefore, the combination of HERFD, HRTEM and UV-vis spectroscopy allow to conclude, that NPs formed from pH 1-4, as well higher pH, are 2 nm particles with the structure of PuO_2 with Pu(IV) as the dominating oxidation state. Pu(III) and Pu(VI) oxidation states also observed in HERFD come from solution since spectrum is a superposition of both liquid and solid phase contributions due to the penetrative nature of X-rays. The factors, which should be taken into account for PuO_2 NP studies are discussed in details in the paper, which is submitted. (*Appendix C: Article 3. To form or not to form : PuO_2 nanoparticles at acidic pH*)

Conclusions and perspectives

The advantage of modern synchrotron methods is the possibility to reveal even slight changes in structural and electronic properties of the investigated objects. This is especially important in case of NPs, as the peculiarities of nanoscale objects affect their properties. However, sometimes the effect is so subtle that it is a challenge to detect it without techniques, providing a high resolution. It was proven that it is the case for NPs of f-elements. Bulk $CatO_2$ (Cat = Th, Ce, U, Pu) reveal similar crystallographic properties such as a fluorite-type structure and a similar lattice parameter. It was expected, that $CatO_2$ NPs would be also similar to each other though some special properties due to the nanoscale are anticipated. The investigation of structural properties reveals that NPs of Th, Ce, U and Pu prepared with a fast chemical deposition technique demonstrate similar crystallographic properties. Disregarding the numerous conditions, which can be varied, nanocrystalline particles are formed with crystal structure of the bulk $CatO_2$. The majority of obtained NPs have an average size of 2-4 nm. The investigation of the electronic properties by HERFD demonstrate, that not only redox inactive Th, but also Ce, U and Pu do not form either over/under stoichiometric $AnO_{2\pm x}$ or higher/lower oxide phases. It is quite surprising that $CatO_2$ NPs retain Cat(IV) as the dominating oxidation state taking into account that redox affinity of U, Ce and Pu is significant.

$CatO_2$ NPs originate from aqueous solutions. Tetravalent cations undergo extensive hydrolysis accompanied with the formation of different hydrolyzed forms: mono- and oligomeric; oxo- and hydroxo-bridged species. It was a challenging task to reveal the actual composition of the inner shell of PuO_2 NPs and it was solved by the combination of HERFD, EXAFS, HEXS methods and EXAFS calculations. The influence of hydrolysed forms have been investigated by HERFD and HEXS for ThO_2 NPs and the role of Th hexamer clusters were shown. Size effect of ThO_2 and CeO_2 NPs was observed thanks to a combination of XRD, HRTEM and HERFD techniques, contribution of hydroxylation in CeO_2 NPs was investigated by HERFD. Finally, the reactivity of UO_2 and PuO_2 NPs (and the whole PuO_2 formation process) have been examined by HERFD. All these findings show the resemblance between the properties of these f-elements in the system $CatO_2$ NPs and to what extent the analogy between these elements is applicable. Due to the successful isolation of hydro/oxo-bridged hexanuclear complexes of f-elements, it became evident, that simple models such as soft acid and base concepts are not sufficient to predict the hydrolysis chemistry of these elements, the real mechanisms are more complicated and demand additional investigations. The results presented in this thesis, enhance our knowledge of these species and give us a clue about fundamental processes, which can be applied to predict the behaviour of radionuclides from contaminated sites and underground repositories. The following investigations of such systems are inextricably linked with the synchrotron methods.

The outlook of this thesis is inevitably related to NPs. It is possible to finish a thesis work but unlikely to complete the scientific study. Even now there are some projects which have already been started and likely will be finished one day, I will show some examples: the redox transitions of U(VI) NPs under certain conditions; the properties of CeO_2 NPs and the processes of their formation etc. Besides that, there many directions in which these studies may be continued and extended: the investigation of NpO_2 NPs, another possible analog of PuO_2 with its own peculiar properties; americium and curium NPs, the investigation of their properties can shed light on the Pu, Am and Cm separation prosecesses. Another perpective research domain is in-situ reactions

of NPs formation. Starting with Ce, the inactive f-element, one can discover many insights about CeO_2 NPs formation and obtained information will reveal a precious information about one of the most complicated chemical task – the real mechanism of the reactions. Being experienced with Ce, one may go further and investigate in-situ reactions with actinides and who knows – probably synchrotron in-situ experiments with actinides allow to make a breakthrough in understanding of technological and environmental processes where f-elements colloids are involved.

Personal contribution

Despite the fact, that modern sciences is mostly done by the group of scientists, I think it is still necessary to describe my personal impact to this work. There are many processes starting from sample synthesis ending by the article preparation. I will discuss everythinh point per point.

Synthetic procedures: all actinide samples were prepared in Helmholtz-Zentrum Dresden-Rossendorf because it has a lisence to transport radioactive samples throughout Europe at certain conditions. I prepared the following samples personally: PuO_2 NPs (at all conditions), Pu(V) intermediate phase, UO_2 NPs. I also participated in preparation of ThO_2 and CeO_2 NPs. Sample packing for the synchrotron measurements is another substantial part of the experimental work which I was done for the vast majority of samples (excluding Ce samples).

Experiments: first of all, as a member of ROBL group I spent quite some time at beamline, assiting with the experiments. The alignment of the HERFD spectrometer was done for each experiment, starting with calculations of the motor positions, then laser and finally X-ray alignment (more details in 2.3.2). I was actively participating in the measurements, method by method:

XRD: The measurements of PuO_2 NPs (see 2.1.2)

HERFD: The measurements of PuO_2 NPs at Pu L_3 and M_4 –edges (details are in paragrahs 2.3.3.1 and 3.2), Pu(V) phase at Pu L_3 and M_4 –edges (2.3.3.2), CeO_2 NPs at Ce M_5 edge (2.3.3.4), UO_2 NPs at M_4 edge (2.3.3.3) and ThO_2 NPs at Th L_3 edge (2.3.3.5).

EXAFS: The measurements of PuO_2 NPs (2.4.3).

HEXS: The measurements of PuO_2 NPs (2.5.3.1) and ThO_2 NPs (2.5.3.2)

Dana analysis: for all Pu and U systems the treatment of XRD, HERFD, EXAFS and HEXS results was done by me. I also participated in the analysis of HEXS data for ThO_2 NPs and HERFD data for ThO_2 and CeO_2 NPs.

Theoretical simulations: FEFF9.6. code was used to calculate XANES spectrum of PuO_2.

Articles: I have written three articles as a first author

Appendix A: Article 1. The missing pieces of the PuO2 nanoparticle puzzle

Appendix B: Article 2. Insight into the structure-property relation of UO2 nanoparticles)

Appendix C: Article 3. To form or not to form : PuO2 nanoparticles at acidic pH (currently is submitted).

Moreover, I have contributed as a coauthor in four other articles:

Appendix D: Article 4. A novel meta-stable pentavalent plutonium solid phase on the pathway from aqueous Pu(VI) to PuO2 nanoparticles

Appendix E: Article 5. Towards the surface hydroxyl species in CeO2 nanoparticles

Appendix F: Article 6. Understanding the size effects on the electronic structure of ThO2 nanoparticles

Appendix G: Article 7. The Application of HEXS and HERFD XANES for Accurate Structural Characterisation of Actinide Nanomaterials: The Case of ThO2

Overall, I participated at the experiments not only at ESRF (at several beamlines), but also at SOLEIL, KARA, SLS and Kurchatov synchrotrons. I got deep experience in data treatment and data analysis of the methods like EXAFS, HERFD, HEXS, XRD, which will help to proceed in my scientific carier further.

Bibliography

1 P. Willmott, *An Introduction to Synchrotron Radiation*, Wiley, 2011.

2 A. C. Scheinost, J. Claussner, J. Exner, M. Feig, S. Findeisen, C. Hennig, K. O. Kvashnina, D. Naudet, D. Prieur, A. Rossberg, M. Schmidt, C. Qiu, P. Colomp, C. Cohen, E. Dettona, V. Dyadkin and T. Stumpf, *J. Synchrotron Rad*, , DOI:10.1107/S1600577520014265.

3 J. Rothe, S. Butorin, K. Dardenne, M. A. Denecke, B. Kienzler, M. Löble, V. Metz, A. Seibert, M. Steppert, T. Vitova, C. Walther and H. Geckeis, *Rev. Sci. Instrum.*, 2012, **83**, 043105.

4 A. Zimina, K. Dardenne, M. A. Denecke, D. E. Doronkin, E. Huttel, H. Lichtenberg, S. Mangold, T. Pruessmann, J. Rothe, T. Spangenberg, R. Steininger, T. Vitova, H. Geckeis and J.-D. Grunwaldt, *Rev. Sci. Instrum.*, 2017, **88**, 113113.

5 I. LLorens, P. L. Solari, B. Sitaud, R. Bes, S. Cammelli, H. Hermange, G. Othmane, S. Safi, P. Moisy, S. Wahu, C. Bresson, M. L. Schlegel, D. Menut, J.-L. Bechade, P. Martin, J.-L. Hazemann, O. Proux and C. Den Auwer, *Radiochim. Acta*, , DOI:10.1515/ract-2013-2241.

6 B. Sitaud, P. L. Solari, S. Schlutig, I. Llorens and H. Hermange, *J. Nucl. Mater.*, 2012, **425**, 238–243.

7 C. N. Borca, D. Grolimund, M. Willimann, B. Meyer, K. Jefimovs, J. Vila-Comamala and C. David, *J. Phys. Conf. Ser.*, 2009, **186**, 012003.

8 V. Dyadkin, P. Pattison, V. Dmitriev and D. Chernyshov, *J. Synchrotron Radiat.*, 2016, **23**, 825–829.

9 J. Perl, J. Shin, J. Schümann, B. Faddegon and H. Paganetti, *Med. Phys.*, 2012, **39**, 6818–6837.

10 L. Akselrud and Y. Grin, *J. Appl. Crystallogr.*, 2014, **47**, 803–805.

11 J. J. Rehr and R. C. Albers, *Rev. Mod. Phys.*, 2000, **72**, 621–654.

12 J. J. Rehr and A. L. Ankudinov, *Coord. Chem. Rev.*, 2005, **249**, 131–140.

13 K. O. Kvashnina and A. C. Scheinost, *J. Synchrotron Radiat.*, 2016, **23**, 836–841.

14 H. H. Johann, *Zeitschrift für Phys.*, 1931, **69**, 185–206.

15 T. Johansson, *Zeitschrift für Phys.*, 1933, **82**, 507–528.

16 S. H. Nowak, R. Armenta, C. P. Schwartz, A. Gallo, B. Abraham, A. T. Garcia-Esparza, E. Biasin, A. Prado, A. Maciel, D. Zhang, D. Day, S. Christensen, T. Kroll, R. Alonso-Mori, D. Nordlund, T.-C. Weng and D. Sokaras, *Rev. Sci. Instrum.*, 2020, **91**, 033101.

17 P. J. Potts, *Mineral. Mag.*, 1995, **59**, 774–774.

18 K. Klementiev, K. Norén, S. Carlson, K. G. V. S. Clauss and I. Persson, *J. Phys. Conf.*

Ser., 2016, **712**, 012023.

19 J. K. Kowalska, F. A. Lima, C. J. Pollock, J. A. Rees and S. DeBeer, *Isr. J. Chem.*

20 L. Von Hamos, *Naturwissenschaften*, 1932, **20**, 705–706.

21 J. Szlachetko and J. Sá, in *Advanced Catalytic Materials - Photocatalysis and Other Current Trends*, InTech, 2016.

22 R. Alonso-Mori, J. Kern, D. Sokaras, T.-C. Weng, D. Nordlund, R. Tran, P. Montanez, J. Delor, V. K. Yachandra, J. Yano and U. Bergmann, *Rev. Sci. Instrum.*, 2012, **83**, 073114.

23 M. Bauer, *Phys. Chem. Chem. Phys.*, 2014, **16**, 13827–13837.

24 S. Gul, J. W. D. Ng, R. Alonso-Mori, J. Kern, D. Sokaras, E. Anzenberg, B. Lassalle-Kaiser, Y. Gorlin, T.-C. Weng, P. H. Zwart, J. Z. Zhang, U. Bergmann, V. K. Yachandra, T. F. Jaramillo and J. Yano, *Phys. Chem. Chem. Phys.*, 2015, **17**, 8901–8912.

25 J. Kern, R. Alonso-Mori, R. Tran, J. Hattne, R. J. Gildea, N. Echols, C. Glockner, J. Hellmich, H. Laksmono, R. G. Sierra, B. Lassalle-Kaiser, S. Koroidov, A. Lampe, G. Han, S. Gul, D. DiFiore, D. Milathianaki, A. R. Fry, A. Miahnahri, D. W. Schafer, M. Messerschmidt, M. M. Seibert, J. E. Koglin, D. Sokaras, T.-C. Weng, J. Sellberg, M. J. Latimer, R. W. Grosse-Kunstleve, P. H. Zwart, W. E. White, P. Glatzel, P. D. Adams, M. J. Bogan, G. J. Williams, S. Boutet, J. Messinger, A. Zouni, N. K. Sauter, V. K. Yachandra, U. Bergmann and J. Yano, *Science (80-.).*, 2013, **340**, 491–495.

26 J. Kern, R. Tran, R. Alonso-Mori, S. Koroidov, N. Echols, J. Hattne, M. Ibrahim, S. Gul, H. Laksmono, R. G. Sierra, R. J. Gildea, G. Han, J. Hellmich, B. Lassalle-Kaiser, R. Chatterjee, A. S. Brewster, C. A. Stan, C. Glöckner, A. Lampe, D. DiFiore, D. Milathianaki, A. R. Fry, M. M. Seibert, J. E. Koglin, E. Gallo, J. Uhlig, D. Sokaras, T.-C. Weng, P. H. Zwart, D. E. Skinner, M. J. Bogan, M. Messerschmidt, P. Glatzel, G. J. Williams, S. Boutet, P. D. Adams, A. Zouni, J. Messinger, N. K. Sauter, U. Bergmann, J. Yano and V. K. Yachandra, *Nat. Commun.*, 2014, **5**, 4371.

27 J. Szlachetko, D. Ferri, V. Marchionni, A. Kambolis, O. V. Safonova, C. J. Milne, O. Kröcher, M. Nachtegaal and J. Sá, *J. Am. Chem. Soc.*, 2013, **135**, 19071–19074.

28 R. Alonso-Mori, J. Kern, R. J. Gildea, D. Sokaras, T.-C. Weng, B. Lassalle-Kaiser, R. Tran, J. Hattne, H. Laksmono, J. Hellmich, C. Glockner, N. Echols, R. G. Sierra, D. W. Schafer, J. Sellberg, C. Kenney, R. Herbst, J. Pines, P. Hart, S. Herrmann, R. W. Grosse-Kunstleve, M. J. Latimer, A. R. Fry, M. M. Messerschmidt, A. Miahnahri, M. M. Seibert, P. H. Zwart, W. E. White, P. D. Adams, M. J. Bogan, S. Boutet, G. J. Williams, A. Zouni, J. Messinger, P. Glatzel, N. K. Sauter, V. K. Yachandra, J. Yano and U. Bergmann, *Proc. Natl. Acad. Sci.*, 2012, **109**, 19103–19107.

29 J. Szlachetko, C. J. Milne, J. Hoszowska, J.-C. Dousse, W. Błachucki, J. Sà, Y. Kayser, M. Messerschmidt, R. Abela, S. Boutet, C. David, G. Williams, M. Pajek, B. D. Patterson, G. Smolentsev, J. A. van Bokhoven and M. Nachtegaal, *Struct. Dyn.*, 2014, **1**, 021101.

30 P. Zimmermann, S. Peredkov, P. M. Abdala, S. DeBeer, M. Tromp, C. Müller and J. A. van Bokhoven, *Coord. Chem. Rev.*, 2020, **423**, 213466.

31 P. Glatzel, F. M. F. de Groot and U. Bergmann, *Synchrotron Radiat. News*, 2009, **22**, 12–16.

32 E. Kleymenov, J. A. van Bokhoven, C. David, P. Glatzel, M. Janousch, R. Alonso-Mori, M. Studer, M. Willimann, A. Bergamaschi, B. Henrich and M. Nachtegaal, *Rev. Sci. Instrum.*, 2011, **82**, 065107.

33 F. de Groot and A. Kotani, *Core Level Spectroscopy of Solids*, CRC Press, 2008.

34 J. A. Van Bokhoven and C. Lamberti, Eds., *X-Ray Absorption and X-Ray Emission Spectroscopy*, John Wiley & Sons, Ltd, Chichester, UK, 2016.

35 P. Glatzel and U. Bergmann, *Coord. Chem. Rev.*, 2005, **249**, 65–95.

36 M. Rovezzi, C. Lapras, A. Manceau, P. Glatzel and R. Verbeni, *Rev. Sci. Instrum.*, 2017, **88**, 013108.

37 K. O. Kvashnina, A. Y. Romanchuk, I. Pidchenko, L. Amidani, E. Gerber, A. Trigub, A. Rossberg, S. Weiss, K. Popa, O. Walter, R. Caciuffo, A. C. Scheinost, S. M. Butorin and S. N. Kalmykov, *Angew. Chemie - Int. Ed.*, 2019, **58**, 17558–17562.

38 L. Amidani, T. V. Plakhova, A. Y. Romanchuk, E. Gerber, S. Weiss, A. Efimenko, C. J. Sahle, S. M. Butorin, S. N. Kalmykov and K. O. Kvashnina, *Phys. Chem. Chem. Phys.*, 2019, **21**, 10635–10643.

39 J. J. Rehr, J. J. Kas, F. D. Vila, P. P. Micah and K. Jorissen, *Phys. Chem. Chem. Phys.*, 2010, **12**, 5503–5513.

40 P. W. Anderson, *Phys. Rev.*, 1961, **124**, 41–53.

41 K. O. Kvashnina, S. M. Butorin, P. Martin and P. Glatzel, *Phys. Rev. Lett.*, 2013, **111**, 253002.

42 C. Gauthier, V. A. Sol, R. Signorato, J. Goulon and E. Moguiline, *J. Synchrotron Radiat.*, 1999, **6**, 164–166.

43 S. M. Butorin, K. O. Kvashnina, A. L. Smith, K. Popa and P. M. Martin, *Chem. Eur. J.*, 2016, **22**, 9693–9698.

44 O. Bunău and Y. Joly, *J. Phys. Condens. Matter*, 2009, **21**, 345501.

45 S. A. Guda, A. A. Guda, M. A. Soldatov, K. A. Lomachenko, A. L. Bugaev, C. Lamberti, W. Gawelda, C. Bressler, G. Smolentsev, A. V. Soldatov and Y. Joly, *J. Chem. Theory Comput.*, 2015, **11**, 4512–4521.

46 J. Rothe, M. Altmaier, R. Dagan, K. Dardenne, D. Fellhauer, X. Gaona, E. G.-R. Corrales, M. Herm, K. O. Kvashnina, V. Metz, I. Pidchenko, D. Schild, T. Vitova and and H. Geckeis, *Geosciences*, 2019, **9**, 91.

47 E. Gerber, A. Y. Romanchuk, S. Weiss, S. Bauters, B. Schacherl, T. Vitova, R. Hübner, S. Shams Aldin Azzam, D. Detollenaere, D. Banerjee, S. M. Butorin, S. N. Kalmykov and K. O. Kvashnina, *Inorg. Chem. Front.*, 2021, **8**, 1102–1110.

48 E. Gerber, A. Y. Romanchuk, I. Pidchenko, L. Amidani, A. Rossberg, C. Hennig, G. B. M. Vaughan, A. Trigub, T. Egorova, S. Bauters, T. Plakhova, M. O. J. Y. Hunault, S. Weiss, S. M. Butorin, A. C. Scheinost, S. N. Kalmykov and K. O. Kvashnina, *Nanoscale*, 2020, **12**, 18039–18048.

49 G. Leinders, R. Bes, J. Pakarinen, K. Kvashnina and M. Verwerft, *Inorg. Chem.*, 2017, **56**, 6784–6787.

50 T. V. Plakhova, A. Y. Romanchuk, S. M. Butorin, A. D. Konyukhova, A. V. Egorov, A. A. Shiryaev, A. E. Baranchikov, P. V. Dorovatovskii, T. Huthwelker, E. Gerber, S. Bauters, M. M. Sozarukova, A. C. Scheinost, V. K. Ivanov, S. N. Kalmykov and K. O. Kvashnina, *Nanoscale*, 2019, **11**, 18142–18149.

51 M. Moretti Sala, K. Martel, C. Henriquet, A. Al Zein, L. Simonelli, C. J. Sahle, H. Gonzalez, M.-C. Lagier, C. Ponchut, S. Huotari, R. Verbeni, M. Krisch and G. Monaco, *J. Synchrotron Radiat.*, 2018, **25**, 580–591.

52 A. Rossberg, T. Reich and G. Bernhard, *Anal. Bioanal. Chem.*, 2003, **376**, 631–638.

53 A. Rossberg and A. C. Scheinost, *Anal. Bioanal. Chem.*, 2005, **383**, 56–66.

54 A. Rossberg and H. Funke, *J. Synchrotron Radiat.*, 2010, **17**, 280–288.

55 K. Domaschke, A. Rossberg and Villmann Thomas, *Eur. Symp. Artif. Neural Networks, Comput. Intell. Mach. Learn.*, 2014, 277–282.

56 S. M. Webb, *Phys. Scr.*, 2005, **T115**, 1011–1014.

57 B. Ravel and M. Newville, *J. Synchrotron Radiat.*, 2005, **12**, 537–541.

58 T. Ressler, *J. Phys. IV*, 1997, **7**, C2-269.

59 A. Ankudinov and J. Rehr, *Phys. Rev. B - Condens. Matter Mater. Phys.*, 1997, **56**, R1712–R1716.

60 A. Ankudinov and B. Ravel, *Phys. Rev. B - Condens. Matter Mater. Phys.*, 1998, **58**, 7565–7576.

61 R. C. Belin, P. J. Valenza, M. A. Reynaud and P. E. Raison, *Appl. Crystallogr.*, 2004, **37**, 1034–1037.

62 P. Debye, *Ann. Phys.*, 1915, **351**, 809–823.

63 F. Zernike and J. A. Prins, *Zeitschrift für Phys. A Hadron. Nucl.*, 1927, **41**, 184–194.

64 M. Zobel, R. B. Neder and S. A. J. Kimber, *Science (80-.).*, 2015, **347**, 292–294.

65 H. F. Poulsen, J. Neuefeind, H.-B. Neumann, J. R. Schneider and M. D. Zeidler, *J. Non. Cryst. Solids*, 1995, **188**, 63–74.

66 K. W. Chapman, *MRS Bull.*, 2016, **41**, 231–240.

67 D. A. Keen, *J. Appl. Crystallogr.*, 2001, **34**, 172–177.

68 P. Juhás, T. Davis, C. L. Farrow and S. J. L. Billinge, *J. Appl. Crystallogr.*, 2013, **46**, 560–

566.

69 J. Kieffer, S. Petitdemange and T. Vincent, *J. Synchrotron Radiat.*, 2018, **25**, 612–617.

70 P. Juhas, C. L. Farrow, X. Yang, K. R. Knox and S. J. L. Billinge, *Acta Crystallogr. A*, 2015, **71**, 562–568.

71 C. J. Benmore, *ISRN Mater. Sci.*, 2012, **2012**, 1–19.

72 G. B. M. Vaughan, R. Baker, R. Barret, J. Bonnefoy, T. Buslaps, S. Checchia, D. Duran, F. Fihman, P. Got, J. Kieffer, S. A. J. Kimber, K. Martel, C. Morawe, D. Mottin, E. Papillon, S. Petitdemange, A. Vamvakeros, J.-P. Vieux and M. Di Michiel, *J. Synchrotron Radiat.*, 2020, **27**, 515–528.

73 C. L. Farrow, P. Juhas, J. W. Liu, D. Bryndin, E. S. Bozin, J. Bloch, T. Proffen and S. J. L. Billinge, *J. Phys. Condens. matter*, 2007, **19**, 335219.

74 L. Amidani, G. B. M. Vaughan, T. V. Plakhova, A. Y. Romanchuk, E. Gerber, R. Svetogorov, S. Weiss, Y. Joly, S. N. Kalmykov and K. O. Kvashnina, *Chem. – A Eur. J.*, 2021, **27**, 252–263.

75 S. Takao, K. Takao, W. Kraus, F. Emmerling, A. C. Scheinost, G. Bernhard and C. Hennig, *Eur. J. Inorg. Chem.*, 2009, **2009**, 4771–4775.

76 C. Hennig, S. Takao, K. Takao, S. Weiss, W. Kraus, F. Emmerling and A. C. Scheinost, *Dalt. Trans.*, 2012, **41**, 12818.

77 K. E. Knope, R. E. Wilson, M. Vasiliu, D. A. Dixon and L. Soderholm, *Inorg. Chem.*, 2011, **50**, 9696–9704.

78 N. Torapava, I. Persson, L. Eriksson and D. Lundberg, *Inorg. Chem.*, 2009, **48**, 11712–11723.

79 M. F. Hochella, D. W. Mogk, J. Ranville, I. C. Allen, G. W. Luther, L. C. Marr, B. P. McGrail, M. Murayama, N. P. Qafoku, K. M. Rosso, N. Sahai, P. A. Schroeder, P. Vikesland, P. Westerhoff and Y. Yang, *Science (80-.).*, 2019, **363**, eaau8299.

80 T. V. Plakhova, A. Y. Romanchuk, D. V. Likhosherstova, A. E. Baranchikov, P. V. Dorovatovskii, R. D. Svetogorov, T. B. Shatalova, T. B. Egorova, A. L. Trigub, K. O. Kvashnina, V. K. Ivanov and S. N. Kalmykov, *J. Phys. Chem. C*, 2019, **123**, 23167–23176.

81 J. Rothe, C. Walther, M. A. Denecke and T. Fanghänel, *Inorg. Chem.*, 2004, **43**, 4708–4718.

82 S. D. Conradson, B. D. Begg, D. L. Clark, C. Den Auwer, M. Ding, P. K. Dorhout, F. J. Espinosa-Faller, P. L. Gordon, R. G. Haire, N. J. Hess, R. F. Hess, D. W. Keogh, L. A. Morales, M. P. Neu, P. Paviet-Hartmann, W. Runde, C. D. Tait, D. K. Veirs and P. M. Villella, *J. Am. Chem. Soc.*, 2004, **126**, 13443–13458.

83 C. Ekberg, K. Larsson, G. Skarnemark and I. Persson, *Dalt. Trans.*, 2013, **42**, 2035–2040.

84 D. Hudry, C. Apostolidis, O. Walter, A. Janßen, D. Manara, J. C. Griveau, E. Colineau, T.

Vitova, T. Prüßmann, D. Wang, C. Kübel and D. Meyer, *Chem. Eur. J.*, 2014, **20**, 10431–10438.

85 E. Dalodière, M. Virot, V. Morosini, T. Chave, T. Dumas, C. Hennig, T. Wiss, O. Dieste Blanco, D. K. Shuh, T. Tyliszcak, L. Venault, P. Moisy and S. I. Nikitenko, *Sci. Rep.*, 2017, **7**, 1–10.

86 E. Dalodière, M. Virot, T. Dumas, D. Guillaumont, M.-C. Illy, C. Berthon, Guerin, Laetitia, A. Rossberg, L. Venault, P. Moisy and S. I. Nikitenko, *Inorg. Chem. Front.*, 2018, **5**, 100–111.

87 L. Bonato, M. Virot, T. Dumas, A. Mesbah, E. Dalodière, O. Dieste Blanco, T. Wiss, X. Le Goff, M. Odorico, D. Prieur, A. Rossberg, L. Venault, N. Dacheux, P. Moisy and S. I. Nikitenko, *Nanoscale Adv.*, 2020, **2**, 214–224.

88 A. C. Scheinost, A. Rossberg, M. Marcus, S. Pfister and R. Kretzschmar, *Phys. Scr.*, 2005, 1038.

Appendix A: Article 1. The missing pieces of the PuO_2 nanoparticle puzzle

Evgeny Gerber[a,b,c], Anna Yu. Romanchuk[c], Ivan Pidchenko[a,b], Lucia Amidani[a,b], Andre Rossberg[a,b], Christoph Hennig[a,b], Gavin B. M. Vaughan[d], Alexander Trigub[e], Tolganay Egorova[c], Stephen Bauters[a,b], Tatiana Plakhova[c], Myrtille O.J.Y. Hunault[f], Stephan Weiss[b], Sergei M. Butorin[g], Andreas C. Scheinost[a,b], Stepan N. Kalmykov[c,e] and Kristina O. Kvashnina*[a,b,c]

[a] *The Rossendorf Beamline at ESRF – The European Synchrotron, CS40220, 38043 Grenoble Cedex 9, France.*

[b] *Helmholtz-Zentrum Dresden-Rossendorf (HZDR), Institute of Resource Ecology, PO Box 510119, 01314, Dresden.*

[c] *Lomonosov Moscow State University, Department of Chemistry, 119991 Moscow, Russia.*

[d] *ESRF – The European Synchrotron, CS40220, 38043 Grenoble Cedex 9, France.*

[e] *National Research Centre "Kurchatov Institute", 123182 Moscow, Russia.*

[f] *Synchrotron SOLEIL, L'Orme des Merisiers, Saint Aubin BP 48, 91192 Gif-sur-Yvette, France.*

[g] *Molecular and Condensed Matter Physics, Department of Physics and Astronomy, Uppsala University, P.O. Box 516, Uppsala, Sweden.*

The nanoscience field often produces results more mystifying than any other discipline. It has been argued that changes in the plutonium dioxide (PuO_2) particle size from bulk to nano can have a drastic effect on PuO_2 properties. Here we report a full characterization of PuO_2 nanoparticles (NPs) at the atomic level and probe their local and electronic structure by a variety of methods available at the synchrotron, including extended X-ray absorption fine structure (EXAFS) at the Pu L_3 edge, X-ray absorption near edge structure (XANES) in high energy resolution fluorescence detection (HERFD) mode at the Pu L_3 and M_4 edges, high energy X-ray scattering (HEXS) and X-ray diffraction (XRD). The particles were synthesized from precursors with different oxidation states of plutonium (III, IV, and V) under various environmentally and waste storage relevant conditions (pH 8 and pH >10). Our experimental results are analyzed with state-of-the-art theoretical approaches. We demonstrate that well dispersed, crystalline NPs with a size of ~2.5 nm in diameter are always formed in spite of diverse chemical conditions. Identical crystal structures and the presence of only the Pu(IV) oxidation state in all NPs, reported here for the first time, indicate that the structure of PuO_2 NPs is very similar to that of the bulk PuO_2. All methods give complementary information and show that investigated fundamental properties of PuO_2 NPs, rather than being exotic, are very similar to those of the bulk PuO_2.

Introduction

Plutonium (Pu) is one of the most complex and fascinating chemical elements in the periodic table.[1] At the end of 2014, there were about 2,400 tonnes of irradiated and unirradiated plutonium from civilian nuclear power reactors located in 33 countries. Over the last ten years, this plutonium stock has grown at an average rate of almost 50 tonnes per year[2]. Nuclear reactors unavoidably generate nuclear waste, among which Pu isotopes are one of the longest-living.

Most countries have adopted the concept of deep geological disposal of spent nuclear fuel and nuclear waste. Nuclear safety is of paramount importance and the main question, which remains unclear – is what will happen to Pu species present in the environment or nuclear wastes over the years? The path to answering these questions is by expanding the fundamental understanding of Pu properties with a special focus on the forms it can take in environmentally relevant conditions.

Pu has at least six oxidation states - from Pu(II)[3] to Pu(VII) - under certain conditions. In environmentally relevant conditions Pu may exist and even co-exist in four of them, from Pu(III) to Pu(VI)[4,5]. Pu(IV) strongly hydrolyses in aqueous solutions resulting in the formation of polynuclear species, intrinsic colloids that may form a stable suspension or precipitates.[6,7] The speciation of Pu in aqueous solutions due to the complexity of its chemical behaviour (solubility and redox reactions[8,9]) combined with a great variety of environmental substrates (ligands, mineral interfaces, bacteria, solids, *etc.*) makes Pu geochemistry very complicated. It has been discovered that Pu may be transported by groundwater from contaminated sites on a scale of kilometres bounded with mineral[10,11] or organic colloids.[12] Recently, it was repeatedly found that PuO_{2+x} NPs are formed during interfacial processes between Pu in different initial oxidation states and various mineral surfaces (hematite, goethite, quartz, and mica) [13-17] and bacteria.[18,19] All these results indicate the high importance of PuO_2 NPs in the context of environmental behaviour. Clearly, the variety of unknown or imprecisely known Pu species and crystal structures and their possible transformations make predictive modelling and extrapolation of the Pu chemical evolution and migration in the environment impossible or at least very challenging.

To improve our understanding of Pu properties, it is necessary to use licensed lab facilities to handle radioactive material safely combined with the most powerful experimental methods and complemented with theoretical advances. X-rays emitted by large-scale facilities - synchrotrons - can be used to study the atomic structure of such materials because of their penetrative behaviour and their sensitivity to the local and electronic structure of the selected element. Here we report a systematic investigation of PuO_2 NPs, synthesized using environmentally and waste storage relevant conditions, *i.e.* varying the pH (*e.g.* pH 8 and pH>10) and the precursor (Pu(III), Pu(IV), Pu(V)). While pH 8 is more typical for far-field of nuclear waste disposal, an alkaline pH (> 10) is possible in alkaline nuclear waste tanks and also can be reached the cement near-field environments.[20] The synthesized PuO_2 NPs are characterized by a variety of experimental methods: high-resolution transmission electron microscopy (HRTEM), selected-area electron diffraction (SAED), extended X-ray absorption fine structure (EXAFS), X-ray absorption near edge structure (XANES) in high energy resolution fluorescence detection (HERFD) mode, high energy X-ray scattering (HEXS), X-ray diffraction (XRD). The theoretical interpretation of the experimental data is based on the Anderson impurity model (AIM)[21] and ab-initio calculations[22]. Fig. 1 shows a schematic illustration of the research methodology applied to PuO_2 NPs studies.

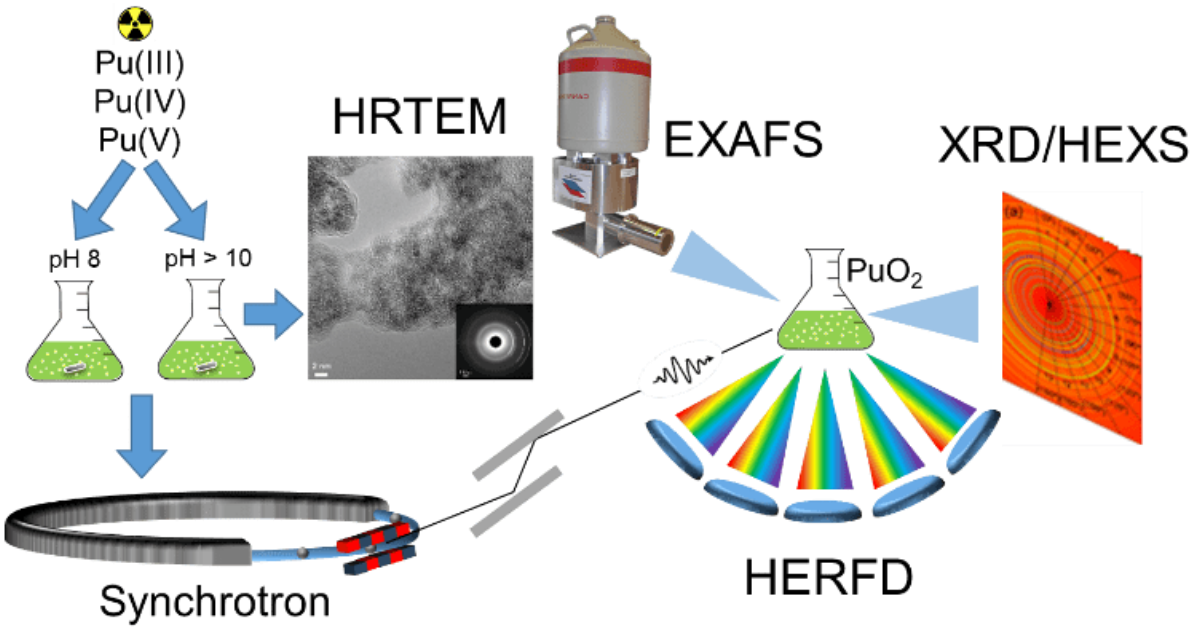

Figure 1. The schematic illustration of the research methodology applied in the PuO_2 NPs studies. PuO_2 NPs synthesized from different precursors (Pu(III), Pu(IV) and Pu(V)) and at pH 8 and pH >10 were analysed with HRTEM and various synchrotron techniques (EXAFS, XRD, HEXS and HERFD).

Experimental section

Synthetic procedures

Pu of 99.74 mass % of ^{242}Pu was used for Pu stock. The Pu(III) solution was prepared from Pu stock solution by reduction with hydroxylamine hydrochloride when slightly heated in 1 M $HClO_4$. The Pu(IV) solution was obtained from Pu(III) oxidation with $NaNO_2$ in 5 M HNO_3. The Pu(V) solution was the result of the reaction of H_2O_2 with Pu(VI) solution (pH = 7), which in turn was also obtained from Pu stock by oxidation with $NaBrO_3$ under slight heating in 1 M $HClO_4$. All Pu valence states were verified by UV-vis spectrometry (TIDAS 100 J&M Analytics) and spectra of all initial solutions are listed in Fig. S1. The presence of only Pu(VI) impurities in the initial solutions was measured to be less than 3%. The Pu(III), Pu(IV) and Pu(V) initial solutions ($\sim 6\times10^{-4}$ M Pu) were divided into two parts to prepare PuO_2 NPs. The aliquots of Pu(III), Pu(IV) and Pu(V) from the first part were added to 3 M $NH_3{\cdot}H_2O$ in the volume ratio 1:10 under continuous stirring. The pH of the 3 M ammonia solution is 12.5, but the pH was slightly decreasing during the synthesis procedure as the Pu cation hydrolyzed with acid formation. This set of samples would be called «from Pu(X) pH >10», where X = III, IV, V. The aliquots of Pu(III), Pu(IV) and Pu(V) from the second part were added to water in the volume ratio 1:10 and then several drops of 3 M $NH_3{\cdot}H_2O$ were added under continuous stirring to reach pH 8. The pH was also decreasing due to the Pu hydrolysis, hence additional drops of the ammonia solution were used to preserve pH 8. This set of samples would be called «from Pu(X) pH 8», where X = III, IV, V. Additional information about the synthesis is listed in SI. PuO_2 reference was purchased from Oakridge National Lab (Batch I.D. No. Pu-242-327A1).

Methods

HRTEM measurements

The HRTEM images on a set of samples were recorded at Lomonosov Moscow State University (LMSU) with an aberration-corrected JEOL 2100F operated at 200 kV, yielding an information limit of 0.8 Å. The dark field (DF) images and energy-dispersive X-ray spectroscopy (EDX) analysis were performed in scanning transmission electron microscope (STEM) mode; the spot size was 1 nm with the HAADF and JED 2300 (JEOL) detectors.

HEXS measurements

High energy X-ray scattering data were collected at room temperature at the ID15A beamline of the European Synchrotron Radiation Facility (ESRF, Grenoble).[23] An incident energy of 120000 eV was selected in order to be below the Pu K-edge at 121791 eV and to minimize absorption. The K-edge XANES spectrum was measured to verify the incident energy (Fig. S2). Data were collected up to 30 $Å^{-1}$ using a Dectris Pilatus 2M CdTe pixel detector. Patterns were corrected for detector geometry, response and transparency, and integrated using a locally modified version of pyFAI[24] with outlier filtering. F(q) and G(r) were calculated from the resulting powder diffraction patterns using modules from DIFFPY-CMI[25] and locally developed cleaning algorithms. The full profile real-space refinement of crystal structures based on the pair distribution function G(r) was made using PDFgui software.[26] PDFgui performs a least-squares refinement of the structural model to the G(r). The parameters refined for the NPs series were lattice parameter *a*, particle diameter for the G(r) shape damping function (spdiameter), the data scale factor, and factor which accounts for low-r sharpening in G(r) due to nearest-neighbour correlations (delta2). Parameters such as the G(r) Gaussian dampening envelope due to limited Q-resolution and isotropic atomic displacement parameters (ADPs) were obtained from the fit of the experimental data of the PuO_2 reference and fixed at these values for the refinements of the NPs experimental sets, in order to minimize the number of refinable parameters and to obtain the most robust values for the coherent domain size. Free water was also included in the model in order to reproduce the contribution of water at the short-range order. All samples were fitted in the range from 1.7 to 20 Å and the maximum wave vector Q of the data used for the generation of G(r) was settled to 26 $Å^{-1}$. The R_w value is a goodness of fit measure to show the agreement between calculated and experimental data.

X-ray absorption near edge structure (XANES) in high energy resolution fluorescence detection (HERFD) mode at the Pu L_3 and M_4 edges and Pu L_3 extended X-ray absorption fine structure (EXAFS) spectroscopy

The Pu L_3 HERFD experiments were performed at The Rossendorf Beamline at ESRF. The energy of the X-ray beam was tuned by a double-crystal monochromator operating in pseudo-channel-cut mode using a Si(111) crystal pair. Two rhodium-coated Si mirrors before and after the monochromator were used to collimate the beam and to reject higher harmonics. XANES spectra were simultaneously measured in total fluorescence yield (TFY) mode with a photodiode and in HERFD mode using an x-ray emission spectrometer.[27] The sample, each crystal analyser, and the silicon drift detector (Ketek) were positioned on their respective vertical Rowland circles of 0.5 m diameter. The Pu L_3 spectra were collected by recording the intensity of the Pu $L_{\alpha 1}$

emission line (~ 14282 eV) as a function of the incident energy. The emission energy was selected using the [777] reflection of five spherically bent Si crystal analysers (with 0.5 m bending radius[28]) aligned at 75.7° Bragg angle. The intensity was normalised to the incident flux. A combined (incident convoluted with emitted) energy resolution of 2.8 eV was obtained as determined by measuring the full width at half maximum (FWHM) of the elastic peak.

The HERFD spectra at the Pu M_4 edge were collected at Beamline ID26 of ESRF.[29] The incident energy was selected using the [111] reflection from a double Si crystal monochromator. Rejection of higher harmonics was achieved by three Si mirrors at angles of 3.0, 3.5, and 4.0 mrad relative to the incident beam. The Pu HERFD spectra at the M_4 edge were obtained by recording the maximum intensity of the Pu M_β emission line (~3534 eV) as a function of the incident energy. The emission energy was selected using the [220] reflection of five spherically bent Si crystal analysers (with 1m bending radius) aligned at 66.0° Bragg angle. The paths of the incident and emitted X-rays through the air were minimized by employing a He filled bag to avoid losses in intensity due to absorption. An estimated energy resolution (incident convoluted with emitted) found to be an order of 0.4 eV.

One HERFD spectrum on PuO_2 NPs synthesized from Pu(III) precursor at pH 8 was collected at the MARS Beamline at SOLEIL using the [111] reflection from a double Si crystal monochromator. The Pu M_β emission line was selected using one spherically bent Si crystal analyser (with 1m bending radius) with [220] reflection. Experimental spectral broadening of HERFD data at the Pu M_4 edge collected at ID26 beamline was compared to one recorded at MARS beamline on PuO_2 reference sample and found to be identical (Fig. S3).

The Pu L_3 edge EXAFS spectra were collected at The Rossendorf beamline (ROBL) in transmission mode using ion chambers. Spectra were collected at room temperature. Energy calibration was performed using the zero crossing of the second derivative of the K-edge of metallic Zr (~17998 eV) and measured in parallel to the sample scans for each sample. Energy calibration and the averaging of the individual scans were performed with the software package SIXpack.[30] More information about EXAFS data analysis is in SI.

Theory

The calculations of the Pu M_4 edge spectra were performed in the framework of the Anderson impurity model.[21] The spectra of bulk PuO_2 were calculated in a manner described in[31,32] for the Pu(IV) system, taking into account the Pu 5f hybridization with the valence states and the full multiplet structure due to intra-atomic and crystal field interactions. The values of the Slater integrals obtained for Pu(IV) using the Hartree-Fock formalism were scaled down to 80% to account for the solid-state effect. Wybourne's crystal field parameters were set to B^4_0=-0.93 eV and B^6_0=0.35 eV. The ground (final) state of the spectroscopic process was described by a linear combination of the $4f^4$ and $4f^5\underline{\upsilon}^1$ ($3d^94f^5$ and $3d^94f^6\underline{\upsilon}^1$) configurations where $\underline{\upsilon}$ stands for an electronic hole in the valence level. The values for the model parameters were as following: the energy for the electron transfer from the valence band to the unoccupied Pu 5f level Δ=0.8 eV; the 5f-5f Coulomb interaction U_{ff}=5.7 eV; the 3d core hole potential acting on the 5f electron U_{fc}=6.5 eV and the Pu 5f – valence state hybridization term V=1.10 eV (0.9 eV) in the ground (final) state of the spectroscopic process.

The calculations of the PuO_2 L_3 edge spectra were performed using the FEFF9.6. code.[22] The input file was based on the atomic unit cell parameter a = 0.540 nm. Full multiple scattering (FMS) calculations were performed using the Hedin-Lundqvist exchange-correlation potential, the potential was calculated self consistently within a radius of 4 Å. The card UNFREEZEF was used to let the occupation of the f orbitals be calculated self-consistently. The core hole lifetime broadening was reduced by using the EXCHANGE card. A full multiple scattering (FMS) radius of 12 Å, selecting 75 atoms around the absorber was used. FEFF input file can be found in SI, Fig. S4.

Powder X-ray diffraction measurements.

Powder X-ray diffraction (PXRD) data were collected at room temperature at the Rossendorf beamline of ESRF (λ=0.72756 Å, $2\theta_{max}$=59°). Samples were wet pastes enclosed in the three Kapton capillaries (triple confinement) with outer diameters of 0.81, 1.0, and 1.3 mm respectively. A diffractogram from an empty Kapton capillary was used in the background subtraction procedure for the samples. The lattice parameters were refined with WinCSD[33] by least-squares fitting. The FWHM and peak position were determined with TOPAS software.[34]

Results and discussion

Pu compounds come in a variety of colours depending on the Pu oxidation state and the counter ion. We used acidic aqueous solutions of light blue Pu(III), yellow Pu(IV), and violet Pu(V) that were precipitated at pH 8 and pH > 10. Precipitates of Pu species of the same light green colour, typical to Pu(IV) solids, were formed from all solutions, suggesting that the electronic structure of the formed Pu materials might be very similar. However, it is unknown if the local structure could be disordered due to the possible presence of oxidized Pu(V) or reduced Pu(III) species. The particle size distribution and crystallinity could also differ depending on the synthetic route.

The HRTEM data reported in Fig. 2a confirm that similar NPs form (with respect to the size distribution and crystallinity), regardless of different precursors and pH conditions. A comparison of selected area electron diffraction (SAED, Fig. 2b) patterns with bulk PuO_2, as well as diffractograms from XRD measurements (*c.f.* SI) show that the crystalline structure of the NPs is similar to that of bulk PuO_2. The particle size varies in the range of 2.3-3.2 nm, without apparent non-crystalline rim. Despite the small size of the NPs (extracted from XRD and reported in Fig. S5-6), lattice parameters only differ slightly from bulk PuO_2 (Table 1), suggesting that Pu from the initial aqueous solutions transfers to PuO_2-like structure with Pu(IV) oxidation state.

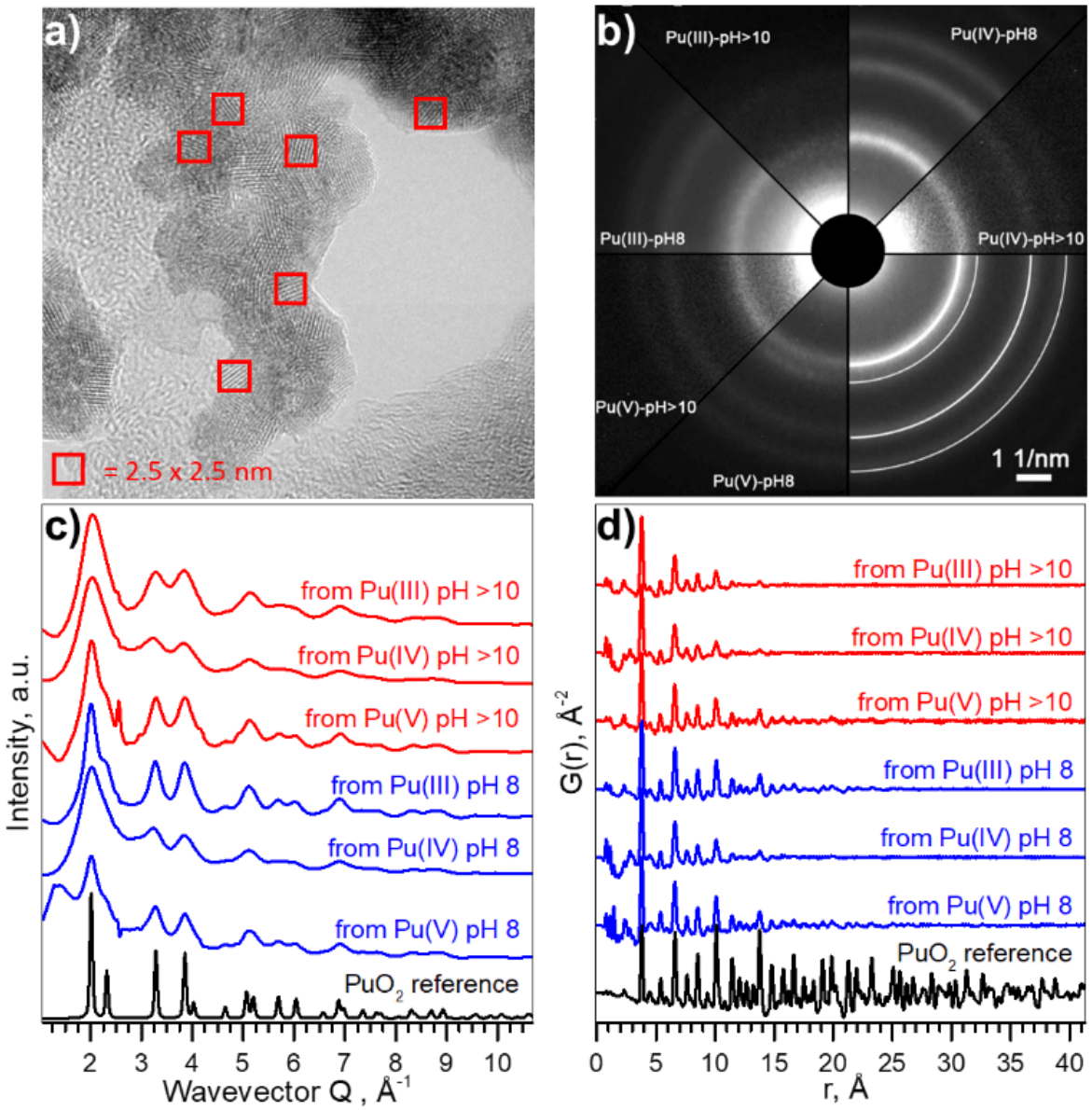

Figure 2. **Size and structure information of PuO_2 NPs. a)** HRTEM image of NPs from Pu(V) pH 8, **b)** SAED patterns of particles, white lines indicate peak positions for PuO_2 standard, **c)** Intensity profiles of the 2D diffraction of Pu samples, obtained by HEXS. **d)** the corresponding reduced pair distribution functions G(r) obtained by Fourier transformation (FT) of the data with Q_{max} = 26.0 $Å^{-1}$. The magnified versions of Fig 2a-b could be found in ESI as Fig S7-8 respectively.

Besides HRTEM and XRD there is another very powerful experimental method for investigating nano-scaled materials - HEXS analysis, as it can provide a fingerprint of the nanoparticle size and discriminate between short-range order (represented by finite non-random displacements from the ideal crystal structure) and random thermal displacements. The intensity profiles of the 2D diffraction for six investigated samples of PuO_2 NPs and a PuO_2 reference are shown in Fig. 2c. As discussed before (Fig. 2b), all diffraction patterns from PuO_2 NPs obtained by HEXS are similar, with the NPs having the same long-range structure as the PuO_2 reference with fcc structure, even though local structural deviations from the bulk should normally be observed in the nanosized materials with HEXS. The peaks are broader in the case of NPs, illustrating the effect of the nanosized coherent domains. The peak appearing at Q ~ 2.40$Å^{-1}$ comes from the background (*i.e.* kapton capillary) and for most samples can be successfully subtracted using the measurement of

the empty capillary. The corresponding reduced pair distribution function G(r) is shown in Fig. 2d. Peaks from short-range correlations in PuO_2 NPs have the same sharpness as peaks of the PuO_2 reference, indicating that the short-range order is identical. The intensity of the oscillations drastically decreases with increasing r, nearly disappearing after r = 20-25 Å; an indication of the coherence length of the PuO_2 particles. The damping of G(r) can be refined in order to extract the average particle size, confirming the direct observation that the NPs diameters are in the range of 1.3 - 2.6 nm, in a good agreement with HRTEM and XRD estimations. The results of the full profile structural refinements are shown in Fig. S9 and Table S1 for all PuO_2 NPs samples and for the PuO_2 reference, where bulk PuO_2 (space group $Fm\bar{3}m$) was used as the structure model.

Table 1 compares the results of the structural investigations of PuO_2 NPs by different methods: HRTEM, XRD, and HEXS. Although there are many factors that may influence the particle size estimation, the different independent methods, which we have implemented are all in a reasonable agreement. Table 2 summarizes the experimental methods and gives an overview of the information each method can supply. HRTEM is a local method, which gives information about particle size while XRD and HEXS provide information about coherent scattering domain size that sometimes may differ from particle size. The sizes calculated from HRTEM are slightly larger compared to other techniques, which might suggest that either there is a disordered or amorphous layer in PuO_2 NPs, restructured due to HRTEM deep vacuum conditions, or that the observed grains contain multiple overlapping subgrains. Low statistic of HRTEM methods may also influence on the result of size determination. Another possible explanation is that particles consisting of several crystallites may be counted as individual particles, resulting in underestimation of size in XRD and HEXS as they collect information about crystallite size.[35,36] HEXS allows the characterization of short-range order and random thermal displacements. The tendency for the particle sizes found to be smaller by this method than those from XRD, although almost all fall with statistical uncertainty. Due to the agreement between several methods, we concluded that coherent diffracting crystalline domains and particle size are very close in our case (within the difference between XRD/HEXS and HRTEM values).

Table 1. The comparison of the parameters particle sizes of NPs with different methods.

Sample	**Diameter, nm**			**a, Å**	
	HRTEM	**XRD**	**HEXS**	**XRD**	**HEXS**
from Pu(III) pH >10	2.3(4)	2.3(2)	1.33 (5)	-	5.384(6)
from Pu(IV) pH >10	2.4(4)	1.6(2)	1.3(2)	5.399(3)	5.38(2)
from Pu(V) pH >10	3.0(5)	2.1(2)	1.75(8)	5.398(5)	5.388(5)
from Pu(III) pH 8	2.7(4)	2.2(3)	2.07(8)	5.404(4)	5.402(4)
from Pu(IV) pH 8	3.2(8)	-	1.5(2)	-	5.39(2)
from Pu(V) pH 8	2.9(5)	2.4(2)	1.7(2)	5.407(6)	5.39(1)
PuO_2 reference	-	-	-	5.4014(3)	5.4032(3)

The most intriguing question concerning PuO_2 nanoparticles is the potential presence of various oxidation states of plutonium (referred to as PuO_{2+x}). Many authors[37,38] investigated the formation of PuO_2 NPs by various methods, but none of them gave an ambitious answer regarding the Pu oxidation state. In this work, we applied a new methodology and obtained straightforward information about Pu oxidation state by the HERFD method at the Pu M_4 edge[39].

Pu complexity and variety of colours is determined by its ground state electronic configuration [Xe] $5f^6 7s^2$. We analysed PuO_2 NPs by the HERFD method at the Pu L_3 and M_4 edges, which is an element-selective technique as the energy of an absorption edge corresponds to the characteristic core-level energy. The information about the electronic structure, oxidation state and the local geometry of the absorbing atom can be obtained from the HERFD spectral shape – thanks to the possibility to record electronic transitions with high energy resolution by an X-ray emission spectrometer.[27] The short overview of the HERFD method is provided in Table 2.

Fig. 3 shows HERFD data recorded for six PuO_2 NPs samples at the Pu L_3 edge compared to both the spectrum of the PuO_2 reference and to the results of calculations. Electrons at the Pu L_3 absorption edge are excited from the core 2p level to the empty Pu 6d electronic levels.[39] All spectral features of PuO_2 NPs are very similar, corresponding to those of the PuO_2 reference and are well reproduced by calculations based on the bulk PuO_2 crystal structure (*c.f.* Methods). There is a slight difference between all the samples and the reference at an incident energy of ~18090 eV (first post-edge feature). The reason is that the first post-edge feature is very sensitive to the lowering of the number of coordinating atoms. A similar effect was found and explained for ThO_2 nanoparticles previously.[40] The shape of the spectra in the near-edge region is determined by Pu 6d electronic density of states, plotted at the bottom of Fig.3. The Pu L_3 HERFD experiment was repeated after 4 months and no changes in the spectral shape were observed (Fig. S10), confirming the stability of PuO_2 NPs over time.

To summarize, HERFD results at the Pu L_3 edge confirm that the local environment of all PuO_2 NPs samples is similar to bulk PuO_2, in agreement with the previous HRTEM, XRD, and HEXS results. This is also supported by a comparison of the area under the white line (WL) and its FWHM (Table. S2). Moreover, the HERFD data confirm the presence of the Pu(IV) oxidation state as the dominant valence of PuO_2 NPs, as seen from the positions of the Pu white line. A minor WL energy shift among the samples is observed (within 0.2-0.4 eV), which prevents exclusion of tiny amounts of other oxidation states being present. A close inspection of the density of states, shown in the bottom of Fig. 3(right), reveals that the Pu 5f density of states is much closer to the Fermi level than that of the Pu 6d states; therefore probing the Pu 5f density of states is more suited to investigate the electronic structure of actinides (An). Previous experiments showed that HERFD measurements at the An M_4 edge, characterized by the An 3d-5f electronic transitions, are very powerful for oxidation state identification.[39,41]

Table 2. Short overview of the implemented analytical methods.

Analytical Method	**Information obtained**	**Comments**
HRTEM	Information about morphology, particle size,	Local method, which gives statistics only for a relatively small amount of particles; sample

	elemental composition, and crystal structure with nano-resolution	state can deviate during measurements due to the high vacuum and possible damage by the electron beam
XRD	Information about crystal structure and coherent scattering domains; statistically reliable; the ability to analyze mixed phases	Fast measurements (from seconds to minutes per sample); cannot easily distinguish between elements with similar Z; atomic level structure of amorphous substances can not be determined; nanoparticle peak broadening complicates the analysis
HEXS	Information about the local structure and coherent size domains; statistically reliable;	Fast measurements (from seconds to minutes per sample); possibility to discriminate between short-range disorder and random thermal displacements; to distinguish amorphous, structurally disordered, and nanocrystalline materials;
HERFD-XANES	Element selective method, which gives information about local site symmetry, oxidation state, and orbital occupancy;	Fast measurements (from seconds to minutes per sample); any size of objects can be studied (from nm to cm); allows determination of low An concentrations; provides fingerprint information; quantitative information can be obtained;
EXAFS	Information about local structure (bond distances, number and type of neighbours), sensitive to the type of absorbing element, local disorder and size effects	Time consuming measurements (from minutes to hours per sample); time consuming post-data collection analysis; provides only semi-quantitative estimations of oxidation state impurities; the results are severely dependent on the data quality and may be misinterpreted;

Fig. 3 (left) shows the Pu M_4 edge measurements on six PuO_2 NPs samples compared to both the spectrum of a PuO_2 reference and to the results of calculations based on Anderson impurity model (AIM). AIM fully accounts for electron correlations and treats the inter-atomic interactions as a perturbation. This approach was already shown to be the best for analysis of the HERFD data at the An M_4 edge.[31,39,41] The shape and the position of the main WLs in the Pu M_4 edge spectra of PuO_2 NPs are similar to those in the spectrum of the PuO_2 reference. The HERFD spectrum of PuO_2 shows a sharp peak at ~3970 eV due to the transitions from the $3d_{3/2}$ core level to the unoccupied $5f_{5/2}$ level and a shoulder at higher energy. This splitting of the Pu M_4 main edge transitions is reproduced very well by theoretical calculations and relates to the multiplet splitting of the Pu 5f states.[39] These results confirm the presence of only the Pu(IV) oxidation state in PuO_2 NPs and settle the controversial debates in the last years about the presence of other oxidation states. There are reports about the presence of Pu(III),[42] Pu(V),[9,43] and Pu(VI)[44] in $PuO_{2\pm x}$ species. Contrary to that, recent studies of Pu nanoclusters claim the presence of only the Pu(IV)[45] oxidation state. These results were obtained on Pu dioxide species

synthesized under different conditions (pH range, concentrations etc). We believe that all previously obtained results might be verified by the newly available HERFD method at the Pu M_4 edge.

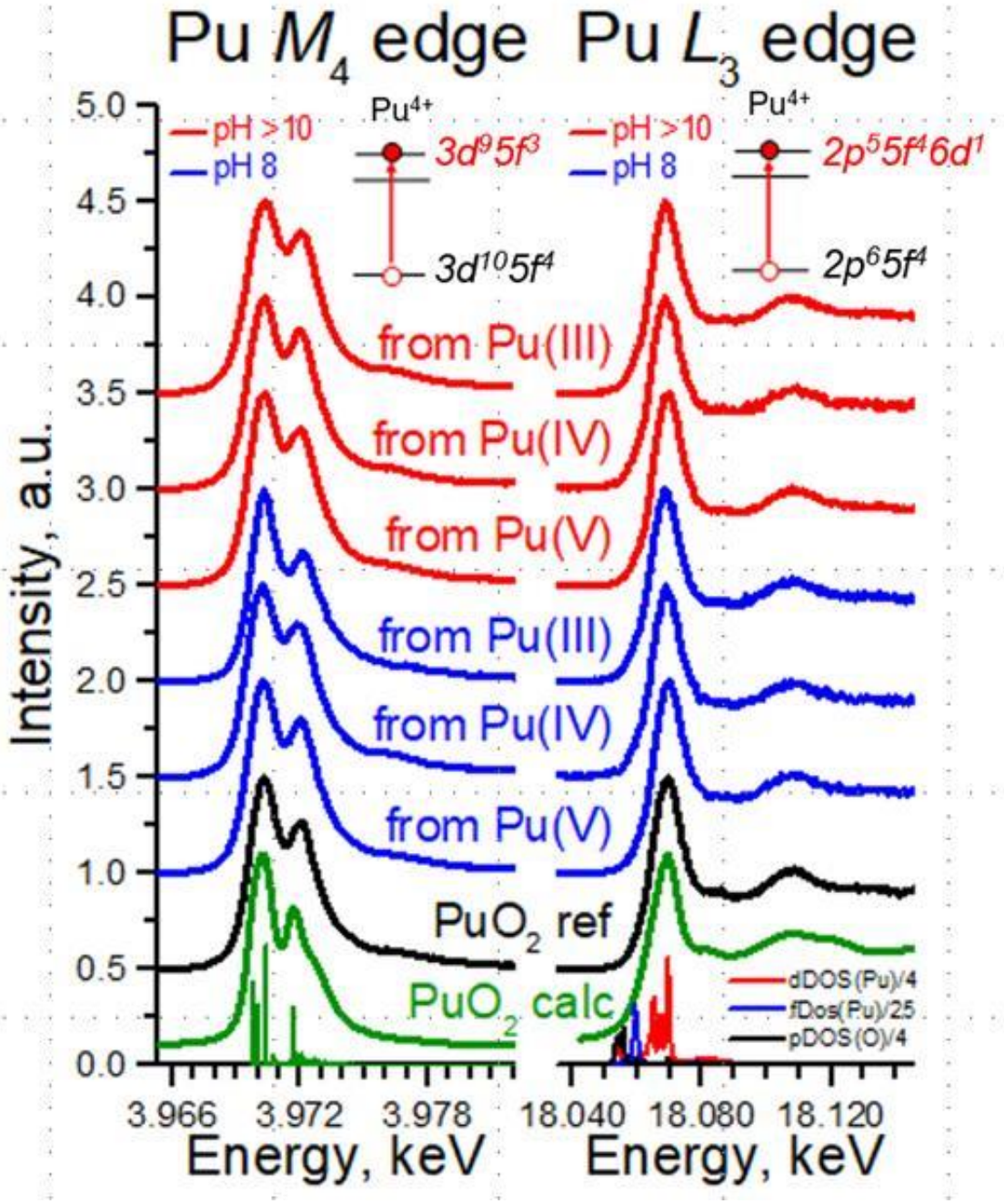

Figure 3. **Pu M_4 and L_3 HERFD experimental data.** Data recorded for six PuO_2 NPs samples and compared with a PuO_2 reference and theoretical calculations, using AIM approximation (left) and FEFF code (right). The density of states is plotted at the bottom for clarity.

In general, spectroscopic methods with standard resolution have been heavily used in studies of An systems in the past years. One of the most popular methods is EXAFS at the An L_3 edge, (information about this method is in Table 2). Pu L_3 edge EXAFS investigations of PuO_2 NPs have been carried out multiple times by different research groups[38,43,46-50], but results are heavily debated and are not in agreement with one another. The main discrepancy is related to the different interpretations of the first coordination sphere, which refers to Pu-O interaction and can be classified as:

1) a single Pu-O interaction similar to the one in PuO_2;

2) several Pu-O interactions (with different coordination of O atoms);

3) several Pu-O interactions, including Pu in various oxidation states.

For example, Conradson et al.[43] claimed that PuO_2 rarely exists and proposed as a description of the PuO_2 phase $PuO_{2+x-y}(OH)_{2y}\cdot zH_2O$ with a variety of Pu-O distances and most likely containing Pu(V). It was reported that EXAFS data shows at least three different oxygen scattering paths between 1.8 and 2.4 Å, however, the distances of all three paths vary significantly between 1.85-1.96, 2.13-2.28, and 2.26-2.39 Å for excess O (PuO_2^+ moieties), Pu-OH and Pu-O respectively.

Rothe et al.[46] found only Pu(IV) during PuO_2 intrinsic colloid formation and explained the observed splitting of the Pu-O coordination sphere by condensation of $Pu_nO_p(OH)_{4n-2p}(H_2O)_z$ units, with the shorter 2.20-2.24 Å Pu-O distances corresponding to surface Pu-OH groups and the longer 2.38-2.42 Å distances to Pu-O groups. Bonato et al.[38] recently reported the splitting of the first oxygen shell in PuO_2 nanoparticles and explained it with a disorder of the local structure at the surface of the NPs. Authors fixed distance parameters and coordination numbers for the first coordination shell, and refined only the Debye-Waller factor. In order to confirm such a splitting of the Pu-O shell previously observed by other authors,[38,43,46] we performed here several analyses of EXAFS data, using one, two, and three different Pu-O shells, with a refinement of Debye-Waller (DW) factors, distances and coordination numbers, assuming that nanosize effects and disorder may impact simultaneously the resulting values.

The one oxygen-shell fit is based on the assumption of a PuO_2-like structure of the samples and includes one Pu-O and one Pu-Pu interaction. Fig. 4a shows Pu L_3-EXAFS shell fit results, which indicate this approach can be implemented for all samples assuming a PuO_2-like structure, with characteristic distances 2.31 Å and 3.81 Å for Pu-O and Pu-Pu respectively. The best fit parameters are listed in Table 3. In comparison to bulk PuO_2, the fit parameters of the NPs show significant differences. First, the DW for the Pu-O shell is higher (note that 0.01 $Å^2$ was imposed as an upper limit to prevent collinearity effects and hence unreasonable values during the least-square refinement[51]), indicative of a higher static disorder due to a larger fraction of surface oxygen atoms. Second, the NPs Pu-Pu CN is lower and their DW is higher than those of the PuO_2 reference, again indicative of a larger fraction of under-coordinated Pu atoms at the surface with the higher static disorder. These observed effects of increased static disorder and reduced coordination numbers are clear influences of the nanometer-size of the particles, without the need to invoke different Pu oxidation states or a substantially different structure. In line with the very similar particle sizes of all NPs samples, their shell fit values remain remarkably similar, while they are significantly different from those of the bulk sample.

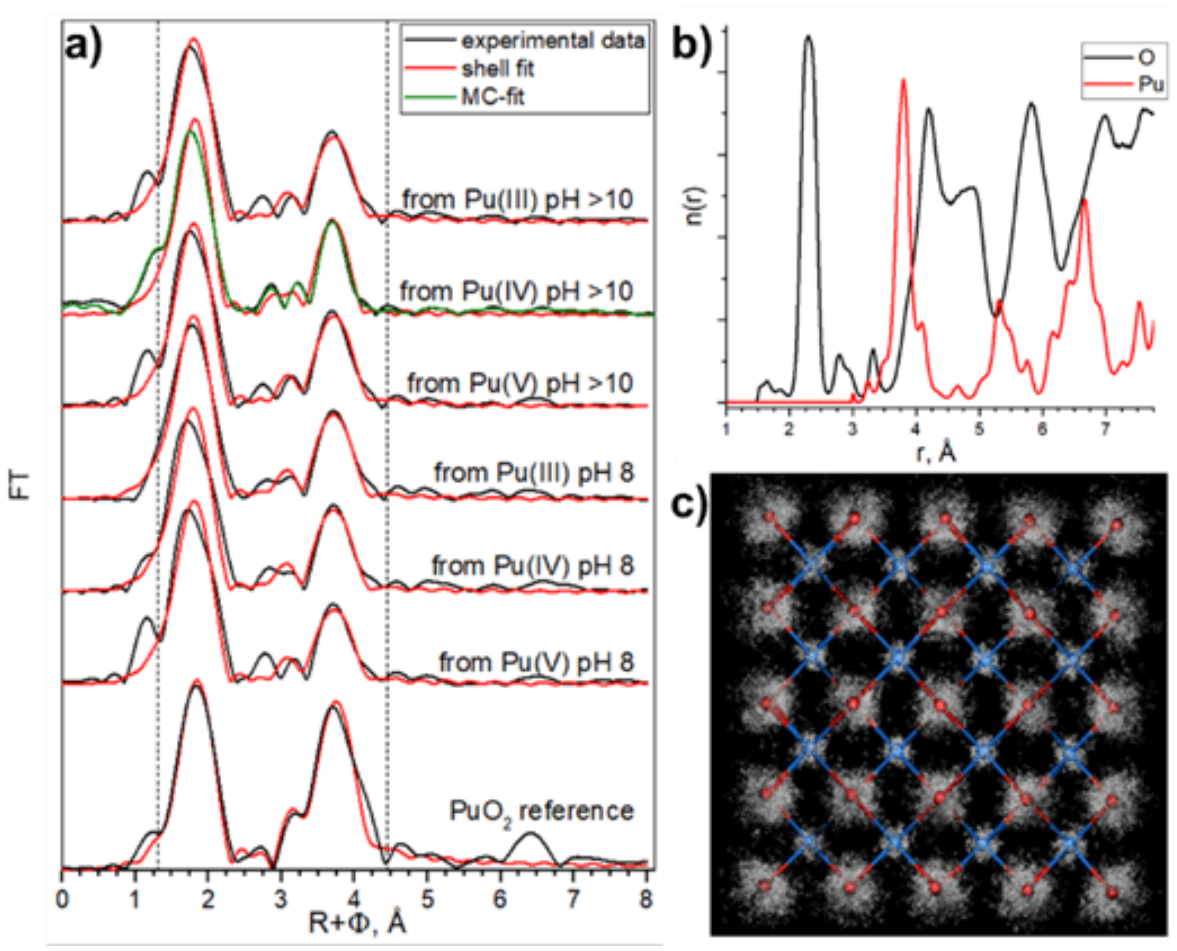

Figure 4. **Pu L_3-EXAFS results.** a) Pu L_3-EXAFS spectra χ(R) fit results, Fourier transform (FT) magnitude of experimental EXAFS data (black) and a one Pu-O, one Pu-Pu shell fit (red), Monte-Carlo simulations fit (green). The area of the shell fit in R-space is marked with two dashed lines, b) MC simulation output: radial particle distribution function (n(r)) for Pu-O and Pu-Pu, c) 3D structural refinement based on bulk PuO_2 starting structure.

Both two and three shell fit models were based on previously published fit attempts. Rothe et al.[46] observed oxygen shell splitting and used a two shell fit model with a dominant oxygen contribution at average distances slightly larger than that for bulk crystalline PuO_2 *i.e.* PuO_2(cr) (2.38-2.43 Å) and a smaller contribution at a significantly shorter distance (around 2.22 Å) and assigned this shorter Pu-O distance to hydroxyl groups. Our three shell fit follows the results of Conradson et al.,[43] where also Pu(V)-O distances in the range of 1.85-1.96 Å were fitted. We applied these assignments to our models and kept the original species assignments for the sake of comparison with previous reports. The results of these approaches are described in SI (Fig. S11-14, Table S3-4).

Similar approaches were used previously for the characterization of Pu colloids.[38,48] We used here the combination of techniques (HERFD, EXAFS, and HEXS) and theoretical calculations in order to find the most consistent approach. The three shell fit approach can be discarded due to the contradiction between EXAFS and HERFD data. The first Pu-O path of 1.83 Å has been previously assigned to the PuO_2^+ moiety, with pentavalent Pu reaching up to 15%, which is not consistent with the HERFD results (more info in SI). Since we cannot discard the presence of several Pu(IV)-O distances with HERFD, we analyzed the EXAFS data in addition to the shell fitting approach with the Landweber iteration (LI),[52,53] which is used to derive the radial particle distribution function

(n(r)) directly from EXAFS without the need to apply a shell fitting scheme based on the symmetric (Gaussian) distribution of interatomic distances. The advantage of this method is hence the possibility to reconstruct also the asymmetric n(r) directly from the EXAFS spectra. In line with the EXAFS shell fit, this LI approach showed only one Pu-O contribution (Fig. S12c). We also calculated a theoretical model EXAFS spectrum (Fig. S13a) based on the EXAFS parameters given by Rothe et al.[46] to confirm the ability of the LI approach for resolving close Pu-O contributions as described in SI. In addition, we performed Monte-Carlo (MC) EXAFS simulations[54-60] as a complementary method to LI. The MC simulation resulted in a very good agreement with the experimental EXAFS spectra (Fig. S14a) and again the symmetric shape of the first shell Pu-O n(r) is observed (Fig. 4b, Fig. S14c), thus only one Pu-O contribution is present in our system. In conclusion, the agreement among the results from the EXAFS shell fit, MC EXAFS simulations (Fig. 4, Fig. S14), EXAFS LI approach and from HEXS all unequivocally indicate that only one Pu(IV)-O interaction with a rather symmetric distance distribution (similar to the PuO_2 reference) is present for all six PuO_2 NPs samples.

Table 3. Metric parameters extracted by least-squares fit analysis of Pu L_3 EXAFS spectra with one Pu-O and one Pu-Pu paths (k range of 2.0-11.5 $Å^{-1}$)*.

Sample	**First coordination shell**			**Further shells**			**ΔE_0 [eV]**	**χ^2_{res} %**
	CN	**R [Å]**	**σ^2 [$Å^2$]**	**CN**	**R [Å]**	**σ^2 [$Å^2$]**		
from Pu(III) pH >10	7.5 O	2.31	0.0100	3.6 Pu	3.80	0.0045	5.1	14.0
from Pu(IV) pH >10	7.5 O	2.30	0.0100	4.3 Pu	3.79	0.0071	4.9	14.8
from Pu(V) pH >10	7.8 O	2.31	0.0100	3.8 Pu	3.81	0.0041	5.1	12.3
from Pu(III) pH 8	7.5 O	2.31	0.0100	4.5 Pu	3.81	0.0060	4.7	12.9
from Pu(IV) pH 8	7.2 O	2.30	0.0100	4.5 Pu	3.80	0.0065	4.9	15.5
from Pu(V) pH 8	7.7 O	2.32	0.0100	3.2 Pu	3.81	0.0043	5.2	16.5
PuO_2 reference	8.7 O	2.33	0.0068	6.7 Pu	3.82 Pu	0.0011	7.3	9.0
PuO_2 structure	8 O	2.337		12 Pu	3.817 Pu			

*CN: Coordination number with error ± 25 %, R: Radial distance with error ± 0.01 Å, σ^2: Debye-Waller factor with error ±0.0005 $Å^2$.

These observations lead us to conclude that the best model is a PuO_2 structure with Pu-O and Pu-Pu scattering paths to describe the features of our samples. However, we cannot claim that there are no hydroxyl groups in the outer shell of NPs, because Pu in aqueous solutions is always hydrolyzed, which means a variety of different kinds of hydrolyzed forms may exist during the formation of NPs. Nevertheless, these conclusions from the oxygen shell may help elucidate the mechanisms of the PuO_2 NPs formation.

There are two proposed mechanisms for PuO_2 NPs formation: The first one involves the condensation of $[Pu(OH)_n]^{(4-n)+}$ to yield hydroxo-bridged species through an olation reaction[7]

$Pu\text{-}OH + Pu\text{-}OH_2 = Pu\text{-}OH\text{-}Pu + H_2O$

According to this theory, oxo-hydroxo particles are formed as intermediate products. In this case several Pu-O contributions with slightly different Pu-O distances should be present[43,61] (such as native Pu-O as well as Pu-O in the terminal positions, Pu-OH and $Pu\text{-}OH_2$) in the EXAFS spectra, hence oxygen shell splitting should appear. The other proposed mechanism is that PuO_2 NPs form directly by an oxolation reaction[62,63]

$2Pu\text{-}OH = Pu\text{-}O\text{-}Pu + H_2O$

hence no oxyhydroxide or hydrous oxides are expected in the inner core of NPs. A bond-length distribution can still result from lattice distortions and different Pu local environments in the inner core and on the surface.[63] However, Monte-Carlo simulations reproduce the distortion effect, where no bond-length distribution appears. Since there is neither evidence of oxygen shell splitting nor Pu-O distances other than the Pu-O oxide distance of the native cubic structure, it is hardly possible to accept that the olation mechanism is responsible for the polymerization reaction leading to the formation of PuO_2 NPs.

Condensation of Pu(IV) by olation reactions is not prevalent in the literature; there is only one published report characterizing a solid-state structure comprised of hydroxobridged oligomers.[64] It is known that Th(IV), which is the softest among the tetravalent ions in Pearson's acid-base concept, is present as a $[Th_2(OH)_2]^{6+}$ cluster in both aqueous solution and solid precipitates,[65,66] but other mononuclear and polynuclear species, with two, four and six atoms of Th in the cluster also exist.[67,68] The hardest tetravalent ions stable in the aqueous solution, Zr(IV) and Hf(IV), have dihydroxo-bridged tetramers $[M_4(OH)_8(H_2O)_{16}]^{8+}$ (M = Zr, Hf) as the dominant solution species,[69] though many others exist under certain conditions[70] Similar well defined Pu polymers have not been found.[71] Ce(IV) and Pu(IV) have a charge-to-radius ratio intermediate to and bounded by Th(IV) and Hf(IV) and consequently their hydrolysis chemistry is similar. For Ce and Pu, predominantly oxo-bridged species have been conclusively isolated.[63,72] However, after the discovery of hydroxo/oxo-bridged hexanuclear complexes for Pu(IV) and Ce (IV), $[M_6(\mu_3\text{-}O)_4(\mu_3\text{-}OH)_4]^{12+}$ (M = Pu, Ce)[73,74] and two dihydroxo-bridged Pu(IV) dimers,[75] it became clear that a simple hard and soft acid and the base concept is not sufficient to predict the hydrolysis chemistry of these metal ions. The real mechanism of Pu hydrolysis appears to be much more complicated than simple olation or oxolation.[76]

Conclusions

In this paper we report a full characterization of PuO_2 NPs at the atomic level and refine the crystal and electronic structure by advanced synchrotron-based methods. Six samples of PuO_2 NPs were synthesized under environmentally and waste storage relevant conditions - at pH 8 and pH > 10 from Pu(III), Pu(IV) and Pu(V) precursors. Despite varying synthesis conditions, the Pu oxidation state in the PuO_2 NPs turns out to be exclusively Pu(IV), as proven here by HERFD methods at M_4 edge for the first time. The array of complementary methods applied in this work, namely EXAFS, HEXS, XRD, and HRTEM, support the conclusion that PuO_2 NPs are surprisingly homogeneous and monodisperse. It is surprising and not understood why always NPs of ~ 2.5 nm are formed. There are certain difficulties in obtaining PuO_2 NPs of bigger size (5-10 or 15 nm) via the chemical precipitation method. All collected information plays an important role in explaining plutonium chemistry under real conditions. It will help to advance, to model and to

predict long-term Pu release from deep underground repositories of nuclear waste and contaminated sites.

Author contributions

K. O. K and S. N. K planned and supervised the project. A.Yu. R, E.G, I. P. and S.W. performed synthesis of PuO_2 NPs. T.E. performed HRTEM characterizations of the samples. K.O.K., A.Yu. R., E.G., I. P, A.T. carried out XRD, EXAFS and HERFD measurements at the Pu L_3. C. H. and E.G. carried out XRD measurements and analysed data. K.O.K, E.G., I.P. and L. A. performed HERFD experiments at the Pu M_4 edge. M.O.J.Y.H., S.B. and T.P. performed Pu M_4 HERFD measurements on one PuO_2 NPs sample, synthesized from Pu(III) precursor at pH 8 at MARS beamline. A.C.S., A.R., A.T. and E.G. performed EXAFS experiment and analysed EXAFS data. G. V., and E.G. carried out and performed the analysis of HEXS data. S.M.B. did theoretical simulations of Pu M_4 data. K.O.K., E.G., A. Yu. R., G. V., A. C. S., S.M. B. and S.N.K. co-wrote the paper. All authors discussed the results and contributed to the final manuscript.

Conflicts of interest

There are no conflicts to declare.

Acknowledgements

This research was funded by European Commission Council under ERC [grant N759696]. Authors thank HZDR for the beamtime allocation at BM20 beamline and thank ESRF for beamtime allocation at ID15a and ID26 beamlines. We thank SOLEIL synchrotron for providing beamtime. We acknowledge help of P. Glatzel and T. Bohdan at ID26 beamline of ESRF during the HERFD experiment at the Pu M_4 edge. The authors would like to thank P. Colomp and R. Murray from the ESRF safety group for their help in handling radioactive samples at ID26, ID15a and ROBL beamlines. A.Yu. R. acknowledges support from RFBR according to the research project No. 16-31-06000 mol_a_dk. E.G. and S.N.K. acknowledge support by the Russian Ministry of Science and Education under grant № 075-15-2019-1891. S.M.B. acknowledges support from the Swedish Research Council (research grant 2017-06465).

1. P. Ball, Science, 2015, 518, 301.

2 D. Albright, S. Kelleher-Vergantini and D. Schnur, ISIS Rep. Plutonium Highly Enriched Uranium 2015.

3 C. J. Windorff, G. P. Chen, J. N. Cross, W. J. Evans, F. Furche, A. J. Gaunt, M. T. Janicke, S. A. Kozimor and B. L. Scott, J. Am. Chem. Soc., 2017, 139, 3970–3973.

4 J. J. Katz, G. T. Seaborg and L. R. Morss, The chemistry of the actinide elements, Chapman and Hall, London, 1986.

5 D. L. Clark, Los Alamos Sci., 2000, 26, 364–381.

6 M. H. Lloyd and R. G. Haire, Radiochim. Acta, 1978, 25, 139–148.

7 D. L. Clark, S. S. Hecker, G. D. Jarvinen and M. P. Neu, The Chemistry of the Actinide and Transactinide Elements, vol. 2, Springer Netherlands, 3rd edn., 2006.

8 D. Rai, R. J. Serne and D. A. Moore, Soil Sci Soc Am J, 1980, 44, 490–495.

9 V. Neck, M. Altmaier, A. Seibert, J. I. Yun, C. M. Marquardt and T. Fanghänel, Radiochim. Acta, 2007, 95, 193–207.

10 A. B. Kersting, D. W. Efurd, D. L. Finnegan, D. J. Rokop, D. K. Smith and J. L. Thompson, Nature, 1999, 397, 56–59.

11 A. P. Novikov, S. N. Kalmykov, S. Utsunomiya, R. C. Ewing, F. Horreard, A. Merkulov, S. B. Clark, V. V Tkachev and B. F. Myasoedov, Nature, 2006, 314, 638–642.

12 C. Xu, P. H. Santschi, J. Y. Zhong, P. G. Hatcher, A. J. Francis, C. J. Dodge, K. A. Roberts, C.-C. Hung and B. D. Honeyman, Environ. Sci. Technol., 2008, 42, 8211–8217.

13 B. A. Powell, Z. Dai, M. Zavarin, P. Zhao and A. B. Kersting, Environ. Sci. Technol., 2011, 45, 2698–2703.

14 A. Y. Romanchuk, S. N. Kalmykov, A. V. Egorov, Y. V. Zubavichus, A. A. Shiryaev, O. N. Batuk, S. D. Conradson, D. A. Pankratov and I. A. Presnyakov, Geochim. Cosmochim. Acta, 2013, 121, 29–40.

15 A. E. Hixon, Y. Arai and B. A. Powell, J. Colloid Interface Sci., 2013, 403, 105–112.

16 M. Schmidt, S. S. Lee, R. E. Wilson, K. E. Knope, F. Bellucci, P. J. Eng, J. E. Stubbs, L. Soderholm and P. Fenter, Environ. Sci. Technol., 2013, 47, 14178–14184.

17 M. Zavarin, P. Zhao, Z. Dai and A. B. Kersting, Radiochim. Acta, 2014, 102, 983–997.

18 M. A. Boggs, Y. Jiao, Z. Dai, M. Zavarin and A. B. Kersting, Appl. Environ. Microbiol., 2016, 82, 7093–7101.

19 A. E. Plymale, V. L. Bailey, J. K. Fredrickson, S. M. Heald, E. C. Buck, L. Shi, Z. Wang, C. T. Resch, D. A. Moore and H. Bolton, Environ. Sci. Technol., 2012, 46, 2132–2140.

20 M. C. Braney, A. Haworth, N. L. Jefferies and A. C. Smith, J. Contam. Hydrol., 1993, 13, 379–402.

21 P. W. Anderson, Phys. Rev., 1961, 124, 41–53.

22 J. J. Rehr, J. J. Kas, F. D. Vila, M. P. Prange and K. Jorissen, Phys. Chem. Chem. Phys., 2010, 12, 5503.

23 G. B. M. Vaughan, R. Baker, R. Barret, J. Bonnefoy, T. Buslaps, S. Checchia, D. Duran, F. Fihman, P. Got, J. Kieffer, S. A. J. Kimber, K. Martel, C. Morawe, D. Mottin, E. Papillon, S. Petitdemange, A. Vamvakeros, J.-P. Vieux and M. Di Michiel, J. Synchrotron Radiat., 2020, 27, 515–528.

24 J. Kieffer, S. Petitdemange and T. Vincent, J. Synchrotron Radiat., 2018, 25, 612–617.

25 P. Juhas, C. L. Farrow, X. Yang, K. R. Knox and S. J. L. Billinge, Acta Crystallogr. A, 2015, 71, 562–568.

26 C. L. Farrow, P. Juhas, J. W. Liu, D. Bryndin, E. S. Bozin, J. Bloch, T. Proffen and S. J. L. Billinge, J. Phys. Condens. matter, 2007, 19, 335219.

27 K. O. Kvashnina and A. C. Scheinost, J. Synchrotron Radiat., 2016, 23, 836–841.

28 M. Rovezzi, C. Lapras, A. Manceau, P. Glatzel and R. Verbeni, Rev. Sci. Instrum., 2017, 88, 013108.

29 C. Gauthier, V. A. Sol, R. Signorato, J. Goulon and E. Moguiline, J. Synchrotron Radiat., 1999, 6, 164–166.

30 S. M. Webb, Phys. Scr., 2005, T115, 1011–1014.

31 S. M. Butorin, K. O. Kvashnina, A. L. Smith, K. Popa and P. M. Martin, Chem. - A Eur. J., 2016, 22, 9693–9698.

32 S. M. Butorin, A. Modin, J. R. Vegelius, K. O. Kvashnina and D. K. Shuh, J. Phys. Chem. C, 2016, 120, 29397–29404.

33 L. Akselrud and Y. Grin, J. Appl. Crystallogr., 2014, 47, 803–805.

34 J. Perl, J. Shin, J. Schümann, B. Faddegon and H. Paganetti, Med. Phys., , DOI:10.1118/1.4758060.

35 F. Boulc'h, M.-C. Schouler, P. Donnadieu, J.-M. Chaix and E. Djurado, Image Anal. Stereol., 2011, 20, 157.

36 K. Popa, O. Walter, O. D. Blanco, A. Guiot, D. Bouëxière, J.-Y. Colle, L. Martel, M. Naji and D. Manara, CrystEngComm, 2018, 20, 4614–4622.

37 A. Y. Romanchuk, T. V. Plakhova, A. V. Egorov, T. B. Egorova, P. V. Dorovatovskii, Y. V. Zubavichus, A. A. Shiryaev and S. N. Kalmykov, Dalt. Trans., 2018, 47, 11239–11244.

38 L. Bonato, M. Virot, T. Dumas, A. Mesbah, E. Dalodière, O. Dieste Blanco, T. Wiss, X. Le Goff, M. Odorico, D. Prieur, A. Rossberg, L. Venault, N. Dacheux, P. Moisy and S. I. Nikitenko, Nanoscale Adv., 2020, 2, 214–224.

39 K. O. Kvashnina, A. Y. Romanchuk, I. Pidchenko, L. Amidani, E. Gerber, A. Trigub, A. Rossberg, S. Weiss, K. Popa, O. Walter, R. Caciuffo, A. C. Scheinost, S. M. Butorin and S. N. Kalmykov, Angew. Chemie Int. Ed., 2019, 58, 17558–17562.

40 L. Amidani, T. V. Plakhova, A. Y. Romanchuk, E. Gerber, S. Weiss, A. Efimenko, C. J. Sahle, S. M. Butorin, S. N. Kalmykov and K. O. Kvashnina, Phys. Chem. Chem. Phys., 2019, 21, 10635–10643.

41 K. O. Kvashnina, S. M. Butorin, P. Martin and P. Glatzel, Phys. Rev. Lett., 2013, 111, 253002.

42 A. Tasi, X. Gaona, D. Fellhauer, M. Böttle, J. Rothe, K. Dardenne, D. Schild, M. Grivé, E. Colàs, J. Bruno, K. Källström and M. Altmaier, Radiochim. Acta, 2018, 106, 259–279.

43 S. D. Conradson, B. D. Begg, D. L. Clark, C. Den Auwer, M. Ding, P. K. Dorhout, F. J. Espinosa-Faller, P. L. Gordon, R. G. Haire, N. J. Hess, R. F. Hess, D. W. Keogh, L. A. Morales, M. P. Neu, P. Paviet-Hartmann, W. Runde, C. D. Tait, D. K. Veirs and P. M. Villella, J. Am. Chem. Soc., 2004, 126, 13443–13458.

44 J. M. Haschke, T. H. Allen and L. A. Morales, Science (80-.)., 2000, 287, 285–287.

45 G. E. Sigmon and A. E. Hixon, Chem. Eur. J., 2019, 25, 2463–2466.

46 J. Rothe, C. Walther, M. A. Denecke and T. Fanghänel, Inorg. Chem., 2004, 43, 4708–4718.

47 C. Ekberg, K. Larsson, G. Skarnemark and I. Persson, Dalt. Trans., 2013, 42, 2035–2040.

48 D. Hudry, C. Apostolidis, O. Walter, A. Janßen, D. Manara, J. C. Griveau, E. Colineau, T. Vitova, T. Prüßmann, D. Wang, C. Kübel and D. Meyer, Chem. Eur. J., 2014, 20, 10431–10438.

49 E. Dalodière, M. Virot, V. Morosini, T. Chave, T. Dumas, C. Hennig, T. Wiss, O. Dieste Blanco, D. K. Shuh, T. Tyliszcak, L. Venault, P. Moisy and S. I. Nikitenko, Sci. Rep., 2017, 7, 43514.

50 E. Dalodière, M. Virot, T. Dumas, D. Guillaumont, M.-C. Illy, C. Berthon, Guerin, Laetitia, A. Rossberg, L. Venault, P. Moisy and S. I. Nikitenko, Inorg. Chem. Front., 2018, 5, 100–111.

51 W. Meyer-Klaucke, M. Gnida and G. Henkel, Ref. Modul. Chem. Mol. Sci. Chem. Eng., , DOI:10.1016/B978-0-12-409547-2.10774-7.

52 L. Landweber, Am. J. Math., 1951, 73, 615–624.

53 A. Rossberg and H. Funke, J. Synchrotron Radiat., 2010, 17, 280–288.

54 A. Rossberg and A. C. Scheinost, Anal. Bioanal. Chem., 2005, 383, 56–66.

55 M. Winterer, J. Appl. Phys., 2000, 88, 5635–5644.

56 M. Winterer, R. Delaplane and R. McGreevy, J. Appl. Crystallogr., 2002, 35, 434–442.

57 M. Winterer and F. Farges, Phys. Scr., 2005, T115, 923–924.

58 S. J. Gurman and R. L. McGreevy, J. Phys. Condens. Matter, 1990, 2, 9463–9473.

59 R. L. McGreevy, J. Phys. Condens. Matter, 2001, 13, R877–R913.

60 J. Timoshenko, A. Kuzmin and J. Purans, Comput. Phys. Commun., 2012, 183, 1237–1245.

61 S. D. Conradson, Appl. Spectrosc., 1998, 52, 252A-279A.

62 M. Henry, J. P. Jolivet and J. Livage, Chem. Spectrosc. Appl. Sol-Gel Glas., 1992, 153–206.

63 L. Soderholm, P. M. Almond, S. Skanthakumar, R. E. Wilson and P. C. Burns, Angew. Chemie - Int. Ed., 2008, 47, 298–302.

64 D. W. Wester, Inorg. Chem., 1982, 21, 3382–3385.

65 G. Johansson, Acta Chem. Scand., 1968, 22, 399–409.

66 R. E. Wilson, S. Skanthakumar, G. Sigmon, P. C. Burns and L. Soderholm, Inorg. Chem., 2007, 46, 2368–2372.

67 V. Neck and J. I. Kim, Radiochim. Acta, 2001, 89, 1–16.

68 C. Walther, M. Fuss and S. Büchner, Radiochim. Acta, 2008, 96, 411–425.

69 C. Hagfeldt, V. Kessler and I. Persson, Dalt. Trans., 2004, 0, 2142–2151.

70 C. Walther, J. Rothe, M. Fuss, S. Büchner, S. Koltsov and T. Bergmann, Anal. Bioanal. Chem., 2007, 388, 409–431.

71 C. Walther, J. Rothe, B. Brendebach, M. Fuss, M. Altmaier, C. M. Marquardt, S. Büchner, H. Cho, J. Yun and A. Seibert, Radiochim. Acta, 2009, 97, 199–207.

72 A. Ikeda-Ohno, S. Tsushima, C. Hennig, T. Yaita and G. Bernhard, Dalt. Trans., 2012, 41, 7190–7192.

73 K. E. Knope and L. Soderholm, Inorg. Chem., 2013, 52, 6770–6772.

74 C. Hennig, A. Ikeda-ohno, W. Kraus, S. Weiss, P. Pattison, H. Emerich, P. M. Abdala and A. C. Scheinost, Inorg. Chem., 2013, 52, 11734–11743.

75 K. E. Knope, S. Skanthakumar and L. Soderholm, Inorg. Chem., 2015, 54, 10192–10196.

76 A. Ikeda-ohno, C. Hennig, S. Weiss, T. Yaita and G. Bernhard, Chem. Eur. J., 2013, 19, 7348–7360.

Supplementary information of Article 1

Table of contents

Figure S12. EXAFS Landweber iteration (LI) for Pu(IV) at pH >10. a) experimental spectrum (black), reconstructed spectrum (red), residual (blue), b) corresponding Fourier transform (FT) magnitude, c) Pu-O (black) and Pu-Pu (red) radial particle distribution function (n(r)).

Figure S13. EXAFS Landweber iteration (LI) for the EXAFS model spectrum. a) model spectrum (black), reconstructed spectrum (red), b) corresponding Fourier transform (FT) magnitude, c) model (black) and LI (red) Pu-O and Pu-Pu radial particle distribution function (n(r)).

Figure S14. Monte-Carlo (MC) EXAFS simulation for Pu(IV) at pH >10. a) experimental spectrum (black), reconstructed spectrum (red), residual (blue), b) corresponding Fourier transform (FT) magnitude, c) Pu-O (black) and Pu-Pu (red) radial particle distribution function (n(r)).

Table S1. The refined parameter values obtained from HEXS.

Table S2. Gauss fit results of the WL for the samples.

Table S3. Parameters extracted by least-squares fit analysis of Pu L_3 EXAFS spectra with three O shells (k-range of 2.0-14.0 $Å^{-1}$)*.

Table S4. Parameters extracted by least-squares fit analysis of Pu L_3 EXAFS spectra with two O shells (k-range of 2.0-14.0 $Å^{-1}$)*.

Table S5. pH and Eh values after the end of the reactions.

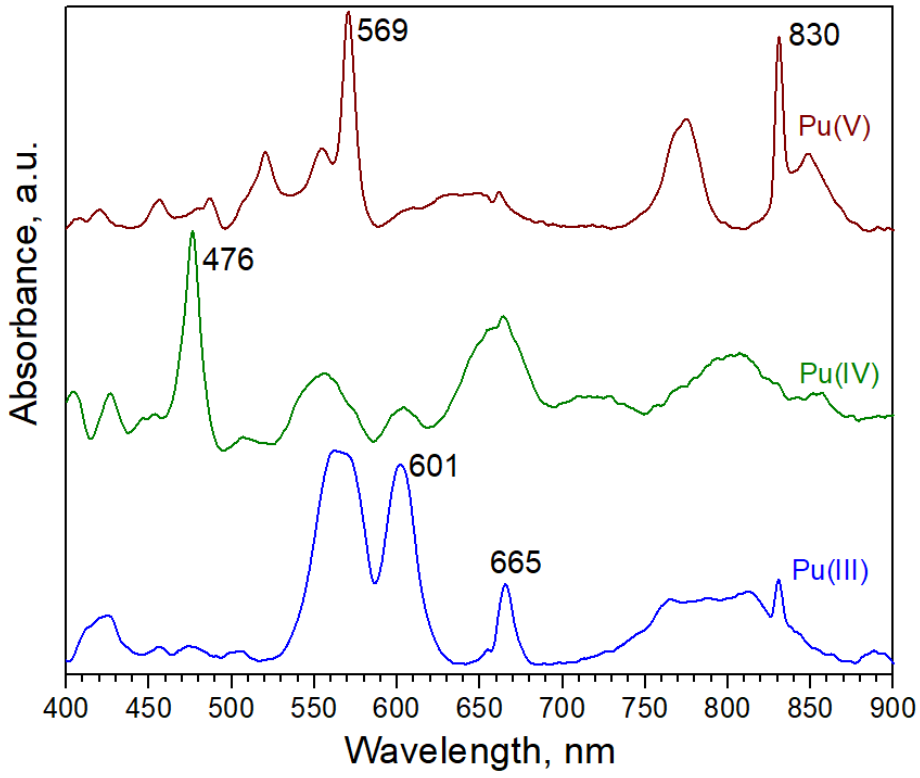

Fig. S1. UV-vis spectra of Pu initial solutions with wavelengths of the characteristic peaks.

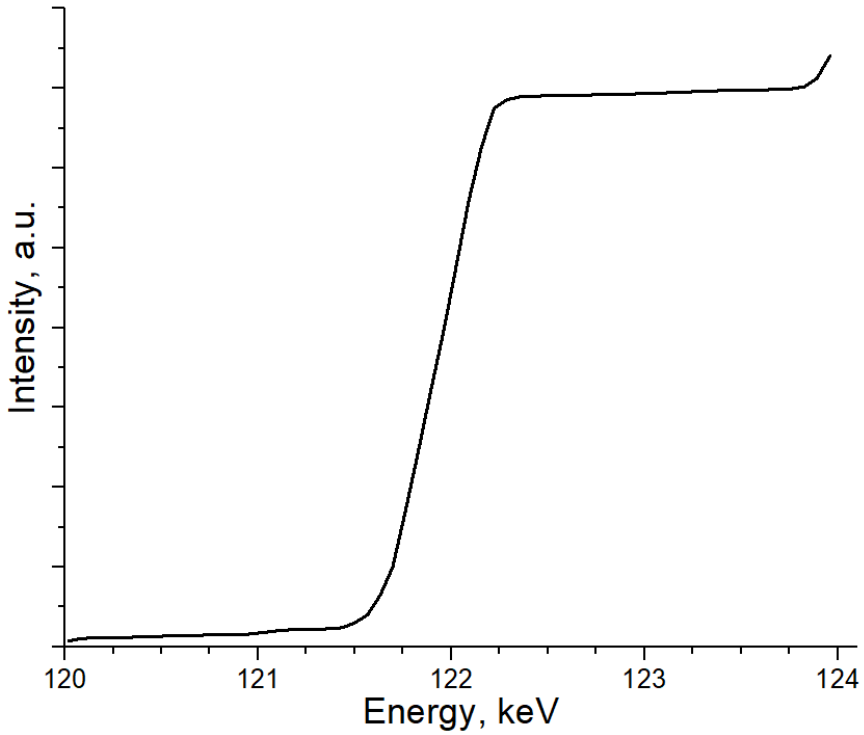

Fig. S2. Pu K-edge XANES spectrum.

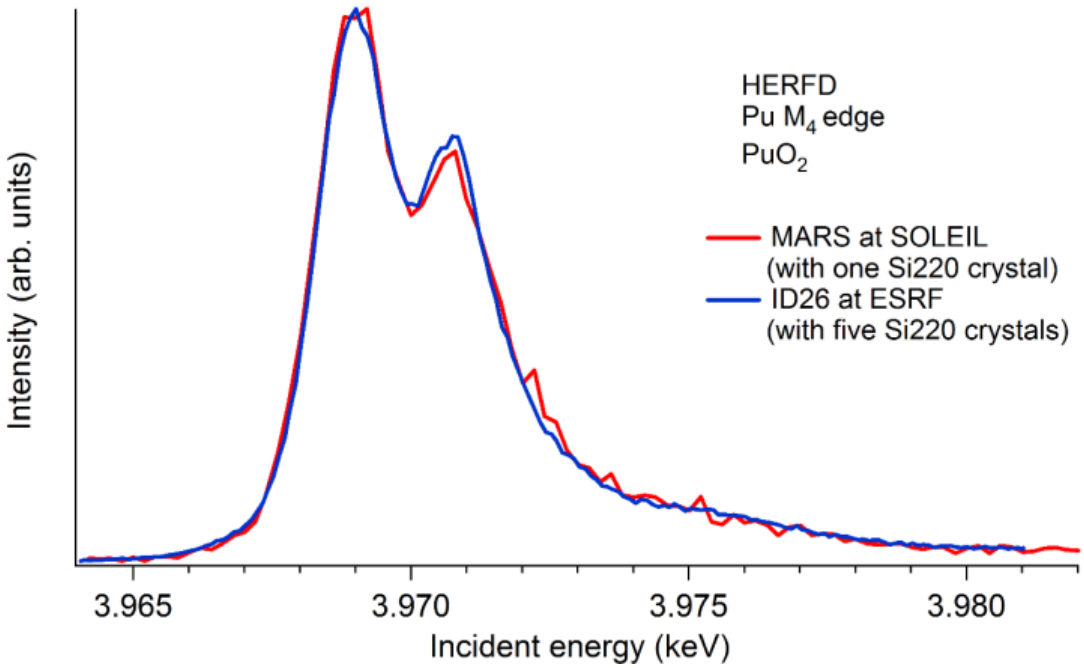

Fig. S3 Comparison of Pu M_4 HERFD data of PuO_2 reference recorded at 2 beamlines: MARS (with single spherically bent Si(220) crystal analyzer) and ID26 beamlines (with five spherically bent crystals analyzers)

```
*  Pu L3 edge
 EDGE      L3
 S02       1.0
 UNFREEZEF
 MULTIPOLE 2 0

 *         pot    xsph  fms   paths genfmt ff2chi
 CONTROL   1      1     1     1     1      1
 PRINT     1      0     0     0     0      0

                          *** ixc=0 means to use Hedin-Lundqvist
 *         ixc  [ Vr  Vi ]
  EXCHANGE  0 0 -1.0

                          *** Radius of small cluster for
                          *** self-consistency calculation
                          *** A sphere including 2 shells is
                          *** a good choice
                          *** l_scf = 0 for a solid, 1 for a molecule
 *         r_scf  [ l_scf   n_scf   ca ]
 SCF       4.0      0       50      0.05   10

                          *** Upper limit of XANES calculation.
                          *** This *must* be uncommented to
                          *** make Feff calculate full multiple
                          *** scattering rather than a path expansion
 *         kmax   [ delta_k  delta_e ]
 XANES     8.0
                          *** Radius of cluster for Full Multiple
                          *** Scattering calculation
                          *** l_fms = 0 for a solid, 1 for a molecule
 *         r_fms     l_fms
 FMS       12        0

                          *** Energy grid over which to calculate
                          *** DOS functions
 *         emin  emax   eimag
 LDOS      -30   20     0.1

                          *** for EXAFS:  RMAX   6.0 and uncomment
                          *** the EXAFS card
 RPATH     0.1
 *EXAFS     20

 POTENTIALS
 *   ipot   Z  element        l_scmt  l_fms   stoichiometry
     0     94     Pu           3       3       0.001
     1     94     Pu           3       3       1
     2     8      O            1       1       2
```

Fig S4. Feff input file for the calculation of Pu L_3 HERFD spectrum.

HRTEM. Regardless of conditions and pH, similar nanoparticles containing Pu and O are formed according to the HRTEM data (Fig. 2, Fig S7-8). In all cases, they are aggregates of small crystalline particles with a structure similar to PuO_2. The average particle size is in the range of 2.3-3.2 nm

by analysing 40-100 particles in each sample. Size distribution analysis was hampered by the fact that NPs stay in aggregates and size detection of single NPs was not straightforward.

X-ray diffraction. All XRD patterns from nanoparticles are shown in Fig. S5. All diffractograms show similar features and are consistent with the bulk PuO_2 structure. This is in agreement with the HRTEM results. All peaks observed in the PuO_2 reference diffractogram are present in the patterns of the samples. However, these peaks are much broader due to the nanoscale size of the crystallites. To determine the particle size, Scherrer's equation was used:

$$d = \frac{K\lambda}{\beta cos\theta},$$

where d is the mean size of the ordered domains, K – dimensionless shape factor (Scherrer's constant) – 0.9 for spherical NPs, λ – X-ray wavelength, β – the line broadening at half the maximum intensity (FWHM) in radians, θ is the Bragg angle. The calculation of crystallite size was based on the FWHM of the selected peaks, for each sample, at least six selected peaks were used. It is known, that other factors besides crystallite size (*e.g.* microstrain) may cause peak broadening, however, they were not taken into account in our approximation.

The PuO_2 nanocrystals that we obtained from the different starting solutions (more details in Methods) are in a narrow size range of 1.6-2.4 nm estimated by Scherrer's equation. The size of the PuO_2 particles may vary from less than 2 nm up to several hundred nm depending on the synthesis conditions.[1-3] The main factors influencing the size of the nanoparticles are temperature, calcination and the synthesis method. There is a clear tendency in increasing particle size as a function of calcination temperature, from few nanometers to micrometric crystals at approx. 1000°C.[2,4] The smallest particles are synthesized from aqueous solutions, either by adding a base to the acidic plutonium solution (and vice versa)[1,5-7] or by simple water dilution of a concentrated plutonium solution.[5,8] Another powerful method to obtain PuO_2 crystallites of 2-4 nm is a hydrothermal decomposition of plutonium oxalates.[9-12] Firing of the samples leads to the increase of the nanograin size.[11,12] Hydrothermal route and oxalate decomposition are also used to obtain ThO_2 and UO_2 nanoparticles.[13,14] Nanoparticles with an average crystallite size of 2 nm can be obtained by the multi-step thermal decomposition up to 280 °C in a mixture of benzyl ether, oleic acid and oleylamine.[15] Another way to obtain nanoparticles is the sonochemical treatment of PuO_2 suspensions in pure water which results in nanocrystals with an average size of 7 nm.[8] It was also shown that the size of the particles depends on the duration and intensity of the heating (both during and after the synthesis process).[2] However, ageing, which plays a role

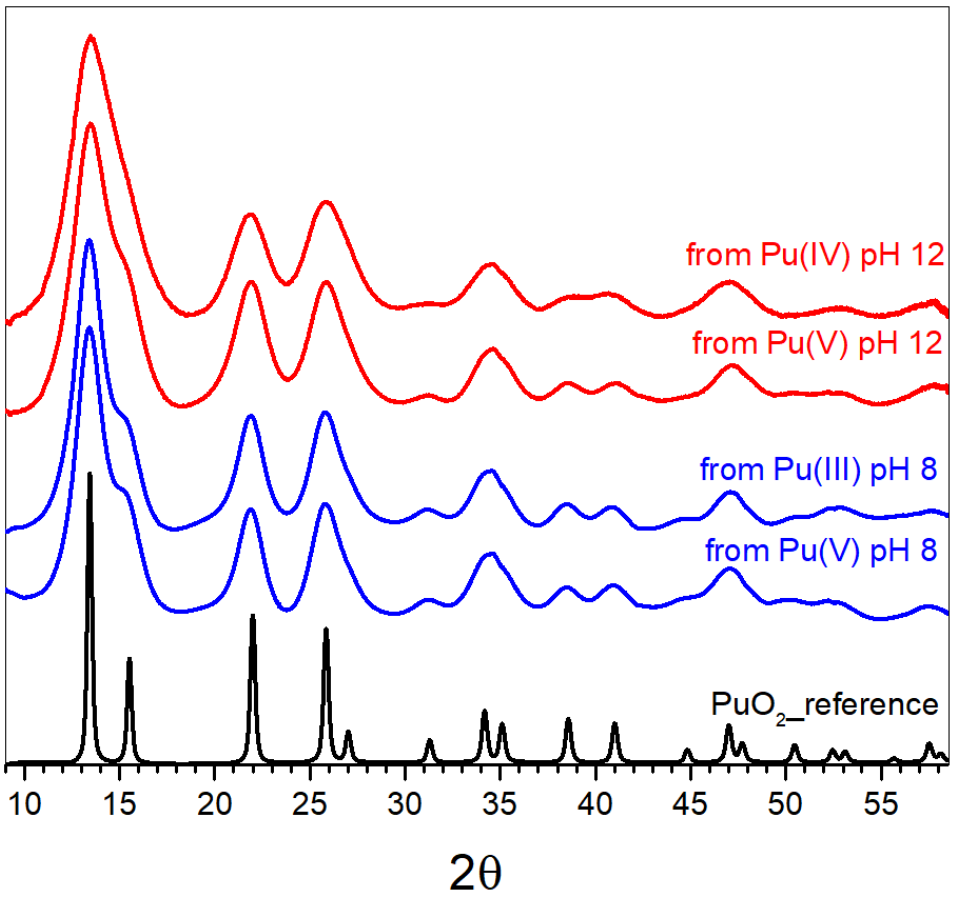

Fig. S5. Diffraction patterns of the precipitates from Pu (III), (IV), (V) in different pH and microcrystalline PuO_2 reference.

in the conversion of particles to the crystalline state, does not discernibly increase the particle size.[1] Fig. S6 shows the correlation between the lattice parameter of PuO_2 nanoparticles and the particle size from our syntheses with data from literature.[1-3,15,16] It should be noted that this dependency is uncertain for small particles as the errors are too large to reveal any significant relation. For larger particles (from 10 nm up to 300 nm) it is apparent that the lattice parameter decreases with increasing particle sizes. The same trend was found for CeO_2 nanoparticles.[17] Hashke et al. reported that the lattice parameter of the PuO_{2+x} changes as a function of x. It is increasing with the O/Pu ratio.[18]

Despite of the small size of the nanoparticles, our reported lattice parameter only differs slightly from PuO_2 bulk (Table 1), meaning that the plutonium from the initial aqueous solutions transfers to a PuO_2-like structure with a clear prevailing Pu(IV) oxidation state. However, there is an equilibrium between several oxidation states in the aqueous solution for the intrinsic colloid formation. Neck and Kim[19] found that the solubility of Pu(IV) oxygen compounds is extremely low. One can suppose that PuO_2 forming from Pu(IV) in solution may shift the equilibrium towards additional Pu(IV) formation and finally lead to PuO_2 as the dominating product in the solid phase. Moreover, as there is no significant difference between XRD data, one can conclude that neither initial oxidation state nor pH affects the PuO_2 structure.

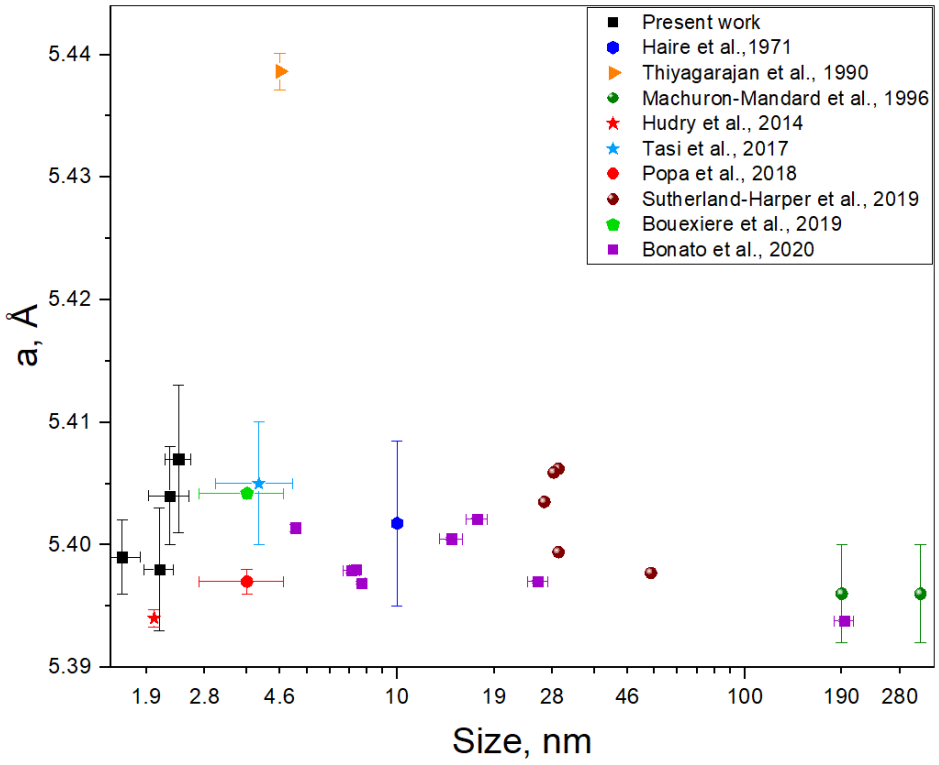

Fig. S6. Lattice parameter distribution of the particle size based on experimental and literature data.[1-3,10-12,15,20]

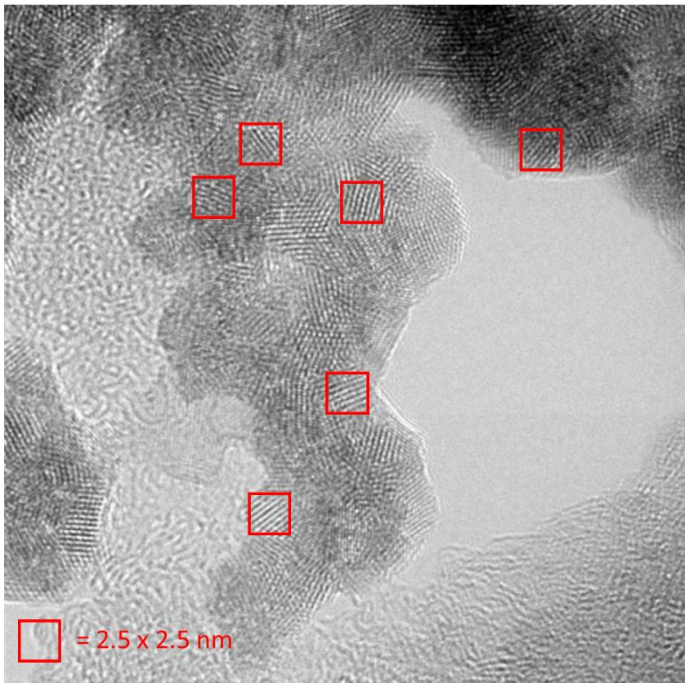

Fig. S7. Size information of PuO_2 NPs. HRTEM image of NPs from Pu(V) pH 8.

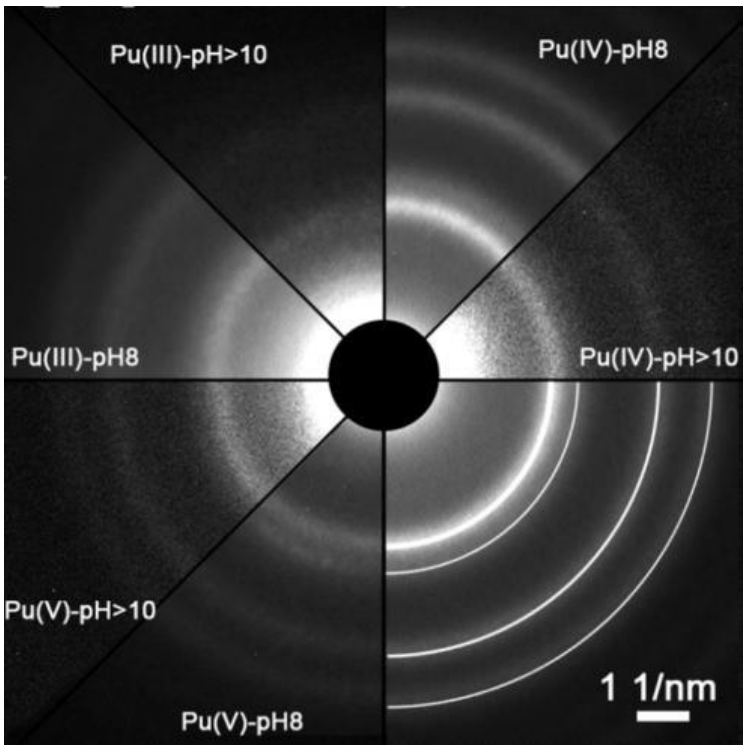

Fig. S8. Structure information of PuO_2 NPs. Selected-area electron diffraction (SAED) patterns of particles, white lines indicate peak positions for PuO_2 standard.

High energy X-ray scattering. The results of the full profile structural refinement are shown in Fig. S9 for all NP samples and the PuO_2 bulk. PuO_2 (space group $Fm\bar{3}m$) was used as a structural model. Water model was used in order to reproduce the contribution of water at the short-range order. The NPs fits are in a good agreement with the PuO_2 structure and the refined parameters are listed in Table S1.

It should be noted that there is only one peak (at 2.31 Å) corresponding to the first shell Pu-O contribution, very similar to the one in PuO_2 bulk. The HEXS results do not show any presence of contributions other than of the Pu-O bond from PuO_2 bulk.

Table S1. The refined parameter values obtained from HEXS.

Sample	Scale factor	a, Å	Particle diameter, nm	Rw
from Pu(III) pH >10	0.81	5.384(6)	1.33(5)	0.20
from Pu(IV) pH >10	0.55	5.38(2)	1.3(2)	0.29
from Pu(V) pH >10	0.64	5.388(5)	1.75(8)	0.23
from Pu(III) pH 8	0.30	5.402(4)	2.07(8)	0.18
from Pu(IV) pH 8	0.44	5.39(2)	1.5(2)	0.32
from Pu(V) pH 8	0.51	5.39(1)	1.7(2)	0.25
PuO_2 reference	0.65	5.4032(3)	-	0.11

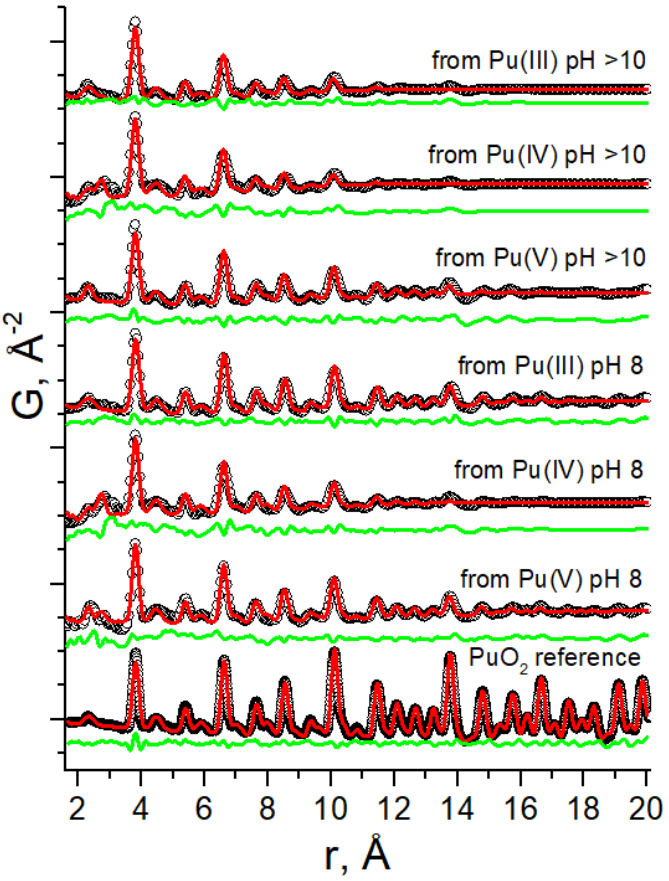

Fig S9. The results of the pair distribution functions (PDFs) fits from all samples and PuO_2 reference. The experimental reduced (PDFs) G(r) obtained by Fourier transformation (FT) of the data with Q_{max} = 26.0 $Å^{-1}$ (black dots), calculated PDFs from the refined structural model (red line) and the difference curve (green line).

HERFD

The Pu L_3 absorption edge refers to the minimum energy needed to excite a core 2*p* electron to the empty Pu 6*d* states. The position and shape of the white line WL gives information about the formal valence. One can see that the WL is the same for all samples and the PuO_2 reference which means the dominating oxidation state for all samples is Pu(IV). However, a minor energy shift among the samples (within 0.5 eV) is observed, and this is most likely the temperature dependence causes such kind of the shift. However, we cannot claim that other oxidation states are not present in tiny (<5%) amounts. Nevertheless, all other spectral features (pre- and post-edge) are corresponding to those of the PuO_2 reference and are perfectly reproduced in the PuO_2 calculated spectra (Fig. 3), thus one can conclude the local environment of all samples is similar to PuO_2. This is also proven with the comparison of the parameters of the WL such as the area under it and FWHM, as seen in Table S2.

The main method to calculate the local density of states (LDOS) is Density Functional Theory (DFT) where either band structure, multiple scattering or chemical DFT codes can be used. FEFF program[21] was used to calculate LDOS and the X-ray

Table S2. Gauss fit results of the WL for the samples.

Sample	Area, (± 1)	FWHM, eV

from Pu(III) pH >10	14	13.0
from Pu(IV) pH >10	13	12.7
from Pu(V) pH >10	13	12.6
from Pu(III) pH 8	14	12.7
from Pu(IV) pH 8	13	13.0
from Pu(V) pH 8	13	12.7
PuO_2 reference	14	13.0

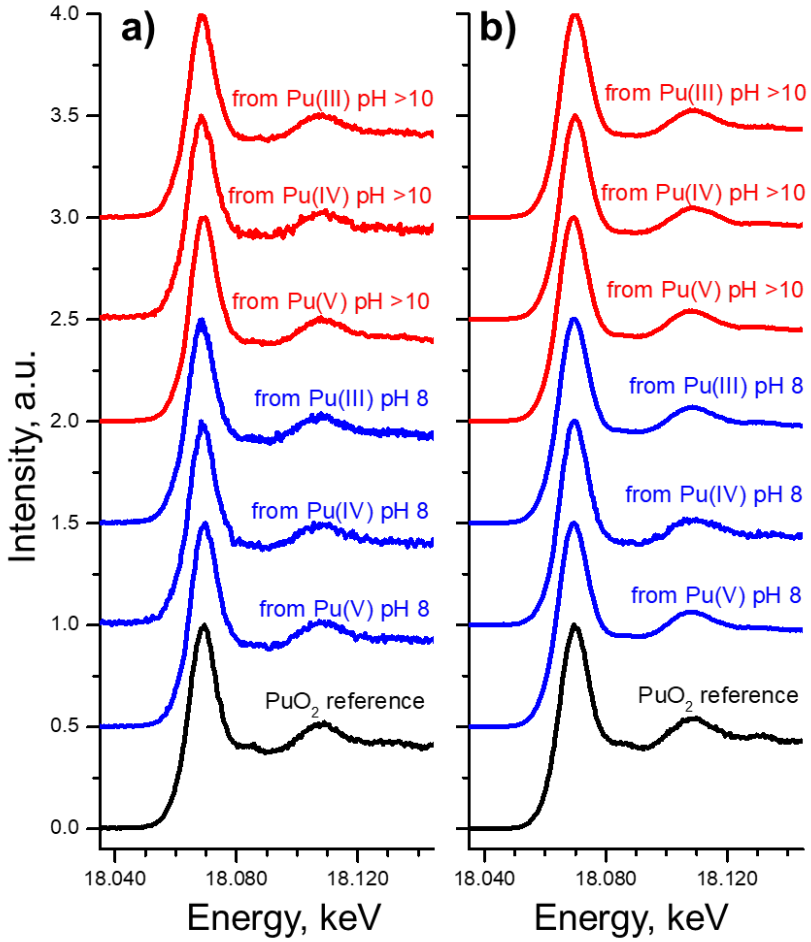

Fig. S10. The normalized HERFD-XANES experimental spectra at the Pu L_3 edge of all samples compared to PuO_2 measured in January (a) and April (b).

absorption spectrum for the PuO_2 cluster. The X-ray absorption spectrum is often related to the density of unoccupied electronic states of the system and one has to calculate the distribution of these unoccupied states in the final state. Pu L_3 edge is probing d-states which are hybridized in our systems. Quadrupole transitions (from 2p to 5f) can be a part of the pre-edge feature as f-states are constituent to the pre-edge part of the spectrum, but these transitions have very low intensity and are not resolved with our resolution.

EXAFS. EXAFS data analysis was based on standard least-squares curve fitting using the ATHENA[22] and the WinXAS[23] program packages. The EXAFS was extracted from the spectra by using a polynomial spline function to approximate the smooth atomic absorption. E_0, the origin for calculating the EXAFS χ(k)-function is fixed at the white line - peak maximum in the XAFS spectra at ~ 18062 eV. Metric parameters (neighbouring atomic distances R_i, EXAFS Debye-Waller factors

σ^2_i and coordination numbers N_i for the different coordination shells i) are determined using the FEFFIT code. All shell fits were carried out in R-space of k^3 - weighted spectra (Fourier transformed (FT) over a k-range of ~2.0 – 14 $Å^{-1}$) using theoretical backscattering amplitudes and phase shifts calculated with FEFF 8.2[24,25] on clusters (R_{max} = 8 Å) derived from the structure of PuO_2.[26] The amplitude reduction factor S_0^2 was fixed at 0.95. Debye-Waller factors were restricted to float between 0.001 and 0.010 $Å^2$.

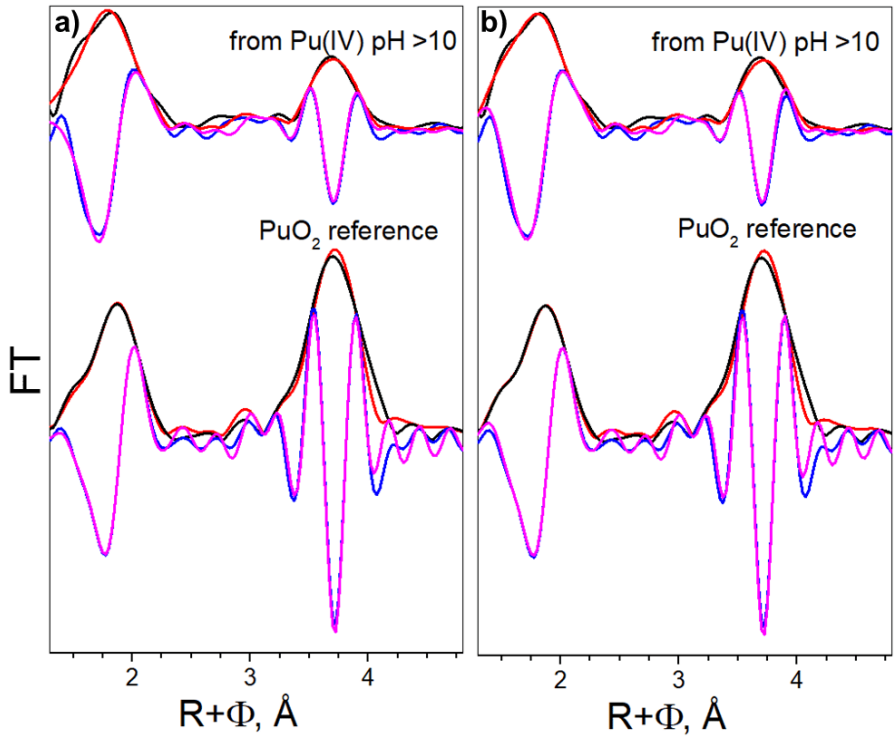

Fig. S11. R-space EXAFS fit results. k-range of 2.0-14.0 $Å^{-1}$, fit range R+Φ 1.30-4.50 Å. Fourier transform of experimental data: magnitude (black) and imaginary part (blue). FT of fit: magnitude (red) and imaginary part (pink). Fit results for two (a) and three (b) oxygen scattering paths, respectively.

Keeping in mind previous reports,[12,15,27,28] we performed additional fittings of EXAFS spectra using different approaches. The "three shell fit" approach considers three different Pu-O interactions in total: Pu(V)-O, Pu(IV)-O and Pu(IV)-OH (or, more generally, the oxygen atom with different coordination in comparison with Pu(IV)-O). The "two shell fit" approach excludes the Pu(V)-O scattering path, hence only two different paths remain. The fit obtained for the reference and one nanoparticle sample are shown in Fig. S11. Fit results of the other samples are reported in Table S3-S4 and Fig. 4a.

Three shell fit: The resulting fits obtained for all samples have only a slight parameter distribution (Table S3). The average distances are $R_{Pu(V)-O}$ - 1.83 Å, $R_{Pu(IV)-OH}$ – 2.28 Å, $R_{Pu(IV)-O}$ – 2.43 Å with coordination numbers 0.3, 4.8 and 1.9 respectively. However, if the first scattering path is ascribed as PuO_2^+, the CN of O would be 2 for pure Pu(V). it assumes the amount of Pu(V) reaches up to 15% ($CN_{Pu(V)-O}/2$, where 2 is the coordination number of oxygen in case of pure Pu(V) as the PuO_2^+ cation) among all Pu present, which would definitely appear in the HERFD-data. In addition, the fit with three scattering paths was also obtained for the annealed reference sample, where

we do not expect any detectable amounts of Pu(V) chemically, however, the fit of this standard appears unstable.

Table S3. Parameters extracted by least-squares fit analysis of Pu L_3 EXAFS spectra with three O shells (k-range of 2.0-14.0 $Å^1$)*.

Sample	Coordination shell									ΔE_0 [eV]	$\chi^2_{res\,\%}$
	First O shell			Second O shell			Third O shell				
	CN	R [Å]	σ^2 [$Å^2$]	CN	R [Å]	σ^2 [$Å^2$]	CN	R [Å]	σ^2 [$Å^2$]		
from Pu(III) pH >10	0.4	1.83	0.0010	4.0	2.29	0.0035	1.8	2.43	0.0010	7.6	14.2
from Pu(IV) pH >10	0.2	1.85	0.0010	5.5	2.29	0.0068	1.5	2.44	0.0027	6.8	10.3
from Pu(V) pH >10	0.2	1.84	0.0010	4.8	2.28	0.0052	2.2	2.42	0.0025	6.4	9.2
from Pu(III) pH 8	0.2	1.82	0.0010	4.4	2.28	0.0049	2.3	2.42	0.0025	6.3	11.5
from Pu(IV) pH 8	0.2	1.81	0.0010	6.1	2.28	0.0083	1.6	2.42	0.0022	5.6	8.77
from Pu(V) pH 8	0.5	1.84	0.0010	3.7	2.29	0.0032	2.1	2.44	0.0053	8.4	18.7
PuO_2 reference	0.7	1.89	0.0100	2.1	2.24	0.004	6.3	2.35	0.0040	6.8	9.3

*CN: Coordination number with error ± 25 %, R: Radial distance with error ± 0.01 Å, σ^2: Debye-Waller factor with error ±0.0005 $Å^2$.

Two shell fit: All parameters of the second approach fit are listed in the Table S4. One can see that the distribution of distances and coordination numbers is larger than in the previous approach, which may be an indirect evidence that the fit is more unstable. Nevertheless, two components can be extracted and assigned as Pu-OH and Pu-O scattering paths. However, despite of improving the EXAFS fit with additional contributions in the first coordination shell, the situation remains again unclear as the same fit could be performed for the reference PuO_2 sample, though this additional path cannot be used for this sample as there should not be any Pu-OH bonds, only Pu-O.

Table S4. Parameters extracted by least-squares fit analysis of Pu L_3 EXAFS spectra with two O shells (k-range of 2.0-14.0 $Å^{-1}$)*.

Sample	Coordination shell						ΔE_0 [eV]	$\chi^2_{res\,\%}$
	First O shell			Second O shell				
	CN	R [Å]	σ^2 [$Å^2$]	CN	R [Å]	σ^2 [$Å^2$]		
from Pu(III) pH >10	7.4	2.30	0.0097	0.6	2.44	0.0010	5.4	16.8
from Pu(IV) pH >10	6.1	2.28	0.0081	1.9	2.42	0.0043	5.4	11.5
from Pu(V) pH >10	6.5	2.29	0.0080	1.5	2.42	0.0025	5.2	9.9

from Pu(III) pH 8	7.2	2.29	0.0096	0.8	2.43	0.0010	4.9	12.8
from Pu(IV) pH 8	5.7	2.26	0.0076	2.3	2.41	0.0030	4.7	13.0
from Pu(V) pH 8	5.5	2.26	0.0076	2.5	2.39	0.0032	3.9	22.4
PuO_2 reference	6.0	2.30	0.0059	2.0	2.38	0.0021	6.44	10.4

*CN: Coordination number with error ± 25 %, R: Radial distance with error ± 0.01 Å, σ^2: Debye-Waller factor with error ±0.0005 Å^2.

To confirm or refute this approach, additional proof is needed while we used the exemplary sample with Pu(IV) at pH >10. In order to clarify the approach, we established a theoretical EXAFS spectrum simulation for PuO_2. We started from EXAFS Landweber iteration (LI),[29,30] which is used to construct the radial particle distribution function (n(r)) from an EXAFS spectrum. The advantage of this method is the possibility to reconstruct also asymmetric n(r) from the EXAFS spectra. An important parameter in the LI approach is the number of iterations, which determines the reliability of the resulting n(r). We used the L-curve method as described in[30,31] in order to determine the number of iterations. The LI calculated n(r) is shown in Fig. S12 together with the reconstructed EXAFS spectra and FTs. In line with the EXAFS shell fit, n(r) shows only one Pu-O contribution (Fig. S12c). However, Rothe et al.[28] detected two Pu-O contributions with average Pu-O distances of R_{O1} = 2.23 Å and R_{O2} = 2.40 Å, while the difference in these distances (R_{O2}, R_{O1}) of 0.17 Å is close to our radial resolution of 0.14 Å as defined by the used k-range of Δk = 11 Å. Consequently, the ability of the LI approach for resolving such close Pu-O contributions should be tested in order to exclude their presence in our system. For this task we calculated a theoretical model EXAFS spectrum (Fig. S13a) based on EXAFS parameters extracted by the least-squares fit analysis given in Table 2 sample E by Rothe et al.[28] For this sample three shells are given: O1 (R_{O1} = 2.22 Å, CN = 0.7, σ^2 = 0.0012 Å^2), O2 (R_{O2} = 2.38 Å, CN = 5.6, σ^2 = 0.00122 Å^2), and Pu (R = 3.85 Å, CN = 4.3, σ^2 = 0.009 Å^2). Due to the close radial distances of O1 and O2, an asymmetric Pu-O n(r) is obtained (Fig. S13c, black line). The LI was performed by applying the same parameters as used in the case of the experimental spectrum (Pu(IV) at pH >10), i.e. k-range, k-weighting and number of iterations. The LI calculated Pu-O n(r) (Fig. S13c, red line) is in good agreement with the n(r) of the model, hence if two Pu-O contributions would be present in our system the LI determined n(r) would have an asymmetric shape which is not the case (Fig. S13c).

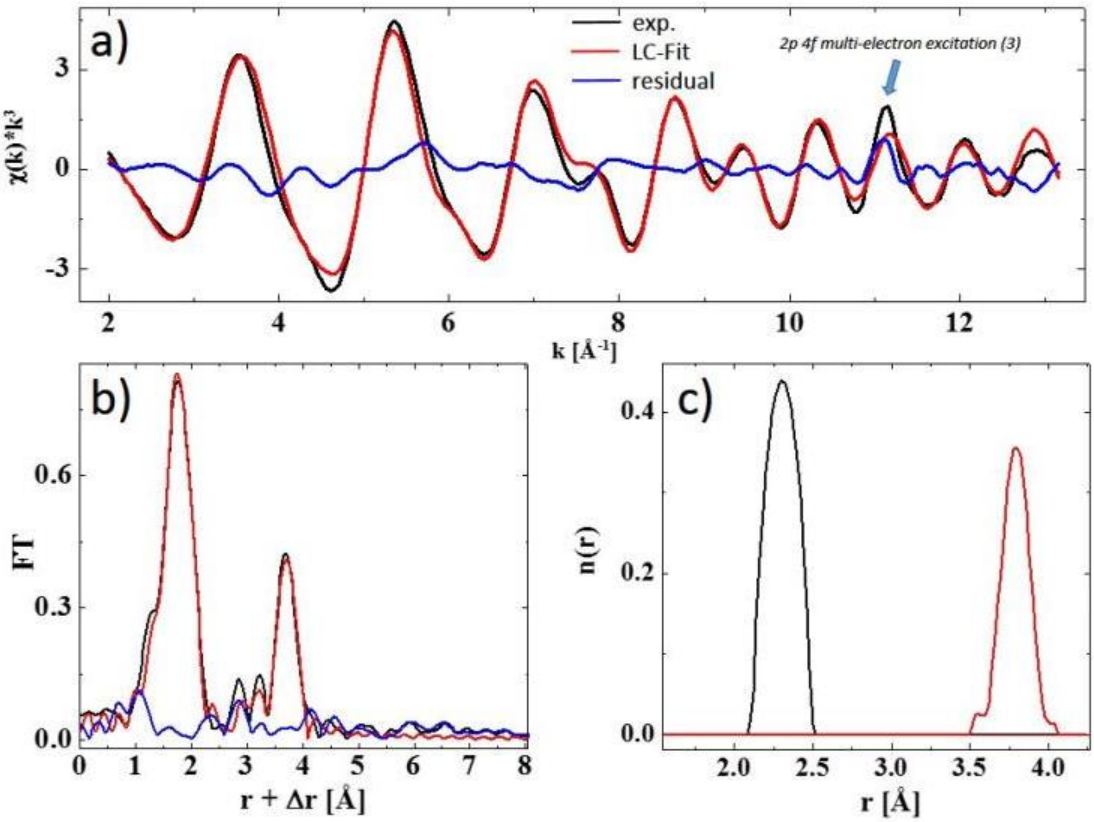

Fig. S12. EXAFS Landweber iteration (LI) for Pu(IV) at pH >10. a) experimental spectrum (black), reconstructed spectrum (red), residual (blue), b) corresponding Fourier transform (FT) magnitude, c) Pu-O (black) and Pu-Pu (red) radial particle distribution function (n(r)).

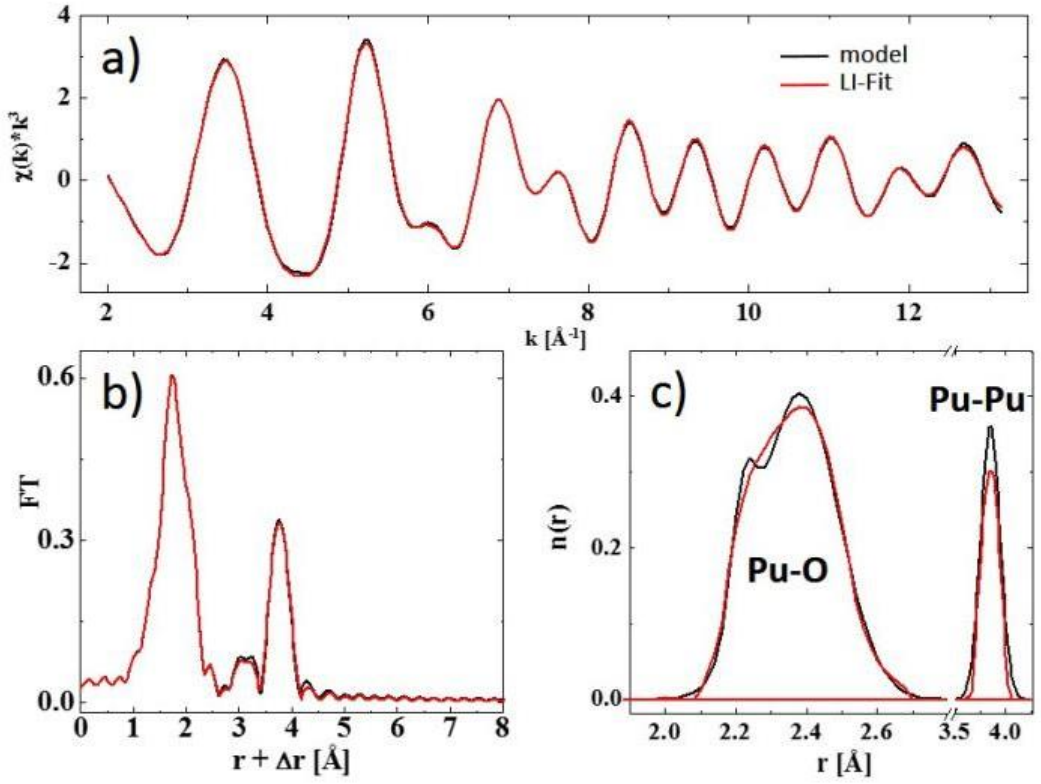

Fig. S13. EXAFS Landweber iteration (LI) for the EXAFS model spectrum. a) model spectrum (black), reconstructed spectrum (red), b) corresponding Fourier transform (FT) magnitude, c) model (black) and LI (red) Pu-O and Pu-Pu radial particle distribution function (n(r)).

We also implemented Monte-Carlo (MC) EXAFS simulations[32-38] as a complementary method to LI. The Metropolis algorithm was included in our MC code as proposed by Gurman et al.[36] For the single scattering (SS) paths the EXAFS kernel (A(k,r)) is calculated with FEFF8.2.0[60] by the method described in[30] and multiple scattering (MS) paths up to the 4th order are calculated during the simulation with a pre-defined spatial precision by FEFF8.2.0.

As a starting structure a PuO_2 cluster with a diagonal length of 14 Å was taken which contains 153 atoms. For the simulation, we used 200 replicas of the PuO_2 cluster. After 20.000.000 atomic movements, i.e. after 650 MC cycles (one cycle corresponds to the number of all atoms), the atomic positions converged to a stationary distribution. After convergence and after each following 10th MC cycle the actual atomic configuration was stored thirty times in order to receive a proper statistical average of n(r).

The MC simulation resulted in a very good agreement with the experimental EXAFS spectrum (Fig. S14a-b) and again the symmetric shape of the first shell Pu-O n(r) is observed (Fig. S14c), thus only one Pu-O contribution is present in our system.

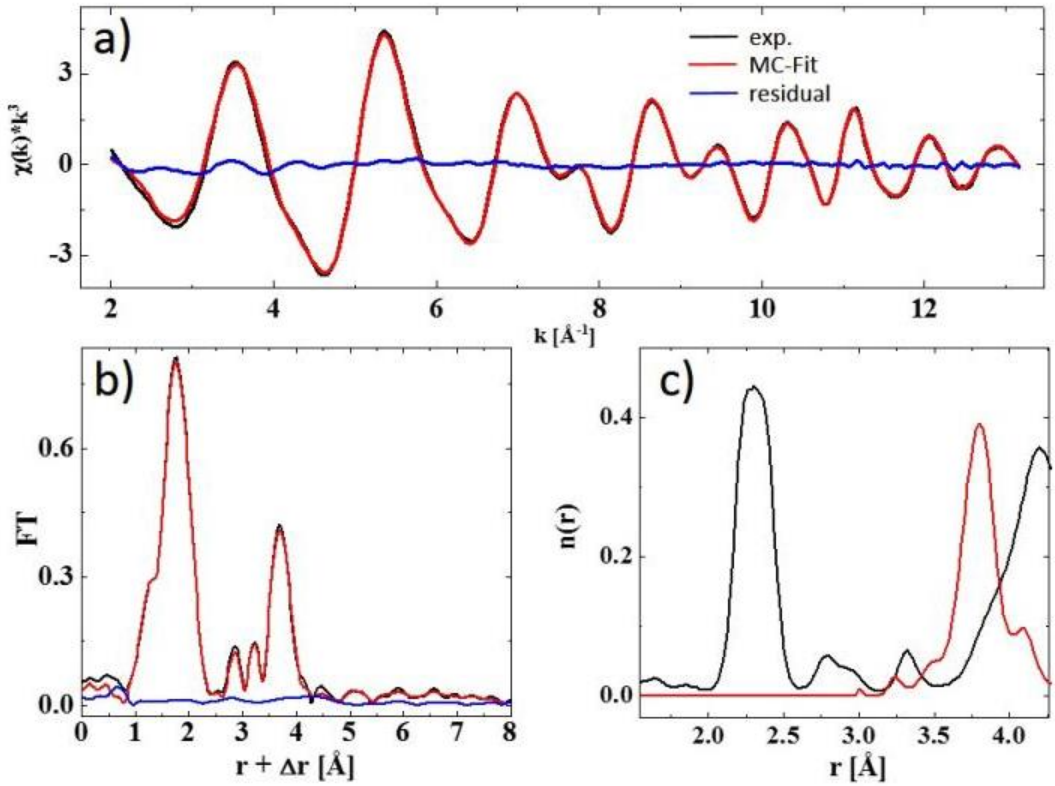

Fig. S14. Monte-Carlo (MC) EXAFS simulation for Pu(IV) at pH >10. a) experimental spectrum (black), reconstructed spectrum (red), residual (blue), b) corresponding Fourier transform (FT) magnitude, c) Pu-O (black) and Pu-Pu (red) radial particle distribution function (n(r)).

Results from HEXS can also clarify the situation. According to the HEXS data (Fig. 2c and d, Fig. S9), there is only one Pu-O contribution with the characteristic distance 2.34 Å, which is in a perfect agreement with the Pu-O distance in the PuO_2 reference structure. The FWHM of the peak is quite large, 0.1-0.2 Å, but the peak is not asymmetric which means that the overlap of two peaks corresponding to the different Pu-O contributions is unlikely for these samples.

Additional information about NP synthesis:

The precipitation process for all samples started shortly (in ten minutes) after adding all reagents. A green precipitate was formed, however, the reaction was continued for about 12 hours to reach equilibrium. Then the pH and redox potential of the precipitation were measured, the results are in Table S5. A Pt electrode relative to an Ag/AgCl reference electrode was used for the redox potential measurement. Eh value was calculated as measured potential (mV) + 208(mV). Due to hydrolysis processes, pH for the samples «from Pu(X) pH >10» was in the range 10-11.5. The electrode potential is higher for samples «from Pu(X) pH 8» and is also increasing with the valence state for these samples.

All sediments «from Pu(X) pH >10» were washed three times with Milli-Q water (18.4 MΩ/cm) to remove the presence of ammonia and samples «from Pu(X) pH 8» were washed once as they already were close to the pH of pure water. To determine the extent of the plutonium precipitation, the following things were done: an aliquot of each suspension was centrifuged (23,900 g, EBA 12 (Hettich)) and the concentration of the Pu in the supernatant was calculated with liquid scintillation spectrometry measurements (Wallac 1414 WIN spectral, PerkinElmer). It was found that for all samples most of the Pu precipitated and was not found in the supernatant.

Table S5. pH and Eh values after the end of the reactions.

Sample	pH	Eh, mV
from Pu(III) pH >10	10.8	-67
from Pu(IV) pH >10	10.2	-40
from Pu(V) pH >10	11.6	-75
from Pu(III) pH 8	8.0	-5
from Pu(IV) pH 8	8.1	80
from Pu(V) pH 8	8.3	155

References

1 R. G. Haire, M. H. Lloyd, M. L. Beasley and W. O. Milligan, J. Electron Microsc. (Tokyo)., 1971, 20, 8–16.

2 X. Machuron-Mandard and C. Madic, J. Alloys Compd., 1996, 235, 216–224.

3 P. Thiyagarajan, H. Diamond, L. Soderholm, E. P. Horwitz, L. M. Toth and L. K. Felker, Inorg. Chem., 1990, 29, 1902–1907.

4 P. K. Smith, G. A. Burney and D. T. Rankin, in Sixth International Materials Symposium, 1976.

5 I. R. Triay, D. E. Hobart, A. J. Mitchell, T. W. Newton, M. A. Ott, P. D. Palmer, R. S. Rundberg and J. L. Thompson, Radiochim. Acta, 1991, 52–53, 127–132.

6 C. Ekberg, K. Larsson, G. Skarnemark and I. Persson, Dalt. Trans., 2013, 42, 2035–2040.

7 A. Y. Romanchuk, T. V Plakhova, A. V Egorov, T. B. Egorova, P. V Dorovatovskii and Y. V Zubavichus, Dalt. Trans., 2018, 47, 11239–11244.

8 E. Dalodière, M. Virot, V. Morosini, T. Chave, T. Dumas, C. Hennig, T. Wiss, O. Dieste Blanco, D. K. Shuh, T. Tyliszcak, L. Venault, P. Moisy and S. I. Nikitenko, Sci. Rep., 2017, 7, 1–10.

9 O. Walter, K. Popa and O. D. Blanco, Open Chem., , DOI:10.1515/chem-2016-0018.

10 K. Popa, O. Walter, O. D. Blanco, A. Guiot, D. Bouëxière, J.-Y. Colle, L. Martel, M. Naji and D. Manara, CrystEngComm, 2018, 20, 4614–4622.

11 D. Bouëxière, K. Popa, O. Walter and M. Cologna, RSC Adv., 2019, 9, 6542–6547.

12 L. Bonato, M. Virot, T. Dumas, A. Mesbah, E. Dalodière, O. Dieste Blanco, T. Wiss, X. Le Goff, M. Odorico, D. Prieur, A. Rossberg, L. Venault, N. Dacheux, P. Moisy and S. I. Nikitenko, Nanoscale Adv., 2020, 2, 214–224.

13 V. Tyrpekl, J.-F. Vigier, D. Manara, T. Wiss, O. Dieste Blanco and J. Somers, J. Nucl. Mater., 2015, 460, 200–208.

14 G. I. Nkou Bouala, N. Clavier, J. Léchelle, J. Monnier, C. Ricolleau, N. Dacheux and R. Podor, J. Eur. Ceram. Soc., 2017, 37, 727–738.

15 D. Hudry, C. Apostolidis, O. Walter, A. Janßen, D. Manara, J. C. Griveau, E. Colineau, T. Vitova, T. Prüßmann, D. Wang, C. Kübel and D. Meyer, Chem. Eur. J., 2014, 20, 10431–10438.

16 S. Sutherland-harper, F. Livens, C. Pearce, J. Hobbs, R. Orr, R. Taylor, K. Webb and N. Kaltsoyannis, J. Nucl. Mater., , DOI:10.1016/j.jnucmat.2019.02.036.

17 X. Zhou and W. Huebner, Appl. Phys. Lett., 2001, 79, 3512–3514.

18 J. M. Haschke, T. H. Allen and L. A. Morales, Science (80-.)., 2000, 287, 285–287.

19 V. Neck and J. I. Kim, Radiochim. Acta, 2001, 89, 1–16.

20 A. Tasi, X. Gaona, D. Fellhauer, M. Böttle, J. Rothe, K. Dardenne, D. Schild, M. Grivé, E. Colàs, J. Bruno, K. Källström and M. Altmaier, Radiochim. Acta, 2018, 106, 259–279.

21 J. J. Rehr, J. J. Kas, F. D. Vila, P. P. Micah and K. Jorissen, Phys. Chem. Chem. Phys., 2010, 12, 5503–5513.

22 B. Ravel and M. Newville, J. Synchrotron Radiat., 2005, 12, 537–541.

23 T. Ressler, J. Phys. Ⅳ, 1997, 7, C2-269.

24 A. Ankudinov and J. Rehr, Phys. Rev. B - Condens. Matter Mater. Phys., 1997, 56, R1712–R1716.

25 A. Ankudinov and B. Ravel, Phys. Rev. B - Condens. Matter Mater. Phys., 1998, 58, 7565–7576.

26 R. C. Belin, P. J. Valenza, M. A. Reynaud and P. E. Raison, Appl. Crystallogr., 2004, 37, 1034–1037.

27 S. D. Conradson, B. D. Begg, D. L. Clark, C. Den Auwer, M. Ding, P. K. Dorhout, F. J. Espinosa-Faller, P. L. Gordon, R. G. Haire, N. J. Hess, R. F. Hess, D. W. Keogh, L. A. Morales, M. P. Neu, P. Paviet-Hartmann, W. Runde, C. D. Tait, D. K. Veirs and P. M. Villella, J. Am. Chem. Soc., 2004, 126, 13443–13458.

28 J. Rothe, C. Walther, M. A. Denecke and T. Fanghänel, Inorg. Chem., 2004, 43, 4708–4718.

29 L. Landweber, Am. J. Math., 1951, 73, 615–624.

30 A. Rossberg and H. Funke, J. Synchrotron Radiat., 2010, 17, 280–288.

31 P. C. Hansen and D. P. O'Leary, SIAM J. Sci. Comput., 2005, 14, 1487–1503.

32 A. Rossberg and A. C. Scheinost, Anal. Bioanal. Chem., 2005, 383, 56–66.

33 M. Winterer, J. Appl. Phys., 2000, 88, 5635–5644.

34 M. Winterer, R. Delaplane and R. McGreevy, J. Appl. Crystallogr., 2002, 35, 434–442.

35 M. Winterer and F. Farges, Phys. Scr., 2005, T115, 923–924.

36 S. J. Gurman and R. L. McGreevy, J. Phys. Condens. Matter, 1990, 2, 9463–9473.

37 R. L. McGreevy, J. Phys. Condens. Matter, 2001, 13, R877–R913.

38 J. Timoshenko, A. Kuzmin and J. Purans, Comput. Phys. Commun., 2012, 183, 1237–1245.

Appendix B: Article 2. Insight into the structure-property relation of UO_2 nanoparticles

Evgeny Gerber[a,b,c], Anna Yu. Romanchuk[c], Stephan Weiss[b], Stephen Bauters[a,b], Bianca Schacherl[d], Tonya Vitova[d], René Hübner[b], Salim Shams Aldin Azzam[b], Dirk Detollenaere[e,f], Dipanjan Banerjee[f,g], Sergei M. Butorin[h], Stepan N. Kalmykov[c] and Kristina O. Kvashnina[a,b,c*]

[a] *The Rossendorf Beamline at ESRF – The European Synchrotron, CS40220, 38043 Grenoble Cedex 9, France.*

[b] *Helmholtz-Zentrum Dresden-Rossendorf (HZDR), Institute of Resource Ecology, PO Box 510119, 01314, Dresden.*

[c] *Lomonosov Moscow State University, Department of Chemistry, 119991 Moscow, Russia.*

[d] *Institute for Nuclear Waste Disposal (INE), Karlsruhe Institute of Technology, P.O. 3640, D-76021 Karlsruhe, Germany*

[e] *Department of Chemistry, X-ray Imaging and Microspectroscopy Research Group, Ghent University, Ghent, Belgium*

[f] *Dutch-Belgian Beamline (DUBBLE), European Synchrotron Radiation Facility, 71 Avenue des Martyrs, CS 40220, 38043 Grenoble Cedex 9, France*

[g] *Department of Chemistry, KU Leuven, Celestijnenlaan 200F, Box 2404, B-3001 Leuven, Belgium*

Molecular and Condensed Matter Physics, Department of Physics and Astronomy, Uppsala University, P.O. Box 516, Uppsala, Sweden

Abstract

Highly crystalline UO_2 nanoparticles (NPs) with sizes of 2-3 nm were produced by fast chemical deposition of uranium(IV) under reducing conditions at pH 8-11. The particles were then characterized by microscopic and spectroscopic techniques including high-resolution transmission electron microscopy (HRTEM), X-ray diffraction (XRD), high-energy resolution fluorescence detection (HERFD) X-ray absorption spectroscopy at the U M_4 edge and extended X-ray absorption fine structure (EXAFS) spectroscopy at the U L_3 edge. The results of this investigation show that despite U(IV) being the dominant oxidation state of the freshly prepared UO_2 NPs, they oxidize to U_4O_9 with time and under the X-ray beam, indicating the high reactivity of U(IV) under these conditions. Moreover, it was found that the oxidation process of NPs is accompanied by their growth in size to 6 nm. We highlight here the major differences and similarities of the UO_2 NPs properties with PuO_2, ThO_2 and CeO_2 NPs.

Introduction

Uranium dioxide remains one of the most essential uranium compounds due to its application as a nuclear fuel in most of the commercial nuclear reactors worldwide.[1] Structural chemistry and physics of the U/O system are very complicated but highly important for reactor performance, spent nuclear fuel storage and its further geological disposal. While bulk UO_2 has been intensively studied, it is still not clear if the investigated properties persist the same at the nanoscale.[2,3] It is known that actinide (An) nanoparticles (NPs) form aggregates of various sizes.[4,5] In particular, UO_2 NPs may be formed by redox reactions from either the reduction of U(VI) by γ- irradiation,[6] minerals,[7–10] microorganisms,[11–17] redox-active chemicals[18] or due to corrosion of metallic U being in contact with water.[4,19,20] It can also be formed via hydrolysis of U(IV) solutions[21–23] or by decomposition of U(IV) compounds.[24]

Under environmental conditions, uranium mineral NPs are found to be ubiquitous and have been identified in a number of studies.[7,25–28] As highly-hydrolysable cation, U(IV) migrates predominantly in the form of pseudo-colloids and intrinsic colloids rather than in the soluble complexed form. UO_2 NPs formed as a result of bacteria mediated redox reactions have an influence on U migration in the far-field conditions of repositories. Accidental (like Chernobyl and Fukushima) and routine releases of radionuclides into the environment result in the formation of U oxide NPs. [29–32] It has also been shown that the dissolution of spent nuclear fuel may result in the formation of UO_2 NPs that should be taken into account in the performance assessment of repositories,[33] considering that conditions in deep geological repositories are expected to be reducing.

The peculiarities of nanoscale objects affect their properties.[2] Nanoscale UO_2 is readily oxidized with the formation of UO_{2+x}, while the crystal structure does not significantly alter.[35–37] Similar AnO_{2+x} NPs with a structure close to bulk AnO_2 were also observed for plutonium,[38] which is not surprising as both UO_2 and PuO_2 are isostructural to the fluorite-type fcc structure with a very similar lattice parameter. However, recent publications show that PuO_2 NPs do not contain other oxidation states except for Pu(IV)[39,40] and their structural properties are close to the bulk. Similar predictions were made for CeO_2 NPs, with the suggestion that CeO_{2-x} NPs were expected to be predominantly composed of Ce(IV), which can be reduced to Ce(III).[41] Later, the absence of the Ce(III) oxidation state was confirmed for NPs even for 2nm particles.[42,43] This could lead to the assumption that there is a similar trend for all highly-hydrolyzed tetravalent Ln or An cations. However, to the best of our knowledge, the tetravalent oxidation state for UO_2 NPs has never been proven.

The main difference between U and Pu lies in multivalent behaviour. Under oxidizing conditions, PuO_2 is the sole stable oxide, but more than ten stable U binary oxides – UO_{2+x} – are known. Similar to plutonium, CeO_2 is the only stable oxide under oxidizing conditions, however both Ce(IV) and Ce(III) ions may present in solution. Later we briefly compare the differences and similarities of various An and Ln oxide NPs properties, based on the results reported here.

Experimental

Nanoparticle synthesis

The UO_2 NPs were synthesized from U(IV) aqueous solution by adding ammonia under reducing conditions. Due to the highly sensitive nature of U(IV) towards oxidation, all synthetic procedures, including the preparation of the samples for the following characterization methods were done in a glovebox under nitrogen atmosphere (<10 ppm O_2).

Special care was taken to avoid any contact with oxygen before and during the measurements. U(IV) stock was prepared by galvanostatic reduction of 0.1 M U(VI) in 0.5 M $HClO_4$ (5 hours, 20 mA). The presence of only U(IV) and the stability of the solution were verified by UV-vis spectrometry (AvaSpec-2048x14, Avantes, Fig. S1). Each U(IV) solution (0.1 M and 0.01 M) was divided into two parts. The first set of aliquots was added to 3 M NH_3 in the volume ratio 1:10 under continuous stirring. The pH of the 3M ammonia solution was 12.5, but the pH slightly decreased due to the interaction with the U(IV) solution, most likely due to hydrolysis reactions. This set of samples was named "0.1 M/0.01 M U(IV) pH > 11". The second set of aliquots of stock U(IV) was added to water in the volume ratio 1:10, after which several drops of 3 M NH_3 were added under continuous stirring to reach pH 8. This set of samples was named "0.1M/0.01M U(IV) pH 8". In all syntheses, mixing rate and vessel geometry were maintained constant. The precipitation process for all samples started shortly (within ten minutes) after addition of all reagents. A black precipitate was formed, and the reaction was continued for about 2 hours to reach equilibrium. Then, the pH and redox potential of the formed suspensions were measured (Table S1). The UO_2 reference was made by pressing industrially obtained uranium dioxide powder into a pellet followed by sintering at 1700°C under H_2/Ar stream. The industrial uranium dioxide, in its turn, was obtained from UF_6 by the gas-flame method, followed by annealing under reducing conditions at 600 – 650 °C.[44] The reference was characterized by X-ray diffraction (XRD) and polarography, the oxygen coefficient of UO_{2+x} was found to be in order of x=0.001.

Characterization

Transmission electron microscopy (TEM)

TEM investigations were performed at the Helmholtz-Zentrum Dresden-Rossendorf (HZDR) using an image-C_s-corrected Titan 80-300 microscope (FEI) operated at an accelerating voltage of 300 kV. In particular, selected area electron diffraction (SAED) patterns using a SA aperture of 40 µm and high-resolution TEM (HRTEM) images were recorded.

Powder X-ray diffraction measurements.

Powder X-ray diffraction (PXRD) data were collected at room temperature at the HZDR. XRD diffractograms data were collected with a MiniFlex 600 diffractometer (Rigaku, Tokyo, Japan) equipped with a Cu Kα X-ray source (40 keV/15 mA operation for X-ray generation) and the D/teX Ultra 1D silicon strip detector in the Bragg-Brentano θ-2θ geometry at a scanning speed of 0.02 degrees per min. The FWHM and peak position were determined with Fityk software.[45]

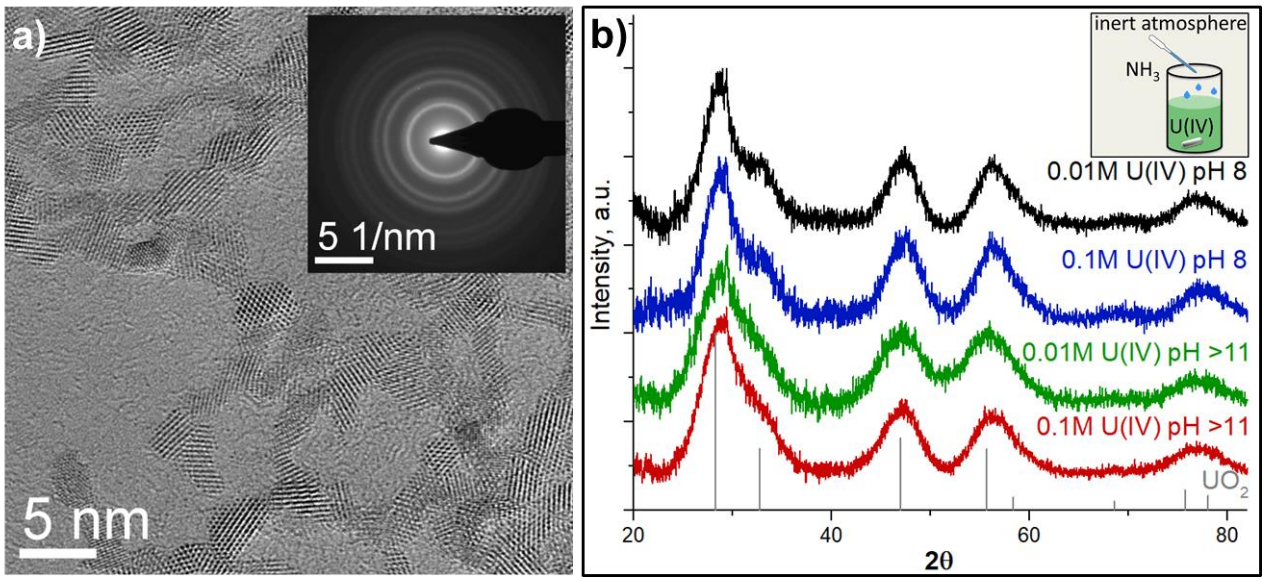

Fig. 1. a) HRTEM image of 0.01M U(IV) pH 8 NPs and corresponding SAED pattern (inset), b) XRD patterns of UO_2 reference and the precipitates from U(IV) with different pH and concentrations. The inset shows the schematic drawing of UO_2 NPs synthesis.

X-ray absorption near edge structure (XANES) in high-energy resolution fluorescence detection (HERFD) mode at the U M_4 edge and U L_3 extended X-ray absorption fine structure (EXAFS) spectroscopy

The HERFD spectra at the U M_4 edge were collected at the CAT-ACT beamline of the KARA (Karlsruhe research accelerator) facility in Karlsruhe, Germany.[46] The incident energy was selected using the [111] reflection from a double Si crystal monochromator. Estimated flux at the sample position was in the order of 10^9 ph/sec at an incident energy of 3.8 keV.[47] The U HERFD spectra at the M_4 edge were obtained by recording at the maximum intensity of the U M_β emission line (3339.8 eV) as a function of the incident energy. The emission energy was selected using the [220] reflection of one spherically bent Si crystal analyser (1 m bending radius) aligned at 75° Bragg angle. Samples were prepared and sealed in a special argon-filled container at the licensed laboratory of HZDR and were transported to KARA under inert conditions. All samples were mounted in the form of wet pastes within triple holders with 8 µm Kapton window on the front side, serving as first confinement. Three of such holders were mounted in one larger cell, with 13 µm Kapton window on the front side. (second confinement, Fig. S2) The second confinement chamber was constantly flushed with He. The entire spectrometer environment was contained within a He box to improve signal statistics. An energy range from 3710.5 to 3790.5 eV was scanned with a step size down to 0.1 eV using a 1s dwell time per energy point. All samples were tested for short-term beam damage. First an extended timescan (>2 min with 0.1sec step) above the excitation edge was performed before data collection, to monitor any long-term variations in fluorescence signal. Later a preliminary fast HERFD scan (<2 min) was collected and compared with all HERFD data collected per sample. Based on that procedure, the estimated X-ray exposure time has been derived for each sample.

The U L_3 edge (17166 eV) EXAFS spectra were collected at BM26A, the Dutch-Belgium beamline (DUBBLE) at the ESRF (the European Synchrotron) in Grenoble, France.[48] The energy of the X-ray beam was tuned by using a double-crystal monochromator operating in a fixed-exit mode using a Si(111) crystal pair. Measurements were performed in transmission mode with N_2/He and

Ar/He filled ionization chambers. Energy calibration was performed by recording the EXAFS spectrum of the K-edge of metallic Y (~17038 eV) which was collected simultaneously with the sample scans for each sample. The samples were measured at room temperature using a double-confined, heat-sealed polyethylene holder. Energy calibration, averaging of the individual scans, EXAFS data extraction and fitting were performed with the software package Demeter.[49]

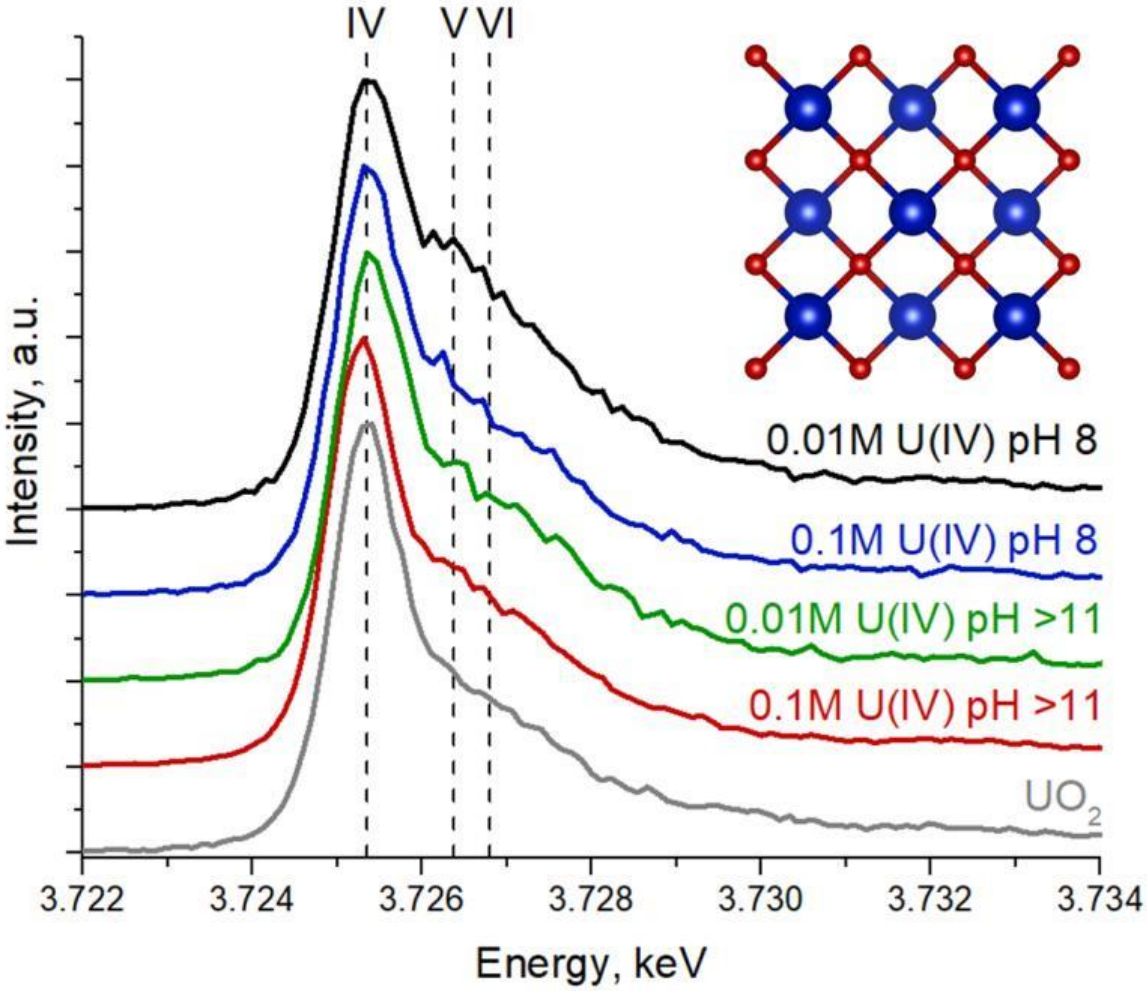

Fig. 2. U M_4 HERFD experimental data recorded for the four UO_2 NPs samples and compared to a UO_2 reference.

Results and discussion

Due to chemical reactivity, the ideal structure of UO_2 can be easily perturbed (even in the bulk crystal).[35,50,51] The particle size distribution and crystallinity could also differ depending on the synthesis route[6,11,52–54]. The HRTEM data reported in Fig. 1a and Fig S3 confirm that regardless of U(IV) concentration and pH conditions, similar NPs are formed (with respect to their size distribution and crystallinity). A comparison of the SAED patterns (Fig. 1a and Fig. S3 (insets)) and diffractograms from XRD measurements (Fig. 1b) with bulk UO_2 show that the crystalline structure of the NPs is similar to that of bulk UO_2 (ICDD 03-065-0285). However, the diffraction peaks are broad, indicating the nanosize dimensions of the samples. The crystallite size was estimated from XRD with Scherrer's equation and found to be similar for all samples, varying in the range of 1.7-2.5 nm (Table S2) with respect to the fact that Scherrer's equation is supposed to give information about coherent domains rather than crystallites. Nevertheless, the diffraction

peaks of NPs obtained at pH 8 are slightly narrower than those for pH >11, indicating that pH has a small but notable effect on the NP size. It was unexpected as previous research showed that synthesis conditions highly impact the UO_2 shape and size. For example, Hu and coauthors[55] made UO_2 in the form of NPs, nanoribbons and nanowires, changing the precursor/organic solvent ratio and temperature. There are many other examples, where the size of the obtained UO_2 NPs varied from several nm up to several microns depending on the synthesis route (radiolytic reduction, organic precursor-assisted syntheses, U(IV) hydrolysis, biogenic reduction etc.) as well as starting precursors and reaction conditions.[8,13,52–54,56–63] Our HRTEM results (Table S2) also confirm the nanosize of crystallites.

For U–O systems, the number of stoichiometric binary oxides and solid solutions with various compositions are known. Uranium upon oxidation may form various oxides with mixed oxidation states of U (like U_2O_5, U_3O_7, U_4O_9, U_3O_8).[64,65] The fluorite structure of UO_2 can accommodate a large amount of excess oxygen up to $UO_{2.25}$, therefore XRD, giving information about coherent scattering domains, is generally less sensitive to this kind of alterations. In other words, the XRD patterns of U_4O_9 and UO_2 are very similar and the presence of those species in UO_2 NPs cannot be detected by XRD (Fig. S4). Further oxidation of $UO_{2.25}$ (U_4O_9) may lead to the formation of UO_{2+x} oxides with $0.25 < x \leq 0.33$ accompanied by a changing of the crystal structure. Subsequent oxidation may proceed through the formation of $UO_{2.5}$ (U_2O_5) and $UO_{2.67}$ (U_3O_8) until UO_3 is formed.

To further complicate matters, there is a peak broadening effect for NPs in XRD, making reliable analysis nearly impossible, especially in the case of extremely small NPs. That is where synchrotron-based high-energy resolution fluorescence detection (HERFD) X-ray absorption spectroscopy at the U M_4 edge really comes in use. Thanks to its high sensitivity, it can easily detect even the tiniest oxidation state impurities, which are present in many uranium oxides (U_4O_9, U_3O_8, U_3O_7).[9,10,46,66–69] The HERFD method at the An M_4 edge probes An 3d-5f electronic transitions and is thus highly effective for the detection of the 5f electron configuration and for oxidation state identification.[9,10,39,40,46,66] Moreover, the shapes of the recorded data on various mixed uranium oxides are so distinct[66,67] that recorded HERFD spectra on uranium systems can be straightforwardly analyzed by a fingerprint approach to detect the presence of U_4O_9/U_3O_8 impurities in UO_2 NPs.

Fig. 2 shows the U M_4 edge measurements on four UO_2 NP samples compared to the spectrum of the UO_2 reference. All spectral features of UO_2 NPs are very similar, corresponding to those of the UO_2 reference, thus confirming the results from XRD and HRTEM. The shape of the main absorption peak in the HERFD spectrum of UO_2 reference shows an asymmetric profile, which was observed before,[66] however for NP spectra the asymmetry of the peak increases, leading to a high-energy shoulder (Fig. S5). It is expected that the asymmetry of the peak originated from partial oxidation and the presence of oxidized uranium species. However, the theoretical calculations of the U(IV) M_4 HERFD spectra (c.f. SI, Fig. S6) show that nanoscale distortion or even different coordination environment has a strong correlation with the high-energy shoulder in U M_4 HERFD. It is not easy to distinguish between the influence of the presence of higher oxidation state in NPs and the distortion contributions to the asymmetry of the peak. However, theoretical results clearly indicate that the distortion at the surface and random changes of the coordination number for surface atoms will affect the intensity (increase and decrease) of the higher energy U M_4 HERFD shoulder. Regardless of the asymmetry origin, one can conclude that U(IV) is the

dominant oxidation state for UO_2 NPs. To the best of our knowledge, this has never been shown and reported for UO_2 NPs at the high sensitivity that HERFD gives for redox speciation.

The crystallinity of the NPs was investigated for structural disorder by uranium L_3-edge EXAFS studies (c.f. Fig. S7, Table S3). EXAFS is actively used for uranium[8,10,63,68,70] to investigate the local chemical environment. It has also been used previously to determine the oxidation state of uranium due to the different U(X)-O bond length (where X is the oxidation state of uranium) and static disorder contributions. Our U L_3-EXAFS data and shell fit results indicate a UO_2-like structure, with characteristic distances 2.33 Å and 3.85 Å for U-O and U-U, respectively (Fig. S7). The absence of other shorter or longer U-O distances suggests that there is no need to invoke different U oxidation states or a substantially different structure (e.g. U_4O_9 or U(V)-O). However, the reduced CN for the U-O shell and high Debye-Waller factors are suggestive of particle-size effect and static and thermal disorders, which was previously observed on similar particles.[8,9,13,63,71]

Taking into account: 1) the significant disorder revealed by EXAFS and 2) the theoretical prediction of the distortion effects on the high-energy shoulder of the U M_4 HERFD spectra, surface distortion might be the predominant reason for the experimental observation of the intensity variation of the high-energy shoulder in U M_4 HERFD data between various UO_2 NPs.

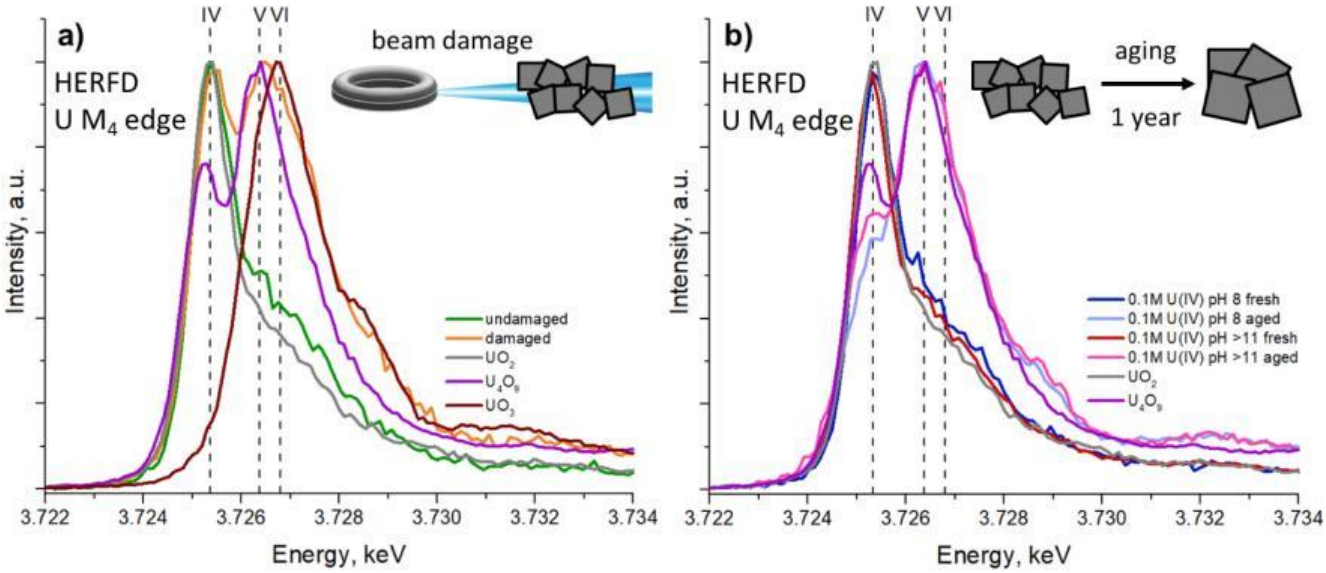

Fig. 3. **HERFD M_4 edge spectra:** a) for 0.01M U(IV) pH >11 before and after beam damage with references. b) for fresh and 1-year-aged 0.1M samples with references. The HERFD spectra of the UO_3 and U_4O_9 references have been reproduced from data, reported by Leinders et al and have shown here for clarity.[60]

Reactivity of the UO_2 NPs

The reactivity of UO_2 NPs under different conditions was studied previously. It was found, that sintering leads to NP growth.[6,13] Rath et al. found that UO_2 NPs obtained with γ-irradiation oxidize in several hours under air conditions, while Singer et al. and Wang et al. did not find any changes after 2 months ageing or several days of air exposure.[11,53,60] However, visual observations of the change in residue colour by UV-vis spectroscopy or the U L_3 edge XANES (used in previous studies) may not be sufficient to detect other oxidation states of uranium.

Here we investigate in detail the reactivity and phase stability of synthesized UO_2 NPs. First, we noticed the impact of the synchrotron X-ray beam on the freshly synthesized materials. In order to verify the damage of samples by X-ray irradiation, all samples were scanned several times at the exact same position to examine how the beam exposure affects the samples. Fig. 3a shows the average of the first U M_4 spectra scans on UO_2 NPs synthesized from 0.01M U(IV) pH >11 and its comparison with the last scans after 45-60 minutes of X-ray exposure. With each subsequent scan (which takes 5 min) the shoulder of the HERFD high-energy side increases and can even be resolved as an individual component, indicating the partial oxidation of the sample to U(V) and U(VI). Other samples were oxidized under exposure as well, leading to the conclusion that beam exposure is responsible for uranium oxidation in NPs. In order to obtain data on freshly made materials, HERFD measurements have been made on newly synthesized UO_2 NPs (reported in Fig. 2), with a short X-ray exposure time (15 min in total over several scans) on samples sealed in a special inert gas-filled container (more info is given in experimental section and SI).

The recorded U M_4 HERFD data on oxidized UO_2 NPs are reported in Fig.3 and compared to the spectra of UO_2, U_4O_9 and UO_3 (reproduced from Leinders et al.[67]). It should be noted that despite the longer duration of L_3-edge EXAFS measurements beam damage does not take place in that case due to the lower unfocused beam intensity, compared to M_4-edge HERFD measurements. Several scans made on the same sample position were reproducible and oxidation (or significant differences from UO_2 structure) was not detected.

Moreover, the stability of NPs over time has also been studied. Two samples synthesized from 0.1M U(IV) concentrations were kept as wet pastes under inert conditions and ambient temperature for a year in closed 2mL plastic tubes with a tiny amount of water left after washing the NPs. Afterwards these samples were analysed with HRTEM, XRD and M_4 edge HERFD techniques. It was found that the size of NPs increases (Table S2, Fig. S8-9) after aging (likely, due to the dissolution-precipitation processes[57]), while partial oxidation was observed by HERFD (Fig. 3b). A rise of U(V) contribution in the damaged NPs is shown (Fig. 3a), though it is clear by the difference in peak intensity ratios that the NPs have not fully converted to pure U_4O_9. Bulk U_4O_9 has equal amounts of U(IV) and U(V), yet the peak intensities in HERFD are not the same due to the different probability of the absorption process, i.e. different absolute absorption cross sections of U(IV) and U(V).[67] Therefore, a significant amount of U(IV) is still retained in our damaged samples. The HERFD spectra on the aged NPs show higher contribution of the U(V) for compare to U(IV). Overall, it leads to the conclusion that small NPs oxidize to U_4O_9 and grow up to 6 nm over time. The size of 6 nm was determined by XRD data and is in agreement with HRTEM size estimations (Table S2).

The strong influence of the X-ray beam and the aging behaviour of the UO_2 NPs are clear evidences of the low stability of the samples; therefore, special care must be taken to avoid sample oxidation and destructive effects of the X-ray beam. The reasonable solution is to keep samples under reducing conditions as long as possible before performing any experiments, to record relatively quick scans and to choose new sample positions for every scan to limit sample exposure. Measurements under cryogenic conditions might also overcome the issue of beam damage, but this has not been tested yet on the UO_2 NPs.

Comparison between various An and Ln oxide NPs

Tetravalent cations (Cat) undergo extensive hydrolysis accompanied by the formation of mono- and oligomeric species. Eventually $CatO_2$ NPs originate from aqueous solutions. Besides uranium, the formation of small (2-4 nm) crystalline NPs was observed for cerium,[43] thorium,[72] neptunium[73] and plutonium.[74] Dioxides of these elements demonstrate similar crystallographic properties: fluorite-type structure with similar lattice parameter. However, the redox properties of these elements are different. Thorium is redox inactive, while Ce, U, Np and Pu may be present in different oxidation states. The correlation between UO_2 and PuO_2 NPs is of high interest as both U(IV) and Pu(IV) are mobile in their colloid forms.[5,75,76] The redox conditions in deep geological repositories are expected to be reducing. Therefore, U(IV), being stable under these conditions, could be a reference for Pu(IV) as well, due to the similarities in An(IV) ionic radii and crystallographic properties of their dioxides. Our investigation shows that there are many resemblances between these An(IV) NPs. It was shown[39] that neither super stoichiometric AnO_{2+x} nor other higher oxide phases are present in PuO_2 NPs though it could be expected due to the stability of Pu(IV) under these conditions. Similar behaviour can be predicted for NpO_2 NPs, however, to the best of our knowledge the presence of other oxidation states in NpO_2 NPs has not been studied yet by HERFD method.

Contrariwise to Pu and especially Np, Ce(III) is stable in aqueous solutions, therefore, one can expect Ce(III) is present in the hydrolysis products. Nevertheless, it was found[42,43], that CeO_2 NPs do not contain even slight amounts of Ce(III), leading to the conclusion that $CatO_2$ NPs formed by fast chemical deposition retain Cat(IV) as the dominating oxidation state regardless of their redox affinity. In this study we confirmed, that it is also valid for UO_2 NPs, synthesized by fast chemical deposition method under pH 8-11. Those results do not include the possibility that the formation of other phases or other oxidation states takes place under different synthesis conditions.

Conclusions

It is reasonable to believe that the properties of UO_2 in bulk and at the nanoscale are different. Due to a larger surface-to-volume ratio, UO_2 NPs are expected to be more reactive and, therefore, to exist as UO_{2+x}, with some of the U oxidized at the surface.[35–37] However, it was found that U(IV) is the dominant oxidation state of the UO_2 NPs, synthesized by fast chemical deposition method at pH 8-11, but their stability is significantly lower then bulk-UO_2 in terms of time and oxidation sensitivity. They are easily oxidized not only in the air but also slowly under inert conditions or during X-ray exposure. Therefore, special care has to be taken while investigating reactions with UO_2 NPs and their properties.

The electronic and local structure of the freshly synthesized UO_2 NPs in size of 2-3nm was revealed by combination of the U L_3-edge EXAFS, U M_4-edge HERFD, XRD and HRTEM methods. We show here that the structural and electronic properties of fresh ultra-small UO_2 NPs (2-3 nm) are similar to bulk UO_2 when inert or reducing conditions restrictions are maintained. It was found that high reactivity of UO_2 NPs in time and under X-ray beam exposure leads to the formation of the U_4O_9 species complemented by the growth of the NP size to 6 nm. We believe that these findings are beneficial to the fundamental understanding of nuclear fuels and tailoring the functionality of UO_2 since most previous studies focus on large-bulk UO_2.

Conflicts of interest

There are no conflicts to declare.

Acknowledgements

This research was funded by European Commission Council under ERC [grant N759696]. E.G. acknowledges support from RFBR (project number No. 19-33-90127). S.N.K. acknowledges support by the Russian Ministry of Science and Education under grant № 075-15-2019-1891. S.M.B. acknowledges support from the Swedish Research Council (Grant 2017-06465). Authors thank HZDR for the beamtime at CAT-ACT beamline of KARA. Moreover, we acknowledge the help of J. Rothe, A. Beck, J. Galanzew and T. Prüßmann at CAT-ACT beamline of KARA during the HERFD experiment at the U M_4 edge. Furthermore, the use of the HZDR Ion Beam Centre TEM facilities is acknowledged.

References

1 R. C. Ewing, Long-term storage of spent nuclear fuel, Nat. Mater., 2015, 14, 252–257.

2 M. F. Hochella, D. W. Mogk, J. Ranville, I. C. Allen, G. W. Luther, L. C. Marr, B. P. McGrail, M. Murayama, N. P. Qafoku, K. M. Rosso, N. Sahai, P. A. Schroeder, P. Vikesland, P. Westerhoff and Y. Yang, Natural, incidental, and engineered nanomaterials and their impacts on the Earth system, Science., 2019, 363, eaau8299.

3 H. Wu, Y. Yang and Y. C. Cao, Synthesis of Colloidal Uranium−Dioxide Nanocrystals, J. Am. Chem. Soc., 2006, 128, 16522–16523.

4 T. S. Neill, K. Morris, C. I. Pearce, L. Abrahamsen-Mills, L. Kovarik, S. Kellet, B. Rigby, T. Vitova, B. Schacherl and S. Shaw, Silicate stabilisation of colloidal UO2 produced by uranium metal corrosion, J. Nucl. Mater., 2019, 526, 151751.

5 S. N. Kalmykov and M. A. Denecke, Eds., Actinide Nanoparticle Research, Springer Berlin Heidelberg, Berlin, Heidelberg, 2011.

6 T. M. Nenoff, B. W. Jacobs, D. B. Robinson, P. P. Provencio, J. Huang, S. Ferreira and D. J. Hanson, Synthesis and Low Temperature In Situ Sintering of Uranium Oxide Nanoparticles, Chem. Mater., 2011, 23, 5185–5190.

7 J. R. Bargar, K. H. Williams, K. M. Campbell, P. E. Long, J. E. Stubbs, E. I. Suvorova, J. S. Lezama-Pacheco, D. S. Alessi, M. Stylo, S. M. Webb, J. A. Davis, D. E. Giammar, L. Y. Blue and R. Bernier-Latmani, Uranium redox transition pathways in acetate-amended sediments, Proc. Natl. Acad. Sci., 2013, 110, 4506–4511.

8 E. J. O'Loughlin, S. D. Kelly, R. E. Cook, R. Csencsits and K. M. Kemner, Reduction of Uranium(VI) by Mixed Iron(II)/Iron(III) Hydroxide (Green Rust): Formation of UO2 Nanoparticles, Environ. Sci. Technol., 2003, 37, 721–727.

9 I. Pidchenko, K. O. Kvashnina, T. Yokosawa, N. Finck, S. Bahl, D. Schild, R. Polly, E. Bohnert, A. Rossberg, J. Göttlicher, K. Dardenne, J. Rothe, T. Schäfer, H. Geckeis and T. Vitova, Uranium Redox Transformations after U(VI) Coprecipitation with Magnetite Nanoparticles, Environ. Sci. Technol., 2017, 51, 2217–2225.

10 Z. Pan, B. Bártová, T. LaGrange, S. M. Butorin, N. C. Hyatt, M. C. Stennett, K. O. Kvashnina and R. Bernier-Latmani, Nanoscale mechanism of UO2 formation through uranium reduction by magnetite, Nat. Commun., 2020, 11, 4001.

11 D. M. Singer, F. Farges and G. E. Brown, in AIP Conference Proceedings, AIP, 2007, vol. 882, pp. 277–279.

12 Y. Suzuki, S. D. Kelly, K. M. Kemner and J. F. Banfield, Nanometre-size products of uranium bioreduction, Nature, 2002, 419, 134–134.

13 D. M. Singer, F. Farges and G. E. Brown, Biogenic nanoparticulate UO2: Synthesis, characterization, and factors affecting surface reactivity, Geochim. Cosmochim. Acta, 2009, 73, 3593–3611.

14 M. I. Boyanov, K. E. Fletcher, M. J. Kwon, X. Rui, E. J. O'Loughlin, F. E. Löffler and K. M. Kemner, Solution and Microbial Controls on the Formation of Reduced U(IV) Species, Environ. Sci. Technol., 2011, 45, 8336–8344.

15 L. Newsome, K. Morris and J. R. Lloyd, The biogeochemistry and bioremediation of uranium and other priority radionuclides, Chem. Geol., 2014, 363, 164–184.

16 J. R. Bargar, R. Bernier-Latmani, D. E. Giammar and B. M. Tebo, Biogenic Uraninite Nanoparticles and Their Importance for Uranium Remediation, Elements, 2008, 4, 407–412.

17 L. Newsome, K. Morris, D. Trivedi, N. Atherton and J. R. Lloyd, Microbial reduction of uranium(VI) in sediments of different lithologies collected from Sellafield, Appl. Geochemistry, 2014, 51, 55–64.

18 K.-U. Ulrich, A. Singh, E. J. Schofield, J. R. Bargar, H. Veeramani, J. O. Sharp, R. Bernier-Latmani and D. E. Giammar, Dissolution of Biogenic and Synthetic UO 2 under Varied Reducing Conditions, Environ. Sci. Technol., 2008, 42, 5600–5606.

19 E. L. Fuller, N. R. Smyrl, J. B. Condon and M. H. Eager, Uranium oxidation: Characterization of oxides formed by reaction with water by infrared and sorption analyses, J. Nucl. Mater., 1984, 120, 174–194.

20 M. D. Kaminski, N. M. Dimitrijevic, C. J. Mertz and M. M. Goldberg, Colloids from the aqueous corrosion of uranium nuclear fuel, J. Nucl. Mater., 2005, 347, 77–87.

21 G. Rousseau, M. Fattahi, B. Grambow, F. Boucher and G. Ouvrard, Coprecipitation of thorium with UO2, Radiochim. Acta, 2002, 90, 523-527.

22 T. Fanghänel and V. Neck, Aquatic chemistry and solubility phenomena of actinide oxides/hydroxides, Pure Appl. Chem., 2002, 74, 1895–1907.

23 V. Neck and J. I. Kim, Solubility and hydrolysis of tetravalent actinides, Radiochim. Acta, 2001, 89, 1–16.

24 O. Walter, K. Popa and O. D. Blanco, Hydrothermal decomposition of actinide(IV) oxalates: a new aqueous route towards reactive actinide oxide nanocrystals, Open Chem., 2016, 14, 170-174.

25 P. Liu, X. Luo, M. Wen, J. Zhang, C. Zheng, W. Gao and F. Ouyang, Geoelectrochemical anomaly prospecting for uranium deposits in southeastern China, Appl. Geochemistry, 2018, 97, 226–237.

26 R. M. Hazen, R. C. Ewing and D. A. Sverjensky, Evolution of uranium and thorium minerals, Am. Mineral., 2009, 94, 1293–1311.

27 M. Schindler, A. J. Lussier, J. Bellrose, S. Rouvimov, P. C. Burns and T. K. Kyser, Mobilization and agglomeration of uraninite nanoparticles: A nano-mineralogical study of samples from the Matoush Uranium ore deposit, Am. Mineral., 2017, 102, 1776–1787.

28 S. Fuchs, D. Schumann, A. E. Williams-Jones and H. Vali, The growth and concentration of uranium and titanium minerals in hydrocarbons of the Carbon Leader Reef, Witwatersrand Supergroup, South Africa, Chem. Geol., 2015, 393–394, 55–66.

29 B. Salbu, K. Janssens, O. C. Lind, K. Proost, L. Gijsels and P. R. Danesi, Oxidation states of uranium in depleted uranium particles from Kuwait, J. Environ. Radioact., 2005, 78, 125–135.

30 P. Pöml and B. Burakov, Study of the redistribution of U, Zr, Nb, Tc, Mo, Ru, Fe, Cr, and Ni between oxide and metallic phases in the matrix of a multiphase Chernobyl hot-particle extracted from a soil sample of the Western Plume, Radiochim. Acta, 2018, 106, 985–990.

31 A. Ochiai, J. Imoto, M. Suetake, T. Komiya, G. Furuki, R. Ikehara, S. Yamasaki, G. T. W. Law, T. Ohnuki, B. Grambow, R. C. Ewing and S. Utsunomiya, Uranium Dioxides and Debris Fragments Released to the Environment with Cesium-Rich Microparticles from the Fukushima Daiichi Nuclear Power Plant, Environ. Sci. Technol., 2018, 52, 2586–2594.

32 V. Kashparov, B. Salbu, S. Levchuk, V. Protsak, I. Maloshtan, C. Simonucci, C. Courbet, H. L. Nguyen, N. Sanzharova and V. Zabrotsky, Environmental behaviour of radioactive particles from chernobyl, J. Environ. Radioact., 2019, 208–209, 106025.

33 K. Spahiu, J. Devoy, D. Cui and M. Lundström, The reduction of U(VI) by near field hydrogen in the presence of UO2(s), Radiochim. Acta, 92, 597-601.

34 M. Rovira, S. El Aamrani, L. Duro, J. Giménez, J. de Pablo and J. Bruno, Interaction of uranium with in situ anoxically generated magnetite on steel, J. Hazard. Mater., 2007, 147, 726–731.

35 G. Leinders, J. Pakarinen, R. Delville, T. Cardinaels, K. Binnemans and M. Verwerft, Low-Temperature Oxidation of Fine UO2 Powders: A Process of Nanosized Domain Development, Inorg. Chem., 2016, 55, 3915–3927.

36 S. Szenknect, D. Alby, M. López García, C. Wang, R. Podor, F. Miserque, A. Mesbah, L. Duro, L. Zetterström Evins, N. Dacheux, J. Bruno and R. C. Ewing, Coffinite formation from UO2+x, Sci. Rep., 2020, 10, 12168.

37 S. R. Spurgeon, M. Sassi, C. Ophus, J. E. Stubbs, E. S. Ilton and E. C. Buck, Nanoscale oxygen defect gradients in UO2+x surfaces, Proc. Natl. Acad. Sci., 2019, 116, 17181–17186.

38 J. M. Haschke, T. H. Allen and L. A. Morales, Reaction of Plutonium Dioxide with Water: Formation and Properties of PuO2+x, Science, 2000, 287, 285–287.

39 E. Gerber, A. Y. Romanchuk, I. Pidchenko, L. Amidani, A. Rossberg, C. Hennig, G. B. M. Vaughan, A. Trigub, T. Egorova, S. Bauters, T. Plakhova, M. O. J. Y. Hunault, S. Weiss, S. M. Butorin, A. C. Scheinost, S. N. Kalmykov and K. O. Kvashnina, The missing pieces of the PuO2 nanoparticle puzzle, Nanoscale, 2020, 12, 18039–18048.

40 K. O. Kvashnina, A. Y. Romanchuk, I. Pidchenko, L. Amidani, E. Gerber, A. Trigub, A. Rossberg, S. Weiss, K. Popa, O. Walter, R. Caciuffo, A. C. Scheinost, S. M. Butorin and S. N. Kalmykov, A Novel Metastable Pentavalent Plutonium Solid Phase on the Pathway from Aqueous Plutonium(VI) to PuO2 Nanoparticles, Angew. Chemie - Int. Ed., 2019, 58, 17558–17562.

41 O. N. Batuk, D. V Szabo, M. A. Denecke, T. Vitova and S. N. Kalmykov, Synthesis and characterization of thorium , uranium and cerium oxide nanoparticles, Radiochim. Acta, 2013, 101, 233–239.

42 J.-D. Cafun, K. O. Kvashnina, E. Casals, V. F. Puntes and P. Glatzel, Absence of Ce3+ Sites in Chemically Active Colloidal Ceria Nanoparticles, ACS Nano, 2013, 7, 10726–10732.

43 T. V. Plakhova, A. Y. Romanchuk, S. M. Butorin, A. D. Konyukhova, A. V. Egorov, A. A. Shiryaev, A. E. Baranchikov, P. V. Dorovatovskii, T. Huthwelker, E. Gerber, S. Bauters, M. M. Sozarukova, A. C. Scheinost, V. K. Ivanov, S. N. Kalmykov and K. O. Kvashnina, Towards the surface hydroxyl species in CeO2 nanoparticles, Nanoscale, 2019, 11, 18142–18149.

44 O. N. Batuk, S. N. Kalmykov, V. G. Petrov, E. V. Zakharova, Y. A. Teterin, A. Y. Teterin, V. I. Shapovalov and M. J. Haire, Neptunium interaction with uranium dioxide in aqueous solution, J. Nucl. Mater., 2007, 362, 426–430.

45 M. Wojdyr, Fityk : a general-purpose peak fitting program, J. Appl. Crystallogr., 2010, 43, 1126–1128.

46 J. Rothe, M. Altmaier, R. Dagan, K. Dardenne, D. Fellhauer, X. Gaona, E. G.-R. Corrales, M. Herm, K. O. Kvashnina, V. Metz, I. Pidchenko, D. Schild, T. Vitova and and H. Geckeis, Fifteen Years of Radionuclide Research at the KIT Synchrotron Source in the Context of the Nuclear Waste Disposal Safety Case, Geosciences, 2019, 9, 91.

47 A. Zimina, K. Dardenne, M. A. Denecke, D. E. Doronkin, E. Huttel, H. Lichtenberg, S. Mangold, T. Pruessmann, J. Rothe, T. Spangenberg, R. Steininger, T. Vitova, H. Geckeis and J.-D. Grunwaldt, CAT-ACT—A new highly versatile x-ray spectroscopy beamline for catalysis and radionuclide science at the KIT synchrotron light facility ANKA, Rev. Sci. Instrum., 2017, 88, 113113.

48 M. Borsboom, W. Bras, I. Cerjak, D. Detollenaere, D. Glastra van Loon, P. Goedtkindt, M. Konijnenburg, P. Lassing, Y. K. Levine, B. Munneke, M. Oversluizen, R. van Tol and E. Vlieg, The Dutch–Belgian beamline at the ESRF, J. Synchrotron Radiat., 1998, 5, 518–520.

49 B. Ravel and M. Newville, ATHENA, ARTEMIS, HEPHAESTUS: Data analysis for X-ray absorption spectroscopy using IFEFFIT, J. Synchrotron Radiat., 2005, 12, 537–541.

50 L. Desgranges, G. Baldinozzi, G. Rousseau, J.-C. Nièpce and G. Calvarin, Neutron Diffraction Study of the in Situ Oxidation of UO2, Inorg. Chem., 2009, 48, 7585–7592.

51 D. A. Andersson, G. Baldinozzi, L. Desgranges, D. R. Conradson and S. D. Conradson, Density Functional Theory Calculations of UO2 Oxidation: Evolution of UO2+x , U4O9–y , U3O7, and U3O8, Inorg. Chem., 2013, 52, 2769–2778.

52 S. Hasan and T. K. Ghosh, Synthesis of Uranium Oxide Nanoparticles in Aqueous Solutions, Nucl. Technol., 2011, 173, 310–317.

53 Y. Wang, Q. Chen and X. Shen, Preparation of low-temperature sintered UO2 nanomaterials by radiolytic reduction of ammonium uranyl tricarbonate, J. Nucl. Mater., 2016, 479, 162–166.

54 M. C. Rath, S. Keny and D. B. Naik, Direct Synthesis of UO2 Nanoparticles in Aqueous Solutions Through Photochemical Method, J. Nanosci. Nanotechnol., 2016, 16, 9575–9582.

55 S. Hu, H. Li, H. Liu, P. He and X. Wang, Nanocrystals of Uranium Oxide: Controlled Synthesis and Enhanced Electrochemical Performance of Hydrogen Evolution by Ce Doping, Small, 2015, 11, 2624–2630.

56 A. Leticia Soldati, D. Carolina Lago and M. Oscar Prado, in Nuclear Materials, IntechOpen, 2020.

57 A. J. Popel, B. T. Tan, T. Gouder, G. I. Lampronti, J. Day, R. Eloirdi, A. Seibert and I. Farnan, Surface alteration evidence for a mechanism of anoxic dissolution of UO2, Appl. Surf. Sci., 2019, 464, 376–379.

58 L. Balice, D. Bouëxière, M. Cologna, A. Cambriani, J. Vigier, E. De Bona, G. Domenico, C. Kübel, O. Walter and K. Popa, Nano and micro U1-xThxO2 solid solutions : From powders to pellets, J. Nucl. Mater., 2018, 498, 307–313.

59 N. P. Martin, C. Volkringer, N. Henry, X. Trivelli, G. Stoclet, A. Ikeda-Ohno and T. Loiseau, Formation of a new type of uranium poly-oxo cluster {U 38 } based on a controlled release of water via esterification reaction, Chem. Sci., 2018, 9, 5021–5032.

60 M. C. Rath, D. B. Naik and S. K. Sarkar, Reversible growth of UO2 nanoparticles in aqueous solutions through 7MeV electron beam irradiation, J. Nucl. Mater., 2013, 438, 26–31.

61 D. Hudry, C. Apostolidis, O. Walter, T. Gouder, E. Courtois, C. Kübel and D. Meyer, Non-aqueous Synthesis of Isotropic and Anisotropic Actinide Oxide Nanocrystals, Chem. - A Eur. J., 2012, 18, 8283–8287.

62 D. Hudry, C. Apostolidis, O. Walter, T. Gouder, E. Courtois, C. Kübel and D. Meyer, Controlled Synthesis of Thorium and Uranium Oxide Nanocrystals, Chem. - A Eur. J., 2013, 19, 5297–5305.

63 L. M. Moreau, A. Herve, M. D. Straub, D. R. Russo, R. J. Abergel, S. Alayoglu, J. Arnold, A. Braun, G. J. P. Deblonde, Y. Liu, T. D. Lohrey, D. T. Olive, Y. Qiao, J. A. Rees, D. K. Shuh, S. J. Teat, C. H. Booth and S. G. Minasian, Structural properties of ultra-small thorium and uranium dioxide nanoparticles embedded in a covalent organic framework, Chem. Sci., 2020, 11, 4648–4668.

64 D. L. Clark, M. P. Neu, W. Runde and D. W. Keogh, in Kirk-Othmer Encyclopedia of Chemical Technology, John Wiley & Sons, Inc., Hoboken, NJ, USA, 2006.

65 T. Gouder, R. Eloirdi and R. Caciuffo, Direct observation of pure pentavalent uranium in U2O5 thin films by high resolution photoemission spectroscopy, Sci. Rep., 2018, 8, 8306.

66 K. O. Kvashnina, S. M. Butorin, P. Martin and P. Glatzel, Chemical State of Complex Uranium Oxides, Phys. Rev. Lett., 2013, 111, 253002.

67 G. Leinders, R. Bes, J. Pakarinen, K. Kvashnina and M. Verwerft, Evolution of the Uranium Chemical State in Mixed-Valence Oxides, Inorg. Chem., 2017, 56, 6784–6787.

68 G. Leinders, R. Bes, K. O. Kvashnina and M. Verwerft, Local Structure in U(IV) and U(V) Environments: The Case of U3O7, Inorg. Chem., 2020, 59, 4576–4587.

69 L. Desfougeres, É. Welcomme, M. Ollivier, P. M. Martin, J. Hennuyer, M. O. J. Y. Hunault, R. Podor, N. Clavier and L. Favergeon, Oxidation as an Early Stage in the Multistep Thermal Decomposition of Uranium(IV) Oxalate into U3O8, Inorg. Chem., 2020, 59, 8589–8602.

70 S. D. Conradson, D. Manara, F. Wastin, D. L. Clark, G. H. Lander, L. A. Morales, J. Rebizant and V. V. Rondinella, Local Structure and Charge Distribution in the UO2 −U4O9 System, Inorg. Chem., 2004, 43, 6922–6935.

71 J. C. Renshaw, L. J. C. Butchins, F. R. Livens, I. May, J. M. Charnock and J. R. Lloyd, Bioreduction of Uranium: Environmental Implications of a Pentavalent Intermediate, Environ. Sci. Technol., 2005, 39, 5657–5660.

72 L. Amidani, T. V. Plakhova, A. Y. Romanchuk, E. Gerber, S. Weiss, A. Efimenko, C. J. Sahle, S. M. Butorin, S. N. Kalmykov and K. O. Kvashnina, Understanding the size effects on the electronic structure of ThO2 nanoparticles, Phys. Chem. Chem. Phys., 2019, 21, 10635–10643.

73 R. Husar, R. Hübner, C. Hennig, P. M. Martin, M. Chollet, S. Weiss, T. Stumpf, H. Zänker and A. Ikeda-Ohno, Intrinsic formation of nanocrystalline neptunium dioxide under neutral aqueous conditions relevant to deep geological repositories, Chem. Commun., 2015, 51, 1301–1304.

74 A. Y. Romanchuk, T. V Plakhova, A. V Egorov, T. B. Egorova, P. V Dorovatovskii and Y. V Zubavichus, Redox-mediated formation of plutonium oxide nanoparticles, Dalt. Trans., 2018, 47, 11239–11244.

75 H. Geckeis, B. Grambow, A. Loida, B. Luckscheiter, E. Smailos and J. Quinones, Formation and Stability of Colloids under Simulated Near Field Conditions, Radiochim. Acta, 1998, 82, 123-128.

76 H. Zänker and C. Hennig, Colloid-borne forms of tetravalent actinides: A brief review, J. Contam. Hydrol., 2014, 157, 87–105.

Supplementary information of Article 2

Experimental

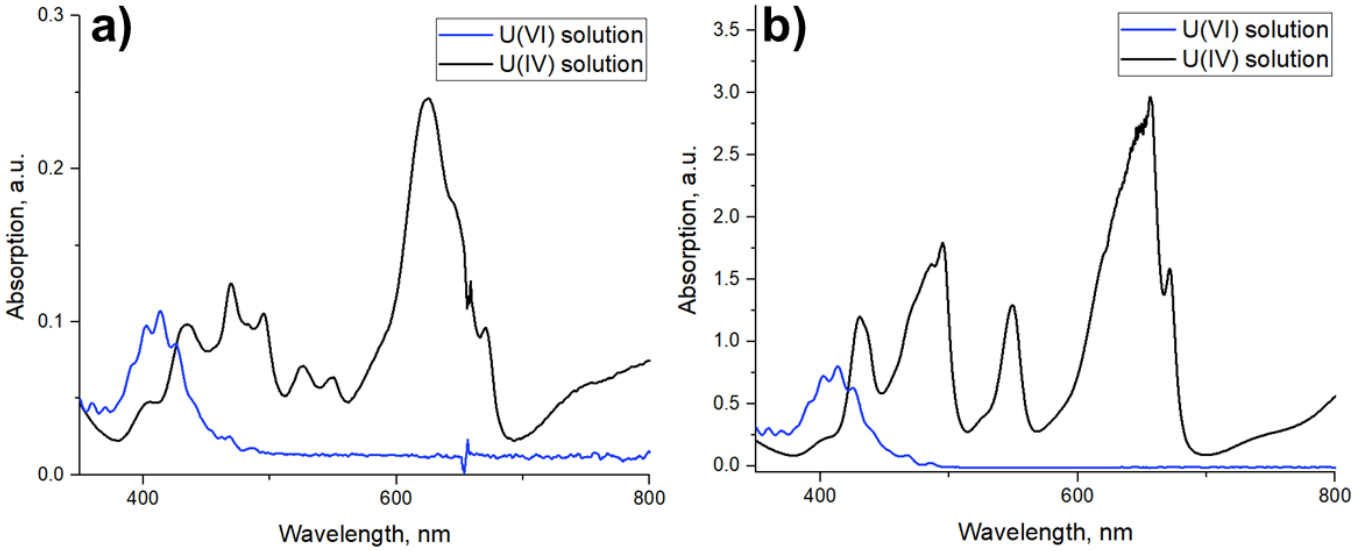

Fig. S1. UV-vis spectra of uranium solutions in $HClO_4$ before and after reduction, a) 0.01M U in 0.05M $HClO_4$, b) 0.1M U in 0.5M $HClO_4$.

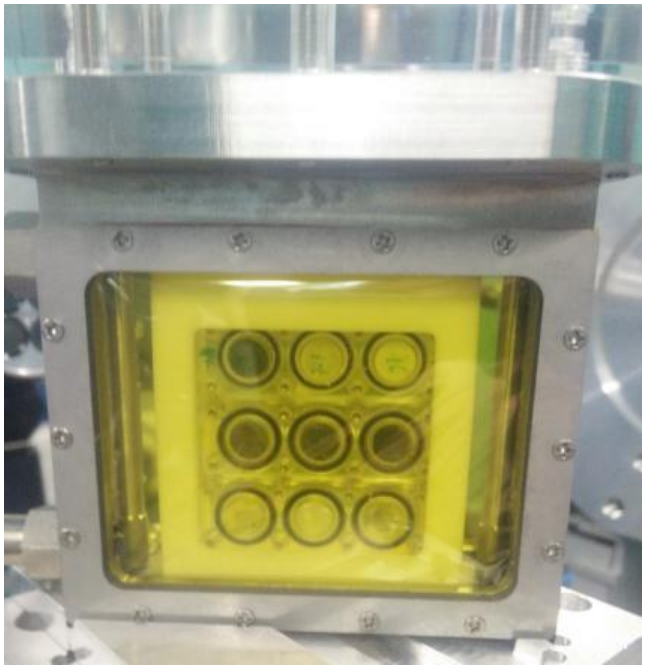

Fig. S1. Photo of the sample cell, including triple holders.

Table S1. pH and Eh values after the end of the reactions.

Sample	**pH**	**Eh, mV**
0.01 M U(IV) pH 8	8.0	-272

0.01 M U(IV) pH >11	11.6	-287
0.1 M U(IV) pH 8	8.0	-84
0.1 M U(IV) pH >11	10.9	-482

Results

Sample characterisation

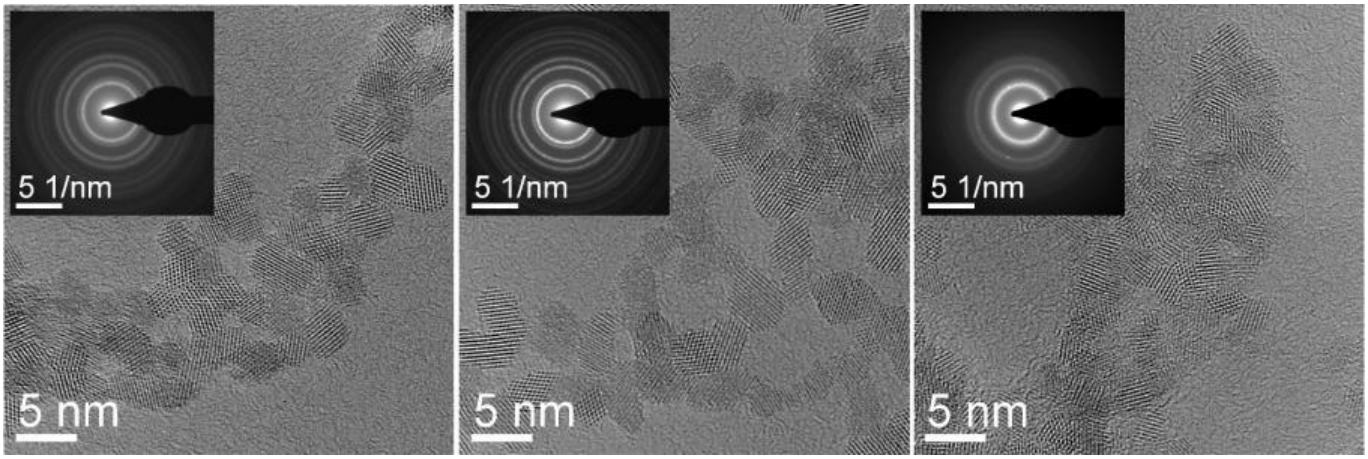

Fig. S2. **HRTEM images of NPs and corresponding SAED patterns (inset)**: a) 0.01M U(IV) pH >11, b) 0.1M U(IV) pH 8, c) 0.1M U(IV) pH >11.

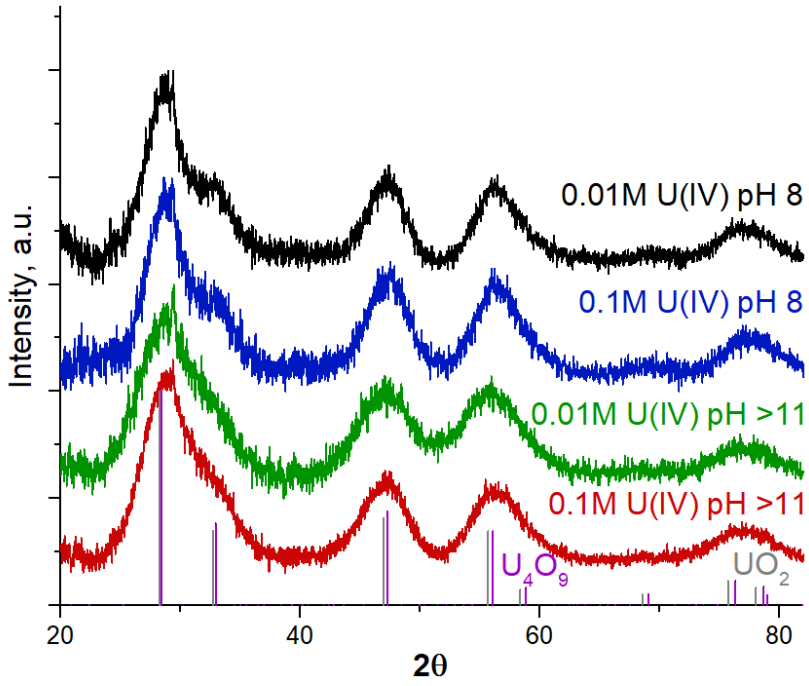

Fig. S3. XRD patterns of the precipitates from U(IV) with different pH and concentrations, UO_2 and U_4O_9 references.

Table S2. Particle size estimation of the samples by XRD.

Sample	Size, nm (XRD)	Size, nm (HRTEM)
0.01 M U(IV) pH 8	2.5±0.6	2.7±0.8
0.01 M U(IV) pH >11	1.7 (one peak)	3.1±0.7
0.1 M U(IV) pH 8	2.5±0.5	3.8±0.9
0.1 M U(IV) pH >11	1.8±0.3	2.7±0.8
0.1 M U(IV) pH 8 aged	6.0±0.2	
0.1 M U(IV) pH >11 aged	4.8±0.1	

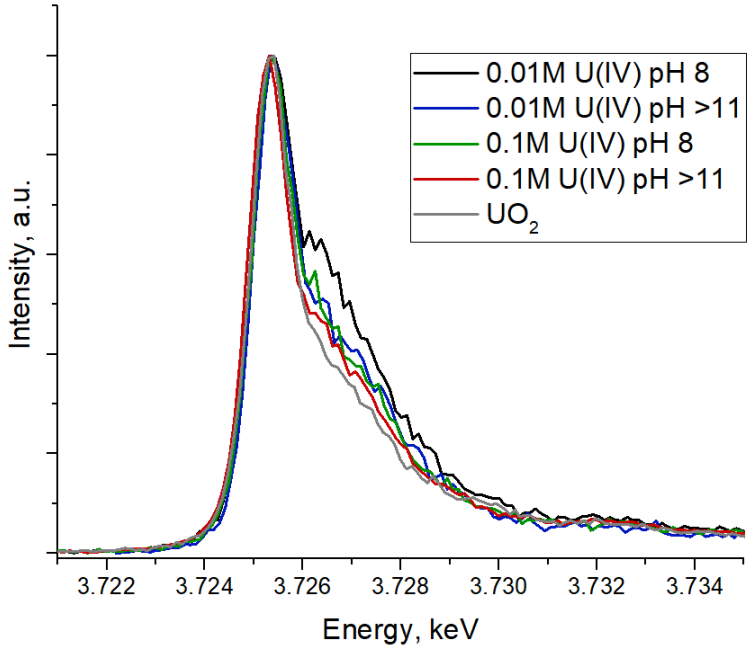

Fig. S4. **U M_4 HERFD experimental data.** The increase of the peak asymmetry is notable.

Calculations of HERFD spectra:

The calculations of the U(IV) M_4 HERFD spectra were performed using crystal field theory. To obtain the HERFD spectra, the core-to core (3d-4f) resonant inelastic x-ray scattering (RIXS) intensity maps were calculated on the emission versus incident photon energy scales and a cut at the constant emission energy, corresponding to the maximum of the RIXS intensity was made along the incident photon energy axis. The RIXS maps were calculated in a manner described in literature[1,2] by taking into account the full multiplet structure due to intra-atomic and crystal field interactions. The Slater integrals $F^k(5f,5f)$, $F^k(3d,5f)$, $F^k(4f,5f)$ as well as $G^k(3d,5f)$ and $G^k(4f,5f)$ calculated for the U(IV) ion were scaled down to 80 % of their *ab-initio* Hartree-Fock values. The ground, intermediate and final states of the spectroscopic process were represented by the $3d^{10}5f^2$, $3d^95f^3$ and $4f^{13}5f^3$ configurations, respectively. To simulate different U(IV) environment in terms of varying U coordination number (CN), the calculations were done in tetrahedral (T_d), octahedral (O_h^6), cubic (O_h^8) and icosahedral (I_h) symmetry for CN equal to 5, 6, 8 and 12, respectively. The Wybourne's crystal field parameters in the calculations were set to Td: B^4_0 = -0.30 eV, B^6_0 = -0.70 eV; O_h^6: B^4_0 = 0.93 eV, B^6_0 = 0.35 eV; O_h^8: B^4_0 =- 0.93 eV, B^6_0 = 0.35 eV; I_h: B^6_0 =

0.65 (-0.65) eV. For I_h symmetry both positive and negative values of the B^6_0 parameter were used which produce different results. The abovementioned choice of values was based on already established values for UO_2[3] and relative changes of parameter values for different symmetries discussed in literature.[4,5]

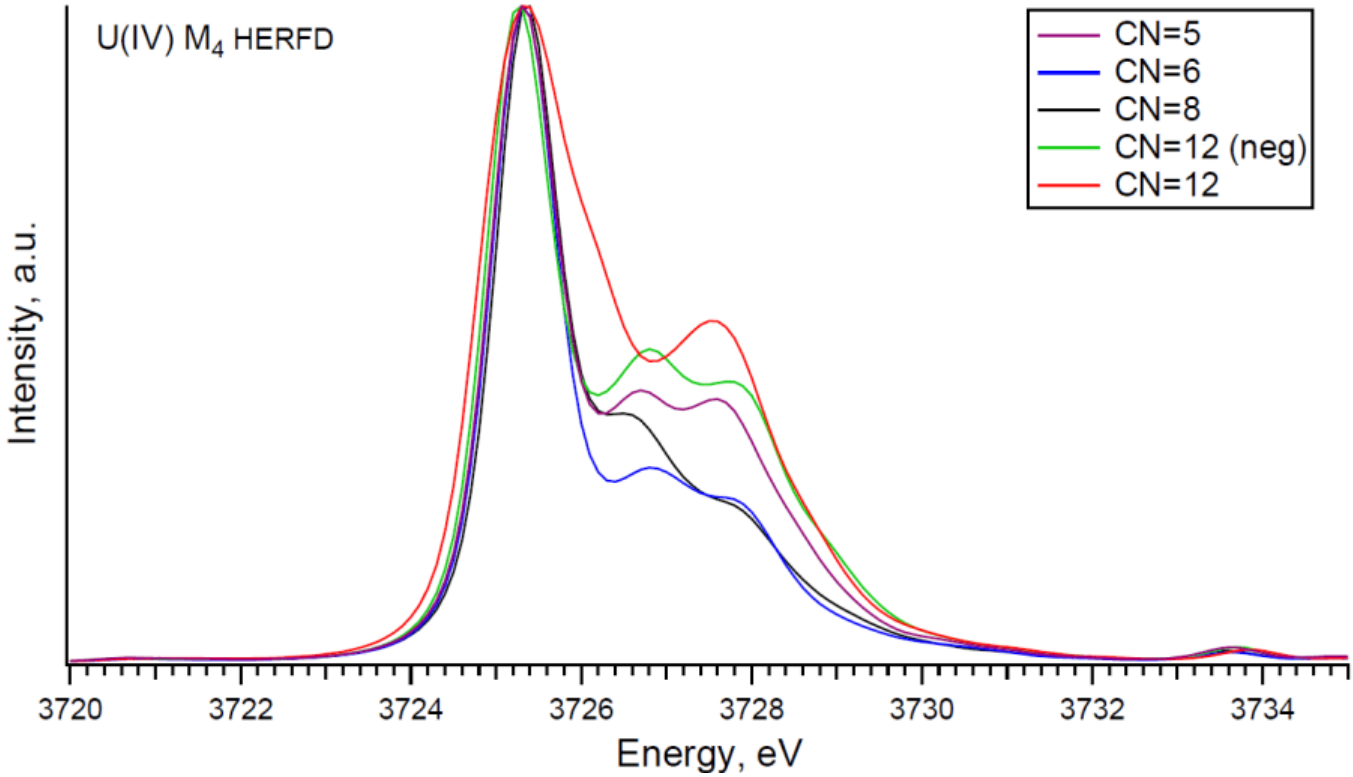

Fig. S5. M_4 HERFD spectra calculated for the U(IV) ion in environments with different coordination number (CN).

EXAFS results:

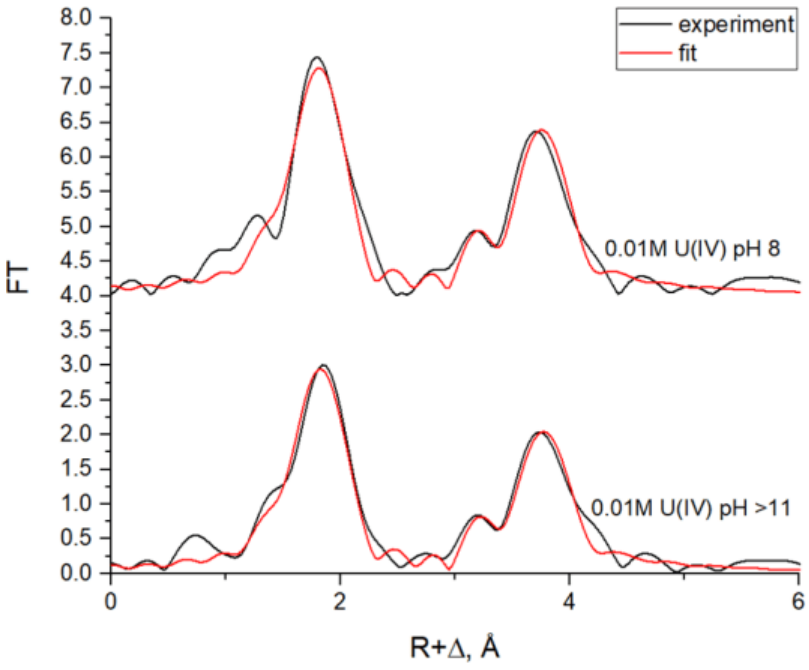

Fig. S6. **U L_3-EXAFS results.** a) U L_3-EXAFS spectra χ(R) fit results, Fourier transform (FT) magnitude of experimental EXAFS data (black) and shell fit (red) with U-O, U-U shells.

Table S3. Metric parameters extracted by least-squares fit analysis of U L_3 EXAFS spectra with U-O, U-U shells, (k range of 2.0-11.5 $Å^{-1}$).

Sample	**First coordination shell**			**Second coordination shell**			**ΔE_0 [eV]**	**R-factor, %**
	CN	**R [Å]**	**σ^2 [$Å^2$]**	**CN**	**R [Å]**	**σ^2 [$Å^2$]**		
0.01M U(IV) pH 8	4.9(0.6) O	2.33(0.01)	0.011	3.6(1.0) U	3.855(0.008)	0.005	5.9	3.1
0.01M U(IV) pH >11	4.2 O (0.5)	2.33(0.01)	0.011	2.9 U(0.8)	3.861(0.007)	0.004	7.0	2.6
UO_2 structure	8 O	2.3677		12 U	3.8665 U			

Reactivity of the NPs

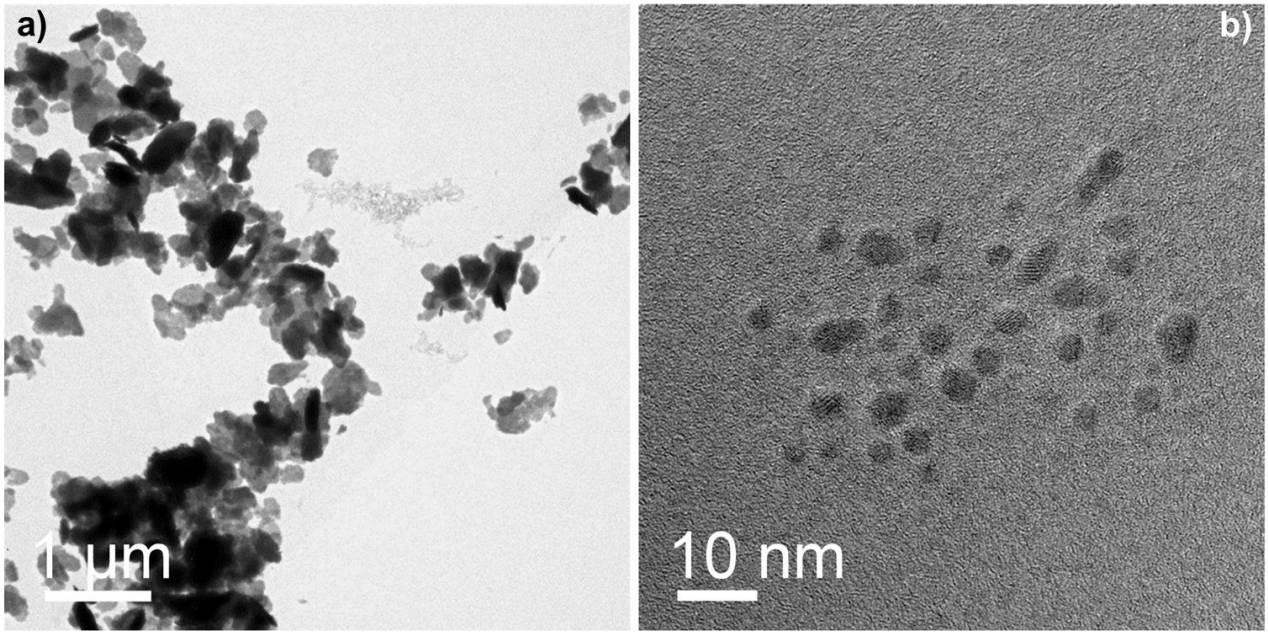

Fig. S7. a) Overview bright-field TEM image b) HRTEM image of the one-year-old 0.1 M U(IV) pH >11 sample.

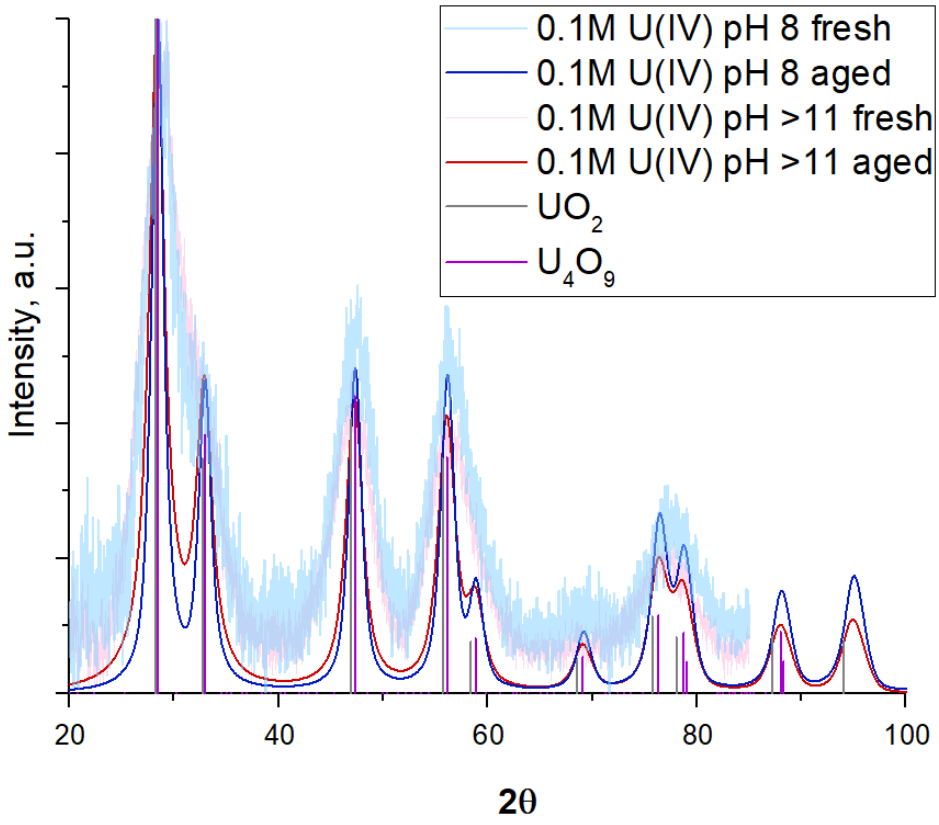

Fig. S8. X-ray diffraction patterns measured from fresh and 1-year old samples.

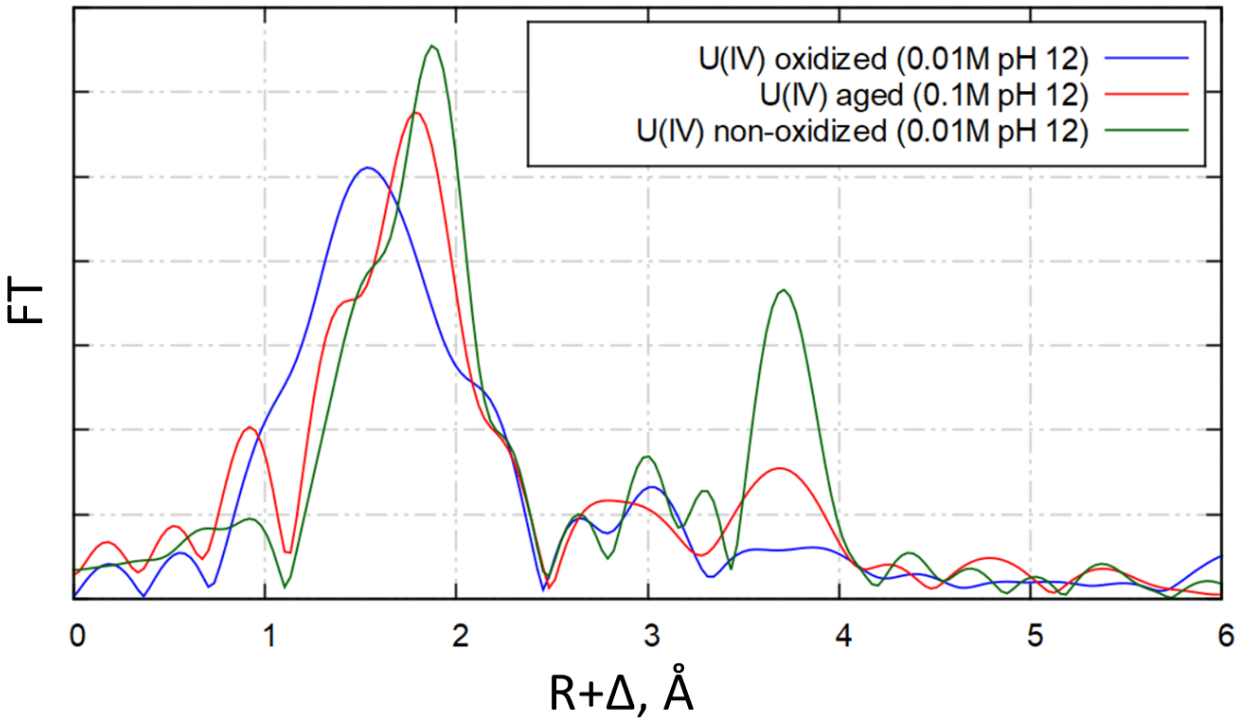

Fig. S9. U L_3-EXAFS spectra, Fourier transform (FT) magnitude of experimental EXAFS data.

References:

1 S. M. Butorin, K. O. Kvashnina, A. L. Smith, K. Popa and P. M. Martin, Crystal-Field and Covalency Effects in Uranates : An X-ray Spectroscopic Study, Chem. Eur. J., 2016, 22, 9693–9698.

2 S. M. Butorin, K. O. Kvashnina, J. R. Vegelius, D. Meyer and D. K. Shuh, High-resolution X-ray absorption spectroscopy as a probe of crystal-field and covalency effects in actinide compounds, Proc. Natl. Acad. Sci., 2016, 113, 8093–8097.

3 S. M. Butorin, A. Modin, J. R. Vegelius, K. O. Kvashnina and D. K. Shuh, Probing Chemical Bonding in Uranium Dioxide by Means of High- Resolution X-ray Absorption Spectroscopy, J. Phys. Chem. C, 2016, 120, 29397–29404.

4 N. Edelstein, Optical and magnetic properties of tetravalent actinide ions and compounds, J. Less Common Met., 1987, 133, 39–51.

5 J. C. Krupa, Spectroscopic properties of tetravalent actinide ions in solids, Inorganica Chim. Acta, 1987, 139, 223–241.

Appendix C: Article 3. To form or not to form : PuO_2 nanoparticles at acidic pH

Evgeny Gerber[a,b,c*], Anna Yu. Romanchuk[a], Stephan Weiss[c], Anastasiia Kuzenkova[a], Myrtille Hynault[d], Stephen Bauters[b,c], Alexander Egorov[a], Sergei M. Butorin[e], Stepan N. Kalmykov[a] and Kristina O. Kvashnina[a,b,c]

[a] *Lomonosov Moscow State University, Department of Chemistry, 119991 Moscow, Russia.*

[b] *The Rossendorf Beamline at ESRF – The European Synchrotron, CS40220, 38043 Grenoble Cedex 9, France.*

[c] *Helmholtz Zentrum Dresden-Rossendorf (HZDR), Institute of Resource Ecology, PO Box 510119, 01314 Dresden, Germany.*

[d] *Synchrotron SOLEIL, L'Orme des Merisiers, Saint Aubin BP 48, 91192 Gif-sur-Yvette, France*

[e] *Molecular and Condensed Matter Physics, Department of Physics and Astronomy, Uppsala University, P.O. Box 516, Uppsala, Sweden*

Introduction

Plutonium (Pu) is undoubtedly one of the most puzzling elements of the periodic table. The ease of redox transformations between various oxidations states is the most prominent peculiarity of its chemical complexity. Being one of the primary nuclear waste components in terms of radiotoxicity, Pu draws attention not only from a fundamental point of view, but also from environmental applied science. The pH of acidic soils can be lower than 5 and high-level waste from the reprocessing of spent nuclear fuel is also highly acidic.[1,2] PuO_2 NPs are part of the crucial Pu species in terms of its environmental behaviour. Despite the fact that PuO_2 solubility is extremely low, Pu has been shown to migrate with mineral[3,4] or organic colloids,[5] therefore, colloid-facilitated transport might play an important role in the transporting of plutonium.[6] Recently, it has been repeatedly found that PuO_{2+x} NPs are formed during interfacial processes between Pu in different initial oxidation states and various mineral surfaces (hematite, goethite, quartz, and mica) [7–11] and bacteria.[12,13]

For any processes involving Pu, its solubility should be taken into consideration. Pu(IV) is extremely prone to hydrolysis which is accompanied by the formation of mono- and oligomeric species. While the solubility of Pu in neutral and alkaline conditions is known to be exceedingly low,[14,15] the Pu concentration in solution significantly increases in acidic conditions. Redox potential and pH are decisive solution parameters for the solubility and oxidation state distribution of Pu.[16] Pérez-Bustamante[17] and Rai with coworkers[18] have found that Pu(IV) solubility increases due to the aqueous species of other Pu oxidation states arising from Pu(IV) oxidation and disproportionation reactions. Kim[19] has detected that Pu(IV) colloids formation may interfere even at pH 0-1, though Knopp[16] has reported that most colloids can be successfully separated with 1 nm –filters. However, extremely small and stable Pu NPs can still be present in the solution and affect solubility and redox processes.

The presence of very small Pu colloids or polynuclear species can lead to enhancement of apparent solubility by up to 2 orders of magnitude, depending on pH. Moreover, it is suggested that Pu(IV) colloids and polymers are in equilibrium with Pu(IV) and Pu(V) and take part in the Pu(IV) to Pu(V) oxidation with its following disproportionation.[20,21] These polymers might be also responsible for the equilibration between the Pu(III)/Pu(IV) and Pu(V)/Pu(VI) plutonyl species.[20] The composition of these colloids and polymers are investigated by nano-electrospray time-of-flight mass-spectrometry (ESI-TOF-MS)[20], laser-induced breakdown detection (LIBD)[20,22] and EXAFS spectroscopy[20,22,23]. The presence of oxo-hydroxo polymers as well as presence of Pu(III) and Pu(V) is claimed and different mechanisms responsible for these processes are considered.[20,22–27] We have recently investigated PuO_2 NPs under other conditions (at pH 8 and pH > 10) with a synchrotron based method - HERFD, which allows for the determination of different oxidation state impurities with a high precision.[26] We have found out that Pu(IV) is the dominating oxidation state for all investigated NPs, synthesized under environmentally relevant and waste storage conditions. The aim of this study is to determine if analogous PuO_2 NPs form under acidic conditions and to investigate Pu oxidation states in NPs. It is also crucial for colloid investigation to determine the oxidation state distribution both in the solid phase and in the solution, and methods used for this task should be sensitive enough to small impurities of other oxidation states aside from Pu(IV).

Here we report a first investigation of PuO_2 NPs, synthesized under various pH from 1 to 4 and characterized by high-resolution transmission electron microscopy (HRTEM), selected-area electron diffraction (SAED) and X-ray absorption near edge structure (XANES) in high energy resolution fluorescence detection (HERFD) mode at the Pu M_4 edge.

Experimental

Synthetic procedures

Initial Pu(IV) solution is obtained from Pu(III) solution by oxidation with $NaNO_2$ in 5M HNO_3 and verified with UV-vis spectrometry (TIDAS 100 J&M Analytics and UV-800, Shimadzu, see Fig. S1). The pH of Pu(IV) precursor is lower than 1 due to the acid presence, therefore, to obtain NPs at pH 1, 2 and 4, ammonia aqueous solution is added under continuous stirring to the aliquots of Pu(IV). The total concentration of Pu in the solution is $0.5 \cdot 10^{-3}$-$1 \cdot 10^{-3}$ M for pH 1 and $0.1 \cdot 10^{-3}$ M for pH 2 - 4. The samples are called “Pu(IV) pH X”, where X is the corresponding pH.

After 2 hours of synthesis the pH and redox potential is measured with pH- and Eh-electrodes (Mettler Toledo), measured values are listed in Table S1.

Solution composition is investigated with UV-vis spectrometry, spectra are registered from 400 to 900 nm. Kinetics of the precipitation is studied as follows: an aliquot of the mixture is centrifuged (31500g, 15 min, Allegra 64R, Beckman Coulter) and the Pu in the supernatant is determined with liquid scintillation counting (LSC, TriCarb 2700TR, Canberra Packard Ind.)

For HERFD measurements a residue is centrifuged after 2h of reaction (3,900 g, EBA 12 (Hettich), 30 min – 2 h). Concentrated samples are not washed from initial solution to preserve the pH and are afterwards packed in special holders in the form of wet pastes.

PuO2 is a commercial sample (Batch I.D. No. Pu-242-327A1, Oak Ridge National Laboratory, USA). To prepare PuF_3 reference, the initial Pu(III) solution was prepared from Pu stock solution by reduction with hydroxylamine hydrochloride when slightly heated in 1 M $HClO_4$ (Fig. S1). Then

fivefold excess of the hydrofluoric acid HF is added to $5 \cdot 10^{-3}$ M Pu(III) solution to precipitate PuF_3. PuF_4 was prepared by adding fivefold excess of the hydrofluoric acid HF to $2 \cdot 10^{-3}$ M Pu(IV) solution.

HRTEM measurements

The HRTEM images on a set of samples are recorded with an aberration-corrected JEOL 2100F operated at 200 kV, yielding an information limit of 0.8 Å. The dark field (DF) images and energy-dispersive X-ray spectroscopy (EDX) analysis are performed in scanning transmission electron microscope (STEM) mode; the spot size is 1 nm with the HAADF and JED 2300 (JEOL) detectors.

X-ray absorption near edge structure (XANES) in high energy resolution fluorescence detection (HERFD) mode at the Pu M_4 edge

The HERFD spectra are collected at the MARS Beamline at SOLEIL using the [111] reflection from a double SI crystal monochromator. The Pu M_β emission line is selected using one spherically bent Si crystal analyser (with 1m bending radius) with [220] reflection.

Theoretical simulations:

To obtain the HERFD spectra at the Pu M_4 edge, the core-to-core (3d-4f) resonant inelastic x-ray scattering (RIXS) intensity maps were calculated on the emission versus incident photon energy scales and a cut at the constant emission energy, corresponding to the maximum of the RIXS intensity was made along the incident photon energy axis. The RIXS maps were calculated as described.[28] For PuF_3 and PuF_4, the crystal field multiplet theory approach was used because the charge-transfer effects, as a result of the Pu 5f – F 2p hybridization, do not contribute significantly to the HERFD spectra due to a large band gap and consequently a large value for the charge-transfer energy. The Slater integrals $F^{2,4,6}$ (5f,5f), $F^{2,4}$ (3d,5f), $F^{2,4,6}$ (4f,5f) as well as $G^{1,3,5}$ (3d,5f) and $G^{0,2,4,6}$ (4f,5f) calculated for the Pu(III) and Pu(IV) ions were scaled down to 80 % of their ab-initio Hartree-Fock values in the computation of the RIXS maps. For PuF_3, the values of Wybourne's crystal field parameters for D_{3h} symmetry were adopted[29] and were set to B^2_0= 0.024, B^4_0= -0.073, B^6_0= -0.214, B^6_6= 0.125 in eV. For PuF_4, the values of the crystal-field parameters for C_{2v} symmetry were set to B^2_0= 0.140, B^2_2= 0.006, B^4_0= -0.350, B^4_2= 0.383, B^4_4= -0.444, B^6_0= -0.177, B^6_2= 0.157, B^6_4= -0.142, B^6_6= 0.226 in eV, as derived from the analysis of the optical absorption spectra.[30] The ground, intermediate and final states of the spectroscopic process were represented by the $3d^{10}5f^n$, $3d^95f^{n+1}$ and $4f^{13}5f^{n+1}$ configurations, respectively, where n=5 for Pu(III) and n=4 for Pu(IV).

Since the inclusion of the charge-transfer effects is important for the description of the high-energy spectroscopic data of PuO_2, (see e.g.[31]), the Pu 3d-to-4f RIXS map was calculated in the framework of the Anderson impurity model (AIM).[32] The model parameter values were chosen to be the same as in previous calculations[33] and their values were as follows: energy for the electron transfer from the O 2p band to the unoccupied Pu 5f states Δ=0.8 eV; 5f-5f Coulomb interaction U_{ff}=5.7 eV; 3d(4f) core hole potential acting on the 5f electron U_{fc}=6.5(6.0) eV and Pu 5f – O 2p hybridization term V=1.1 eV (0.9 eV) in the ground (intermediate and final) state of the spectroscopic process. A linear combination of the $4f^4$ and $4f^5\underline{\upsilon}^1$ configurations was used to describe the ground state of the spectroscopic process and intermediate (final) state was represented by a combination of $3d^94f^5$ and $3d^94f^6\underline{\upsilon}^1$ ($4f^{13}4f^5$ and $4f^{13}4f^6\underline{\upsilon}^1$), where $\underline{\upsilon}$ stands for an electronic hole in the O 2p band. The values of the Slater integrals obtained for Pu(IV) using

the Hartree-Fock formalism were scaled down to 80% to account for the solid state effect. Wybourne's crystal field parameters for cubic symmetry were set to B^4_0=-0.93 eV and B^6_0=0.35 eV.

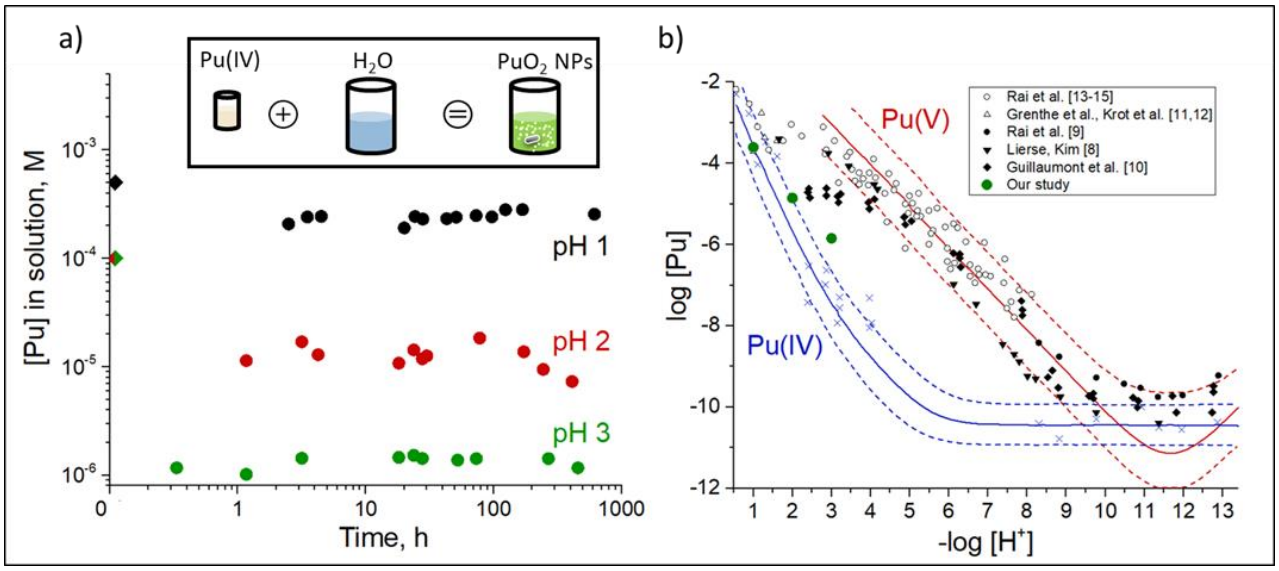

Fig. 1. a) Pu concentration in solution (supernatants after centrifugation) during the PuO_2 synthesis at different pH. The rhombuses at 0 h are the initial Pu concentrations. Inset: the scheme of the synthetic route, b) Solubility of PuO_2 at 20–25 oC as a function of $[H^+]$ in the presence of oxygen compared to the Pu(IV) and Pu(V) solubility data and literature data.[29]

Results and discussion

We have recently studied the formation of PuO_2 NPs at pH 8 and >10 and we have used the total Pu concentration $6 \cdot 10^{-5}$ M, which exceeds its solubility in line with the available thermodynamic prediction.[15,26,34] Thinking about acidic conditions, it turns out that a precipitate cannot form considering this concentration at pH<4, according to available Pu solubility data (Fig. 1b).[34] Therefore we have decided to use $1 \cdot 10^{-4}$ M Pu concentration. According to thermodynamic information, this concentration is still not sufficient for Pu precipitation; nevertheless, we have achieved a precipitate at pH 4 and even pH 2 (which is remarkable). An even higher Pu concentration of $1 \cdot 10^{-3}$ M is used to obtain PuO_2 NPs at pH 1. The instant decrease of the Pu solution concentration unequivocally confirms that precipitate forms during the first minutes of the reaction; simultaneously Pu concentration of the solution is established at a certain level (Fig. 1a). Steady-state concentration of Pu in solution is influenced by pH and correlated with the solubility control of the NP formation process. It is known, that Pu solubility decreases with the increase of pH [14,15,18] and our results perfectly reproduce this trend, however, the absolute values of the Pu concentration are not consistent with previous results (Fig. 1b). Regardless of this disparity, it is quite surprising that NPs are still formed even at pH 1.

First we investigated structural and electronic properties of the formed PuO_2 NPs with HRTEM and HERFD methods.

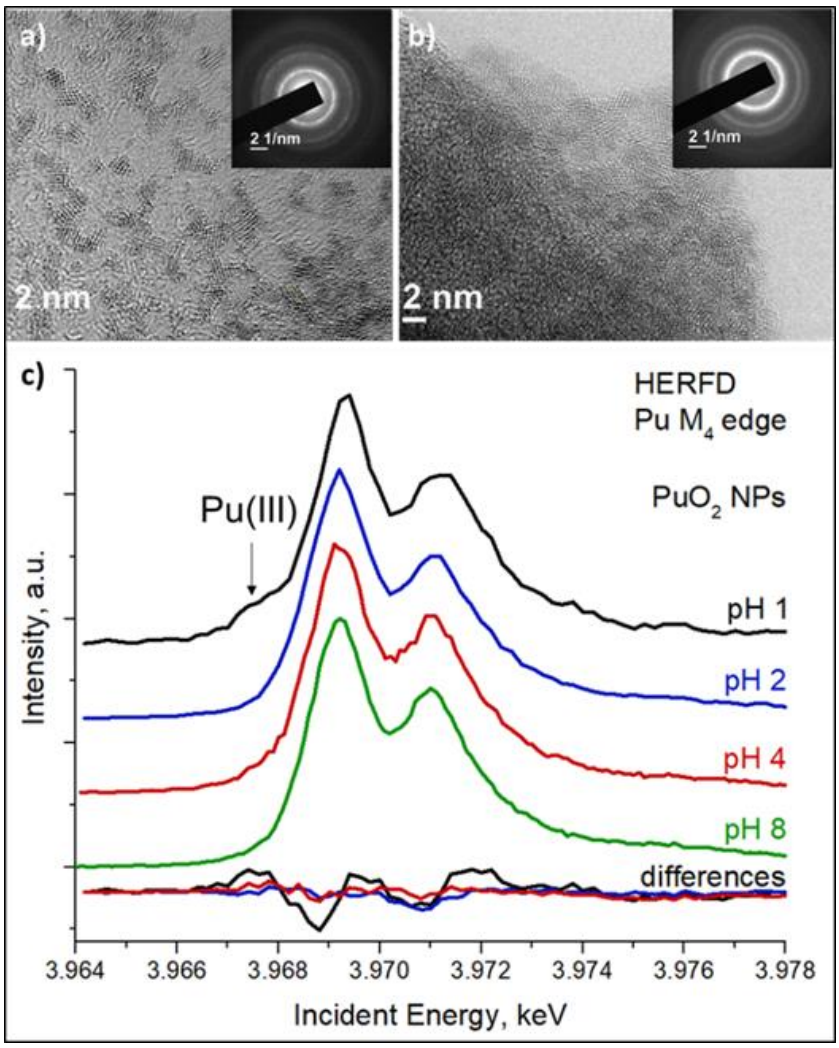

Fig. 2. Solid phase characterisation: a) HRTEM images of NPs from Pu(IV) pH 1, b) pH 2. Inset: corresponding SAED patterns, c) Pu M_4 HERFD experimental data from NPs samples. Difference curves between samples and reference "Pu (IV) from pH 8" are shown below.[26]

The HRTEM data reveals that, regardless of pH conditions, small crystalline nanoparticles are formed with an average particle size of 2 nm, as reported in Fig. 2a-b. A comparison of the selected area electron diffraction (SAED, Fig. 2a-b insets) with bulk PuO2 show that the crystalline structure of the NPs is similar to bulk PuO_2. Thus, we conclude that NPs formed during fast chemical precipitation from Pu aqueous solutions are the same for acidic and alkaline pH conditions, i.e. 2 nm crystalline NPs with structure similar to bulk PuO_2. However, at pH 1 particles are less agglomerated – one can see separated particles in the HRTEM's grid (Fig. 2a), while for pH 2 sample (Fig. 2b) and pH 8 and >10 they are mainly presented as agglomerates (Fig. S2).[26]

HERFD method also shows in Fig. 2c resemblance among the three investigated PuO_2 NP samples, formed at pH 1, 2 and 4. HERFD method at the Pu M_4 edge is a highly effective method of oxidation state identification, spectra recorded on plutonium systems can be straightforwardly analysed by a fingerprint approach.[26,33,35] They are compared to the spectrum of PuO_2 NPs obtained from Pu(IV) at pH 8, which was confirmed to have a PuO_2-like structure and therefore is used as reference in this study together with bulk PuO_2 spectrum.[26] Inspection of Fig. 2c shows that all spectral features are very similar, corresponding to those of the reference, though for Pu(IV) pH 1 peaks are broader and there is a shoulder on the left side from the main edge (at

3.967 keV). This low energy shoulder in X-ray spectroscopy process is generally attributed to a change towards lower oxidation state, and could indicate the presence of Pu(III) in this case. The peak broadening of the absorption feature at the 3971.5 eV indicates the presence of higher oxidation states (Pu(VI), most likely). At the same time the main edge transitions are identical to the Pu(IV), which allows us to suggest that PuO_2 NPs formed at the pH 1 contain the mixture of the Pu(III), Pu(VI) and Pu(IV) oxidation states. It should be noted that even well-known Pu(III) compounds have never been studied before by the HERFD at the Pu M_4 edge.

As such, we have recorded experimental data on the PuF_3 reference to verify the position and the shape of the HERFD features at the Pu M_4 edge (Fig. 3). Surprisingly, two intense peaks at 3.967 keV and 3.969 keV in the Pu M_4 HERFD are detected, which might indicate the presence of the Pu(III) and Pu(IV) oxidation states. However, the theoretical simulations based on the single Anderson impurity model shows that both intense peaks are associated with Pu 3d-5f transitions for the Pu(III) oxidation state. This result is very remarkable and should be taken into account in the next studies of any Pu(III) systems by the Pu M_4 HERFD method. Thus our assumption that PuO_2 NPs formed at pH 1 has Pu(IV) as a dominating oxidation state with additional presence of Pu(III) species, is confirmed.

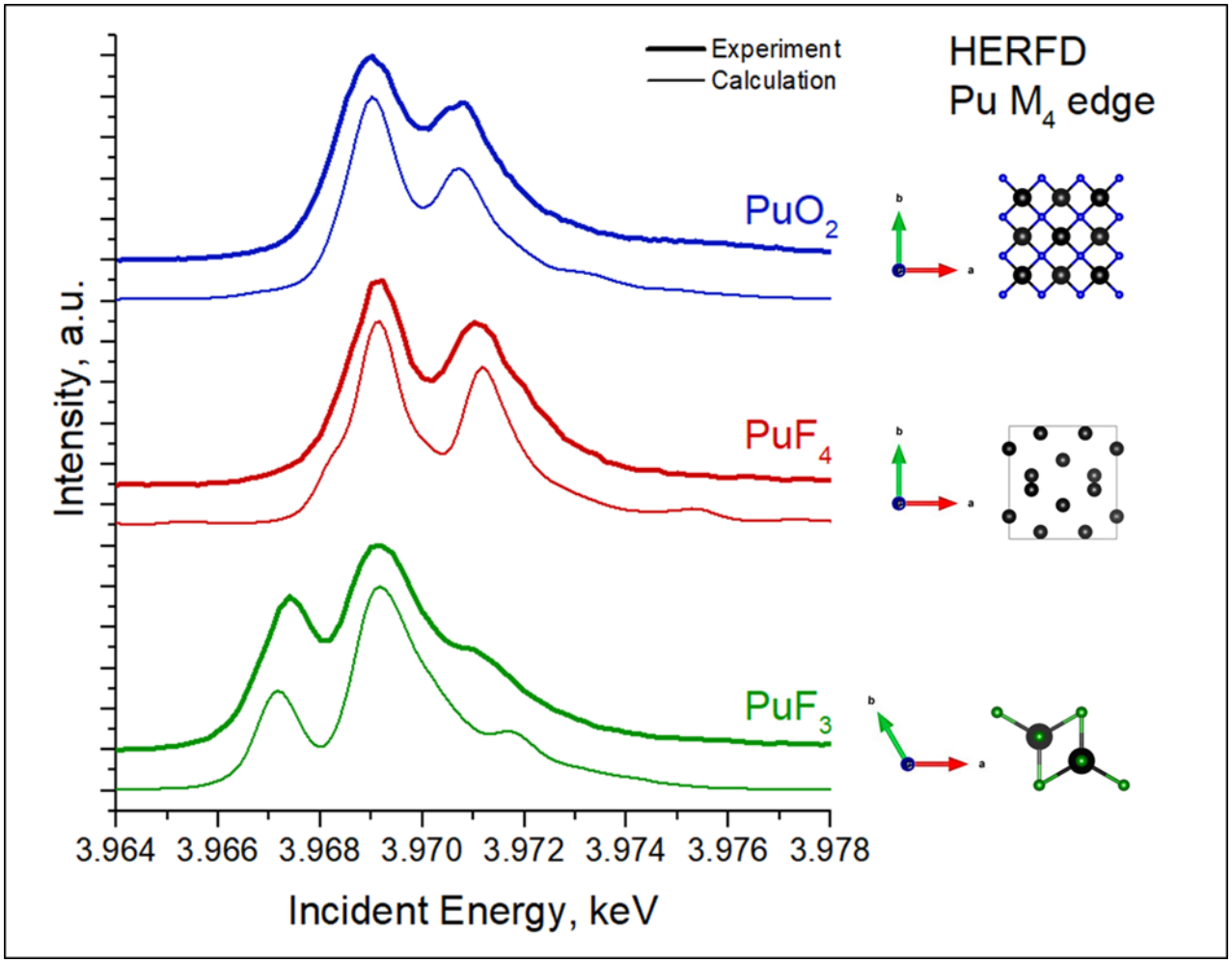

Fig. 38. Pu M_4 HERFD experimental data for PuO_2, PuF_4 and PuF_3 samples and compared with theoretical calculations, using AIM approximation. Inset – crystal structures of the compounds.

Based on the theoretical achievements and experimental data, recorded for our Pu model systems, we estimated the exact contribution of the Pu(III), Pu(IV) and Pu(VI) oxidation states in

the Pu M_4 HERFD data for the PuO_2 NPs formed at the pH 1 with the ITFA package,[36,37] which turns out to be in order of 10% for Pu(III) and 10% for Pu(VI) Nonetheless, Pu(IV) remains the dominating oxidation state and found to be in order of 80%. For the PuO_2 NPs synthesized at pH of 2 and 4, the main edge is observed at 3.969 keV, indicating that both compounds are in the Pu(IV) oxidation state. No Pu(III) contribution has been detected for both compounds (the characteristic spectral difference for all PuO_2 NPs compounds at various pH is shown at the bottom of the Fig. 2c).

As a first conclusion, we have found by HERFD and HRTEM that NPs obtained from pH 1, 2 and 4 are very similar to PuO_2 NPs obtained from alkaline pH: identical crystal structures and Pu(IV) as the dominating oxidation state in all NPs. However, HRTEM shows that PuO_2 particles formed at pH 1 are less agglomerated. This indicates the possible increase of NP stability in solution as well and complicates the process of particle separation from the solution, requiring high speed centrifuges or ultrafiltration.[38] By reason of instrumental limitations during sample preparation caused by plutonium handling restrictions, we cannot exclude presence of a mother liquid used to transfer minor amounts of solid phase samples at pH 1 for the HERFD measurements. To answer the most confusing question why Pu(III) and Pu(VI) is present only in HERFD spectrum of this sample, we have examined presence of various Pu species in the solution and their evolution over time by UV-vis spectroscopy. It might help to verify whether other oxidation states originated from the mother liquid or the PuO_2 NPs itself contain Pu(III) and Pu(VI) species. However, the absence of differences in HRTEM and the PuO_2 –like structure according to SAED are already strong arguments against the statement that NPs contain Pu different from Pu(IV). Therefore, as a next step we studied the evolution of the initial Pu solution over time.

UV-vis spectra of the Pu solution recorded at different time intervals are shown in Fig. 4. At the beginning of the reaction Pu(IV) is the dominating oxidation state with traces of Pu(VI) (see peak at 831 nm), while eventually the Pu(IV) concentration decreases and significant amounts of Pu(III) (see peak at 601 nm) appear. Pu concentrations were calculated from UV-vis data using the Beer–Lambert law. After 20 hours of interaction (which corresponds to the time needed for the preparation of the samples for HERFD) the distribution of Pu oxidation states in solution is as follows: Pu(IV) is $1.4 \cdot 10^{-4}$ M, Pu(III) is $0.4 \cdot 10^{-4}$ M and Pu(VI) is $0.09 \cdot 10^{-4}$ M, i.e. 85% for Pu(IV), 15% - for Pu(III) and 5% - Pu(VI), which is in proper agreement with the ITFA results obtained from HERFD. Moreover, the Pu(V) contribution cannot be excluded by UV-vis due to the detection limit of this method and the low molar extinction coefficient ε for the Pu(V) characteristic peaks, though according to the total concentration in solution the upper limit of Pu(V) amount must be less than $2 \cdot 10^{-6}$ M. Interestingly the Pu(III) concentration decreases after 20 h while Pu(VI) increases, wherein the total Pu concentration in solution remains constant. This leads to the conclusion that redox reactions are still occurring in the system.

Summarizing the results of solid and solution characterisation, we conclude that Pu oxidation states other than the Pu(IV) observed in the HERFD spectrum of the sample at pH 1 come directly from the solution, since the amount of dissolved Pu is enough to be detected. HERFD samples are prepared as wet pastes hence some solution is caught during sample preparation. In the case of PuO_2 NPs from pH 1, the steady-state concentration of Pu is higher (Fig. 1), allowing a liquid phase contribution to be detected. Moreover, the HERFD method can be used to study all matters (liquids, solids and gases) and the detection limit is so superior that even a tiny Pu concentration, which is still present in solution is detectable. This is the case for the PuO_2 NPs

sample, formed at pH 1, where the HERFD spectrum is a superposition of signals, recorded on both the solid and liquid phases. Therefore, it allows us to conclude that all PuO_2 NPs themselves, made at different pH levels in the range of 1 to >10, contain only Pu(IV) oxidation state.

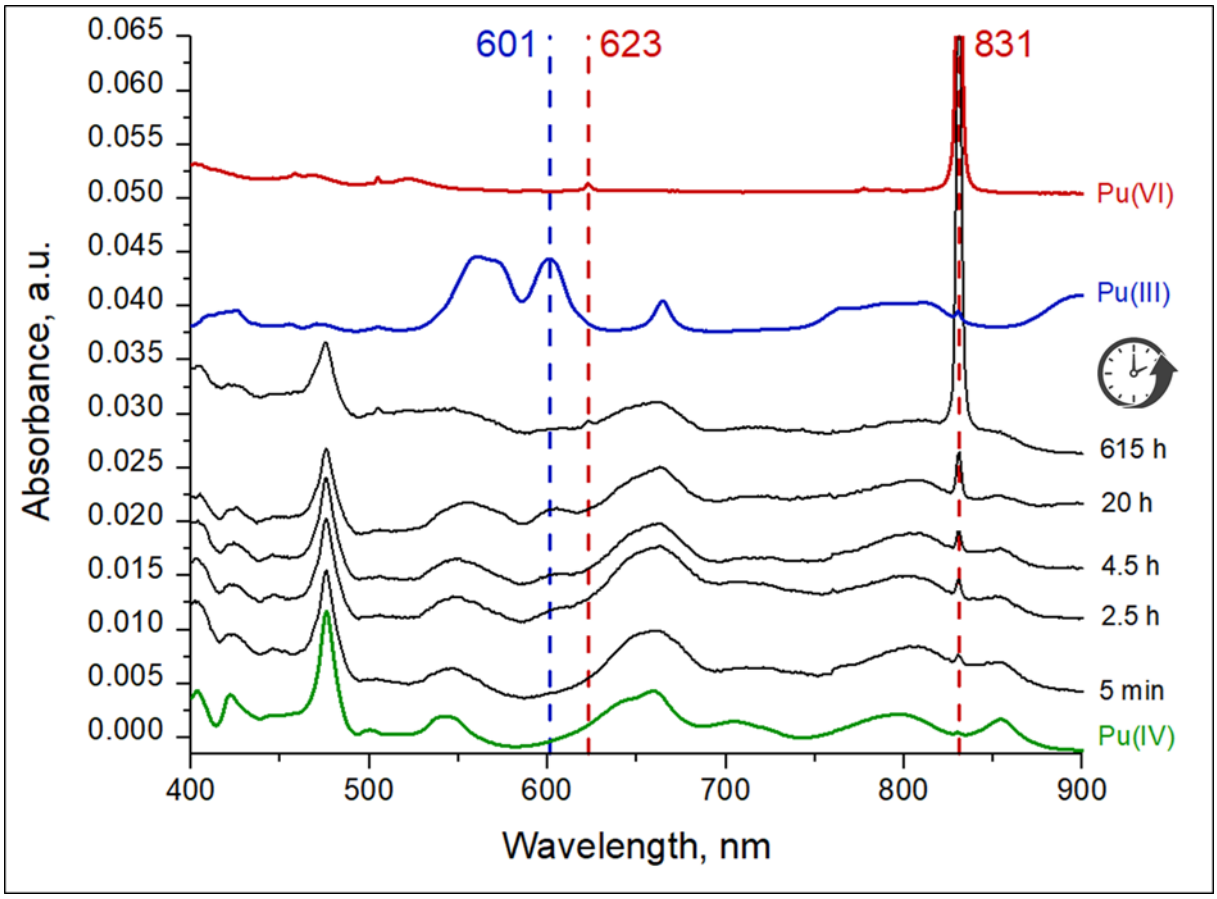

Fig. 39. UV-vis spectra of Pu (IV) pH 1 sample solutions after different times of reactions and reference solutions with wavelengths of the characteristic peaks.

It is essential to discuss the discrepancies in steady-state solution concentrations of Pu for this study and the one reported in literature previously (Fig. 1b). There are several factors that might be potentially responsible.

Unlike this study, in previous solubility investigations, the morphology and crystallinity of the particles have not been studied in details thus these parameters may invoke diverse solubility values. Neck[15] investigated thermodynamic stability of PuO_2 and linked particle size and solubility with the Schindler equation. It draws a relation between experimental solubility products (colloid, amorphous and crystalline PuO_2) and the corresponding particle size. Enhanced solubility of Pu(IV) may be interpreted as an effect of particle size on the Gibbs energy of the small fractions.

In addition, nanoparticles at low pH stabilize in the solution hence in case of insufficient separation may cause systematical solubility overstatement. Nanoparticle stability is related to agglomeration reactions, which are controlled by the colloid surface charge and the solution composition.[39]

Besides that, Neck and Rai have suggested that Pu(V)/Pu(VI) is present in solution and it is considered in the thermodynamic model (Fig. 5). Neck[15] investigated solubility and redox

reactions of Pu(IV) hydrous oxide and found, that solubility is controlled by hydrous PuO_{2+x}(s, hyd) and mixed valent $(Pu^{V})_{2x}(Pu^{IV})_{1-2x}O_{2+x}$ (s, hyd) solid phases. Rai[18] showed that at pH 1-3 redox potentials are controlled by the oxidative dissolution of amorphous PuO_2(am, hyd) and the redox equilibrium between PuO_2^+ and PuO_2^{2+} :

PuO_2 (am, hyd) ⇆ $PuO_2^+ + e^-$

PuO_2^+ ⇆ $PuO_2^{2+} + e^-$

Based on this, the appearance of Pu(III) in the solution just after formation of the solids might be surprising (Fig. 5). Despite the assumption that Pu(III) does not contribute much to the Pu reactions at ambient conditions (with a few exceptions though[20,40]), our results undoubtedly confirm its presence in the solution.

We consider Pu(IV) disproportionation to Pu(III) and Pu(V)/Pu(VI) as the main mechanism of Pu(III) formation at pH 1. Due to the thermodynamical instability of Pu(III) and Pu(V) under such pH and Eh conditions, they eventually oxidize to Pu(VI) as observed in this study. It should be noted that after 615 h the Pu(VI) fraction has increased significantly (Fig. 4), testifying that redox reactions occur during this period.

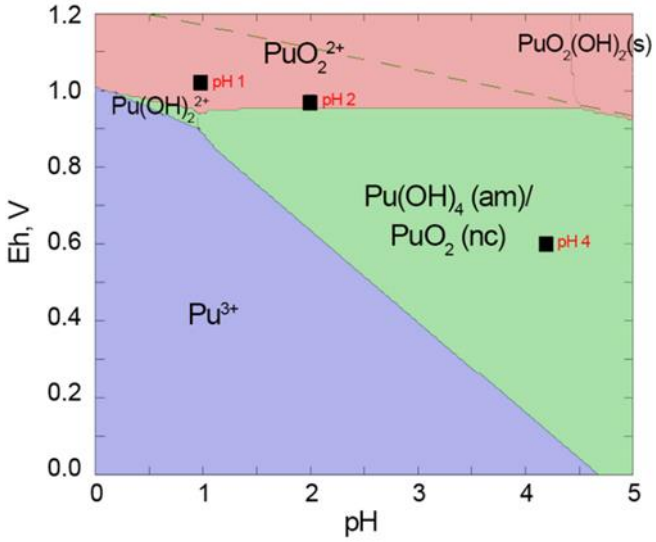

Fig. 5. Pourbaix diagrams for Pu, calculated in MEDUSA software[41] ([Pu] = 5·10-4 M) together with experimental data on pH-Eh conditions of the synthesis. The thermodynamic data from NEA database is used.

Conclusions

It was shown that nanoparticles formed under acidic conditions (pH 1-4) with PuO_2-like structure according to HRTEM and HERFD data. Mechanisms of formation and growth of plutonium dioxide nanoparticles in solutions are under extensive debate in the open literature. Therefore, it is important to synthesize the PuO_2 nanoparticles under various chemical conditions and to determine the physico-chemical parameters that control properties and NPs behavior in the natural environment. In this work, we explore in details the formation of the PuO_2 NPs at acidic conditions and compare it with NPs formed in alkaline media. Taking into account our previous investigations,[26,33] we show that for the wide pH range from 1 to >10 small crystalline PuO_2 NPs are formed with an average size of 2 nm. The dominating oxidation state for the particles is

proven to be Pu(IV) by the use of the HERFD method at the Pu M_4 edge in combination with electronic structure calculations by AIM.

Furthermore, we demonstrate that at pH 1 a stable Pu colloid is formed with a significant amount of Pu in solution. Due to its presence and due to the complicated redox behaviour, plutonium in acidic solutions is eventually present at several oxidation states: Pu(III), Pu(IV), Pu(VI) and, likely, Pu(V). Nevertheless, the solid phase remains intact during these processes, though Pu from solution may misrepresent results due to the exceptional stability of obtained colloids. Therefore, the contribution of Pu(III) and Pu(VI) in HERFD spectrum of PuO_2 NPs at pH 1 originates from the solution rather than from the NPs themselves and can be detected due to the high steady-state concentration of Pu at these conditions. It is possible to estimate the Pu(III) contribution from the M_4 edge HERFD spectrum, measured for the first time, by ITFA program. Theoretical calculations confirm that spectral shape of Pu(III) HERFD spectrum looks very different from Pu(IV) depending on the local structure near Pu. Nevertheless, both HERFD and HRTEM show the PuO_2-like structure in all NPs.

To sum up, there are many factors, which should be considered for proper studies of plutonium NPs: not only its properties such as crystallinity, morphology and degree of agglomeration, but also the solutions may influence the results, especially if it is still present in the investigated sample. NP formation at low pH is even more specific due to the high colloid stability under these conditions as well as relatively significant solubility. The difficulties of solid phase and solution separation may lead to misinterpretation of solubility and characterization results. Stable agglomerates maintain sustainability of Pu colloids and their behaviour is fundamentally different from simple aqueous solution. All specific properties of such systems must be carefully considered for technological processes where Pu colloid is involved.

Author Contributions

K.O.K. A.Yu. R and S.N.K. planned and supervised the project. . E.G, A. Yu. R., A.K. and S.W. performed the synthesis. E.G., M.H, S.B. and K.O.K. performed HERFD experiments at the Pu M_4 edge. A.E. performed HRTEM characterization of the samples. S.M.B. performed Pu M4 electronic structure calculations. K.O.K., E.G., A. Yu. R., and S.N.K. co-wrote the paper. All authors discussed the results and contributed to the final manuscript.

Conflicts of interest

There are no conflicts to declare

Acknowledgements

This research was funded by European Commission Council under ERC grant N759696. E.G. acknowledges support from RFBR (project number No. 19-33-90127). E.G. , A.K. and S.N.K. acknowledge support by the Russian Ministry of Science and Education under grant № 075-15-2019-1891. S.M.B. acknowledges support from the Swedish Research Council (Grant 2017-06465). Authors thank Soleil synchrotron for the beamtime allocation at MARS beamline. Moreover, we acknowledge the help of L. Amidani, I. Pidchenko and T. Plakhova at MARS beamline during the HERFD experiment at the Pu M_4 edge.

References

1 S. Bargrizan, R. J. Smernik, R. W. Fitzpatrick and L. M. Mosley, *Talanta*, 2018, 186, 421–426.

2 P. Matveev, P. K. Mohapatra, S. N. Kalmykov and V. Petrov, *Solvent Extr. Ion Exch.*, 2020, 1–35.

3 A. B. Kersting, D. W. Efurd, D. L. Finnegan, D. J. Rokop, D. K. Smith and J. L. Thompson, *Nature*, 1999, 397, 56–59.

4 A. P. Novikov, S. N. Kalmykov, S. Utsunomiya, R. C. Ewing, F. Horreard, A. Merkulov, S. B. Clark, V. V Tkachev and B. F. Myasoedov, *Science (80-.).*, 2006, 314, 638–642.

5 C. Xu, P. H. Santschi, J. Y. Zhong, P. G. Hatcher, A. J. Francis, C. J. Dodge, K. A. Roberts, H. C. C. and B. D. Honeyman, *Environ. Sci. Technol.*, 2008, 42, 8211–8217.

6 A. B. Kersting, *Inorg. Chem.*, 2013, 52, 3533–3546.

7 B. A. Powell, Z. Dai, M. Zavarin, P. Zhao and A. B. Kersting, *Environ. Sci. Technol.*, 2011, 45, 2698–2703.

8 A. Y. Romanchuk, S. N. Kalmykov, A. V. Egorov, Y. V. Zubavichus, A. A. Shiryaev, O. N. Batuk, S. D. Conradson, D. A. Pankratov and I. A. Presnyakov, *Geochim. Cosmochim. Acta*, 2013, 121, 29–40.

9 A. E. Hixon, Y. Arai and B. A. Powell, *J. Colloid Interface Sci.*, 2013, 403, 105–112.

10 M. Schmidt, S. S. Lee, R. E. Wilson, K. E. Knope, F. Bellucci, P. J. Eng, J. E. Stubbs, L. Soderholm and P. Fenter, *Environ. Sci. Technol.*, 2013, 47, 14178–14184.

11 M. Zavarin, P. Zhao, Z. Dai and A. B. Kersting, *Radiochim. Acta*, 2014, 102, 983–997.

12 M. A. Boggs, Y. Jiao, Z. Dai, M. Zavarin and A. B. Kersting, *Appl. Environ. Microbiol.*, 2016, 82, 7093–7101.

13 A. E. Plymale, V. L. Bailey, J. K. Fredrickson, S. M. Heald, E. C. Buck, L. Shi, Z. Wang, C. T. Resch, D. A. Moore and H. Bolton, *Environ. Sci. Technol.*, 2012, 46, 2132–2140.

14 V. Neck and J. I. Kim, *Radiochim. Acta*, 2001, 89, 1–16.

15 V. Neck, M. Altmaier, A. Seibert, J. I. Yun, C. M. Marquardt and T. Fanghänel, *Radiochim. Acta*, 2007, 95, 193–207.

16 R. Knopp, V. Neck and J. I. Kim, *Radiochim. Acta*, , DOI:10.1524/ract.1999.86.34.101.

17 J. A. Pérez-Bustamante, *Radiochim. Acta*, , DOI:10.1524/ract.1965.4.2.67.

18 D. RAI, *Radiochim. Acta*, , DOI:10.1524/ract.1984.35.2.97.

19 J. I. Kim and B. Kanellakopulos, *Radiochim. Acta*, , DOI:10.1524/ract.1989.48.34.145.

20 C. Walther, J. Rothe, B. Brendebach, M. Fuss, M. Altmaier, C. M. Marquardt, S. Büchner, H. Cho, J. Yun and A. Seibert, *Radiochim. Acta*, 2009, 97, 199–207.

21 M. Icker, C. Walther, V. Neck and H. Geckeis, *IOP Conf. Ser. Mater. Sci. Eng.*, 2010, 9, 012060.

22 J. Rothe, C. Walther, M. A. Denecke and T. Fanghänel, *Inorg. Chem.*, 2004, 43, 4708–4718.

23 S. D. Conradson, B. D. Begg, D. L. Clark, C. Den Auwer, M. Ding, P. K. Dorhout, F. J. Espinosa-Faller, P. L. Gordon, R. G. Haire, N. J. Hess, R. F. Hess, D. W. Keogh, L. A. Morales, M. P. Neu, P.

Paviet-Hartmann, W. Runde, C. D. Tait, D. K. Veirs and P. M. Villella, *J. Am. Chem. Soc.*, 2004, 126, 13443–13458.

24 L. Soderholm, P. M. Almond, S. Skanthakumar, R. E. Wilson and P. C. Burns, *Angew. Chemie - Int. Ed.*, 2008, 47, 298–302.

25 K. E. Knope and L. Soderholm, *Inorg. Chem.*, 2013, 52, 6770–6772.

26 E. Gerber, A. Y. Romanchuk, I. Pidchenko, L. Amidani, A. Rossberg, C. Hennig, G. B. M. Vaughan, A. Trigub, T. Egorova, S. Bauters, T. Plakhova, M. O. J. Y. Hunault, S. Weiss, S. M. Butorin, A. C. Scheinost, S. N. Kalmykov and K. O. Kvashnina, *Nanoscale*, 2020, 12, 18039–18048.

27 L. Bonato, M. Virot, T. Dumas, A. Mesbah, E. Dalodière, O. Dieste Blanco, T. Wiss, X. Le Goff, M. Odorico, D. Prieur, A. Rossberg, L. Venault, N. Dacheux, P. Moisy and S. I. Nikitenko, *Nanoscale Adv.*, 2020, 2, 214–224.

28 S. M. Butorin, *Inorg. Chem.*, 2020, 59, 16251–16264.

29 W. T. Carnall, *J. Chem. Phys.*, 1992, 96, 8713–8726.

30 W. T. Carnall, G. K. Liu, C. W. Williams and M. F. Reid, *J. Chem. Phys.*, 1991, 95, 7194–7203.

31 A. Kotani and H. Ogasawara, *Phys. B Condens. Matter*, 1993, 186–188, 16–20.

32 P. W. Anderson, *Phys. Rev.*, 1961, 124, 41–53.

33 K. O. Kvashnina, A. Y. Romanchuk, I. Pidchenko, L. Amidani, E. Gerber, A. Trigub, A. Rossberg, S. Weiss, K. Popa, O. Walter, R. Caciuffo, A. C. Scheinost, S. M. Butorin and S. N. Kalmykov, *Angew. Chemie - Int. Ed.*, 2019, 58, 17558–17562.

34 V. Neck, M. Altmaier and T. Fanghänel, *Comptes Rendus Chim.*, 2007, 10, 959–977.

35 I. Pidchenko, J. März, M. O. J. Y. Hunault, S. Bauters, S. M. Butorin and K. O. Kvashnina, *Inorg. Chem.*, 2020, 59, 11889–11893.

36 A. Rossberg, T. Reich and G. Bernhard, *Anal. Bioanal. Chem.*, 2003, 376, 631–638.

37 A. C. Scheinost, A. Rossberg, M. Marcus, S. Pfister and R. Kretzschmar, *Phys. Scr.*, 2005, 1038.

38 C. Ekberg, K. Larsson, G. Skarnemark and I. Persson, *Dalt. Trans.*, 2013, 42, 2035–2040.

39 H. Geckeis, T. Rabung and T. Schäfer, in *Actinide Nanoparticle Research*, eds. S. N. Kalmykov and M. A. Denecke, Springer Berlin Heidelberg, Berlin, Heidelberg, 2011, pp. 1–30.

40 A. Y. Romanchuk, S. N. Kalmykov, A. V. Egorov, Y. V. Zubavichus, A. A. Shiryaev, E. A. Smirnov and A. V. Garshev, *Radiochim. Acta*, , DOI:10.1515/ract-2015-2494.

41 I. Puigdomenech, 2010.

Appendix D: Article 4. A novel meta-stable pentavalent plutonium solid phase on the pathway from aqueous Pu(VI) to PuO_2 nanoparticles

Kristina O. Kvashnina*[a,b], Anna Yu. Romanchuk[c], Ivan Pidchenko[a,b], Lucia Amidani[a,b], Evgeny Gerber[a,b,c], Alexander Trigub[d], Andre Rossberg[a,b] , Stephan Weiss[b], Karin Popa[e], Olaf Walter[e], Roberto Caciuffo[e], Andreas C. Scheinost[a,b], Sergei M. Butorin[f], Stepan N. Kalmykov[c,d]

Abstract: *We report here the evidence that the formation of PuO_2 nanoparticles from oxidized Pu(VI) under alkaline conditions proceeds through the formation of an intermediate Pu(V) solid phase, similar to $NH_4PuO_2CO_3$, which is stable over a period of several months. For the first time, state-of-the-art experiments at Pu M_4 and at L_3 absorption edges combined with theoretical calculations unambiguously allowed to determine the oxidation state and the local structure of this intermediate phase.*

Plutonium (Pu) plays a prominent role in the nuclear energy production but nuclear accidents and nuclear weapons tests have led in the past to the release of Pu and other hazardous isotopes to the environment and Pu contamination has been detected in waters and soils[1]. Based on such cases, several countries decided to shut down the operation of the oldest nuclear facilities and put effort to improve the safety of the nuclear waste storage in order to prevent further release of radioactive nuclides to the environment. To progress in this direction, it is fundamental to deepen our basic knowledge of the chemistry of actinides in environmentally relevant conditions, by making compounds, characterizing them and understanding them experimentally and theoretically. Thanks to the increased experimental sensitivity, recent cross-activities between theory and experiment in combination with different synthetic approaches, such a goal becomes reachable.

In spite of the low solubility of the most prevalent environmental species, Pu has been shown to be transported by groundwaters from contaminated sites on a scale of kilometers in the form of colloids, with Pu being absorbed on clays[2], iron oxides[3] or natural organic matter[4]. In the near-field conditions of geological repositories of spent nuclear fuel and other radioactive wastes, the formation of intrinsic PuO_2 colloids is a key scenario[5]. Therefore, the characterization of such intrinsic colloidal nanoparticles (NPs) in aqueous solution have recently received much attention[6–10]. The most debated question is the structural nature of these NPs (crystalline versus amorphous), as well as the presence of the Pu(V) and other oxidation states in small NPs (< 3nm)[9,11–15]. Various studies used different synthetic approaches and different solution conditions to examine the precipitated product, which may be either amorphous or crystalline. This has led to the controversy which is not resolved. For example, Walther et al.[14] found evidence for multiple Pu oxidation states (III, IV, V) in the early stages of hydrolysis and polymerization of PuO_2 colloids at pH 0.5-1.0, while Rothe et al.[9] reported about the Pu(IV)

oxyhydroxide-colloid formation. Conradson et al.[11] examined solid precipitates prepared by a variety of synthetic approaches and argued for the presence of Pu(V) in nonstoichiometric PuO_{2+x} solids.

One of the most fundamental properties of the Pu chemical behaviour is the variety of its oxidation states. The oxidation state is defined by the number of electrons that are removed from the valence orbitals of a neutral atom. Pu in the pentavalent oxidation state has three electrons in the 5f shell, leaving the 6d orbitals empty. The oxidation state of Pu determines its chemical behaviour and speciation. Four oxidation states (from III to VI) may co-exist under environmental conditions, (VII) and even (VIII) states are proposed to be stable under highly alkaline oxidative conditions[16]. Pu oxidation states of aqueous, solid state and interfacial Pu species have been determined previously using Pu L_3 edge[6,7,17] X-ray absorption near edge structure (XANES) spectroscopy. The Pu edge of the L_3 XANES spectrum of Pu(V) always shows a characteristic energy shift towards low energy compared to that of Pu(IV) and Pu(VI) XANES spectra. The experimental energy resolution of the recorded XANES data can be improved if the spectra are recorded in the high energy resolution fluorescence detection (HERFD) mode[8]. Nevertheless, at the Pu L_3 edge, the electrons are excited from the 2p core level to the 6d level, which is always unoccupied independently on the Pu oxidation state. For uranium systems, we have previously shown that HERFD experiments at the U M_4 edge[18–20] are much more informative on the oxidation state and electronic structure than measurements at the L-edges. X-ray absorption at the M_4 edge of actinides probes 5f states via transitions from the 3d core level. To the best of our knowledge, HERFD data at the Pu M_4 edge have never been reported in the literature and have never been exploited.

Fig. 1a shows the first experimental HERFD data at the Pu M_4 edge for $Pu^{IV}O_2$ and $KPu^{V}O_2CO_{3(s)}$ (solid) systems with Pu(IV) and Pu(V) oxidation states, respectively. Data were collected with an X-ray emission spectrometer[21] set to the maximum of the M_β emission line at 3534 eV. Synthesis procedures and characterization of both materials are reported in SI. The HERFD spectrum of PuO_2 clearly shows two intense peaks, at ~3970.2 eV and ~3971.8 eV. According to the results of calculations carried out in the framework of the Anderson impurity model (AIM)[22–24] (Fig. 1b), the intensity and energy of these two peaks are a result of multiple factors, such as the strength of the intra-atomic and crystal-field interactions and the degree of the Pu 5f – ligand 2p hybridization in the ground and final states of the spectroscopic process. In comparison with PuO_2, the HERFD spectrum of $KPuO_2CO_{3(s)}$ shifts towards higher incident energy and shows a narrow profile with an asymmetric shape and a shoulder at the higher incident energy side. The results of the AIM calculations reported in Fig.1b are in fairly good agreement with the experimental $KPuO_2CO_{3(s)}$ HERFD spectrum, confirming the presence of the pentavalent Pu oxidation state in $KPuO_2CO_{3(s)}$.

Due to dipole selection rules (J =0;±1), the shape of the Pu M_4 and M_5 HERFD transitions is expected to be different. At the Pu M_5 edge, the unoccupied 5f electronic levels with J = 5/2 and 7/2 can be reached by an electron excited from the Pu 3d5/2 state, whereas only the J = 5/2 state can be reached at the Pu M_4 edge[25]. A comparison between Pu M_4 and Pu M_5 spectra for several Pu systems is shown in Fig. S1. The energy shifts between Pu(III), Pu(IV), and Pu(V) in solid compounds are found to be in the order of 2 eV (between Pu (III) and Pu (IV)) and 0.4 eV between Pu (IV) and Pu (V) (Table S1). A correct determination of the Pu oxidation state, therefore, requires the improved energy resolution of the absorption spectra provided by HERFD.

Fig.1a shows experimental HERFD data recorded at different stages during the synthesis of PuO2 NPs from the aqueous Pu(VI) precursor. For this purpose, a solution of Pu(VI) was added to an excess of ammonia. The measured pH value of the solution was 11. The kinetics of the Pu(VI) to PuO_2 transformation reveal a two-step process: during the first minutes, we observed the formation of an intermediate Pu phase consisting of a yellow sludge (c.f. Fig.2). Later, during the formation of PuO_2 NPs, this intermediate phase dissolved and a different equilibrium phase, named "final phase", was formed[26]. The Pu M_4 HERFD spectrum recorded at the intermediate stage of the reaction is shown by the blue curve in Fig. 1a. The spectrum clearly indicates the presence of the Pu(V) oxidation state. This is supported by the good correspondence between energy and relative intensities of the main features of the Pu M_4 edge spectrum for $KPuO_2CO_{3(s)}$ (green curve) and the Pu intermediate phase (blue curve).

Furthermore, the HERFD spectrum of the final product of the reaction, formed after 3 weeks of the precipitated reaction, shows a profile identical to the one detected for a PuO_2 single crystal, confirming that the reaction terminates with the formation of PuO_2 NPs with cubic structure and with Pu (IV) oxidation state, as reported by Soderholm et al.[15] for Pu38 clusters – $(Li_{14}(H_2O)_n[Pu_{38}O_{56}Cl_{54}(H_2O)_8])$ - isolated from the initially alkaline peroxide solution [15].

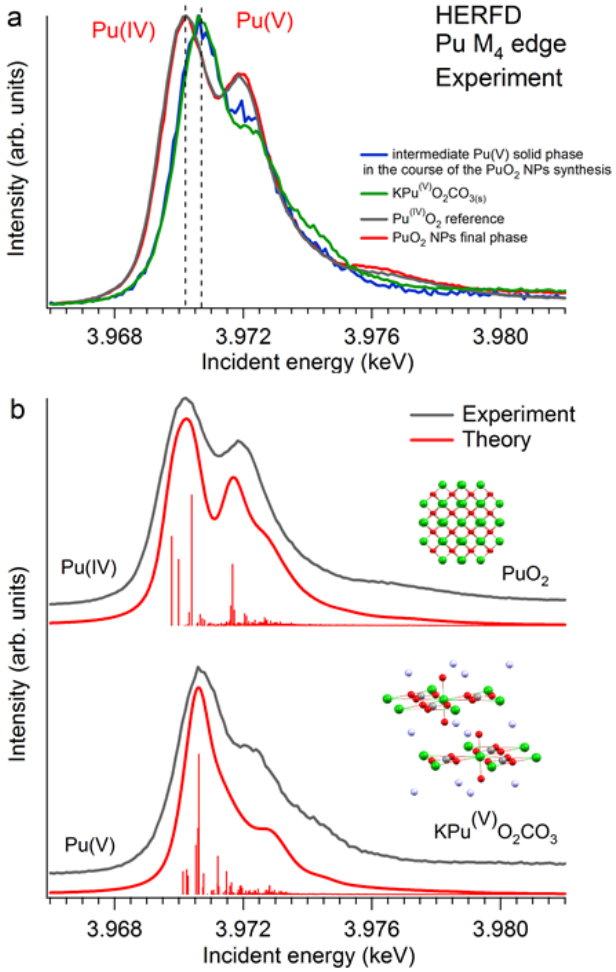

Figure 1. a) Experimental HERFD data at the Pu M_4 edge from two plutonium phases obtained during the synthesis of PuO_2 nanoparticles (NPs) from a Pu(VI) precursor at pH 11. The blue curve is the spectrum of the intermediate Pu(V) solid phase appearing during the synthesis of the PuO_2 NPs; the red curve is the spectrum of the final phase of PuO_2 NPs. The spectra of a PuO_2 bulk sample (grey curve) and of $KPuO_2CO_{3(s)}$ (green curve) are also shown as references for

Pu(IV) and Pu(V) oxidation states, respectively. Data were collected with an X-ray emission spectrometer set to the maximum of the Mβ emission line at 3534 eV. b) Experimental HERFD spectra of PuO_2 and $KPuO_2CO_{3(s)}$ compared with the results of Anderson Impurity Model calculations.

The experimental data collected for the intermediate phase during the PuO_2 NPs synthesis show evidence of the Pu(V) oxidation state. The exact contribution of the different chemical states in the Pu M_4 HERFD data reported in Fig.1a was estimated by ITFA[27]. The results indicate that the spectrum of the intermediate Pu phase contains 87% of Pu(V) and 13% of Pu(IV) (with estimated root mean square error of less than 2%, c.f. SI, Fig. S2). We did not observe a significant contribution of Pu(V) in the final phase (after the PuO_2 NPs were formed) nor a quantifiable amount of Pu(VI) (Table S2). The absence of Pu(V) in the final phase and the presence of 100% of Pu(IV) oxidation state after the PuO_2 NPs formation is an important result. At the same time, our data demonstrate that Pu(VI) to Pu(IV) reduction does not happen in a single step[26]. The Pu(VI) is first reduced to Pu(V) and then to Pu(IV).

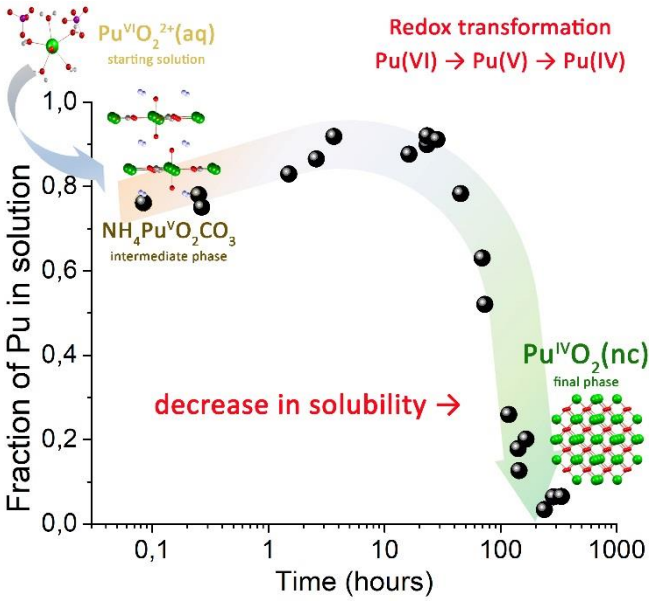

Figure 2. Kinetics of precipitation of Pu starting from Pu(VI) at pH 11 ([Pu] = $6 \cdot 10^{-5}$ M). The crystal structure of the formed phases is shown as inset.

Moreover, additional HERFD and EXAFS (Extended X-ray Absorption Fine Structure) experiments at the Pu L_3 edge gave us the opportunity to identify the intermediate phase forming in the course of the PuO_2 NPs formation. Fig.3 shows the comparison of the Pu HERFD L_3 edge data recorded for PuO_2 and the intermediate Pu phase during the PuO_2 NPs formation. As discussed previously, the L_3 spectrum of Pu(V) compounds always shows a very characteristic energy shift towards low energies and a decrease of the L3 white line intensity compared to Pu(IV) and Pu(VI) systems[6–8,17] (Fig. S3). The chemical shift of the intermediate Pu phase is clearly resolved in the HERFD data reported in Fig.3 and indicates the presence of the Pu(V) oxidation state, in agreement with the Pu M4 HERFD results. However, for actinide systems, the HERFD at the L3 edge is not as sensitive as the M_4 edge HERFD to the presence of minor contributions (<10%) from different oxidation states [28,29]. HERFD at the L_3 edge is, however, extremely sensitive to the local structure around the absorber, which results in specific post-edge features[19,30,31].

Ab-initio calculations on different structures were used to identify the intermediate Pu phase during the synthesis of PuO_2 NPs. We simulated the HERFD spectra of several compounds containing Pu (Fig. S4 – S5) in order to determine the Pu speciation of the intermediate Pu phase structure. The best agreement is found for $NH_4PuO_2CO_3$, in which Pu is present in the pentavalent state. The HERFD spectral shape reflects the d-density of states (DOS) of Pu, apart from the small shoulder at the absorption edge, barely visible in the data but well resolved in the simulation, which is due to the Pu 5f-DOS (Fig. S6). The Pu d-DOS is involved in the bonds with O, C and N. The Pu L_3 EXAFS data confirmed that the intermediate Pu phase formed during the PuO2 NPs synthesis is compatible with $NH_4PuO_2CO_3$. Furthermore, the EXAFS spectrum (Fig.S7, Table S3) could be fitted with a model based on the crystal structure of $NH_4PuO_2CO_3$ previously published. The fitted Pu – O distance of the triply-bond –yl group is 1.82 Å, well in agreement with previously determined distances of 1.80-1.81 Å for Pu(V) compounds[7,17,32] (c.f. Table S4), while the crystallographic distance of 1.93 Å is most likely biased by the very weak scattering of oxygen in comparison to Pu[33] . We also found that the Pu – Pu coordination number in the experimental EXAFS spectra of the intermediate phase is lower than for the structural data, which can be explained either by a (partially) amorphous nature or by nano-sized particles.

The intermediate $NH_4PuO_2CO_3$ phase was completely dissolved within ~10 hours and then, as a result of longer redox reactions (cf. Fig.2), the PuO_2 NPs were formed. Finally, a part of the intermediate Pu(V) phase was centrifuged out of suspension and dried at room temperature in order to check its stability over months. Surprisingly, the dried $NH_4PuO_2CO_3$ phase was found to be stable over months. We recorded additional Pu L3 HERFD spectra after 3 months and the spectral shape remains the same (Fig. S8). Therefore, the method reported here can be used to synthesize this Pu(V) phase.

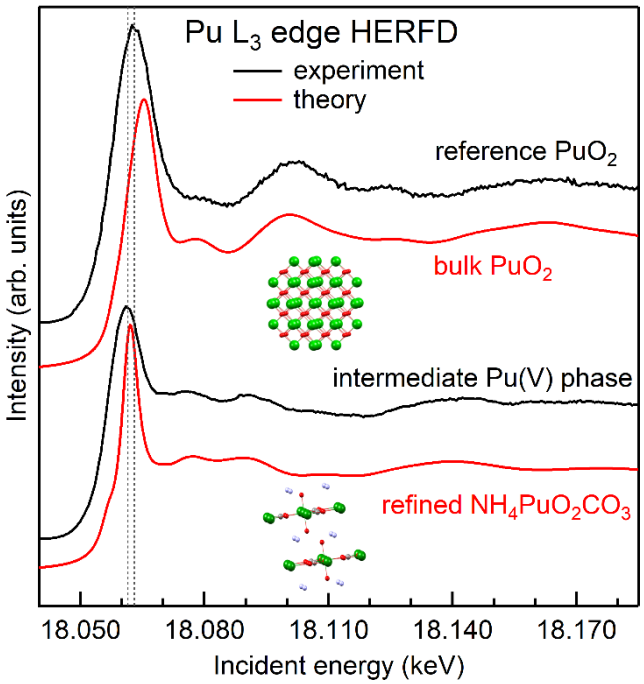

Figure 3. Pu L_3 HERFD spectra of single crystalline PuO_2 and of the Pu(V) intermediate phase formed during the synthesis of PuO_2 nanoparticles from Pu(VI) precursors at pH 11. Experimental data (black lines) are compared with FDMNES calculations for bulk PuO_2 and $NH_4PuO_2CO_3$ (red lines).

In order to understand the pH influence, we performed a similar experiment at pH 8. The kinetics of the Pu precipitation is quite similar to the experiment at pH 11, while the quantity of the intermediate Pu(V) phase is lower (Fig.S9). The comparison of the experimental conditions with the available thermodynamic data shows that Eh/pH values during our synthesis correspond to the area of stability of the Pu(IV) phase, close to the phase boundary (Fig.S10). It makes the formation of the intermediate Pu(V) phase possible, but at the same time, the high thermodynamic stability of PuO_2 and its extremely low solubility lead to further transformation of the Pu(V) phase into PuO_2.

We show here for the first time that while Pu(V) solid state complexes are always viewed as exotic compounds, a thermodynamically meta-stable Pu(V) solid phase is formed during the reductive precipitation of PuO_2 NPs from the Pu(VI) precursor at pH 11. The intermediate Pu(V) phase is characterized for the first time using HERFD at the Pu M_4 edge and model calculations in the framework of AIM. The Pu M_4 HERFD method allows for the unambiguous identification of the Pu oxidation state, demonstrates the Pu(V) existence and provides quantitative estimates for varying Pu chemical states. The local structure of the intermediate Pu(V) phase, similar to $NH_4PuO_2CO_3$, is identified by a combination of the Pu L_3 HERFD experiment and ab-initio calculations and is found to be stable over a period of several months. The redox reactions behind aqueous Pu(VI) – PuO_2 NPs and formation of Pu(V) affect the substantial increase of the solubility. This finding provides a significant step towards a better understanding of the Pu chemistry and emphasizes the value of the HERFD technique for studies of the PuO_2 NPs formation under different solution conditions.

Acknowledgements

This research was funded by European Commission Council under ERC grant N759696. The authors are grateful to HZDR for the beamtime allocation at beamline BM20 and to ESRF for beamtime allocation at beamline ID26. We also thank P. Glatzel and T. Bohdan for the help at beamline ID26 during the HERFD experiment at the Pu M_4 edge. S.M.B. acknowledges support from the Swedish Research Council (research grant 2017-06465). A.Yu.R. and A.T. acknowledge support from the Russian Foundation for Basic Research (project 18-33-20129). The authors would like to thank Patrick Colomp and Ross Murray from the ESRF safety group for their help in handling radioactive samples at the ID26 and BM20 beamlines.

Keywords: plutonium dioxide nanoparticles • pentavalent plutonium solid phase • Pu M_4 HERFD • electronic structure calculations• actinide chemistry

[1] N. Armaroli, V. Balzani, Energy Environ. Sci. 2011, 4, 3193.

[2] A. B. Kersting, D. W. Efurd, D. L. Finnegan, D. J. Rokop, D. K. Smith, J. L. Thompson, Nature 1999, 397, 56–59.

[3] A. P. Novikov, S. N. Kalmykov, S. Utsunomiya, R. C. Ewing, F. Horreard, A. Merkulov, S. B. Clark, V. V. Tkachev, B. F. Myasoedov, Science (80-.). 2006, 314, 638–641.

[4] C. Xu, P. H. Santschi, J. Y. Zhong, P. G. Hatcher, A. J. Francis, C. J. Dodge, K. A. Roberts, C.-C. Hung, B. D. Honeyman, Environ. Sci. Technol. 2008, 42, 8211–8217.

[5] V. Neck, M. Altmaier, T. Fanghänel, Comptes Rendus Chim. 2007, 10, 959–977.

[6] E. Dalodière, M. Virot, V. Morosini, T. Chave, T. Dumas, C. Hennig, T. Wiss, O. Dieste Blanco, D. K. Shuh, T. Tyliszcak, et al., Sci. Rep. 2017, 7, 43514.

[7] E. Dalodière, M. Virot, T. Dumas, D. Guillaumont, M.-C. Illy, C. Berthon, L. Guerin, A. Rossberg, L. Venault, P. Moisy, et al., Inorg. Chem. Front. 2018, 5, 100–111.

[8] T. Vitova, I. Pidchenko, D. Fellhauer, T. Pruessmann, S. Bahl, K. Dardenne, T. Yokosawa, B. Schimmelpfennig, M. Altmaier, M. Denecke, et al., Chem. Commun. 2018, 54, 12824–12827.

[9] J. Rothe, C. Walther, M. A. Denecke, T. Fanghänel, Inorg. Chem. 2004, 43, 4708–4718.

[10] A. B. Kersting, Inorg. Chem. 2013, 52, 3533–3546.

[11] S. D. Conradson, B. D. Begg, D. L. Clark, C. den Auwer, M. Ding, P. K. Dorhout, F. J. Espinosa-Faller, P. L. Gordon, R. G. Haire, N. J. Hess, et al., J. Am. Chem. Soc. 2004, 126, 13443–13458.

[12] G. E. Sigmon, A. E. Hixon, Chem. - A Eur. J. 2019, 25, 2463–2466.

[13] C. Ekberg, K. Larsson, G. Skarnemark, A. Ödegaard-Jensen, I. Persson, Dalt. Trans. 2013, 42, 2035–2040.

[14] C. Walther, J. Rothe, B. Brendebach, M. Fuss, M. Altmaier, C. M. Marquardt, S. Büchner, H. Cho, J. Yun, A. Seibert, Radiochim. Acta 2009, 97, 199–207.

[15] L. Soderholm, P. M. Almond, S. Skanthakumar, R. E. Wilson, P. C. Burns, Angew. Chemie - Int. Ed. 2008, 47, 298–302.

[16] I. G. Tananaev, M. V. Nikonov, B. F. Myasoedov, D. L. Clark, J. Alloys Compd. 2007, 444–445, 668–672.

[17] S. D. Conradson, K. D. Abney, B. D. Begg, E. D. Brady, D. L. Clark, C. den Auwer, M. Ding, P. K. Dorhout, F. J. Espinosa-Faller, P. L. Gordon, et al., Inorg. Chem. 2004, 43, 116–131.

[18] K. O. Kvashnina, S. M. Butorin, P. Martin, P. Glatzel, Phys. Rev. Lett. 2013, 111, 253002.

[19] K. O. Kvashnina, Y. O. Kvashnin, S. M. Butorin, J. Electron Spectros. Relat. Phenomena 2014, 194, 27–36.

[20] S. M. Butorin, K. O. Kvashnina, D. Prieur, M. Rivenet, P. M. Martin, Chem. Commun. 2017, 53, 115–118.

[21] K. O. Kvashnina, A. C. Scheinost, J. Synchrotron Radiat. 2016, 23, 836–841.

[22] P. W. Anderson, Phys. Rev. 1961, 124, 41–53.

[23] S. M. Butorin, K. O. Kvashnina, A. L. Smith, K. Popa, P. M. Martin, Chem. - A Eur. J. 2016, 22, 9693–9698.

[24] S. M. Butorin, A. Modin, J. R. Vegelius, K. O. Kvashnina, D. K. Shuh, J. Phys. Chem. C 2016, 120, 29397–29404.

[25] K. O. Kvashnina, H. C. Walker, N. Magnani, G. H. Lander, R. Caciuffo, Phys. Rev. B 2017, 95, 245103.

[26] A. Y. Romanchuk, T. V. Plakhova, A. V. Egorov, T. B. Egorova, P. V. Dorovatovskii, Y. V. Zubavichus, A. A. Shiryaev, S. N. Kalmykov, Dalt. Trans. 2018, 47, 11239–11244.

[27] A. Rossberg, T. Reich, G. Bernhard, Anal. Bioanal. Chem. 2003, 376, 631–638.

[28] G. Leinders, R. Bes, J. Pakarinen, K. Kvashnina, M. Verwerft, Inorg. Chem. 2017, 56, 6784–6787.

[29] I. Pidchenko, K. O. Kvashnina, T. Yokosawa, N. Finck, S. Bahl, D. Schild, R. Polly, E. Bohnert, A. Rossberg, J. Göttlicher, et al., Environ. Sci. Technol. 2017, 51, 2217–2225.

[30] L. Amidani, T. V. Plakhova, A. Y. Romanchuk, E. Gerber, S. Weiss, A. Efimenko, C. J. Sahle, S. M. Butorin, S. N. Kalmykov, K. O. Kvashnina, Phys. Chem. Chem. Phys. 2019, 21, 10635–10643.

[31] K. O. Kvashnina, Y. O. Kvashnin, J. R. Vegelius, A. Bosak, P. M. Martin, S. M. Butorin, Anal. Chem. 2015, 87, 8772–8780.

[32] M. V. Di Giandomenico, C. Le Naour, E. Simoni, D. Guillaumont, P. Moisy, C. Hennig, S. D. Conradson, C. Den Auwer, Radiochim. Acta 2009, 97, DOI 10.1524/ract.2009.1620.

[33] F. H. Ellinger, W. H. Zachariasen, J. Phys. Chem. 1954, 58, 405–408.

Appendix E: Article 5. Towards the surface hydroxyl species in CeO_2 nanoparticles

Tatiana V. Plakhova[a], Anna Yu. Romanchuk[a], Sergei M. Butorin[b] , Anastasia D. Konyukhova[a], Alexander V. Egorov[a], Andrey A. Shiryaev[a,c], Alexander E. Baranchikov[a,d], Madina M. Sozarukova[d], Pavel V. Dorovatovskii[e], Thomas Huthwelker[f], Evgeny Gerber[g,h], Stephen Bauters[g,h], Andreas C. Scheinost[g,h], Vladimir K. Ivanov[a,d], Stepan N. Kalmykov [a,c] and Kristina O. Kvashnina[g,h] *

Lomonosov Moscow State University, Department of Chemistry, Leninskije Gory 1, Moscow, Russia.

[a] *Molecular and Condensed Matter Physics, Department of Physics and Astronomy, Uppsala University, P.O. Box 516, Uppsala, Sweden*

[b] *Frumkin Institute of Physical Chemistry and Electrochemistry of Russian Academy of Science, Moscow, Russia*

[c] *Kurnakov Institute of General and Inorganic Chemistry, Russian Academy of Sciences, Moscow, Russia*

[d] *National Research Centre "Kurchatov Institute", Moscow, Russia*

[e] *Paul Scherrer Institute, Swiss Light Source, WLGA 211, CH-5232, Villigen, The Switzerland*

[f] *The Rossendorf Beamline at ESRF – The European Synchrotron, CS40220, 38043 Grenoble Cedex 9, France*

[g] *Helmholtz Zentrum Dresden-Rossendorf (HZDR), Institute of Resource Ecology, PO Box 510119, 01314 Dresden, Germany.*

* Corresponding author: Kristina O. Kvashnina kristina.kvashnina@esrf.fr

Introduction

Nanotechnology is a rapidly growing field, with one of the most active areas being the development of nanomedical products to develop new therapeutic strategies against cancer. Cerium oxide possesses excellent pro- and anti-oxidant properties because of the action of the Ce(III)/Ce(IV) redox couple at its surface.[1-5] Approaching the nanoscale, ceria catalysts become profoundly more reactive due to the enhanced surface area to volume ratio, indicating that the interface chemistry is crucial. Many studies have indicated that the shape and size of nanoparticles (NPs) considerably affects the selectivity and activity of reactions involving CeO_2 NPs. The ability to understand the NP surface science is vital, as it allows interactions between NPs and surrounding environments to be characterized and understood, and finally also to be tuned to obtain even higher efficacy.

It has been repeatedly shown that CeO_2 NPs actively participate in processes occurring in biological media at ambient temperatures,[6,7] with the performance of the NPs dictated by NP

size. CeO_2 NPs with sizes larger than 10 nm cause oxidative stress, which leads to the formation of reactive oxygen species (ROS) such as hydrogen peroxide, superoxide radical, hydroxyl radical and so forth in living cells.[8-10] Conversely, ceria NPs of 2-10 nm typically act as anti-oxidants by ROS scavenging. However, the size effect is not solely responsible for ceria efficiencies and several other factors have to be taken into account. These factors include particle shape, surface chemistry, and surface modifiers or ligands that can participate in complexation and redox reactions.[11-14] It is commonly believed that the behavior of ceria NPs is closely related to the changes in oxygen non-stoichiometry, e.g., the Ce(IV)/Ce(III) ratio.[8,15-18]

The dependence of complex reactivity on the ceria oxidation state and the presence of Ce(III) species at the surface have been studied earlier, using multiple analytical techniques, including X-ray photoelectron spectroscopy (XPS),[10,19-22] resonant photoemission spectroscopy (RPES),[23,24] X-ray absorption spectroscopy (XAS),[25-28] electron energy loss spectroscopy (EELS),[29-30] electron magnetic resonance spectroscopy (EMS)[31] and chemical methods.[32] Unfortunately, high-vacuum conditions and X-ray exposure can affect the Ce(IV)/Ce(III) ratio in CeO_2 NPs. Zhang and co-authors[27] demonstrated that the concentration of Ce(III) determined by XPS increases dramatically after specimen are stored overnight in a vacuum chamber (from 11.6% immediately after sample-loading to 29.3%). Our previous work[33] also confirmed the partial reduction of Ce(IV) to Ce(III) during XPS measurements. In turn, in the majority of papers in which XAS has been used for ceria NP characterization,[25-27] the Ce(III) concentration does not exceed 5% (i.e., close to the lower detection limit) and is independent of particle size. These results suggest that the differences in biological activity of ceria NPs of various origins cannot be explained simply by variations in Ce(III) content.

Despite the large body of experimental evidence showing the beneficial effects of nanoceria in living systems, the underlying key chemical mechanisms and the nature of the active species responsible for these outstanding properties remains elusive. This mainly results from the likelihood of relatively low concentrations of the active species and the inability to distinguish the contributions from surface and sub-surface species and structures. This requires direct, advanced characterization and theoretical validation. Here, we use X-ray diffraction (XRD), high-resolution transmission electron microscopy (HRTEM), small angle X-ray scattering (SAXS), high energy resolution fluorescence detected hard X-ray absorption spectroscopy (HERFD-XAS) and soft X-ray XAS techniques to elucidate the structure, surface and chemical states of monodispersed ceria NPs varying in diameter from 2 to 8 nm.

Soft X-ray spectroscopy at the Ce M_5 edge probes 4f states,[34]while HERFD-XAS at the Ce L_3 edge interrogates the 5d orbitals, which are involved in chemical bonding[35,36] (Fig. S1). Additionally, Ce L_3 edge measurements yield complementary information concerning the number of 4f electrons through quadrupole-allowed electronic transitions.[25,37] Coupling these two techniques, we show that spectral profiles at the Ce L_3 and Ce M_5 edges of ceria NPs exhibit different features. The results are compared to those of bulk CeO_2 (particles larger than 25 nm). These experiments confirm the absence of Ce(III) at the surface of all NPs, while revealing the influence of the surface on the electronic structure of ceria NPs. Experimental results are supported by state-of-the-art ab-initio calculations and theory based on the single Anderson impurity method (SIAM). Furthermore, the HERFD-XAS studies at the Ce L_3 edge demonstrate how conventional drying procedures affect the surface of nanoceria, which in turn modifies the physical and chemical properties of the resulting nanomaterials.

Figure 1 illustrates the processes involved in the HERFD-XAS and soft XAS experiments that are key to the results. The energy diagrams and electronic transitions, which involve the creation of core holes in the 3d and 2p states, thereby probing the Ce 4f and Ce 5d valence shells, are also shown in Figure 1.

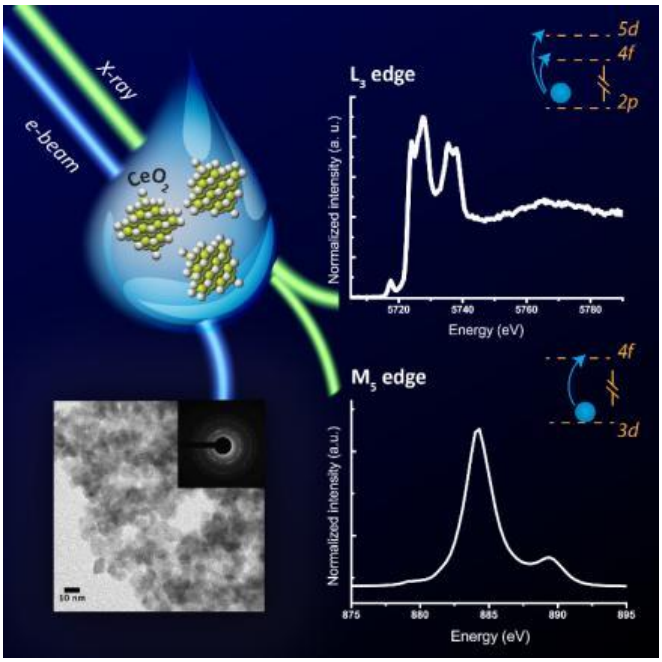

Figure 1. Illustration of the advanced experimental probes and processes. Valence and surface features of ceria NPs were studied by high resolution X-ray absorption techniques: HERFD-XAS for L_3 edge absorption and soft XAS for M_5 edge. Together with the spectroscopic investigation of NPs, they were examined with HRTEM (bottom left) for a comprehensive analysis.

Experimental section

Synthesis route

Aqueous solution of cerium (III) nitrate hexahydrate was used as stock solutions. To prepare the solutions, a calculated amount of cerium salt was dissolved in MilliQ water (18.4 MOhm/cm). Final concentrations of $Ce(NO_3)_3 \cdot 6H_2O$ were determined to be 0.001M, 0.1M and 0.8M. For NP precipitation, the cerium stock solution was added to a fivefold excess of 3M aqueous ammonia at room temperature under continuous stirring. The precipitate formed was allowed to age for 12 h. After that the yellow precipitate was separated by centrifugation and washed three times with MilliQ water to remove soluble admixtures. For further characterization, CeO_2 samples were prepared in three different ways: “as-prepared sample” – CeO_2 NPs after washing procedure without any thermal treatment; “sample dried at 40 °C” – as-prepared NP after drying overnight under ambient environment at 40 °C; “sample dried at 150 °C” – as-prepared NP after drying overnight under an ambient environment at 150 °C.

Characterizations of CeO_2 NPs

The XRD data were recorded using a Bruker D8 Advance diffractometer (Cu Kα radiation). The PC- PDF database was used for the identification of the crystalline phases. No traces of amorphous phases in the XRD pattern were detected. The synchrotron-based XRD measurements were performed at the “XSA (X-ray Structural Analysis)” beamline of the Kurchatov Synchrotron Radiation Source (NRC “Kurchatov Institute”, Moscow). For synchrotron-

based XRD measurements CeO_2, NPs samples were placed in synthetic vacuum oil and mounted on 20 µm nylon CryoLoop. The measurements were performed in the transmission mode using a Rayonix SX-165 CCD detector at a wavelength of 0.80 Å. Raw 2D scattering images were integrated using the Fit2D program.

Microstructural evaluation studies were performed using JEOL-2100F transmission electron microscopes (HRTEMs) with accelerating voltages of 200 kV. Electron diffraction patterns were recorded using the same instruments.

Small-angle X-ray scattering patterns were registered using monochromatic Cu Kα radiation in a broad angular range (scattering vectors(s) between 0.1 and 27 nm^{-1}), using a SAXSess diffractometer (Anton Paar). Samples were placed in standard X-ray capillaries. A Kratki collimation scheme was used. Slit geometry providing a highly intense primary X-ray beam was employed; reduction to point geometry (desmearing) was performed using a standard algorithm.[38] All measurements were performed at room temperature in an evacuated chamber (residual pressure 5−10 mbar).

HERFD-XAS experiments were performed at beamline BM20 of the European Synchrotron Radiation Facility in Grenoble. The incident energy was selected using the <111> reflection from a double Si crystal monochromator. Rejection of higher harmonics was achieved by two Si mirrors working at an angle of 2.5 mrad relative to the incident beam. The incident X-ray flux was ~10^{10} photons·s^{-1} at the sample position. HERFD-XAS spectra were measured using an X-ray emission spectrometer[39] at 90° horizontal scattering angle. Sample, analyzer crystal and photon detector (avalanche photodiode) were arranged in a vertical Rowland geometry. The Ce HERFD-XAS spectra at the L_3 edge were obtained by recording the maximum intensity of the Ce $L\alpha_1$ emission line (4839 eV) as a function of the incident energy. The emission energy was selected using the <331> reflection of one spherically bent Ge crystal analyzer (with R = 1m) aligned at a 87° Bragg angle. A combined (incident convoluted with emitted) energy resolution of 0.9 eV was obtained, as determined by measuring the FWHM of the elastic peak.

The ceria M_5 XAS edge spectra were measured at the PHOENIX beamline located at the Swiss Light Source (SLS) in Villigen, Switzerland. The beamline covers soft and tender X-rays ranging from 0.4-8 keV, by use of two branchlines: A low energy branchline serves 0.4-2 keV and a high energy branchline serves 0.8-8 keV. The source of the beamline is an elliptical undulator. Both branchlines provide either an unfocussed beam or a micro-focus of about 3 □m. The measurements presented here were made on the high energy branchline. This branch employs a double crystal monochromator and a high harmonics suppressor consisting of 2 planar mirrors. To generate monochromatic light at energies about 0.8 keV, a Beryl crystal was used. The incoming flux (I_0) was measured from the total electron yield taken from a polyester foil (0.5 □m thickness), which was coated with 50 nm of nickel. The beamsize used in the experiments was 0.7 X 0.9 mm^2. Both total fluorescence and total electron yield were measured on the sample. As fluorescence yields are low at $M_{4,5}$ edges, only the total electron yield data were used. A Keithley ampere meter was used to collect the current from a I_0 signal and sample.

Theoretical simulations

The Ce L_3 theoretical calculations were performed using the FEFF 9.6. code.[40] The input files were based on the atomic unit cell parameter a=0.541 nm. Calculations were made in a similar way, as reported by Li et al.[41] previously for bulk CeO_2. Full multiple scattering (FMS) calculations were

performed using a Hedin-Lundqvist self-energy correction and other standard cards. The apparent reduction of the core hole lifetime broadening was achieved by using the EXCHANGE card. The spectrum for the CeO_2 2 nm NPs with OH groups has been calculated for a cluster of 315 atoms. The structure was optimized using an Avogadro program.

The calculations of the Ce M_5 edge spectra were performed in a framework of the Anderson impurity model.[42] The spectra of bulk CeO_2 were calculated in a manner described in Ref.[34] for the Ce(IV) system, taking into account the Ce 4f hybridization with the valence states and the full multiplet structure, due to intra-atomic interactions. The ground (final) state of the spectroscopic process was described by a linear combination of the $4f^0$, $4f^1\underline{\upsilon}^1$ and $4f^2\underline{\upsilon}^2$ ($3d^94f^1$, $3d^94f^2\underline{\upsilon}^1$ and $3d^94f^3\underline{\upsilon}^2$) configurations, where $\underline{\upsilon}$ stands for an electronic hole in the valence level. The values for the model parameters were set the same as in Ref. [34]: the energy for the electron transfer from the valence band to the unoccupied Ce 4f level Δ=2.0 eV; the 4f-4f Coulomb interaction U_{ff}=9.0 eV; the 3d core hole potential acting on the 4f electron U_{fc}=12.6 eV and the Ce 4f – valence state hybridization term V=1.0 eV (0.6 eV) in the ground (final) state of the spectroscopic process.

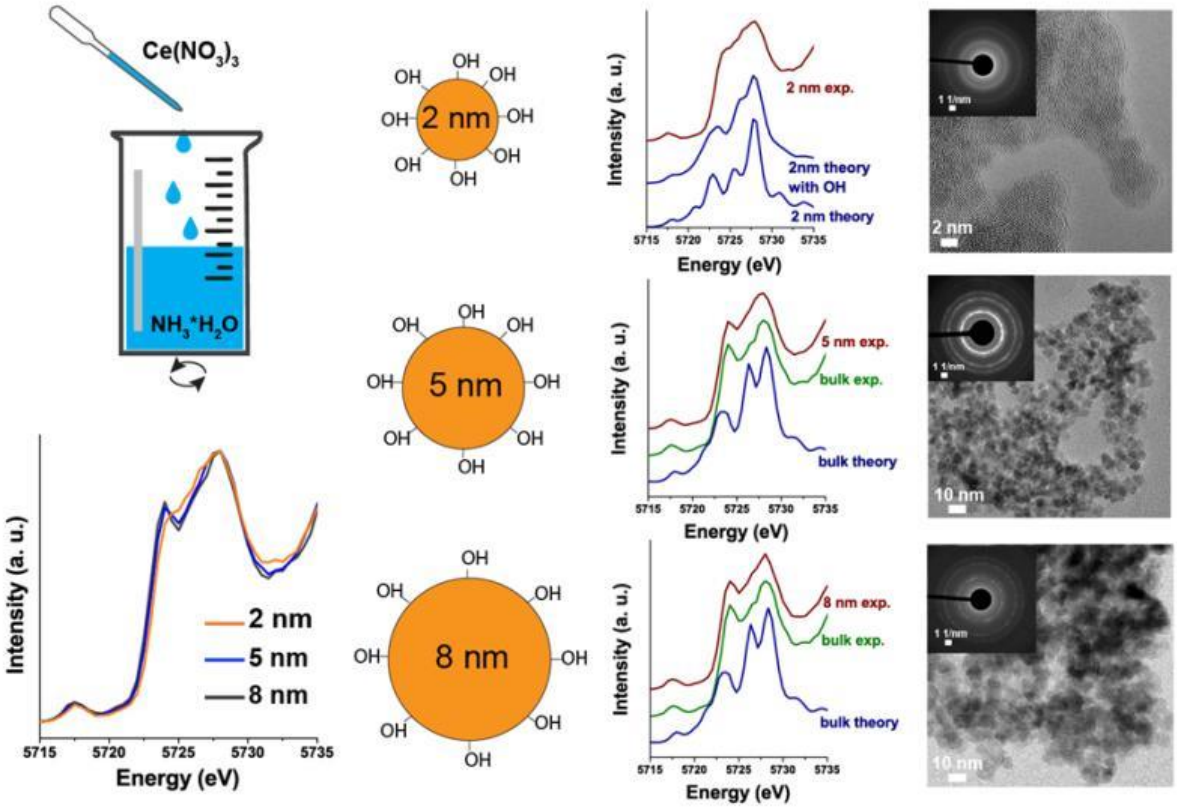

Figure 2. Schematic drawing of the synthesis of CeO_2 NPs and conceptual depictions of NPs structure with hydroxyl groups at the surface. Representative Ce HERFD-XAS spectra for 2 nm; 5 nm; 8 nm CeO_2 NPs recorded at the Ce L_3 edge compared to the bulk CeO_2 (> 25 nm) and theoretical calculations. The HRTEM images of CeO_2 NPs of 2 nm, 5 nm and 8 nm size and selected area electron diffraction (SAED) data (upper left inserts) are also shown.

Results and discussion

The present study solidly identifies, for the first time, the active species of ceria NPs by applying experimental X-ray spectroscopy methods and theoretical calculations. Nanoceria of different sizes were prepared using a facile, rapid chemical precipitation method[33]. The CeO_2 NPs obtained

were characterized by XRD, HRTEM and SAXS methods to determine size, morphology, and chemical composition. Based on the analytical results (Fig. S2, S3, S4), NP diameters were 2 nm for CeO_2 prepared from 0.001M $Ce(NO_3)_3$, 5 nm for CeO_2 prepared from 0,1M $Ce(NO_3)_3$ and 8 nm for CeO_2 prepared from 0.8M $Ce(NO_3)_3$.

Figure 2 shows the HERFD-XAS experimental spectra (red curves) of CeO_2 NPs with 2 nm, 5 nm and 8 nm diameters recorded at the Ce L_3 edge, in comparison to the spectrum of bulk CeO_2 (particles > 25 nm in diameter, green curve). Green curves are identical in all panels of Figure 2 and are plotted here for clarity of results. Measurements were carried out at the Ce 2p core level, which means that the electron being excited by the incident X-rays is from the 2p orbital of Ce at the energy of 5723 eV. It was excited into an empty valence orbital of CeO_2 NPs.

The spectra reveal the presence of the dipole-allowed 2p-5d transitions (main edge transitions in the energy range 5720-5730 eV) and of the forbidden quadrupole 2p-4f transitions (at the pre-edge in the energy range 5715-5720 eV). These experiments utilized an X-ray emission spectrometer[39] to record transitions with high-energy resolution that reveal the fine structure of the 5d and 4f orbitals. This allows us to discern and compare the spectral features and structures originating at the surface (in this case for 2 nm NPs) and from the bulk of the ceria.

In accordance with previous investigations,[25] the pre-edge structure for the three sizes of NPs reveals solely the presence of the Ce(IV) oxidation state (Fig. S5.) This is in agreement with the previously observed absence of Ce(III) inside CeO_2 NPs, even with sizes around 2 nm[25] without any post-synthesis treatment. In contrast, the 5d electronic states in HERFD-XAS spectra (or main edge transitions) have different shapes.[26,43] We found that peaks in the L_3 HERFD-XAS spectra of 2 nm CeO_2 are essentially just starting to develop and are broad in comparison to those obtained from 5 nm, 8 nm and bulk CeO_2. This would be in line with electron delocalization at the surface of NPs, and hence there is a decreasing probability of discrete electron transfer from the 2p to the 5d orbital. Note that it is the cerium 5d orbitals which are chemically active and can form additional bonds with precursor or surfactant materials. Therefore, we investigate here the impact of hydroxyl groups on the electronic structure of nanoceria.

The nature of hydroxylation of the CeO_2 surface is still an open question. Previously, the formation of OH groups onto the CeO_2 surface as a result of water dissociation was observed for samples prepared by vapor chemical deposition.[44,45] In the present work, the CeO_2 was synthesized from water solution; therefore the presence of cerium hydroxide phase is also possible. Badri et al.[46] investigated CeO_2 obtained by a similar synthesized method, using infrared spectroscopy, and observed the presence of OH groups that disappeared during calcination. The authors explain the observed OH groups as evidence of “cerium oxyhydroxide microphases”. The XRD data in the current research (Fig.S7) confirm that nanoparticle samples (as prepared) consist of a pure CeO_2 phase; the presence of amorphous hydroxide layers cannot be fully excluded, however, by XRD measurements. The OH groups on the metal oxide surface will form in water or under water vapor by protonation of the surface oxygen groups, depending on the pH. In the present study, the aqueous suspension of the as-prepared CeO_2 samples has a near neutral pH, i.e., slightly below the point of zero charge for CeO_2 (8.1).[47] Therefore, formation of surface OH groups is, in fact, likely for the non-dried samples.

With the help of ab-initio calculations (the blue curves in Figure 2), it is shown that spectral shape changes because of the presence of OH-groups at the surface of NPs, pointing towards the strong

influence of the surface composition on the reactivity and performance of nanomaterials in specific applications. Theoretical calculations for bulk CeO_2 have been performed using an identical procedure, as reported by Li et al.[41] Similar to the work of Li et al., we show here only part of the absorption spectra, which corresponds to the 2p-5d transitions, and omit multi-electron excitations from the experimental data, which appear at higher incident energy (reported in Figure 1 in the incident energy range 5736-5738 eV). The theoretical spectrum for 2 nm CeO_2 (Figure 2 top, lower blue curve) has been calculated using the same input file and parameters as for bulk CeO_2, but with a cluster size corresponding to 2 nm particles. A noticeable difference between the two calculations is evident. More drastic changes occur, however, once the oxygen surface groups of the 2 nm NPs are hydroxylated at the surface of the 2 nm CeO_2 NPs (Fig. 2 top, upper blue curve denoted 2 nm theory with OH). As soon as particles grow large, the effects of the OH groups at the surface are diminished in the spectra, but are still visible in the case of 5 nm CeO_2 and disappear completely for particles as large as 8 nm. The theoretical results show that changes in the HERFD-XAS spectral profiles originate from the different distribution of the unoccupied Ce 5d states near the Fermi levels in three different cases (bulk CeO_2, 2nm CeO_2 and 2nm CeO_2 with OH groups).

Besides providing new insight into the structure of NPs at the surface, these results pose new questions to the field of chemistry and, on a more technical level, on the coupling mechanism of X-ray excited states to the surface electronic structure and the localization of the valence electrons in very small NPs.

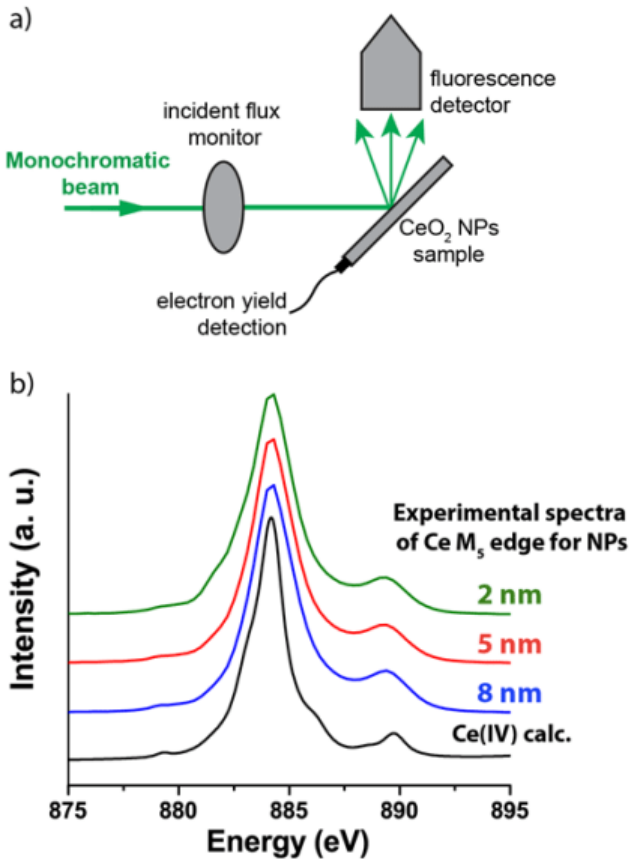

Figure 3. Schematic of the experimental setup for XAS measurements at the Ce M_5 edge (a). Spectra of 2, 5 and 8 nm CeO_2 NPs (green, red and blue curves) have been measured in total-electron-yield mode and compared to the calculations for CeO_2 using the SIAM (black curves).

Counting electrons on NPs surfaces

Structural insights on the surface layers present in 2 nm and 5 nm NPs were obtained by soft XAS experiments. The results provided by the HERFD-XAS experiments were confirmed by measurements in the soft X-ray energy range (~800 eV) at the Ce M_5 edge, as reported in Figure 3. An excited 4f state, which is coupled to the ground 3d state, reveals the absence of Ce(III) at the surface of NPs. The spectra of the CeO_2 NPs at the Ce $M_{4,5}$ edges were previously described[48] as consisting of surface and bulk components.[49] The contribution of the surface component increases with decreasing NP sizes.

Our measurements at the Ce L_3 edge do not confirm the presence of any Ce(III) in our samples. Figure 3 shows that the shape of the Ce M_5 spectra is very similar for all CeO_2 NPs and can be well reproduced by model calculations for the Ce(IV) system, which take into account the Ce 4f - O 2p hybridization and the full multiplet structure, due to intra-atomic interactions at the Ce site. The spectra exhibit a distinct and strong high-energy satellite at ~5.5 eV above the main line.

This high-energy satellite has been discussed before for bulk CeO_2 (e.g. Ref. [34]) and shown to be due to Ce 4f - O 2p charge-transfer, as a result of strong Ce 4f - O 2p hybridization and configurational mixing. A good agreement of the calculations with the experiments suggests that contributions of the $4f^0$, $4f^1\underline{\upsilon}^1$ and $4f^2\underline{\upsilon}^2$ configurations in the ground state amount to 49%, 46% and 5%, respectively. The Ce 4f occupancy in the ground state was found to be 0.56 electrons, which indeed indicates a highly covalent character of the chemical bonding, as in bulk CeO_2. The soft XAS approach reconciles previous disparities in the results obtained by different spectroscopic methods and importantly acknowledges that NPs show identical electronic structure information by soft and hard X-ray spectroscopy if they are performed at identical conditions.

Post-processing temperature treatment of NPs

We have previously discussed the measurement results and theoretical calculations for the samples obtained immediately after synthesis (as-prepared samples). To further elucidate the effect of surface hydroxylation on the electronic structure of the NPs, we subjected them to a 24-h heat treatment at 40 °C and 150 °C in air. According to XRD and HRTEM measurements (Fig. 4, Fig. S7, S8), the drying process did not affect the phase crystallinity, morphology, and particle size distribution. In contrast, the spectral shapes at the Ce L_3 edge changed when going from as-prepared to dried CeO_2 NPs, suggesting changes of the electronic structure.

Figure 4 shows that drying 2 nm CeO_2 at 40 °C and 150 °C resulted in a change of the main Ce L_3 edge transitions corresponding to the excitations to the Ce 5d orbitals. The intensity difference of the 2p-5d transitions between three ceria samples (as-prepared; dried at 40 °C and 150 °C) is pronounced in the case of small NPs. For the 5 nm NPs, drying still induces weak spectral changes, while no effect of temperature treatment is observed for the 8 nm NPs. As expected, changes of the electronic structure in 2 and 5 nm CeO_2 NPs are associated with a dehydroxylation of the NP surface: Upon thermal treatment, ceria NPs lose OH groups from their surface and the effect is more pronounced for small NPs. According to thermogravimetric analysis coupled with a mass spectrometry for 2 nm NPs, sample water is released in the temperature range 40 – 200°C (Fig.S8). Surface contributions from the NPs structure decrease with the increase in size.

Understanding the electronic structure changes at the surface is important for many surface-related processes associated with ceria NPs. As noted previously, ceria NPs with a size of less than 10 nm exhibit antioxidant activity scavenging ROS. Such property is commonly attributed to an increase of Ce(III) concentration at the surface, with a decrease of particle size.[50] However, at present, the discussion concerning the mechanisms of ceria biological activity needs further revision to recognize the absence of Ce(III) in the NPs. For instance, Cafun et al.[25] demonstrated that 3 nm ceria NPs, prepared by a wet chemistry technique, catalyse hydrogen peroxide (type of ROS) decomposition. The mechanism of such a reaction remained uncertain, but it was suggested that NP electronic structure changes drastically compared to the bulk CeO_2 (mostly due to the Ce-O orbital mixing), since no Ce(III) species were detected in these ceria NPs. We also did not find any indication of the Ce(III) species, but the present study is the first, to our knowledge, to provide the evidence and explore the electronic structure changes of CeO_2 NPs associated with the hydroxyl species at the surface of NPs. Due to different surface area to volume ratios for 8, 5 and 2 nm NPs, the surface effect of hydroxyl species should be more pronounced for smaller ceria NPs. Even a very soft thermal treatment of ceria NPs at 40 °C leads to significant changes and a decrease in surface hydroxylation. This leads us to assume that the antioxidant activity of the particles is directly related to concentration of hydroxyl species at the surface: with an increase of surface area to volume ratio, the antioxidant activity of NPs increase. Our direct measurements of CeO_2 NPs antioxidant activity supported this assumption. It was found 2 nm CeO_2 NPs do possess higher radical scavenger ability in comparison to 8 nm CeO_2 NPs (Fig. S9).

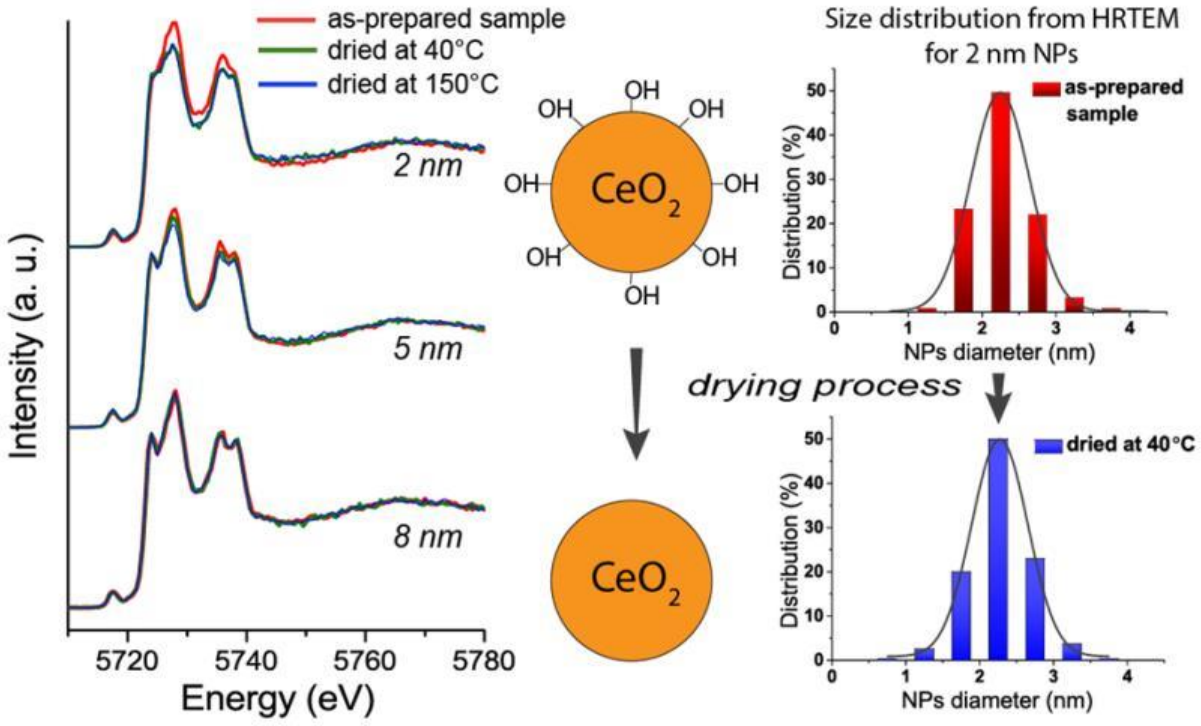

Figure 4. Representative Ce L_3 edge HERFD-XAS spectra and size distribution histograms of NPs extracted from HRTEM data for as-prepared NPs and dried NPs at different temperatures

It should be noted that surface hydroxyl species affect not only the biological activity of ceria but also their behavior in several industrial applications. As demonstrated in numerous papers, the presence of water molecules in a catalytic system affects the adsorption properties of ceria oxide.[51] Earlier, it was proposed that O_2 cannot adsorb on a perfect CeO_2 surface, but strongly

binds at oxygen vacancies. With the development of low-temperature catalysts, the proposed mechanism of oxygen sorption has become questionable. There have been extensive experimental studies,[52,53] which showed that water plays an important role in CO oxidation. According to density functional theory calculations, OH groups can facilitate O_2 adsorption on CeO_2, even at low OH coverage.[53] Our investigation on the electronic structure of as-prepared and dried ceria NPs clearly demonstrates that OH groups on CeO_2 surfaces possess a long-range effect on the O_2 adsorption.

Conclusions

Electronic interactions between the bulk and the surface of NPs control the functionality of nanomaterials. In this study, we have used two large scale synchrotron facilities to study the surface effects of nanoceria at the atomic level. For lanthanide ions, soft X-ray M_5 edge spectroscopy allows access to f-orbitals and hard X-ray L_3 edge to f- and d-orbitals, which are involved in chemical bonding. Using those techniques, we show that the electronic structure of nanoceria is directly affected by the presence of the hydroxyl groups at the surface. We confirm the entire absence of the Ce(III) oxidation state in CeO_2 NPs of different size. Moreover, we study the effect of surface modification by drying NPs of different size at several temperatures. After the temperature treatment the Ce charge remains as Ce(IV); however, the observed difference in the experimentally obtained spectra is attributed to the changes in hydroxylation of the NP surface (CeO_2 NPs loose OH groups from their surface). The observed temperature related effect is more pronounced for small NPs, since the surface contributions versus bulk increases for smaller NPs. In this work, we present two distinct theoretical approaches to analyze the experimental evidence, which together confirm our hypothesis of strongly coordinated hydroxyl ligands at the surface of NPs synthesized from aqueous solutions of cerium salts. This finding suggests that changing the cerium ligand bonding of the surface cerium atoms can change its chemical properties and biological activity substantially.

Conflicts of interest

There are no conflicts to declare.

Acknowledgements

Authors thank HZDR for the beamtime allocation of project 20-01-800 and P. Glatzel at ID26 beamline of ESRF for providing Ge crystal for the Ce L_3 HERFD-XAS measurements. We are also grateful to the “Nanochemistry and Nanomaterials” user facility of the Department of Chemistry of MSU for providing the HRTEM measurements. SAXS measurements were performed using equipment of CKP FMI IPCE RAS.

K.O.K, E.G and S.B. acknowledge support from European Commission Council under ERC grant No. 759696. A.Yu.R, T.V.P. and A.D.K. acknowledge support from RFBR according to the research project No. 18-33-20129. V.K.I. acknowledge support from Russian Science Foundation, grant No. 19-13-00416. S.M.B. acknowledges support from the Swedish Research Council (research grant 2017-06465) and support of travel costs to perform the experiment at SLS from the European Union’s Horizon 2020 research and innovation programme under grant agreement n.° 730872, project CALIPSOplus.

Author Contributions

T.V.P, A.Yu.R. and K.A.D carried out the NP synthesis work. A.V.E., A.E.B. and A.A.S. performed characterizations of the samples using an in-house laboratory equipment. P.V.D. performed synchrotron XRD. K.O.K., A.Yu.R., T.V.P. carried out HERFD-XAS measurements at the Ce L_3 edge. E.G, S.B, T.H and S.M.B performed soft X-ray measurements at the Ce M_5 edge. S.M.B. and K.O.K. did theoretical simulations of experimental spectra. V.K.I., K.O.K., A.C.S., and S.N.K. were involved in planning and supervision of the work. K.O.K., T.V.P, A.Yu.R, S.M.B., V.K.I., and S.N.K. co-wrote the paper. M.M.S. performed antioxidant activity measurements. All authors discussed the results and contributed to the final manuscript.

References

1. A. R. Gliga, K. Edoff, F. Caputo, T. Källman, H. Blom, H. L. Karlsson, L. Ghibelli, E. Traversa, S. Ceccatelli and B. Fadeel, Sci. Rep., 2017, 7, 9284.

2. J. Das, Y.-J. Choi, J. W. Han, A. M. T. Reza and J.-H. Kim, Sci. Rep., 2017, 7, 9513.

3. L. A. Wills, X. Qu, I. Y. Chang, T. J. L. Mustard, D. A. Keszler, K. A. Persson and P. H.-Y. Cheong, Nat. Commun., 2017, 8, 15852.

4. M. E. Khan, M. M. Khan and M. H. Cho, Sci. Rep., 2017, 7, 1-17.

5. A. B. Shcherbakov, N. M. Zholobak and V. K. Ivanov, in Cerium Oxide (CeO2): Synthesis, Properties and Applications, eds. S. Scirè and L. Palmisano, Elsevier, 2019, pp. 279-328.

6. C. Walkey, S. Das, S. Seal, J. Erlichman, K. Heckman, L. Ghibelli, E. Traversa, J. F. McGinnis and W. T. Self, Environ. Sci. Nano, 2015, 2, 33-53.

7. S. Das, J. M. Dowding, K. E. Klump, J. F. McGinnis, W. Self and S. Seal, Nanomedicine, 2013, 8, 1483-1508.

8. T. Pirmohamed, J. M. Dowding, S. Singh, B. Wasserman, E. Heckert, A. S. Karakoti, J. E. S. King, S. Seal and W. T. Self, Chem. Commun., 2010, 46, 2736-2738.

9. N. M. Zholobak, A. B. Shcherbakov, E. O. Vitukova, A. V. Yegorova, Y. V. Scripinets, I. I. Leonenko, A. Y. Baranchikov, V. P. Antonovich and V. K. Ivanov RSC Adv., 2014, 4, 51703-51710.

10. X. Jiao, H. Song, H. Zhao, W. Bai, L. Zhang and Y. Lv, Anal. Methods, 2012, 4, 3261-3267.

11. E.-J. Park, J. Choi, Y.-K. Park and K. Park, Toxicology, 2008, 245, 90-100.

12. L. Weisheng, H. Yue-wern, Z. Xiao-Dong and M. Yinfa, Int. J. Toxicol., 2006, 25, 451-457.

13. A. B. Shcherbakov, N. M. Zholobak, V. K. Ivanov, O. S. Ivanova, A. V. Marchevsky, A. E. Baranchikov, N. Y. Spivak and Y. D. Tretyakov, Russ. J. Inorg. Chem., 2012, 57, 1411-1418.

14. J. Colon, L. Herrera, J. Smith, S. Patil, C. Komanski, P. Kupelian, S. Seal, D. W. Jenkins and C. H. Baker, Nanomed. Nanotechnol. Biol. Med., 2009, 5, 225-231.

15. Y. Tsai, J. Oca-Cossio, K. Agering, N. E. Simpson, M. A. Atkinson, C. H. Wasserfall, I. Constantinidis and W. Sigmund, Nanomedicine 2007 2, 325 - 332.

16. K. Reed, A. Cormack, A. Kulkarni, M. Mayton, D. Sayle, F. Klaessig and B. Stadler, Environ. Sci.: Nano., 2014, 1, 390-405.

17. C. Korsvik, S. Patil, S. Seal and W. T. Self, Chem. Commun., 2007, 10, 1056-1058.

18. V. K. Ivanov, A. B. Shcherbakov and A. V. Usatenko, Russ. Chem. Rev., 2009, 78, 855-871.

19. I. Celardo, M. De Nicola, C. Mandoli, J. Z. Pedersen, E. Traversa and L. Ghibelli, ACS Nano, 2011, 5, 4537-4549.

20. S. Deshpande, S. Patil, S. V. Kuchibhatla and S. Seal, Appl. Phys. Lett., 2005, 87, 87-89.

21. N. J. Lawrence, J. R. Brewer, L. Wang, T.-S. Wu, J. Wells-Kingsbury, M. M. Ihrig, G. Wang, Y.-L. Soo, W.-N. Mei and C. L. Cheung, Nano Lett., 2011, 11, 2666-2671.

22. F. Schwabe, R. Schulin, P. Rupper, A. Rotzetter, W. Stark and B. Nowack, J. Nanopart. Res., 2014, 16, 2668.

23. Y. Lykhach, S. M. Kozlov, T. Skála, A. Tovt, V. Stetsovych, N. Tsud, F. Dvořák, V. Johánek, A. Neitzel, J. Mysliveček, S. Fabris, V. Matolín, K. M. Neyman and J. Libuda, Nat. Mater., 2015, 15, 284.

24. G. N. Vayssilov, Y. Lykhach, A. Migani, T. Staudt, G. P. Petrova, N. Tsud, T. Skála, A. Bruix, F. Illas, K. C. Prince, V. r. Matolı´n, K. M. Neyman and J. Libuda, Nat. Mater., 2011, 10, 310.

25. J.-D. Cafun, K. O. Kvashnina, E. Casals, V. F. Puntes and P. Glatzel, ACS Nano, 2013, 7, 10726-10732.

26. C. Paun, O. V. Safonova, J. Szlachetko, P. M. Abdala, M. Nachtegaal, J. Sa, E. Kleymenov, A. Cervellino, F. Krumeich and J. A. van Bokhoven, J. Phys. Chem. C, 2012, 116, 7312-7317.

27. F. Zhang, P. Wang, J. Koberstein, S. Khalid and S.-W. Chan, Surf. Sci., 2004, 563, 74-82.

28. L. Artiglia, F. Orlando, K. Roy, R. Kopelent, O. Safonova, M. Nachtegaal, T. Huthwelker and J. A. van Bokhoven, J. Phys. Chem. Lett., 2017, 8, 102-108.

29. B. Goris, S. Turner, S. Bals and G. Van Tendeloo, ACS Nano, 2014, 8, 10878-10884.

30. U. M. Graham, M. T. Tseng, J. B. Jasinski, R. A. Yokel, J. M. Unrine, B. H. Davis, A. K. Dozier, S. S. Hardas, R. Sultana, E. A. Grulke and D. A. Butterfield, ChemPlusChem, 2014, 79, 1083-1088.

31. P. Dutta, S. Pal, M. S. Seehra, Y. Shi, E. M. Eyring and R. D. Ernst, Chem. Mater., 2006, 18, 5144-5146.

32. O. O. Stoianov, V. K. Ivanov, A. B. Shcherbakov, I. V. Stoyanova, N. A. Chivireva and V. P. Antonovich, Russ. J. Inorg. Chem., 2014, 59, 15-23.

33. T. V. Plakhova, A. Y. Romanchuk, S. N. Yakunin, T. Dumas, S. Demir, S. Wang, S. G. Minasian, D. K. Shuh, T. Tyliszczak, A. A. Shiryaev, A. V. Egorov, V. K. Ivanov and S. N. Kalmykov, J. Phys. Chem. C, 2016, 120, 22615-22626.

34. S. M. Butorin, D. C. Mancini, J. H. Guo, N. Wassdahl, J. Nordgren, M. Nakazawa, S. Tanaka, T. Uozumi, A. Kotani, Y. Ma, K. E. Myano, B. A. Karlin and D. K. Shuh, Phys. Rev. Lett., 1996, 77, 574-577.

35. A. V. Soldatov, T. S. Ivanchenko, S. Della Longa, A. Kotani, Y. Iwamoto and A. Bianconi, Phys. Rev. B, 1994, 50, 5074-5080.

36. A. Kotani, K. O. Kvashnina, S. M. Butorin and P. Glatzel, Eur. Phys. J. B, 2012, 85.

37. K. O. Kvashnina, S. M. Butorin and P. Glatzel, J. Anal. At. Spectrom., 2011, 26, 1265-1272.

38. J. A. Lake, Acta Cryst., 1967, 23, 191-194.

39. K. O. Kvashnina and A. C. Scheinost, J. Synchrotron Radiat, 2016, 23, 836–841.

40. J. J. Rehr, J. J. Kas, F. D. Vila, M. P. Prange and K. Jorissen, Phys. Chem. Chem. Phys., 2010, 12, 5503-5513.

41. Y. Li, O. Kraynis, J. Kas, T.-C. Weng, D. Sokaras, R. Zacharowicz, I. Lubomirsky and A. I. Frenkel, AIP Adv., 2016, 6, 055320.

42. P. W. Anderson, Phys. Rev. , 1961, 124, 41-53.

43. R. Kopelent, J. A. van Bokhoven, J. Szlachetko, J. Edebeli, C. Paun, M. Nachtegaal and O. V. Safonova, Angew. Chem. , 2015, 127, 8852-8855.

44. Y. Lykhach, V. Johánek, H. A. Aleksandrov, S. M. Kozlov, M. Happel, T. Skála, P. S. Petkov, N. Tsud, G. N. Vayssilov, K. C. Prince, K. M. Neyman, V. Matolín and J. Libuda, The Journal of Physical Chemistry C, 2012, 116, 12103-12113.

45. M. Molinari, S. C. Parker, D. C. Sayle and M. S. Islam, J. Phys. Chem. C, 2012, 116, 7073-7082.

46. A. Badri, C. Binet and J.-C. Lavalley, J. Chem. Soc., Faraday Trans., 1996, 92, 4669-4673.

47. L. A. De Faria and S. Trasatti, J. Colloid Interface Sci., 1994, 167, 352-357.

48. S. Turner, S. Lazar, B. Freitag, R. Egoavil, J. Verbeeck, S. Put, Y. Strauven and G. Van Tendeloo, Nanoscale, 2011, 3, 3385-3390.

49. S. Kato, M. Ammann, T. Huthwelker, C. Paun, M. Lampimäki, M.-T. Lee, M. Rothensteiner and J. Bokhoven, Phys. Chem. Chem. Phys., 2015, 17, 5078-5083

50. A. Migani, G. N. Vayssilov, S. T. Bromley, F. Illas and K. M. Neyman, J. Mater. Chem., 2010, 20, 10535-10546.

51. S. Hayun, T. Y. Shvareva and A. Navrotsky, J. Am. Ceram. Soc. , 2011, 94, 3992-3999.

52. L. Ding, F. Xiong, Y. Jin, Z. Wang, G. Sun and W. Huang, Phys. Chem. Chem. Phys., 2016, 18, 32551-32559.

53. H.-L. Chen and H.-T. Chen, Chem. Phys. Lett., 2010, 493, 269-272.

Supplementary information of Article 5

Supporting information

Figure S1 describes schematically the main principles of HERFD-XAS and soft XAS experiments as applied in studies of CeO_2 NPs. The absorbed photons cause excitation of the inner shell electrons of the atoms in the material. These excited inner shell (core) electrons can be promoted to unoccupied energy levels to form a short-lived excited state. CeO_2 soft XAS spectrum shows peaks in M_5 region. The peaks, which occur at the energies 883.6 and 888.6 eV, are attributed to the transitions from $3d_{5/2}$ to 4f states. At the Ce L_3 edge, the electrons are excited from the 2p to 5d states due to the dipole transitions. Pre-edge Ce L_3 edge structure is attributed to the quadrupole 2p to 4f states.

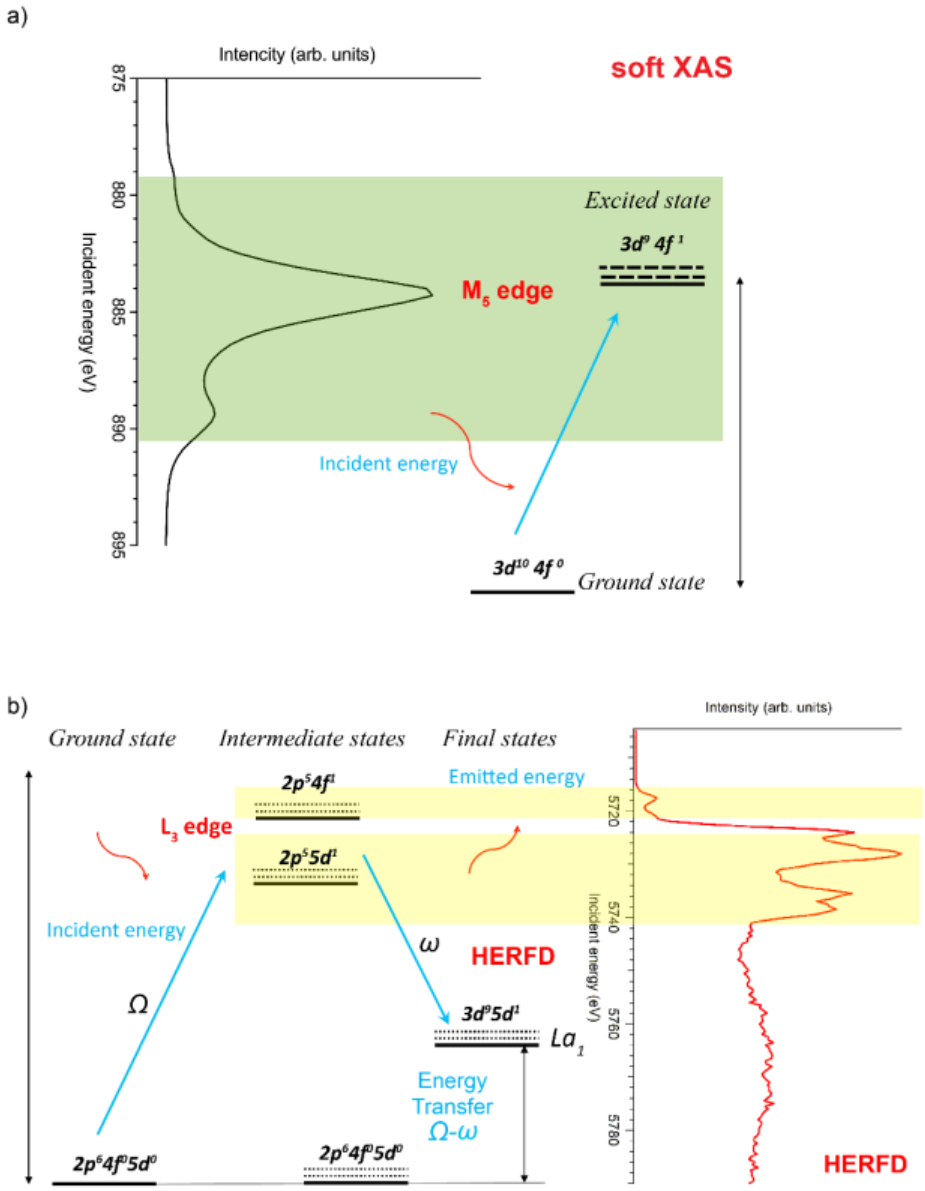

Figure S1. Schematic of a) HERFD-XAS and b) soft XAS techniques.

Figure S2 shows results of the powder XRD analysis for ceria NPs samples. XRD has shown that all samples are of a single phase and correspond to cubic CeO_2 (PCPDF 81-792), that confirms the electron diffraction data obtained from the same samples. The particle size of nanocrystalline ceria (D) from XRD data was calculated using the Scherrer equation (1):

$$D_{hkl} = \frac{K\lambda}{\beta_{hkl}(2\theta)\cos(\theta)}, \quad (1)$$

where λ is the wavelength (0.15 nm); K is the coefficient of anisotropy that is generally set to be 1.0 for spherical particles; θ is the scattering angle in radians; β_{hkl} is full width at half-maximum (FWHM) for diffraction peak expressed in radians. Line profiles for (111) and (200) reflections were fit to pseudo-Voigt functions. Particle size was calculated from FWHM of (111) and (200) diffraction lines. Instrumental broadening was taken into account when calculating the particle size by direct subtraction from the FWHM values. Instrumental broadening for the laboratory XRD equipment was considered to be 0.09 ± 0.01 °2θ. Particle size calculated using Scherrer formula was 2.5 nm for CeO_2 prepared from 0.001M $Ce(NO_3)_3$, 5.5 nm for CeO_2 prepared from 0.1M $Ce(NO_3)_3$ and 8.8 nm for CeO_2 prepared from 0.8M $Ce(NO_3)_3$.

HRTEM images (Fig. S3) show that NPs are fairly uniform in size and mostly have a truncated octahedral shapes. This is in agreement with previously published data from a computer simulations.[1] Electron diffraction patterns for the analyzed samples confirm a fluorite crystal structure. To obtain the average size and distribution from HRTEM images, the calculation of diameters for more than 200 particles were conducted. The measured size distributions are plotted in Figure S3 d), e), and f). All three samples show relatively small polydispersity, and their size distributions can be fitted well by a Gaussian function. Average NPs diameter were 2.3 ± 0.4, 5.9 ± 1.1 and 7.8 ± 1.2 for samples synthesized from 0.001M, 0.1 M and 0.8 M $Ce(NO_3)_2$ respectively. The increase in NPs size with an increase in concentration of initial cerium (III) salt is consistent with previous studies. This fact is usually attributed to the presence of an intermediate stage formation of cerium hydroxide (III) [2]. The crystallite size determined from the XRD data is in a good agreement with the average size found from HRTEM data.

SAXS curves were recorded for ceria NPs samples are reported in Fig. S4. Volume size distributions for NPs were calculated from these curves by the GNOM program[3]. The average particle size was 2, 4 and 8 nm for samples synthesized from 0.001M, 0.1 M and 0.8 M $Ce(NO_3)_2$ correspondingly.

Based on results presented in Fig. S2, S3 and S4, samples are marked as “2 nm” for CeO_2 prepared from 0.001M $Ce(NO_3)_3$, “5 nm” for CeO_2 prepared from 0.1M $Ce(NO_3)_3$ and for “8 nm” for CeO_2 prepared from 0.8M $Ce(NO_3)_3$.

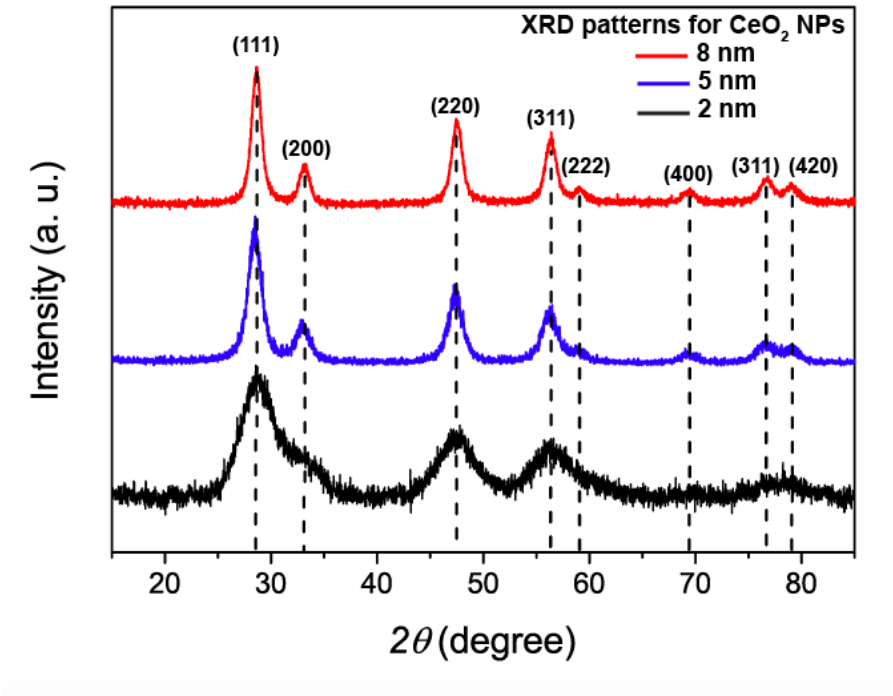

Figure S2. Powder XRD patterns for ceria NPs samples.

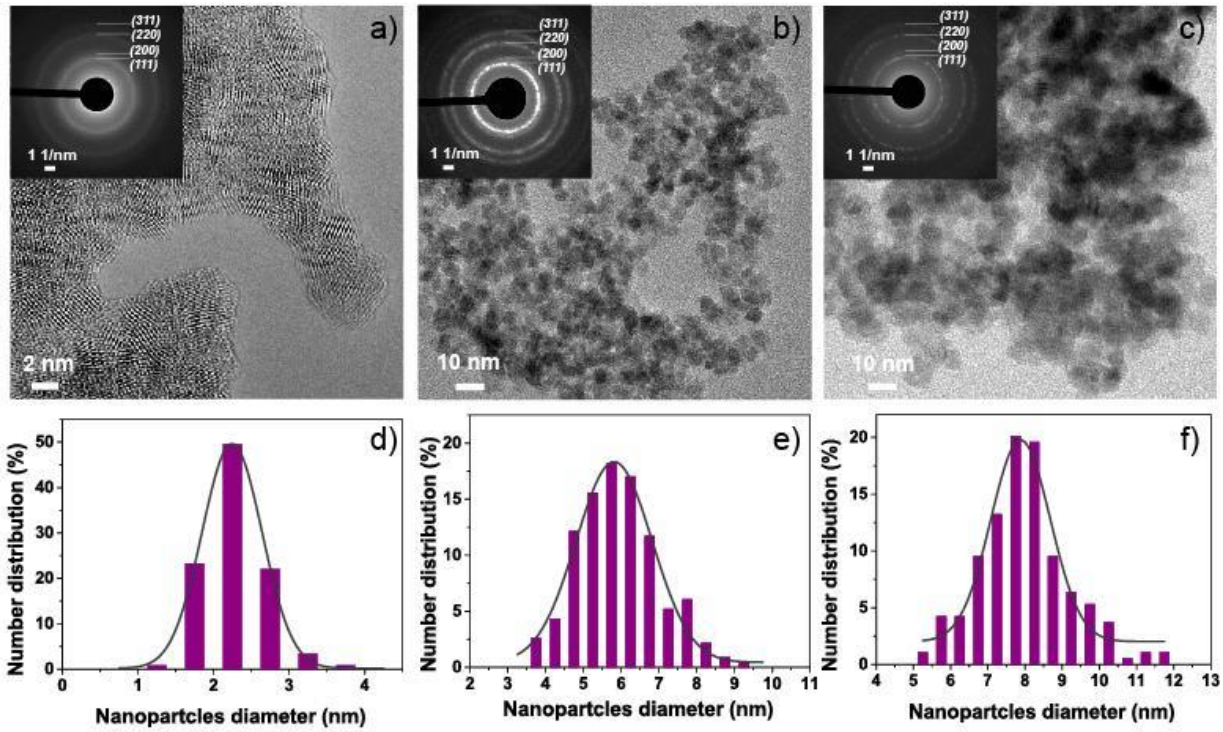

Figure S3. HRTEM images and size distributions from HRTEM for the CeO_2 NPs samples.

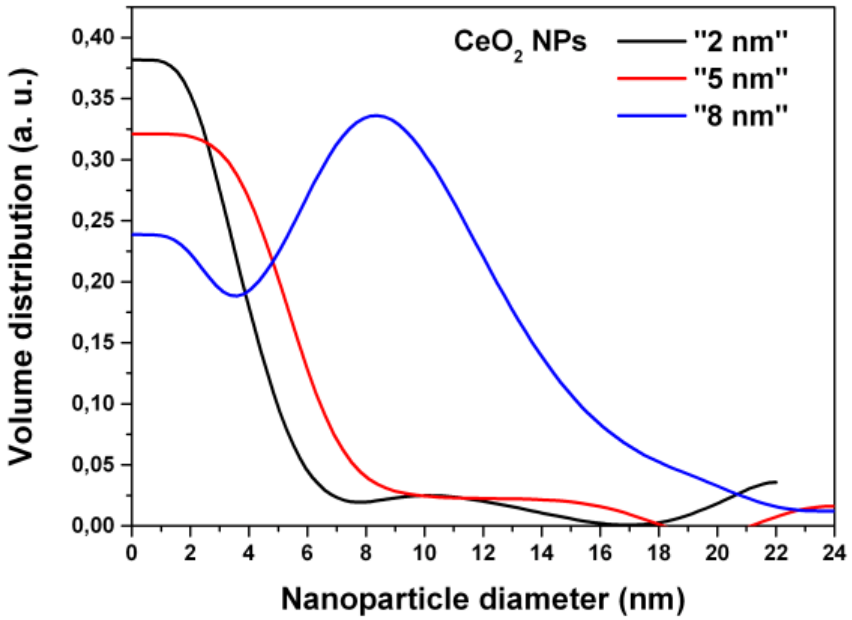

Figure S4. NP size distribution calculated from SAXS data using GNOM program [3].

Figure S5 shows HERFD-XAS pre-edge spectra at the Ce L_3 edge of CeO_2 NPs (2, 5 and 8 nm) in different states (as prepared and after the heat treatment) compared to the spectra of Ce(III) and Ce(IV) reference materials. The HERFD-XAS spectra recorded by monitoring the maximum of L□1 ($3d_{5/2}$-$2p_{3/2}$) intensity as a function of incident energy. The advantage of such a setup is two-fold: the width of the spectral features is no longer limited by the $2p_{3/2}$ core hole lifetime but the sharper $3d_{5/2}$ core hole width in the final state. Furthermore, electron–electron interactions in the final state between the 3d hole and 4f electrons can be observed that provide valuable information on the 4f electron configuration.

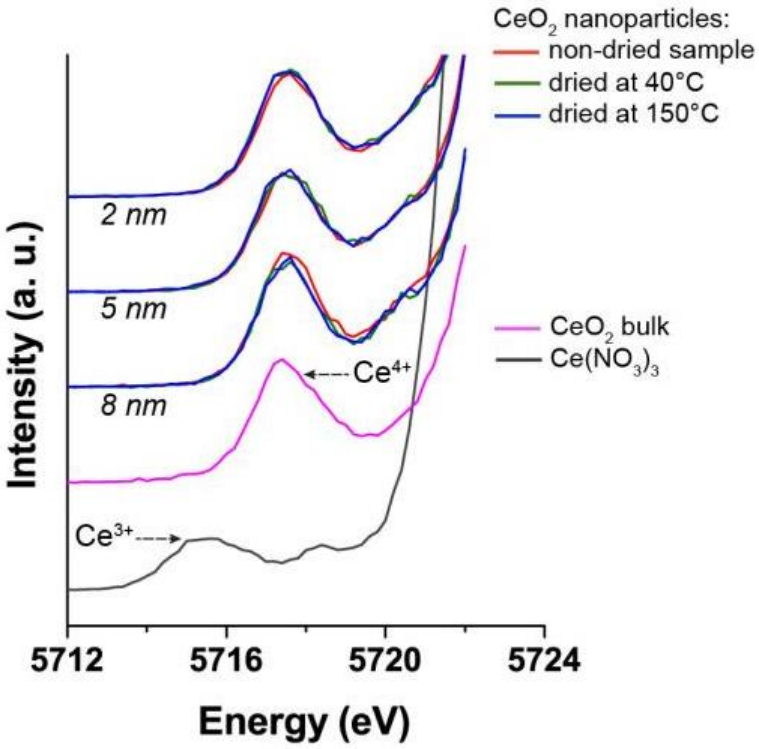

Figure S5. Pre-edge HERFD-XAS spectra for CeO_2 bulk material, cerium nitrate and for NPs studied in the present work.

In our previous studies, the pre-edge transitions below the absorption edge are attributed to the excitations into the 4f states [4]. A Ce(IV) compound formally contains no 4f electrons in the ground state and one 4f electron in the XAS final state. The CeO_2 HERFD-XAS spectrum shows a single peak at 5717.5 eV in the pre-edge region. When the number of 4f electrons in the final state is increased to two for Ce(III) the spectral shape becomes broader. In that case the number of contributing states is increased due to electron–electron interactions in the 4f valence orbital and the pre-edge profile becomes more complicated. The transitions to these states are split in two groups (Fig. S5 bottom, spectrum of $Ce(NO_3)_3$).

The present results show that pre-edge HERFD-XAS structure in spectra of CeO_2 NPs (in different size and at different conditions – treated under various temperatures) exhibit only single profile, confirming the presence of only Ce(IV) oxidation state.

The synchrotron XRD patterns of “2 nm” sample collected after the synthesis and after thermal treatment at 40 °C and 150 °C are shown in Fig. S7. All diffraction peaks can be attributed to the CeO_2 phase. The peaks position and its broadening do not change after the thermal treatment of the NPs samples. To support the XRD data, electron diffraction patterns were collected during HRTEM measurements of “as–prepared” 2 nm sample, and the same samples after 40 °C temperature treatment (Fig. S8). The electron diffraction results confirm the phase stability of the studied samples. According to the HRTEM images analysis, an average NP size for “as-prepared” and dried sample is established to be 2.3 ± 0.4.

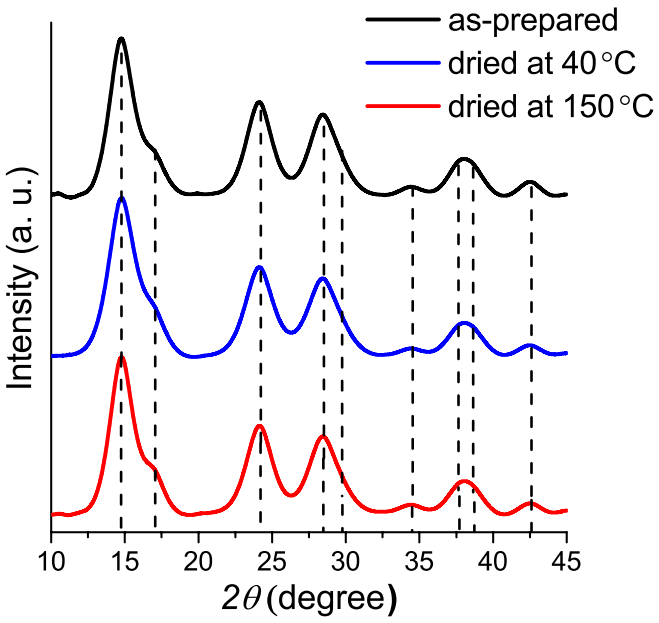

Figure S6. Synchrotron XRD data for as-prepared and dried at 40 °C and 150 °C CeO_2 samples.

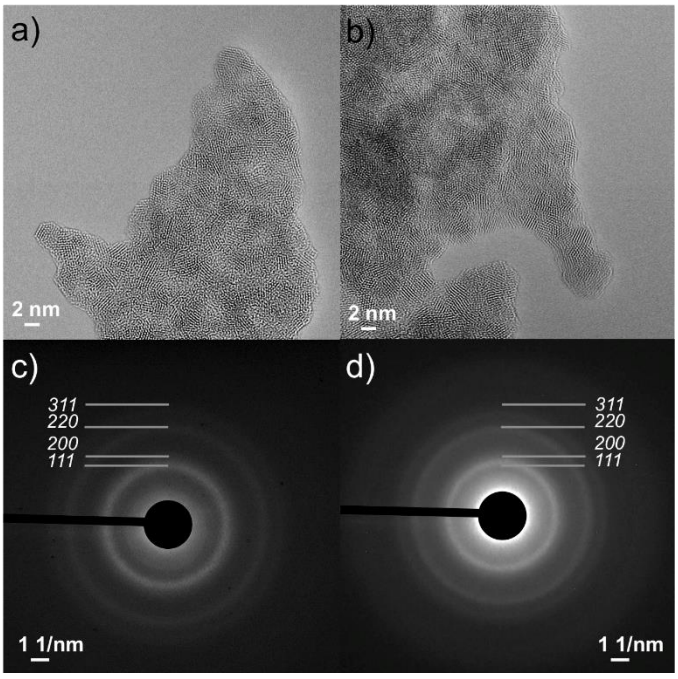

Figure S7. HRTEM data and electron diffraction patterns for CeO_2 samples a) c) as-prepared and b) d) dried at 40 °C.

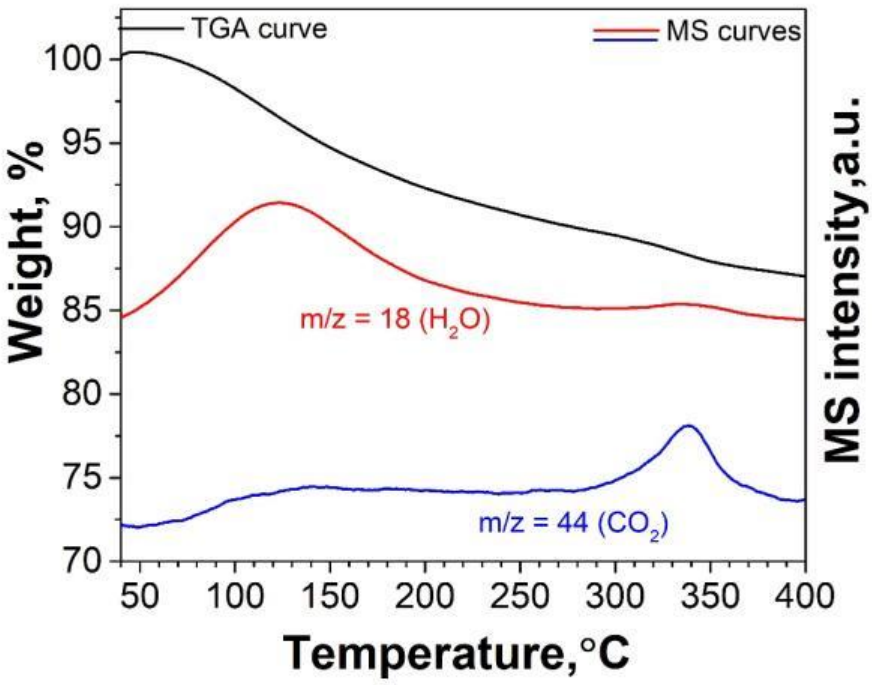

Figure S8. Thermogravimetric analysis (TGA) data and the corresponding mass spectral data for H_2O (MW 18) and CO_2 (MW 44) evolution from CeO_2 NPs of 2 nm size. TGA curve for CeO_2 sample demonstrate 15% total weight loss during the heating process. The mass spectra of 2 nm sample contain peaks corresponding to H_2O and CO_2 evolution. The presence of water in the mass spectrum in the range of 40 – 200 °C indicates that the 2 nm CeO_2 sample contain the water sorbed on the surface as well as water trapped in the bulk.

Chemiluminescence kinetic measurements

Chemiluminescence (CL) techniques possess the highest sensitivity in determination of ROS scavenger ability of substances. In particular, the TRAP (Total Radical-Trapping Antioxidant Potential) method is widely used in practice. This method is based on the ability of substances to intercept free radicals formed during the decomposition of thermolabile compounds, for example, 2,2′ -azo-bis (2-amidinopropane) (ABAP) [5,6]. In the present study, the antioxidant activity of NPs was estimated using luminol (5-amino-1,2,3,4-tetrahydro-1,4-phthalazinedione) – by activated CL method [7]. The CL kinetics was measured using Lum-100 luminometer (DiSoft, Russia). The operation of the device, the analysis of the results of photon counting, and plotting were performed using the Power Graph software. Measurements were conducted at 37°C. For the measurements, we used two different buffer solutions: the citrate buffer, pH 7.4 (30 mM trisodium citrate), and the phosphate buffer, pH 7.4 (100 mM potassium dihydrogen phosphate) both prepared using ultrapure water. Reagents were mixed directly in the CL cuvette. 50 µL of 0.05 M ABAP aqueous solution and 20 µL of 0.1 mM luminol in the appropriate buffer solution were preincubated in the dark at room temperature for 20 min. Thermal decomposition of the radical source was triggered by adding the necessary amount of a preheated buffer solution (37°C) (Fig. S9, “step 1”). The final system volume was 1.0 mL. After the CL curve reached a plateau, an aliquot of the analyzed sample was injected into the system.

In this way, the antioxidant activity of aqueous suspensions of freshly precipitated CeO_2 NPs with average sizes of 2 and 8 nm were analyzed. Suppression of luminescence due to radical scavenger ability of both samples was clearly. At the next step (Fig. S9), CL intensity increased with time. Under the chosen experimental conditions, the registration of kinetics was continued until the system reached the stationary mode ("step 3" on Fig. S9). The antioxidant activity of the samples was evaluated by measuring the area under the CL curve in the range corresponding to step 2. For each system measurement were made three times.

CL of the ABAP–luminol system was recorded in a control experiment. Addition of pure phosphate buffer exerted no effect on the curve shape. In the case of citrate buffer, the slight antioxidant effect was registered. This contribution was taken into account when evaluating the antioxidant activity of CeO_2 NPs samples in citrate buffer. Estimated antioxidant activity of the samples was expressed in equivalent units of a water-soluble analog of vitamin E, Trolox (6-hydroxy-2,5,7,8-tetramethylchroman-2-carboxylic acid).

According to CL kinetic curves for citrate and phosphate buffer solutions (Fig. S9a and Fig. S9b correspondingly), 2 nm CeO_2 NPs possess higher antioxidant activity in comparison with 8 nm CeO_2 NPs. The estimated value of antioxidant activity for 8.6 mg/L colloid solution of 2 nm CeO_2 NPs in citrate buffer was found to be 0.23 ± 0.07 µM in Trolox units, and 0.04 ± 0.01 µM in Trolox units for 8 nm CeO_2 NPs sample of the same concentration.

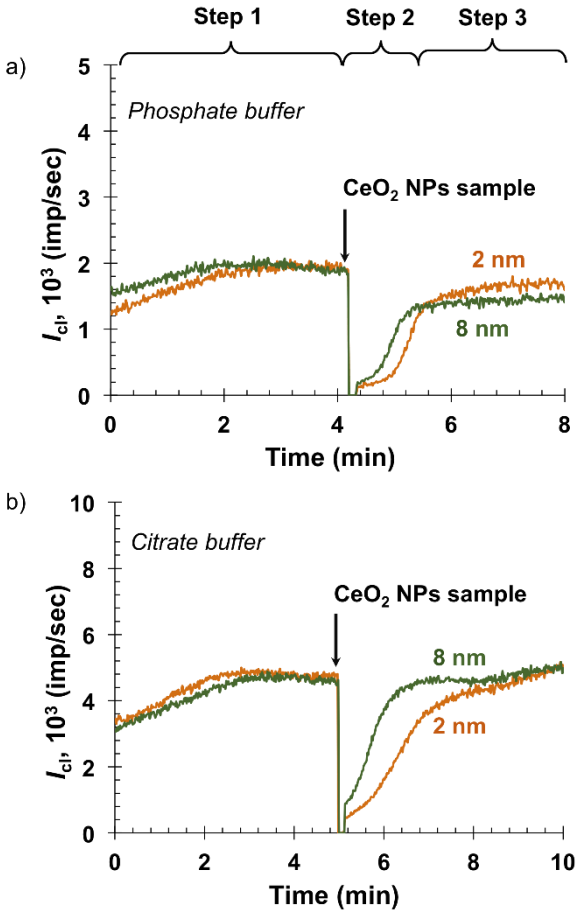

Figure S9. The CL curves of the ABAP (2.5 µM) + luminol (2.0 µM) a) in phosphate buffer (100 mM, pH 7.4), and b) in citrate buffer (30 mM pH 7.4) containing 2 nm and 8 nm CeO_2 NPs (8.6 mg/L). Total system volume is 1.0 mL.

References

1. T. X. T. Sayle, S. C. Parker and D. C. Sayle, *Chem. Commun.*, 2004, 2438-2439.

2. L. Yin, Y. Wang, G. Pang, Y. Koltypin and A. Gedanken, *J. Colloid Interface Sci.*, 2002, **246**, 78-84.

3. D. I. Svergun, *J. Appl. Crystallogr.*, 1992, **25**, 495-503.

4. K. O. Kvashnina, S. M. Butorin and P. Glatzel, *J. Anal. At. Spectrom.*, 2011, **26**, 1265-1272.

5. E. A. Lissi, C. P. Pascual and M. D. Castillo, *Free Radic. Res. Commun.*, 1992, **17 5**, 299-311.

6. E. Lissi, M. Salim-Hanna, C. Pascual and M. D. Castillo, *Free Radical Bio. Med.*, 1995, **18**, 153-158.

7. A. V. Alekseev, E. V. Proskurnina and Y. A. Vladimirov, *Moscow Univ. Chem. Bull.*, 2012, **67**, 127-132.

Appendix F: Article 6. Understanding the size effects on the electronic structure of ThO_2 nanoparticles

Lucia Amidani,*[a,b] Tatiana V. Plakhova,[c] Anna Yu. Romanchuk,[c] Evgeny Gerber,[a,b,c] Stephan Weiss,[b] Anna Efimenko,[d] Christoph J. Sahle,[d] Sergei M. Butorin,[e] Stepan N. Kalmykov[c] and Kristina O. Kvashnina*[a,b]

[a] *Rossendorf Beamline at ESRF – The European Synchrotron, CS40220, 38043 Grenoble Cedex 9, France.*

[b] *Helmholtz Zentrum Dresden-Rossendorf (HZDR), Institute of Resource Ecology, PO Box 510119, 01314 Dresden, Germany.*

[c] *Department of Chemistry, Lomonosov Moscow State University, Leninskie Gory 1/3, 119991, Moscow.*

[d] *ESRF – The European Synchrotron, CS40220, 38043 Grenoble Cedex 9, France.*

[e] *Molecular and Condensed Matter Physics, Department of Physics and Astronomy, Uppsala University, P.O. Box 516, Uppsala, Sweden.*

Introduction

Nanotechnology and nanomaterials are dominating the stage of scientific research since decades. When the size of a material is reduced to the nanoscale, exotic phenomena due to quantum confinement can appear and unique modifications of the optical, electronic, and mechanical properties show up, which can find application in fields spanning optoelectronic, catalysis, and medicine.[1] To understand and control the structure and the properties of nanomaterials, it is fundamental to develop a toolkit to adequately characterize these systems.[2]

Characterizing nanomaterials is a real challenge that requires a combination of different techniques as well as the development of analysis methodologies adapted to the very small particle's size.[3-5] The surface properties are of particular importance and very hard to investigate. X-rays Photoemission Spectroscopy (XPS), methods associated with Transmission Electron Microscopy (TEM), and total electron yield X-ray Absorption Spectroscopy (XAS) allow for structural and electronic characterization of the surface. However, the need of ultra-high vacuum prevents in situ investigations, the characterization of the sample under more realistic conditions, and in the case of oxides can induce changes in the local atomic environment, surface morphology and partial reduction.[6] In these regards X-ray Absorption Near-Edge Structure (XANES) and Extended X-ray Absorption Fine Structure (EXAFS) in the hard X-ray regime are very powerful techniques since they probe the local geometry and the local electronic structure of selected atomic species without imposing severe constrains on the sample conditions.[7-9] At the surface, the local properties differ drastically from those of the bulk material. When the size is

progressively reduced and the ratio of surface to core atoms increases, size effects on the local geometry and on the electronic structure become visible in XANES and EXAFS spectra. EXAFS and XANES have indeed been widely applied to nanosystems, especially in pioneering fields like metal clusters for catalysis.[10,11] The appearance of size effects in XANES does not follow a unique and general behaviour. XANES spectra of nanoparticles (NPs) often present a broadening of spectral features compared to their bulk analogue, but trends specific to the system under investigation can be also observed and each case needs an *ad hoc* analysis to be correctly interpreted. Size effects most often appear as small variations in the NP's spectrum compared to that of the bulk system. Direct interpretation can be achieved only to a small extent with fingerprint approaches and the support of modelling and simulations are necessary to extract as much information as possible about the respective system. The use of High-Energy Resolution Fluorescence Detected (HERFD) XANES instead of conventional XANES can be crucial when the investigation relies on small spectral differences.[12,13] When XANES is acquired by integrating a portion of the characteristic X-ray fluorescence with a bandwidth smaller than the core-hole lifetime broadening, XANES features are sharpened and the detection of small spectral variations is facilitated.[14] Some recent works illustrated how the use of HERFD XANES boosts the investigation of nanoscale materials to probe not only their structure but also the dynamics of charge carriers.[15-20]

In the past, EXAFS was the technique of choice to investigate the structure of nanomaterials, but recently the advantages of XANES over EXAFS when investigating nanosystems have been stressed.[7,21,22] XANES is extremely sensitive to the absorber's local structural, i.e., bond distances, bond angles and the overall symmetry,[23] and it is a direct probe of the local electronic structure of the selected species with high sensitivity to the chemical state and local charge transfers. The quality of XANES is less affected by structural and thermal disorder and it can be collected on more diluted systems. The complexity of XANES interpretation has been for years the main bottleneck to its more diffused use as a characterization technique. The last decades have seen a remarkable improvement of *ab initio* codes dedicated to XANES, to Density Functional Theory (DFT) and to Molecular Dynamics (MD) and computer resources have constantly increased. These progresses have boosted the capabilities to interpret XANES and recently *ab initio* XANES simulations were used to train a neural network capable of retrieving the 3D structure of metal nanoparticles from experimental XANES.[22]

The great potential of XANES applied to nanomaterials is well established in fields where nanotechnology is well developed and the controlled synthesis, the characterization and the theoretical modelling of nanomaterials are advanced.[21] The potential of this technique remains mostly unexplored in fields where the nanotechnology is at its infancy like that of actinide-based nanomaterials. NPs are of fundamental concern in nuclear material research: they have a primary role in the migration of radionuclides in contaminated sites and nanostructuring the nuclear fuel pellets can potentially improve their mechanical and thermal properties.[24,25] The interest in actinide-based NPs is increasing,[26-31] however the size and shape effects on the chemical and physical properties are poorly investigated compared to systems made of lighter and stable elements. The reasons being the safety issues of handling radioactive samples during experiments and the problem of modelling heavy atoms with a partially filled f-shell theoretically.[29,32]

The use of ultra-high vacuum techniques on actinide-based nanoparticles is not trivial and measurements at ambient pressure are preferable. Despite approaches to XANES interpretation combining DFT and MD with *ab initio* codes for XAS are not yet applicable to actinide-based NPs,[32] simpler approaches can give important insight into the structural and chemical properties of these systems. Moreover, HERFD XANES in the hard X-rays is particularly advantageous for actinide-based nanomaterials since the gain in resolution at the L_3 edge of actinides is huge and the penetration depth of X-rays allows measuring in air and using multiple kapton confinements.

In this work, we present for the first time the investigation of ThO_2 NPs of different sizes with Th L_3 edge HERFD XANES. We observed a size effect in the post-edge region of spectra corresponding to NPs with a diameter below 3 nm and we applied a systematic approach based on *ab initio* simulations to link the changes observed in the electronic structure with the structure and the local environment of atoms at the surface. We found that the observed effect is a signature of surface Th atoms which are particularly exposed and for which the number of coordinating anions and cations are severely reduced compared to those characterizing bulk ThO_2.

Experimental methods

Nanoparticle synthesis

Samples were prepared by a chemical precipitation technique with subsequent drying under different conditions.[33] The primary particles were obtained with the following procedures: (A) 0.1M aqueous solution of thorium nitrate pentahydrate ($Th(NO_3)_4 \times 5H_2O$) was added under continuous stirring to a 3M sodium hydroxide aqueous solution. The obtained precipitate was repeatedly washed with MilliQ water to achieve the neutral pH value and divided in two equal parts. The two parts were dried for 12 hours in air in a drying oven at 40°C and at 150°C, respectively. (B) Aqueous solutions of 1M $Th(NO_3)_4 \times 5H_2O$ and 3M ammonia were mixed under continuous stirring, the obtained precipitate was washed and divided similarly to sample (A). The two parts were annealed in a muffle furnace for 4 hours at 400°C and 800°C, respectively.

Characterization

The phase composition of the obtained powders was determined by X-ray diffraction (XRD) measurements with a Bruker D8 Advance diffractometer using a Cu Kα source (wavelength 1.54 Å). High-Resolution Transmission Electron Microscopy (HRTEM) images were acquired with Jeol-2100F HRTEM operated at 200 kV. The particle size was estimated from both XRD data and HRTEM images. The Scherrer equation was used to determine the ThO_2 NPs size from the XRD peaks broadening. The diameters of more than 200 well-defined NPs from HRTEM images were used to estimate the average ThO_2 particle size. The full results are reported in Ref. [33] and the HRTEM and size estimation of the smallest NPs are reported in the electronic supplementary information (ESI).

Th L_3 edge spectra on ThO_2 NPs were measured on the ROBL beamline at the ESRF.[34] The incident energy was selected with a Si(111) double crystal monochromator, the size of the beam at the sample was 400 □m horizontal times 150 □m vertical. The HERFD XANES were collected with an X-ray emission spectrometer[35] in Rowland geometry equipped with one Ge(880) spherically bent (0.5 m) crystal analyzer[36] to measure the maximum of the Th L□$_1$ characteristic fluorescence line resulting in a total energy resolution of 2.9 eV. The Th L_3 edge HERFD XANES of ThO_2 bulk collected with improved resolution was measured on ID20 beamline at the ESRF.[37] The incident

energy was selected with a cryogenically cooled Si(111) double crystal monochromator and a successive Si(311) channel-cut monocromator, the size of the beam at the sample was 20 □m horizontal times 10 □m vertical. The maximum of the Th L_5 characteristic fluorescence line was selected with an X-ray emission spectrometer in Rowland geometry equipped with a Si(10 10 0) diced (1 m) crystal analyser. The overall resolution was 0.5 eV. Samples for HERFD XANES measurements were prepared as dried powders and wet pastes and sealed with single kapton confinement.

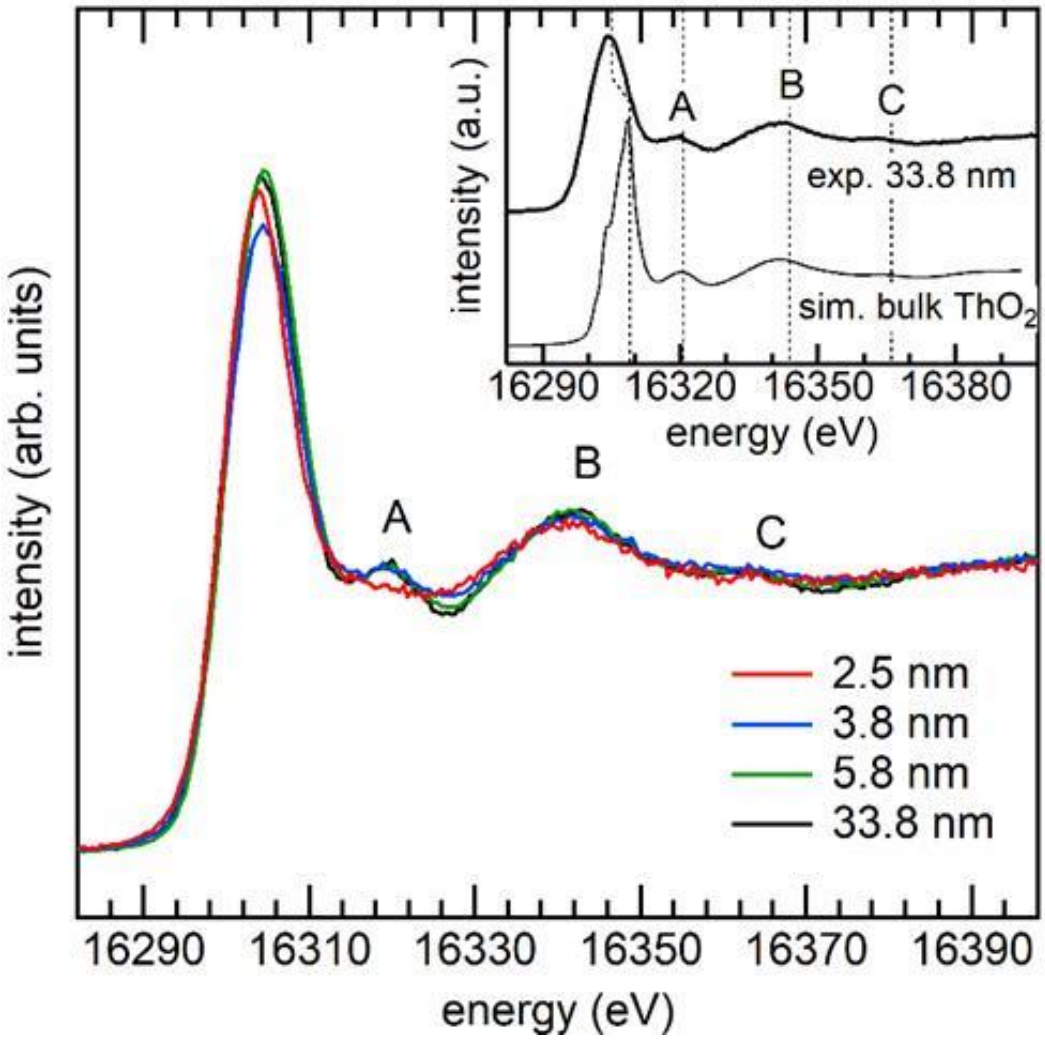

Figure 1. Main panel: experimental Th L_3 edge HERFD XANES on ThO_2 NPs of different sizes. Inset: HERFD XANES on 33.8 nm NPs and XANES simulation of bulk ThO_2 obtained with FDMNES. Vertical lines are added as guide to the eye to mark the main spectral features.

Computational details

Simulations of Th L_3 edge HERFD XANES were done with the FDMNES code.[38] The parameters of the simulation were tuned to obtain the best agreement for the HERFD XANES of bulk ThO_2 and then applied to simulate the HERFD XANES of structural models of ThO_2 NPs. Spin-orbit coupling and relativistic effects were included. The Fermi energy was estimated by a Self-Consistent Field (SCF) cycle including only the first oxygen coordination shell around the absorber, while the potential for the XANES calculation was built without SCF loop. The absorber was set to be excited and the density of states (DOS) projected on the absorber was also calculated. The error on the Fermi energy estimation was corrected by 3 eV for all simulations to have it in the middle of the

energy gap. The convolution parameters *Gamma_hole* and *Gamma_max* were set to 1 eV and 15 eV, respectively, to obtain simulations comparable to HERFD XANES data on NPs, while *Gamma_max* was reduced to 10 eV to better match the spectrum of bulk ThO_2 acquired with higher resolution. The cluster radius, the method of calculation, and the use of SCF were carefully tested. We found that with a full multiple scattering (FMS) radius of 7 Å, selecting 98 atoms around the absorber, all the spectral features are well reproduced and increasing it further results only in minor variations of the spectral shape. Very similar results were found using the Green's function method and the Finite Difference Method (FDM) as well as with and without SCF. In particular, the post-edge region, which is the focus of the present work, was well reproduced with the Green's function method and without the need of SCF. We therefore used a FMS radius of 7 Å, no SCF and the Green's function method for all models of NPs considered. To investigate the effect of reducing the size of ThO_2 and of different NP shapes, we built three model NPs with tetrahedral, octahedral, and spherical shape cutting them from a chunk of ThO_2. We chose the NP size as close as possible to 2.5 nm, i.e., the average diameter for which we observe a size effect on the experimental data. Each model NP was simulated at once by using the keywords *all_conv* that calculates the spectrum of all inequivalent Th atoms present in the structure and their relative shifts of the Fermi level in order to appropriately calculate the weighted average.

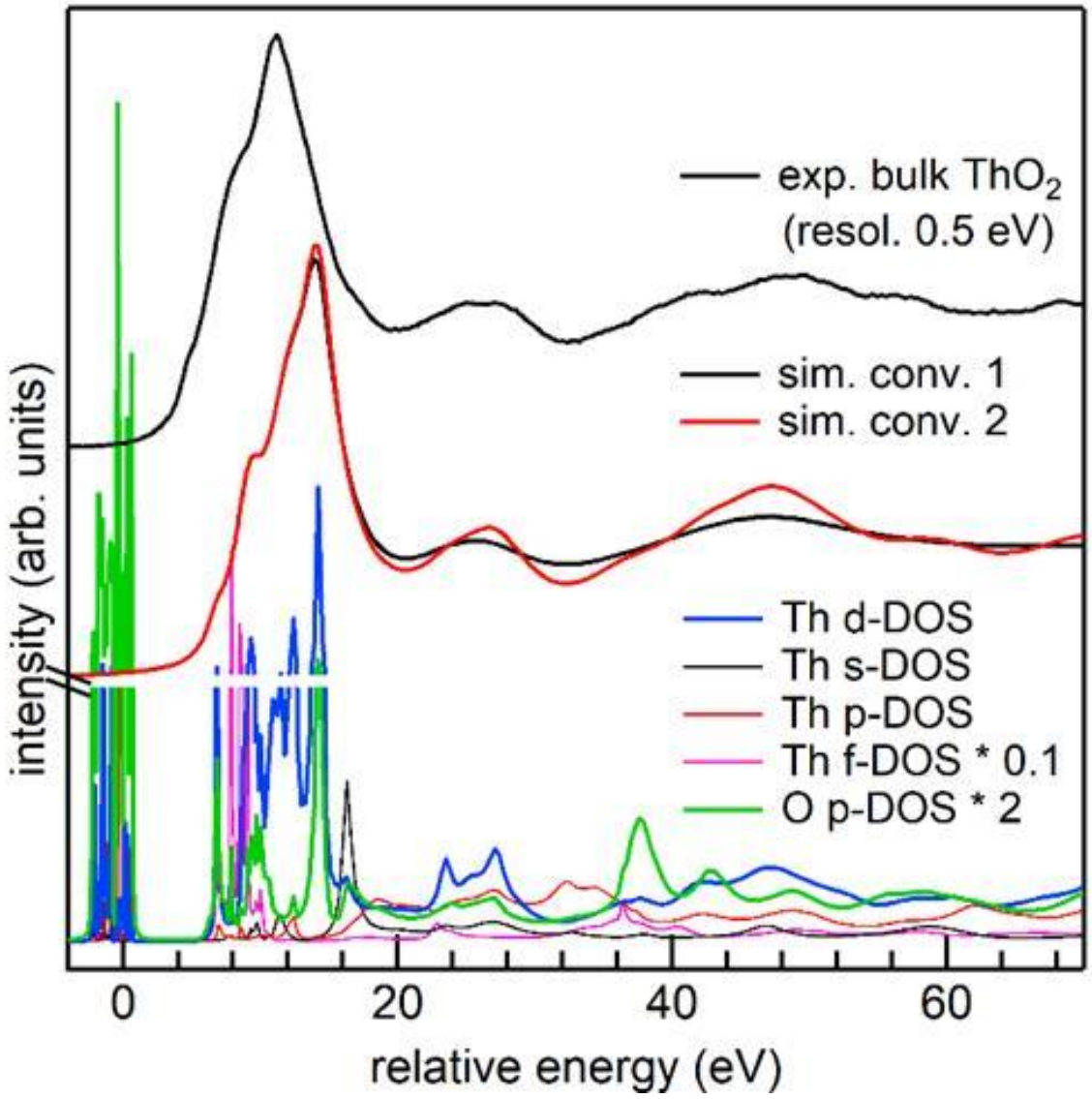

Figure 2. HERFD XANES collected with 0.5 eV resolution (top, black line) compared with two simulations of the L_3 edge XANES of Th in bulk ThO_2 obtained with different convolution parameters. The simulation in red is less convolved and the spectral features are in very good agreement with experimental data on top of the graph. On the bottom the partial DOSs of Th absorber and of the neighbouring O atoms are shown.

Results and Discussion

According to XRD data,[33] crystalline NPs of 2.5±0.3, 3.8±0.4, 5.8±0.6 and 33.8±3.3 nm in diameter were obtained depending on the synthesis conditions. The average crystallite size of the first two samples was also determined from HRTEM images. Average diameters of 2.7±0.4 and 4.0±0.6 were found, which are consistent with the XRD results within the error. The XRD and HRTEM of the smallest NPs are reported in the ESI and all details on the synthesis and characterization of the samples can be found in ref. [33]. Figure 1 shows the experimental HERFD XANES data at Th L_3 edge of a series of such NPs. While numerous investigations reported the use of HERFD for U L_3 edge XANES,[13,39,40] its application to Th L_3 edge XANES represents a novelty. The XANES spectrum of the 33.8 nm NPs was found identical to that of bulk ThO_2 and will be used as reference. Inspection of the post-edge region along the series reveals a trend with decreasing size: the spectrum of 5.8 nm NPs is still identical to that of bulk ThO_2, when reducing the size to 3.8 nm the post-edge features A, B, and C are slightly broadened and feature A is less pronounced. Finally, for 2.5 nm NPs the broadening is more pronounced and feature A disappears. To understand the origin of the size effect observed in Figure 1, we focused on the smallest NPs and tried to reproduce the disappearance of feature A and the broadening of the rest of the post-edge using FDMNES. The simulation of bulk ThO_2 is shown together with the experimental spectrum of 33.8 nm NPs in the inset of Figure 1, where the simulation has been shifted to best match the post-edge features of the experimental spectrum. The agreement is very good, with the features A, B and C well reproduced in terms of energy position and relative intensity. The shape and the intensity of the main absorption peak, the white line (WL), are also in good agreement with the experimental data. We notice that the simulation predicts two shoulders on the rising edge of the WL that are not resolved in the data acquired on NPs, however they appear in HERFD XANES spectra acquired with higher resolution on bulk ThO_2 and shown in Figure 2. The simulation underestimates the separation between the WL and feature A, a common situation for codes dedicated to XANES. One possible reason is the strength of the 2p core-hole potential, not attracting enough the unoccupied 6d states of Th. We considered the agreement satisfactory for the scope of this work and avoided the use of special parameters to tune the strength of the screening. The same parameters used for bulk ThO_2 were applied to simulate the NPs. In particular, we chose the Green's function method because the use of the Finite Difference Method (FDM) was affecting mostly the WL at the expense of a much longer computational time.

The projected DOS obtained with FDMNES helps to understand the origin of the spectral features observed. L_3 edge XANES probes transitions from the 2p core state to the unoccupied DOS with d- and s- symmetry. In Figure 2, the HERFD XANES acquired with higher energy resolution (0.5 eV) on bulk ThO_2, the FDMNES simulations and the DOSs of Th and O are compared. Two simulations are shown, one matching the data on NPs (same as in Figure 1) and one with reduced convolution to match the experimental data acquired with higher resolution and shown in Figure 2. The agreement between the high-resolution data and the simulation is excellent: three shoulders on the rising absorption edge and substructures of feature A and B are well resolved

in the data and well reproduced by the simulation. The shape of the simulated XANES follows the d-DOS of Th both at the WL and in the post-edge. The p-DOS of O contributes to some of the features of the WL and it presents many features in common with the Th d-DOS in the post-edge, indicating the presence of hybridization. We notice that the spectrum of bulk ThO_2 presented in Figure 2 differs from data presented in ref 41 despite it was obtained with better energy resolution.

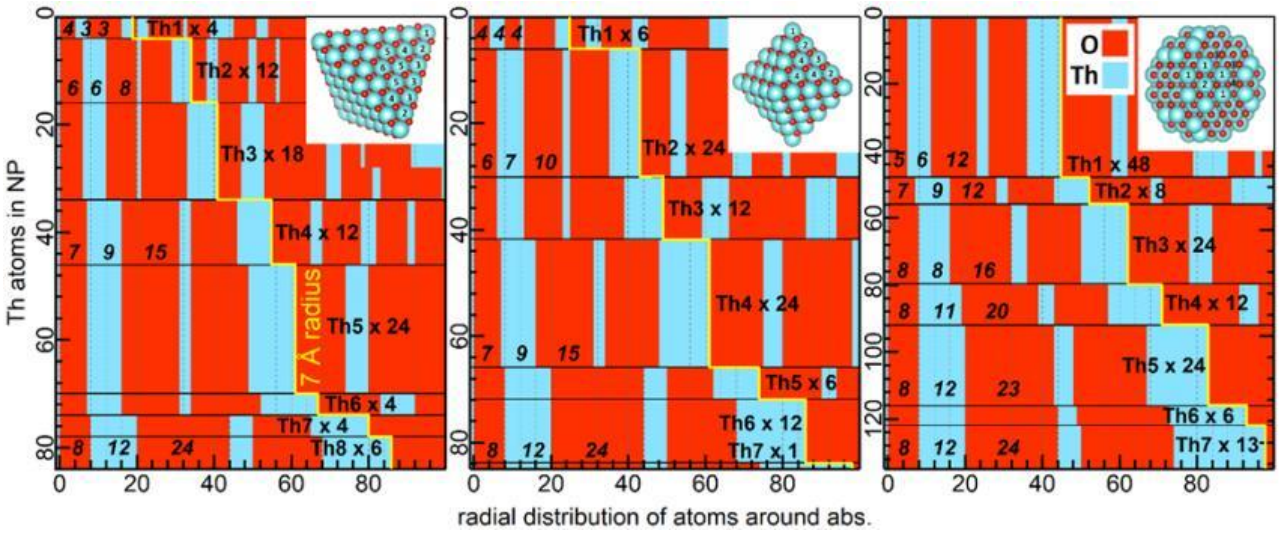

Figure 5. 2D images depicting the local environment of all Th atoms in the tetrahedral, octahedral, and spherical model NPs. The first element of each row is a Th atom of the NP, all the rest of the atoms in the NP are ordered according to increasing distance from the Th leading the row. Oxygen atoms are in red and Th atoms in light blue. The different coordination shells are easily recognized as well as the groups of equivalent Th atoms whose label Th# and multiplicity are indicated. The coordination numbers of the first three coordination shells are indicated. A yellow line delimits the atoms within a 7 Å radius from the Th leading the row.

The capability of the FDMNES code to precisely reproduce the spectral features observed in the experimental data for bulk ThO_2 justifies its use to investigate the origin of the size effect observed in the data. XANES is extremely sensitive to the local structure of the absorber, which is drastically different for Th atoms in bulk ThO_2 and Th at the surface of a NP. To understand at what extent the atoms at the surface can affect the XANES, we built model NPs from ThO_2 bulk and simulated with FDMNES the resulting XANES. We built three model NPs of different shapes and with size as close as possible to 2.5 nm. We considered a tetrahedral, an octahedral and a spherical nanoparticle.

The three models used in the calculations are shown in Figure 3. Together with the more general case of a spherical NP, we considered octahedral and tetrahedral models. The octahedral and the tetrahedral NPs expose only {111} facets, i.e., the most energetically favourable surface for many oxides with fluorite structure,[29,42,43] and are expected to be the most favourable shapes at small size.[44] The competition between these two shapes in case of small CeO_2 NPs has been investigated theoretically by Migani et al..[45] They found that below 3 nm the tetrahedral shape is even more favourable than the octahedral. CeO_2 NPs have the same crystal structure as ThO_2 and often serve as analogues of ThO_2 NPs. We cut the model ThO_2 NPs from a chunk of ThO_2 bulk without applying relaxation and charge compensation. We believe that this approach is indeed very useful to evaluate the effects of the shape and of the surface atoms on the XANES lineshape

before introducing disorder. The resulting tetrahedral NP has 2.38 nm edges and is a $Th_{84}O_{172}$ cluster with 4 oxygen atoms in excess; the octahedral NP has the two opposite corners at 2.24 nm distance and is a $Th_{85}O_{160}$ cluster with 5 thorium atoms in excess. Finally, the spherical NP has a diameter of 2.1 nm and is a $Th_{135}O_{280}$ cluster with 10 oxygen atoms in excess.

Differently from ThO_2 bulk where all Th atoms are equivalent, in a NP different groups of non-equivalent Th cations are present due to the break of symmetry introduced by the surface. The shape and the size of the NP define a specific collection of non-equivalent Th atoms, each of which is characterized by a specific local environment. Figure 3 illustrates it schematically for the three model NPs we investigated: an image is built where each Th atom in the NP is in turn occupying the first element of the row. The row is then filled with the atoms composing the NP ordered by increasing distance from the Th leading the row. Only the first 100 atoms of each row are shown. This is enough to display all atoms within 7 Å distance, corresponding to the cluster cut-off considered in our calculations and indicated with a yellow line. Oxygen and thorium atoms are in red and light blue, respectively. This schematic view allows to distinguish at a glance the different layers of anions and cations surrounding the Th absorbers and referred to as coordination shells in the following. The scheme in Figure 3 allows also to easily group the Th with the same local environment within the 7 Å distance. We can distinguish several non-equivalent Th in each model: 8 in the tetrahedral, 7 in the octahedral and 7 in the spherical NP.

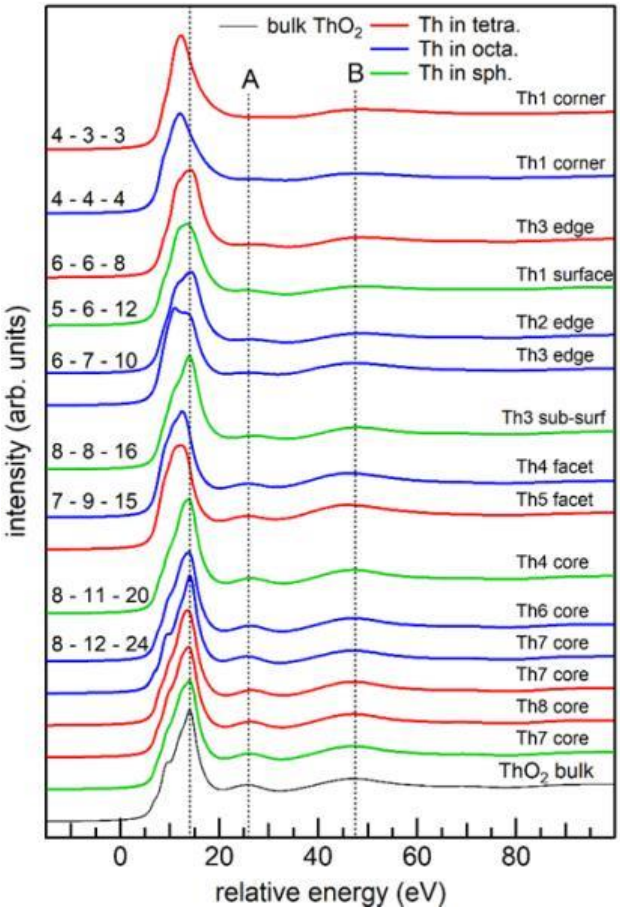

Figure 4. XANES simulations of single Th absorbers from the octahedral (blue lines), tetrahedral (red lines), and spherical (green lines) model NPs. A label with the reference Th# and the position it occupies in the NP is reported on the right of the spectrum. The XANES simulation of bulk ThO_2 is reported on the bottom of the graph (black thin line). The simulated spectra are grouped

according to the coordination numbers of the first three coordination shells which are reported on the top-left for each group. Vertical lines to guide the eye have been added in correspondence of the white line, the post-edge feature A, and B.

Each model presents Th atoms having the coordination numbers of the first three coordination shells almost identical to that of bulk ThO_2, i.e., 8O – 12Th – 24O. Those Th can be assigned to the core of the NP. From Figure 3 we see that there are 10 core Th atoms in the tetrahedral NP (Th7 and Th8), 19 core Th in the octahedral NP (Th 5, Th6 and Th7), and 43 core Th in the spherical NP (Th5, Th6 and Th7). Th at the surface on the other hand have a reduced number of neighbouring atoms compared to Th in bulk ThO_2. The extreme case is that of a Th at the corner of a tetrahedral NP which has 4O – 3Th – 3O. The presence of sharp edges can be seen in the scaling of the coordination numbers of the first three shells, which in the case of the sphere increases more smoothly towards those of Th in bulk ThO_2 compared to the case of the octahedral and tetrahedral NPs. In our model NPs the surface Th atoms constitute 88%, 77% and 68% of the total cations for the tetrahedral, the octahedral and the spherical model, respectively. However, differentiate only between core and surface Th is not sufficient and inspection of the different kind of Th at the surface is important to understand their impact on the spectral shape.

To determine how the diverse local environments of Th atoms affect the XANES spectrum we performed atom-specific calculations with FDMNES. The XANES spectra of the non-equivalent Th absorbers are obtained with a single simulation run in which the relative shifts of the Fermi energy are calculated. Figure 4 shows the simulated spectra of selected non-equivalent Th absorbers for the three model NPs. The spectra are grouped according to the coordination numbers of the first three shells starting from the Th in bulk ThO_2 and scaling up to Th at the corners which have the lowest coordination numbers for the first three coordination shells. The spectrum of Th in bulk ThO_2 is reported on the bottom. The post-edge feature A is particularly sensitive to the progressive decrease of neighbouring atoms and it practically disappears for coordinations lower than 7 – 9 – 15, i.e., for the more exposed cations at the surface. Feature B is also affected but at a lesser extent. On the other hand, Th atoms with coordination identical to Th in bulk ThO_2 are almost unchanged. Relevant spectral deviations from bulk ThO_2 are clearly observed at the WL. However, to correctly simulate the very first part of the XANES, a SCF loop to calculate the potential and the use of the FDM are more appropriate. At the same time, modifying the simulation approach in this direction needs a better description of the structure including local disorder and charge balance. We can therefore consider the remarkable spectral differences at the WL as an indication that this region of the spectrum may also be very sensitive to size effects and that improving the modelling of the structure at the surface would allow the use of a more sophisticated approach to simulations.

The simulation representing the XANES of the whole NP is given by the weighted average of all non-equivalent Th absorbers in the NP. Figure 5 shows the results obtained for the three model NPs considered. The experimental data on the biggest (33.8 nm) and smallest (2.5 nm) NPs are reported and compared with three groups of calculations, one for each model NP. Each group reports the simulation of bulk ThO_2 (black line) superimposed on the spectrum representing a specific model NP (red line). All three model NPs present spectral differences with bulk ThO_2. In the post-edge region the main effect is the lowering of feature A, in agreement with the experimental data. As expected, the spherical NP presents the smallest variations while the effect is more pronounced for the octahedral and tetrahedral models. A very slight broadening of

feature B is also reproduced by the simulations. In general, the size effect observed on the post-edge of the experimental data is qualitatively reproduced by all three models and almost quantitatively by the octahedral and tetrahedral models. These results stem from the presence of Th absorbers with coordination numbers for the first coordination shells drastically reduced from the bulk values and from the specific collection of Th local environments which is directly determined by the size and the shape of the NP.

The flattening of feature A observed in the post edge region of Th L_3 edge HERFD XANES for very small NPs differs from the general broadening observed in XANES of nanosized materials. The latter is generally ascribed to the structural disorder associated with nanomaterials while what we observed is more specific and can conceal information on the structure of the nanoparticles. An ideal approach to understand the significance of small spectral differences in XANES is to obtain the atomic coordinates of the atoms composing the NP from state-of-the-art theoretical approaches and utilize them as structural input for *ab initio* codes designed for XANES.[4,10,16,17] This workflow to XANES and EXAFS analysis is becoming relatively common, with DFT and MD being the preferred methods to treat systems with a large number of atoms.[7,46,47] Despite the impressive improvements of computational resources and simulation methods, obtaining the structure of small actinide nanoparticles from first principles is still beyond the current possibilities[32] and a simpler approach to the analysis is necessary.

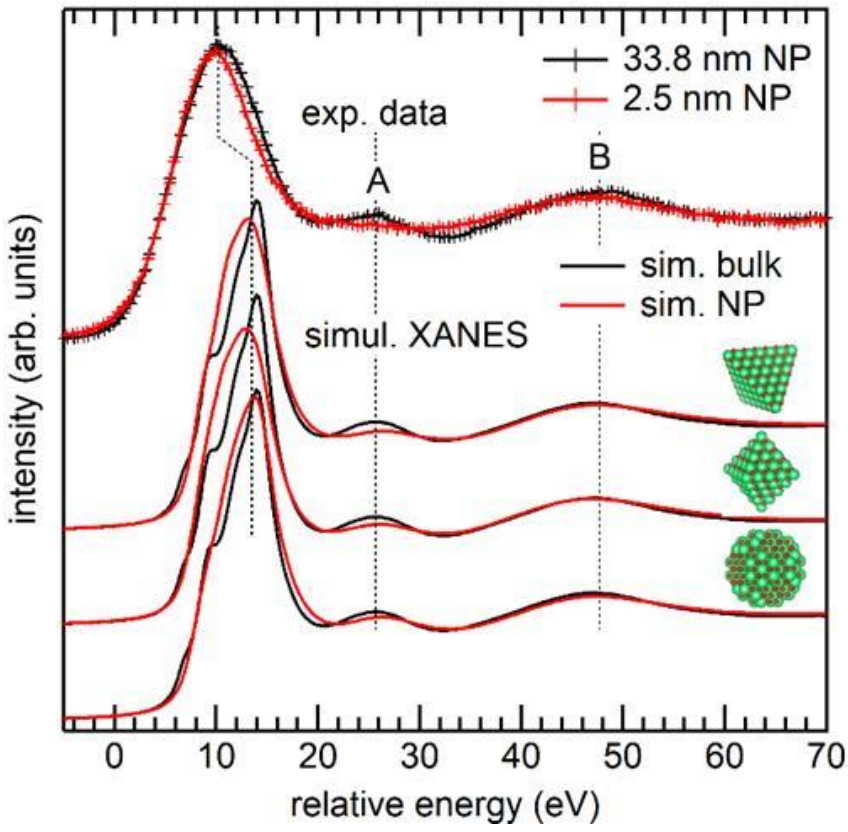

Figure 5. Experimental (top) and simulated (bottom) HERFD XANES at Th L_3 edge are compared. The data on big (33.8 nm, black curve) and small (2.5 nm, red curve) ThO_2 NPs are compared with the weighted average of all Th absorbers in the specific model NP (red lines). The spectrum of Th in bulk ThO_2 (black line) is reported for each model NP to highlight the spectral variations.

The precondition for a reliable analysis of XANES based on spectral simulations is the ability of the code of choice to reproduce correctly the reference spectra. In our case bulk ThO_2 is the only

reference and as shown in Figure 2 the agreement between the less convoluted FDMNES simulation and data acquired with 0.5 eV resolution is excellent and the details of the spectral lineshape of HERFD XANES on ThO_2 bulk are well reproduced. Feature A is in the post edge region, which is known to be more sensitive to the local structure around the absorber rather than to its chemical state.

The model NPs that we built have all similar number of Th atoms, i.e., 84, 85 and 135 for the tetrahedral, octahedral and spherical NP, respectively. The average coordination numbers (CNs) of the first three coordination shells computed from the information resumed in Figure 3 are 5.95 – 8 – 13 for the tetrahedral, 6.59 – 8.47 – 14.12 for the octahedral and 6.87 – 8.89 – 17.07 for the spherical to be compared with 8 – 12 – 24 of the fluorite structure. The decrease of the average CNs quantifies the general impact of the surface atoms on the local structure of Th atoms. However, the consideration of the specific local environments of Th atoms present in each model provides additional information. The inspection of the spectra of single Th evidences how the progressive decrease of CNs is reflected in the post-edge feature A. In Figure 4, where spectra from single Th absorbers are grouped according to CNs independently from the NP model they belong to, the lowering of feature A is particularly pronounced for CNs lower than 7 – 9 – 15. For CNs between 8 – 12 – 24 and 7 – 9 – 15 the post-edge is only slightly changed, with both feature A and B undergoing a shift rather than a flattening or broadening. For lower CNs the changes are more important: feature A is flattened and features B is broadened. The spectra of single Th reveal the strong sensitivity of feature A to low CNs, i.e., to the more exposed Th at the surface. CNs lower than 7 – 9 – 15 correspond indeed to edges and corners in the tetrahedral and octahedral models and to Th at the surface in the spherical model.

From Figure 5, all the averages obtained by weighting the non-equivalent Th atoms spectra for each model NPs reproduce the trends observed on the experimental data. All models indeed, if compared to the simulation of bulk ThO_2 present a lowering of feature A and a broadening of feature B. However, the effect is very small for the spherical NP and more pronounced for the octahedral and the tetrahedral NPs. This reflects the percentage of Th with very low CNs for which the flattening of feature A is more pronounced as from Figure 4. The results presented illustrate how the different Th local environments resulting from the reduced size affect the XANES lineshape and what is the overall impact on the average spectrum. The size effect on the experimental spectra is stronger than in any of the models considered, indicating that additional factors impact on the intensity of feature A. The first to be considered is the local disorder, which in NP is expected to be stronger at the surface that in the bulk. Local distortions spread the ranges of Th – O and Th – Th distances and the contributions from nearest neighbours that sum up coherently in an unrelaxed structure undergo a de-phasing in a disorder structure. In this regards local disorder could induce additional decrease of feature A and bring the results to better match the experimental data. However, obtaining the extent and repartition of disorder in nanoparticles from first principles is not a trivial task,[4] especially for actinide-based nanomaterials. The interaction of the surface with the solvent should also be considered. Water molecules and hydroxyl groups attached to the surface will increase the number of O in the first coordination shell of surface Th. Inspection of the DOSs in Figure 2 indicates that the dominant contribution to feature A is Th d-DOS suggesting that few additional O from surfactants would induce minor effects.

The modelling approach we presented does not aim at determining the shape of the NPs from XANES. Instead, it provides an insight into the origin of size effects in XANES and demonstrate that a consistent contribution to the decrease of feature A is accounted by the more exposed Th atoms at the surface. We also suggest that local disorder at the surface is accounting for the additional lowering of feature A. We notice that the impact on XANES spectral shape of disorder in nanoparticles and clusters is poorly investigated and most of the studies using relaxed structures never discuss the impact that relaxation has on the results. Results presented here can guide future experimental investigations and suggest that a similar effect can be found in other oxide nanosystems. Post-edge features similar to feature A can be found in L_3 edge XANES of other actinide and lanthanide elements. The sensitivity of the first post-edge feature to the surface cations demonstrated in this work may be a point in common with other oxide NPs. To conclude, our work demonstrates that the post edge feature A of Th L_3 edge HERFD XANES spectrum is specifically sensitive to low coordinated surface cations. XANES and specifically feature A can therefore be sensitive to modifications of the surface atoms induced by chemical processes and surfactants. Some final remarks on the edge region and in particular on the WL can be drawn based on the data presented here. The edge region of the XANES is the most sensitive to the charge transfer, to the chemical state of the absorber and to the fine details of the local electronic structure. Previous studies have often observed that the size of NPs can affect the intensity of the WL and simple structural models like the one presented here have been used to reproduce the effect in the case of metal clusters.[48] A similar effect has been observed in actinide NPs and was ascribed to the reduced size rather than to charge transfer effects.[49,50] Our data do not present relevant variations of the WL intensity with decreasing size and our purely structural models do not predict strong effects on the WL intensity for small size ThO_2 NPs. We stress that the model NPs that we constructed are meant to represent only the structural effects introduced by the surface and not the electronic effects, therefore the spectral variations at the WL resulting from the simulations have to be taken with care. In Figure 4 the spectra of single Th absorbers show marked differences at the WL, hinting to the high sensitivity of this region of the spectrum. The differences at the WL on the average spectra are less pronounced but sizable. In particular, the three shoulders on the rising absorption edge that can be resolved if the resolution is increased (Figure 2) are smeared when size is reduced. These results are affected by strong approximations but suggest two important points when measuring HERFD XANES on actinide-based NPs: i) an increase in the energy resolution is fundamental to appreciate small spectral variations like the one expected when the size is reduced to the nanoscale; ii) a structural model of the surface accounting not only for the structural but also for the electronic effects is required as input for simulations that aims at an accurate description of the edge region.

Conclusions

We presented HERFD XANES at Th L_3 edge on ThO_2 NPs of different sizes which show the flattening of the first post edge feature A for NPs with diameter < 2.5 nm. We performed XANES FDMNES simulations on three different structural models of small ThO_2 NPs considering the tetrahedral, the octahedral, and the spherical shape. Inspection of the simulations of single Th absorbers clearly shows that the progressive decrease of coordinating atoms induces a flattening of feature A, which is therefore particularly pronounced for the more exposed Th atoms at the surface. The comparison between experimental data and the simulations representing the model NPs shows that the size effect observed on the data is qualitatively reproduced by all the models and that the flattening of feature A is more pronounced and closer to the measured effect for

models with higher number of the more exposed Th at the surface. The sensitivity of ThO_2 electronic structure to the number and the arrangement of surrounding atoms stems from the strong hybridization of Th d-DOS with both O and Th neighbours. In perspective, the sensitivity of the post-edge of Th L_3 edge HERFD XANES to the low coordinated atoms at the surface can be part of a toolkit of characterization techniques to investigate interactions at the surface and may not be limited to the case of ThO_2 but can be extended to other oxide nanosystems.

Conflicts of interest

There are no conflicts to declare.

Acknowledgements

The authors would like to acknowledge the ESRF for providing beamtime and C. Henriquet for providing technical support at ID20 beamline. This research was funded by European Research Council (ERC) under grant agreement No 759696. The synthesis of ThO_2 nanoparticles was funded by RFBR, according to the research projects No. 16-33-60043 mol_a_dk and No. 18-33-01067 mol_a. S.M.B. acknowledges support from the Swedish Research Council (research grant 2017-06465).

References

1 H. Goesmann and C. Feldmann, Angew. Chem. Int. Ed., 2010, 49, 1362–1395.

2 S. J. L. Billinge and I. Levin, Science, 2007, 316, 561–565.

3 G. Agostini, A. Piovano, L. Bertinetti, R. Pellegrini, G. Leofanti, E. Groppo and C. Lamberti, J. Phys. Chem. C, 2014, 118, 4085–4094.

4 B. Gilbert, H. Zhang, F. Huang, J. F. Banfield, Y. Ren, D. Haskel, J. C. Lang, G. Srajer, A. Jürgensen and G. A. Waychunas, J. Chem. Phys., 2004, 120, 11785–11795.

5 B. Palosz, E. Grzanka, S. Gierlotka, S. Stel'makh, R. Pielaszek, U. Bismayer, J. Neuefeind, T. Proffen, R. V. Dreele and W. Palosz, Z. Für Krist., 2002, 217, 497–509.

6 F. Zhang, P. Wang, J. Koberstein, S. Khalid and S.-W. Chan, Surf. Sci., 2004, 563, 74–82.

7 A. Kuzmin and J. Chaboy, IUCrJ, 2014, 1, 571–589.

8 A. I. Frenkel, Chem. Soc. Rev., 2012, 41, 8163.

9 L. Mino, G. Agostini, E. Borfecchia, D. Gianolio, A. Piovano, E. Gallo and C. Lamberti, J. Phys. Appl. Phys., 2013, 46, 423001.

10 A. L. Ankudinov, J. J. Rehr, J. J. Low and S. R. Bare, J. Chem. Phys., 2002, 116, 1911–1919.

11 F. Vila, J. J. Rehr, J. Kas, R. G. Nuzzo and A. I. Frenkel, Phys. Rev. B, 2008, 78, 121404(R).

12 S. M. Butorin, K. O. Kvashnina, J. R. Vegelius, D. Meyer and D. K. Shuh, Proc. Natl. Acad. Sci., 2016, 113, 8093–8097.

13 K. O. Kvashnina and F. M. F. de Groot, J. Electron Spectrosc. Relat. Phenom., 2014, 194, 88–93.

14 P. Glatzel, T.-C. Weng, K. Kvashnina, J. Swarbrick, M. Sikora, E. Gallo, N. Smolentsev and R. A. Mori, J. Electron Spectrosc. Relat. Phenom., 2013, 188, 17–25.

15 J.-D. Cafun, K. O. Kvashnina, E. Casals, V. F. Puntes and P. Glatzel, ACS Nano, 2013, 7, 10726–10732.

16 O. V. Safonova, A. A. Guda, C. Paun, N. Smolentsev, P. M. Abdala, G. Smolentsev, M. Nachtegaal, J. Szlachetko, M. A. Soldatov, A. V. Soldatov and J. A. van Bokhoven, J. Phys. Chem. C, 2014, 118, 1974–1982.

17 A. Gorczyca, V. Moizan, C. Chizallet, O. Proux, W. Del Net, E. Lahera, J.-L. Hazemann, P. Raybaud and Y. Joly, Angew. Chem., 2014, 126, 12634–12637.

18 L. Amidani, A. Naldoni, M. Malvestuto, M. Marelli, P. Glatzel, V. Dal Santo and F. Boscherini, Angew. Chem. Int. Ed., 2015, 54, 5413–5416.

19 G. Rossi, M. Calizzi, L. Amidani, A. Migliori, F. Boscherini and L. Pasquini, Phys. Rev. B, 2017, 96, 045303.

20 M. van der Linden, A. J. van Bunningen, L. Amidani, M. Bransen, H. Elnaggar, P. Glatzel, A. Meijerink and F. M. F. de Groot, ACS Nano, 2018, 12, 12751–12760.

21 J. Timoshenko, A. Shivhare, R. W. J. Scott, D. Lu and A. I. Frenkel, Phys. Chem. Chem. Phys., 2016, 18, 19621–19630.

22 J. Timoshenko, D. Lu, Y. Lin and A. I. Frenkel, J. Phys. Chem. Lett., 2017, 8, 5091–5098.

23 J. Chaboy and S. Díaz-Moreno, J. Phys. Chem. A, 2011, 115, 2345–2349.

24 S. N. Kalmykov and M. A. Denecke, Eds., Actinide nanoparticle research, Springer, Berlin ; London, 2010.

25 C. Walther and M. A. Denecke, Chem. Rev., 2013, 113, 995–1015.

26 H. Wu, Y. Yang and Y. C. Cao, J. Am. Chem. Soc., 2006, 128, 16522–16523.

27 O. N. Batuk, D. V. Szabó, M. A. Denecke, T. Vitova and S. N. Kalmykov, Radiochim. Acta, 2013, 101, 233–240.

28 D. Hudry, J.-C. Griveau, C. Apostolidis, O. Walter, E. Colineau, G. Rasmussen, D. Wang, V. S. K. Chakravadhaluna, E. Courtois, C. Kübel and D. Meyer, Nano Res., 2014, 7, 119–131.

29 G. Wang, E. R. Batista and P. Yang, Phys. Chem. Chem. Phys., 2018, 20, 17563–17573.

30 D. Hudry, C. Apostolidis, O. Walter, T. Gouder, E. Courtois, C. Kübel and D. Meyer, Chem. - Eur. J., 2013, 19, 5297–5305.

31 D. Hudry, C. Apostolidis, O. Walter, A. Janßen, D. Manara, J.-C. Griveau, E. Colineau, T. Vitova, T. Prüßmann, D. Wang, C. Kübel and D. Meyer, Chem. - Eur. J., 2014, 20, 10431–10438.

32 B. Schimmelpfennig, in Actinide Nanoparticle Research, eds. S. N. Kalmykov and M. A. Denecke, Springer Berlin Heidelberg, Berlin, Heidelberg, 2011, pp. 187–193.

33 T. V. Plakhova, A. Y. Romanchuk, D. V. Lykhosherstova, A. E. Baranchikov, P. V. Dorovatovskii, R. D. Svetogorov, T. B. Shatalova, T. B. Egorova, A. L. Trigub, K. O. Kvashnina, V. K. Ivanov and S. N. Kalmykov, Submitt. Dalton Trans.

34 T. Reich, G. Bernhard, G. Geipel, H. Funke, C. Hennig, A. Roßberg, W. Matz, N. Schell and H. Nitsche, Radiochim. Acta, 2000, 88, 633–637.

35 K. O. Kvashnina and A. C. Scheinost, J. Synchrotron Radiat., 2016, 23, 836–841.

36 M. Rovezzi, C. Lapras, A. Manceau, P. Glatzel and R. Verbeni, Rev. Sci. Instrum., 2017, 88, 013108.

37 M. Moretti Sala, K. Martel, C. Henriquet, A. Al Zein, L. Simonelli, C. J. Sahle, H. Gonzalez, M.-C. Lagier, C. Ponchut, S. Huotari, R. Verbeni, M. Krisch and G. Monaco, J. Synchrotron Radiat., 2018, 25, 580–591.

38 Y. Joly, O. Bunău, J. E. Lorenzo, R. M. Galéra, S. Grenier and B. Thompson, J. Phys. Conf. Ser., 2009, 190, 012007.

39 T. Vitova, K. O. Kvashnina, G. Nocton, G. Sukharina, M. A. Denecke, S. M. Butorin, M. Mazzanti, R. Caciuffo, A. Soldatov, T. Behrends and H. Geckeis, Phys. Rev. B, 2010, 82, 235118.

40 K. O. Kvashnina, Y. O. Kvashnin, J. R. Vegelius, A. Bosak, P. M. Martin and S. M. Butorin, Anal. Chem., 2015, 87, 8772–8780.

41 H. Bao, P. Duan, J. Zhou, H. Cao, J. Li, H. Yu, Z. Jiang, H. Liu, L. Zhang, J. Lin, N. Chen, X. Lin, Y. Liu, Y. Huang and J.-Q. Wang, Inorg. Chem., 2018, 57, 11404–11413.

42 R. K. Behera and C. S. Deo, J. Phys. Condens. Matter, 2012, 24, 215405.

43 N. V. Skorodumova, M. Baudin and K. Hermansson, Phys. Rev. B, 2004, 69, 075401.

44 Z. L. Wang and X. Feng, J. Phys. Chem. B, 2003, 107, 13563–13566.

45 A. Migani, K. M. Neyman and S. T. Bromley, Chem. Commun., 2012, 48, 4199.

46 S. T. Bromley, I. de P. R. Moreira, K. M. Neyman and F. Illas, Chem. Soc. Rev., 2009, 38, 2657.

47 A. R. Puigdollers, F. Illas and G. Pacchioni, J. Phys. Chem. C, 2016, 120, 4392–4402.

48 D. Bazin, D. Sayers, J. J. Rehr and C. Mottet, J. Phys. Chem. B, 1997, 101, 5332–5336.

49 J. Rothe, M. A. Denecke, V. Neck, R. Müller and J. I. Kim, Inorg. Chem., 2002, 41, 249–258.

50 J. Rothe, C. Walther, M. A. Denecke and T. Fanghänel, Inorg. Chem., 2004, 43, 4708–4718.

Appendix G: Article 7. The Application of HEXS and HERFD XANES for Accurate Structural Characterisation of Actinide Nanomaterials: The Case of ThO_2

Lucia Amidani,[*[a, b]] Gavin B. M. Vaughan,[[c]] Tatiana V. Plakhova,[[d]] Anna Yu. Romanchuk,[[d]] Evgeny Gerber,[[a, d]] Roman Svetogorov,[[e]] Stephan Weiss,[[b]] Yves Joly,[[f]] Stepan N. Kalmykov,[[d]] and Kristina O. Kvashnina[[a, b, d]]

[a] Dr. L. Amidani, E. Gerber and Dr. K. O. Kvashnina
The Rossendorf Beamline at ESRF
The European Synchrotron
CS40220, 38043 Grenoble Cedex 9, France
E-mail: lucia.amidani@esrf.fr

[b] Dr. L. Amidani, S. Weiss and Dr. K. O. Kvashnina
Institute of Resource Ecology
Helmholtz Zentrum Dresden-Rossendorf (HZDR)
PO Box 510119, 01314 Dresden

[c] Dr. G. B. M. Vaughan
ESRF – The European Synchrotron
CS40220, 38043 Grenoble Cedex 9, France

[d] Dr. T. V. Plakhova, Dr. A. Yu. Romanchuk, E. Gerber, S. N. Kalmykov and K. O. Kvashnina
Department of Chemistry,
Lomonosov Moscow State University,
119991 Moscow, Russia

[e] Dr. R. Svetogorov
National Research Centre "Kurchatov Institute",
123182 Moscow, Russia.

[f] Dr. Y. Joly
Université Grenoble Alpes, CNRS, Grenoble INP, Institut Néel,
38042 Grenoble, France

Abstract: Structural characterization of actinide nanoparticles (NPs) is of primary importance and hard to achieve, especially for non-homogeneous samples with NPs below 3 nm. By combining High Energy X-ray Scattering (HEXS) and High-Energy-Resolution Fluorescence Detected X-ray Near-Edge Structure (HERFD XANES), we characterized for the first time both short- and medium-range order of ThO_2 NPs obtained by chemical precipitation. With this methodology, a novel insight into the structure of NPs at different steps of their formation process is achieved. The Pair Distribution Function (PDF) reveals a high concentration of ThO_2 small units similar to Th hexamer clusters mixed with 1 nm ThO_2 NPs in the initial steps of formation. Drying the precipitates at

~150 °C promotes recrystallization of the smallest units into more thermodynamically stable ThO_2 NPs. HERFD XANES at Th M_4 edge, a direct probe of the f states, shows variations that we correlate to the break of the local symmetry around Th atoms, which most likely concerns surface atoms. Together, HEXS and HERFD are a powerful methodology to investigate actinide NPs and their formation mechanism.

Introduction

The investigation of actinide materials at the nanoscale is emerging as a fascinating field of research, challenged by fundamental questions about their formation mechanism, their interaction with the environment, their migration capabilities, fundamental properties and chemical stability.[1,2] Despite the fact that nanotechnology has been rapidly developing since late 20th century and NPs are nowadays ubiquitous in many fields of science, the stage has been dominated by d-block systems. The f-block systems, in particular actinides, have been left behind, to the point that to date the properties of actinide materials at the nanoscale remain largely unknown. The proved tendency of actinides to aggregate in colloidal nanoparticles that are responsible for their environmental behaviour[2] calls for an in-depth understanding of their behaviour as nanoclusters and nanoparticles, since they may present special behaviour, reactivity and structure. Moreover, the high specific surface area of nanosized systems can find application in the design of high burn-up nuclear fuels.[3] The need for specialized facilities makes actinide research difficult and expensive. On the other hand, the increasing interest in actinides is promoting collaborations among universities, national laboratories, large-scale facilities and industries, and relevant progresses have been made. The many gaps and challenges of actinide nanoscience are recently being addressed more systematically thanks also to the increasing ability in controlling NPs synthesis.[4-11] In the roadmap to study NPs, mastering their synthesis goes hand in hand with the ability to accurately characterize the structure of the products. For actinide NPs, a field in its infancy, improvements in the structural characterization of non-homogeneous samples would enormously accelerate the understanding of the systems studied.

One of the most investigated topics of radiochemistry at the nanoscale is the formation of tetravalent actinide oxide NPs in aqueous solution.[7-9,12-17] Tracking their aggregation mechanism at different chemical conditions, identifying the presence of multiple oxidation states and characterizing their surface are real challenges. Even what is considered the simpler system, ThO_2, for which only the tetravalent oxidation state is stable, is very debated. Th(IV) is the softest among the tetravalent actinide ions and its tendency to hydrolyse is lower compared to other An(IV). Th(IV) in solution can form not only mononuclear hydrolysis complexes, but also a number of polynuclear species.[18-23] The fluorite structure of ThO_2 is the ultimate product of Th(IV) hydrolysis, but its well-defined structure is often identified only after temperature treatments or as the result of ageing processes. Despite attempts to characterize Th(IV) precipitates have been made since 1960s,[24] the information on the structure and consequently on ThO_2 formation mechanisms in solution remain very scarce. In most cases, highly hydrolysed thorium salts form Th(IV) precipitates with ill-defined structure. In previous studies, such precipitates are classified as amorphous and in turned called "$Th(OH)_4$(am)" or hydrous oxides "$ThO_2{\cdot}xH_2O$(am)" or "ThO_2(am, hyd)", where the amorphous character is only identified by the absence of peaks in the XRD pattern.[25-27] The short-range local structure of amorphous and crystalline Th(IV) precipitates have been investigated with EXAFS by Rothe et al.,[28] who first found that in amorphous samples the first Th – O shell is compatible with bond lengths heavily scattered

around the value of crystalline ThO_2. Apart from the evidence of local disorder and the absence of long-range order, almost no structural information is available up to date on Th(IV) hydrous oxide.

Few works identified small crystallites of ThO_2 in the precipitates obtained with synthesis conditions compatible with the formation of the amorphous Th(IV) hydrous oxide.[9,29-32] Magini et al.[31] investigated hydrolysed thorium salts with wide and small angle X-ray scattering and found small clusters of atoms and microcrystalline ThO_2 particles up to 4 nm in heat-treated solutions at relatively mild temperatures (below 100 °C). Dzimitrowicz et al.32 observed ThO_2 crystallites of more than 3 nm in X-ray amorphous precipitates using TEM and electron diffraction. Overall, the nature of Th(IV) precipitates in aqueous solution remains highly debated because of the absence of a clear-cut structural characterization of the products formed, which can be a mixture of different phases difficult to isolate. One way to solve the controversy would be to obtain monodispersed NPs, a goal that up to now was achieved using surfactants[5,33-35] or the pores of a covalent organic framework as an inert template.[14] In the first case, strong binding ligands from the organic acids alter the energetics of the surface[36] and ultimately give ThO_2 NPs of a given morphology and size. In the second case, Moreau et al. obtained monodispersed ThO_2 NPs below 3 nm and were able to structurally characterize the NPs with XANES and EXAFS. They found a fluorite structure with substantial local disorder at the surface without the need to invoke an amorphous phase.[14] In all cases, the synthesis routes use different organic Th precursors so the verification on ThO_2 sample produced by chemical precipitation in aqueous media is required. Ultimately, the debate around ThO_2 and more generally the study of actinide NPs formation need structural characterization tools able to probe both short- and medium-range order on solids and liquids.[37-38] It is indeed ideal to measure the sample without altering its state after synthesis and to characterize all relevant length scales of the system. Up to now, EXAFS is the structural technique of preference to determine anomalies in the local coordination of actinide NPs compared to bulk. However, it only provides information on the closest coordination shells.

High Energy X-ray Scattering (HEXS) and X-ray Absorption Near-Edge Structure (XANES) in the hard X-ray regime respond to these requirements and present specific advantages when applied to actinides. HEXS is among the most powerful techniques for the structural investigation of nanomaterials.[39] It measures the arrangement of atoms with ångström resolution without requiring long-range order, making it suitable for the characterization of amorphous and nanostructured systems.[40,41] HEXS is typically analysed through the pair distribution function (PDF), which is the appropriately normalized Fourier transform of the scattering signal and provides the probability to find a pair of atoms separated by a distance r. When applied to actinide materials, HEXS provides actinide-centric pair correlations due to the huge scattering power difference between the metal and the anion, as well as an optimal contrast with the solvent. Soderholm and co-workers were the first to make systematic use of HEXS to investigate the structure of actinide hydrolysis and condensation products and to promoted its use in actinide research[23,37,42-44] Despite their notable results, application of HEXS to actinide systems remains limited and focused on subnano systems having only few coordination shells. To our knowledge, we provide here the first in-depth analysis of HEXS data on heterogeneous samples containing actinide NPs on the nano- and subnano scale.

XANES is also very powerful for the study of nanomaterials.[45,46] The high sensitivity to the local electronic structure of a selected species is very appealing for the study of surface atoms: the

sudden break of periodicity, the presence of local distortions, the rearrangement of valence charges due to dangling bonds and surfactants are all effects that affect XANES spectral shape. While in bulk materials the signal from the surface represents a negligible contribution, the surface to volume ratio increases steeply with decreasing size and in spherical NPs below 5 nm surface atoms are already few tens percent of the total amount. On such systems, XANES bears valuable information on the local structure of surface atoms. The adoption of the High-Energy-Resolution Fluorescence Detected (HERFD) mode enhances the sensitivity of XANES. The reduced core-hole lifetime broadening allows the detection of smaller spectral changes and of features that would otherwise be invisible in conventional XANES.[17,47-49] Application of HERFD to $M_{4,5}$ edges of actinide materials revolutionized the use of XANES in the field because it provided a direct probe of the 5f states with sufficient resolution to determine the oxidation state and observe the splitting due to f-electron interactions.[47,49-51] Despite $M_{4,5}$ HERFD XANES is considerably exploited in the actinide fields,[15,16,52] only very few examples applied it to NPs and to our knowledge no size-effect has been reported yet at these absorption edges.

In this work, we demonstrate the fundamental structural insight given by HEXS and HERFD XANES applied to ThO_2 NPs synthesized by chemical precipitation followed by thermal treatment. With HEXS, carefully analysed with model structures of NPs, we were able to distinguish and quantify particles of different sizes and in particular to detect the presence of small clusters of atoms in the first stages of synthesis. HERFD XANES spectra at the Th M_4 edge of different steps of the synthesis show modifications of the f density of states (DOS) which thanks to the structural insight obtained by HEXS and by using theoretical simulations, we could correlate to the break of Th local symmetry, most likely happening at the surface. The combination of these two techniques thus gives a complete view of the structure of the NPs over all relevant length scales and can tackle the structural characterization of non-homogeneous samples of actinide NPs synthesised by chemical precipitation.

Results and Discussion

Samples of ThO_2 NPs were synthesized by sequential heat treatment of freshly precipitated Th(IV) samples. Sample 1 and sample 2 result from drying in air the precipitate at 40 °C and at 150 °C, respectively. To obtain ThO_2 nanoparticles of various sizes, the freshly precipitated Th(IV) was annealed at 400 °C, 800 °C and 1200 °C in air in a muffle furnace. According to XRD, sample 1 and sample 2 contain crystalline ThO_2 NPs with average coherent scattering domains of 2.0 and 3.8 nm, respectively (Figure S1). With annealing, particles grow significantly. The average size of crystallites in samples annealed at 400 °C, 800 °C and 1200 °C was around 6 nm, 34 nm and >100 nm, respectively. A table summarizing the information on samples sizes obtained by XRD and HRTEM can be found in the ESI (Table S1), while for a detailed description the reader is referred to Plakhova et al.[9]

Figure 1 shows the Pair Distribution Function (PDF) obtained by HEXS measurements on sample 1, sample 2 and bulk ThO_2. All peaks in the PDF of samples correspond to peaks of bulk ThO_2, with the only exception of a feature of sample 1 at ~7.5 Å that will be discussed later in the text. Due to the low scattering power of O compared to Th, the signal is dominated by Th – Th and Th – O pairs. The latter appear as distinguished peaks below 7 Å, then above 7 Å the intensity drops rapidly and they become small shoulders at the bottom of Th –Th peaks. Figure S2 (ESI) shows peak assignment based on Th-centred distances in ThO_2 structure. Compared to bulk ThO_2, the signal from the samples is progressively damped with increasing *r* and shows only moderate

broadening, a direct indication of the presence of NPs. The maximum distance at which oscillations are visible, i.e. 4 nm for sample 1 and 6 nm for sample 2, marks the upper limit of NP size. Further inspection of the data also reveals that peaks of sample 1 and 2 tend to shift to higher *r* compared to bulk ThO_2. This is highlighted in the upper panel of Figure 1, where data between 10 – 16 Å are superimposed and scaled.

Figure S3 (ESI) shows the relative shifts between peaks of bulk and samples in the range 0 – 20 Å. The trend of sample 2 is a linearly increasing shift to higher *r*, indicating lattice expansion[40] in agreement with what was recently reported by some of the authors based on XRD measurements.[9] The trend of sample 1 is more complex, with specific Th – Th peaks showing bigger deviations than the rest. We finally note that sample 1 presents an abrupt intensity drop after the second peak, corresponding to the first Th – Th distance, and the rest of the signal. This is not the case of sample 2, where the intensity of peaks decreases smoothly with increasing *r*.

To extract quantitative information about the size and the distribution of NPs, we first fit the data with two semi-empirical models based on imposing a size envelope function to the PDF of bulk ThO_2: the single sphere model, which considers the sample as an ensemble of identical spherical NPs, and the lognormal distribution of spherical NPs model. The parameters of the fits were: a scale factor, the lattice parameter *a* and the isotropic displacement parameters (U_{iso}) for Th and O. In addition, the single sphere model fits the average diameter of the NPs (P_{size}) and the lognormal model the mean diameter (P_{size}) and the variance (P_{sig}^2) of the distribution. The parameters resulting from the fits together with the square of the residual, R_w, are reported in Table 1 and the comparison between fits and data in Figure 2a and b. For sample 2 (Figure 2b), both models give good fits of the data. The average NP size from the single sphere model is 3.6 nm, while the resulting lognormal distribution spreads over a large range of sizes and is characterized by finds a mean size of only 0.8 nm and a variance of 0.6 nm. The latter is shown in the inset of Figure 2b, together with the envelope functions used by the semi-empirical models to modulate the signal of the bulk. Comparison of the envelope functions and visual inspection of the fits show that with the single sphere model, the signal above the average diameter, i.e. 3.6 nm, is set to zero while with a lognormal distribution small oscillations are found also at high *r*. Indeed, the fit with the lognormal model has a slightly lower R_w, reflecting the better agreement with data at both low and high *r*.

Table 1. Fit results obtained with the semi-empirical models. P_{size} is the NP size from the spherical model or the mean value of the lognormal distribution. P_{sig}^2 is the variance of the lognormal distribution.

	model	Scale	a, Å	Th U_{iso}	O U_{iso}	P_{size}, nm	P_{sig}^2, nm	R_w
	1 sph	1.49	5.610	0.011	0.075	0.93	-	0.30
	1 logn	1.80	5.607	0.010	0.080	0.5	0.2	0.28
	2 sph	0.13	5.616	0.009	0.293	3.1	-	0.29
	2 logn	0.18	5.616	0.008	0.060	1.5	0.7	0.31
	sph	0.96	5.619	0.008	0.059	3.6	-	0.17
	logn	1.13	5.619	0.008	0.063	0.8	0.6	0.12
bulk	-	0.57	5.600	0.004	0.036	-	-	0.11

The results for sample 1 are shown in Figure 2a. Fitting sample 1 was more complex and we tried two *r* ranges: 1.5 – 30 Å (fits labelled 1) and 8.3 – 30 Å (fits labelled 2). Fits 1 in the full range (Figure 2a, bottom) give poor agreement above 10 Å: both models minimize the residual at low *r*, where the signal is stronger, and they are almost featureless above 10 Å.

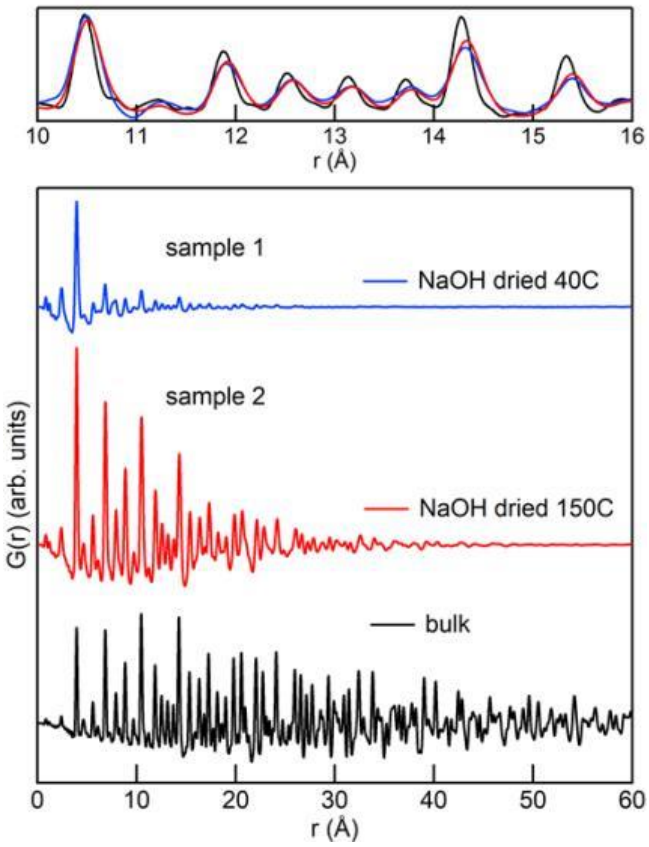

Figure 1. Unscaled PDF of samples 1, 2 and bulk ThO_2. Top panel: the same PDF data, scaled and superimposed, are shown in the 10 – 16 Å range to highlight the shift to higher *r* of peaks of sample 1 and 2.

By fitting over the full *r* range, the single sphere model gives NPs of 0.93 nm average size and the lognormal model a very sharp distribution (P_{sig} of 0.2 nm) peaked below 1 nm (P_{size} of 0.5 nm). R_w indicates that the lognormal fit 1 is slightly better. By excluding the low *r* from the fit range as in fits 2, (Figure 2a, top), the agreement above 10 Å improves considerably. Above 10 Å the sample is well represented by uniform spheres of 3.1 nm or by a lognormal distribution peaked at 1.5 nm with a 0.7 nm variance. In contrast, when extrapolated to low *r*, fits 2 severely underestimate the signal below 5 Å. R_w of fits 2, which cannot be compared with the others because of the different range, is slightly better for the single sphere model. However, visual inspection of the residuals in Figure 2a shows that fits 2 are of identical quality for the purposes of this work.

The results on sample 1 are very interesting because they indicate that the data are not well described by a single distribution or a single NP size. One characteristic size dominates the signal at low *r* and is detected by fits where the whole range is considered (fits 1). In this case, both models find average sizes below 1 nm. The residual at higher *r* definitely indicates the presence of bigger particles that can only be fitted by excluding the signal at low *r*, as done for fits 2. This

is not the case for sample 2, where a single distribution is sufficient to reproduce the data. The semi-empirical models provide valuable insight into the different sizes present in the samples. However, they find considerable concentrations of NPs with diameter in the range 0.5 – 1.5 nm, predicted by assuming that diameters can take any value. This assumption is approximate below 1.5 nm and becomes appropriate only at larger diameters.

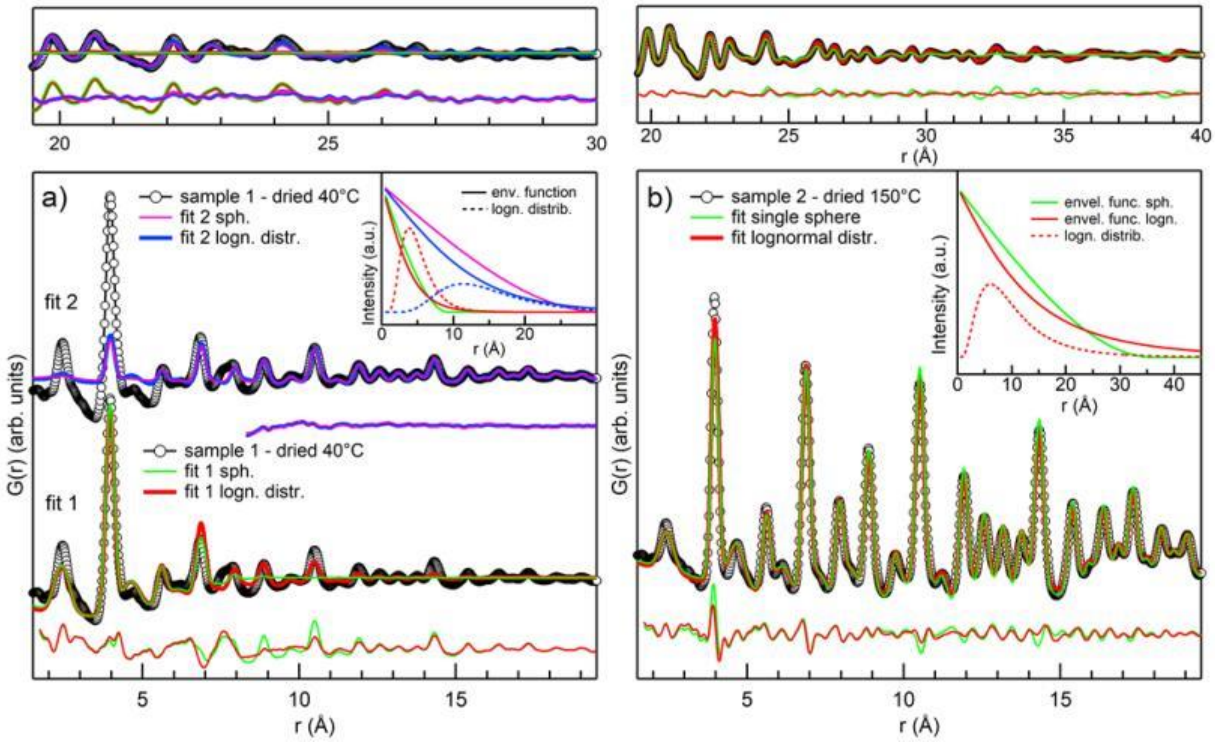

Figure 2. a) data on sample 1 (black circles) and fit results (coloured lines). Fit 1 is on the full range (1.5 – 30 Å), fit 2 on the reduced range 8.3 – 30 Å but fit results have been extrapolated to 1.5 Å. Residuals are shown on the bottom of relative fits and have not been extrapolated beyond the fitted range. The inset shows the envelope functions (continuous lines) for all fits and the lognormal distributions (dashed curves). b) data on sample 2 (black circles) and fit results with the single sphere (green) and the lognormal (red) models. The inset shows envelope functions (continuous lines) for both fits and the resulting lognormal distribution (dashed line). The top panel of a) and b) shows the high *r* range.

By cutting the smallest units with almost spherical shape out of a chunk of ThO_2 and labelling each one with the larger Th – Th distance, only few values between 0.5 and 1.5 nm are obtained, as shown in Figure S4 of ESI.For more precise identification of the NP < 1.5 nm in our samples, we implemented a fit model based on a minimal set of ThO_2 NPs structures cut from the bulk. Fits were done with diffpy-CMI[53] using Debye equation.

We isolated from bulk ThO_2 a set of NPs of almost spherical shape with diameters between 0.5 and 6.0 nm. We carefully cut all structures below 1.5 nm and above 1.5 nm we constructed spheres centred on Th of increasing radius up to 5.6 nm. The list of structures considered is reported in ESI. We fitted samples 1 and 2 in the ranges 1.7 – 40 Å and 1.7 – 60 Å, respectively, with the minimal subset of structures. PDF of ideal structures are calculated from the atomic coordinates using the Debye scattering equation implemented in diffpy-CMI (DebyePDFGenerator and DebyePDFCalculator). Each NP structure adds to the fit two parameters: a lattice expansion coefficient and a scale factor. The latter, when divided by the

sum of all scale factors, gives the concentration of the corresponding structure in the sample. The isotropic displacement parameters (U_{iso}) for Th and O common to all structures were also fitted. In order to find the best fit, we first added big NPs and optimized the agreement in the tail of the PDF signal, where oscillations are weak and only biggest NPs contribute. Extrapolating the fit to lower *r* and comparing it with data reveals where intensity is still missing and allows estimating which sizes to include in the ensemble to improve the fit. Due to the limited number of structures and samples, we proceeded with a manual fit that allows visual inspection of results. The results of the new fits are reported in Table 2 and Figure 3a and b report the new results in comparison with those of the lognormal fits from semi-empirical models. The new fits improve the agreement for both samples: for sample 2 the R_w decreases slightly. The inspection of the residuals in Figure 3 reveals small improvements over the full *r* range.

Table 2. Fit results for sample 1 and 2 with a set of NP structures.

NP	Scale	concentration	*a**exp. coeff.	Th U_{iso}	O U_{iso}	R_w
Sample 1 – dried 40 °C						
0.56 nm	0.60	61.3%	5.614			
1.0 nm	0.24	24.5%	5.580			
2.0 nm	0.072	7.4%	5.601			
3.5 nm	0.067	6.8%	5.619			
Sample 2 – dried 150 °C						
1.0 nm	0.24	24%	5.603			
2.5 nm	0.41	41%	5.603			
5.6 nm	0.34	34%	5.624			

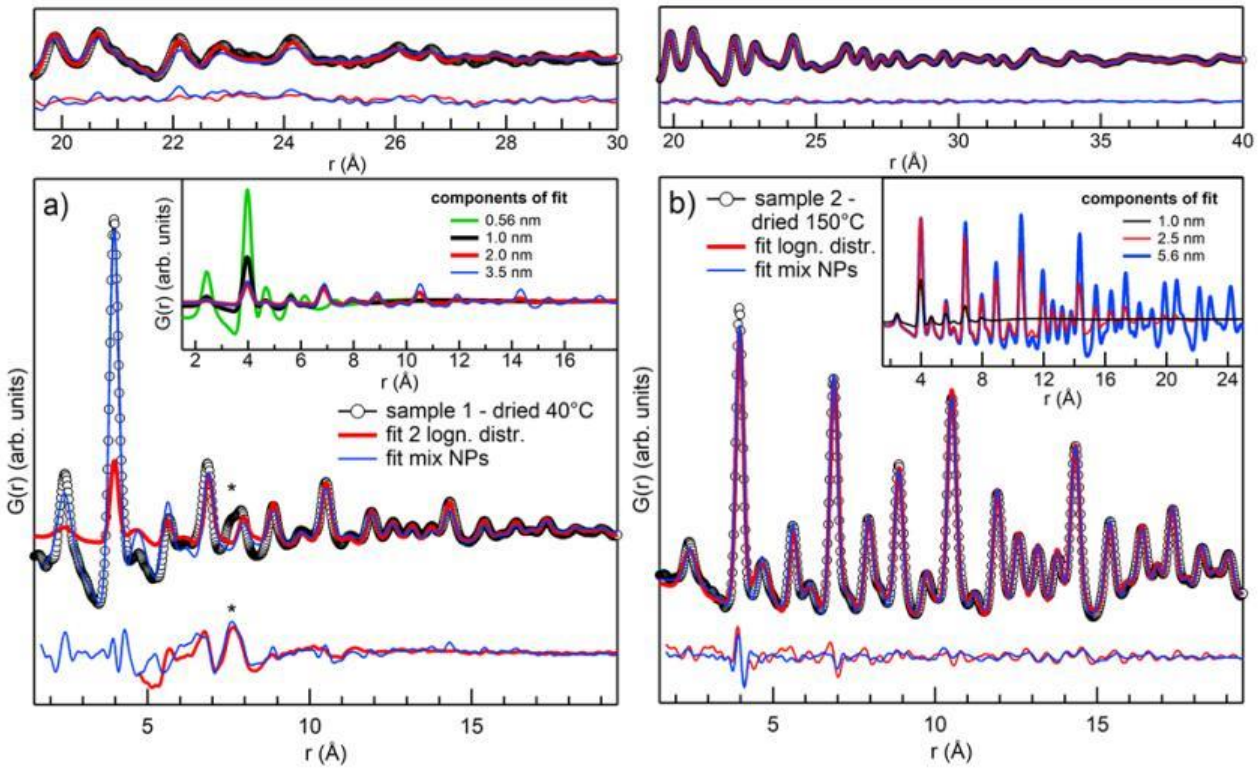

Figure 3. a) data on sample 1 (black circles) compared to fit results for the lognormal fit 2 (red line) and the fit with NPs structures (blue line). b) data on sample 2 (black circles) compared to fit results for the lognormal fit (red line) and the fit with NPs structures (blue line). Residuals are

shown below the fits and the insets of a) and b) show the calculated PDF for each NP structure added in the fit. The high *r* range is shown in the upper panels.

For sample 1, the R_w improves considerably compared to that of lognormal fit 1, which was over the full range. R_w of lognormal fit 2 cannot be compared since a different range was used. However, the direct comparison shown in Figure 3a illustrates that above 6 Å the fits give very similar results while below 6 Å the new fit reproduces very well the abrupt drop of intensity. According to the results reported in Table 2, sample 1 is made for 61.3% of 0.56 nm NPs, i.e. the smallest units that can be cut from bulk ThO_2, mixed with 24.5% of 1.0 nm NPs and small concentrations of 2.0 and 3.5 nm NPs. Sample 2 is made by a more homogeneous mixture of 1.0 nm (24%), 2.5 nm (41%) and 5.6 nm (34%) NPs.

The calculated PDF from each NP contributing to the fits are shown in the insets of Figure 3a and b. These results confirm what suggested by the semi-empirical models: sample 1 has a high concentration of very small particles mixed with bigger ones, while sample 2 is described by a more homogeneous distribution of sizes. Notably, the high concentration of 0.56 nm units disappears upon heating at 150 °C. This small octahedral unit that we artificially cut from ThO_2 bulk is very similar to Th hexamer clusters, which have been frequently reported in literature.[18-21,44] We notice that even if we applied a fit exclusively based on NP structures, a fit approach mixing NP structures for small sizes and a lognormal distribution gives results of very similar quality. Figure S5 and Table S2 in ESI report the comparison of these two approaches for sample 1. Nevertheless, with the fit using only NP structures a lattice parameter for each structure can be fit, different NP shapes can be easily implemented as well as core-shell structures. The high flexibility of this method can help to get even more detailed structural information and could be exploited in studies on larger data sets. Despite the good results obtained, there is still room for substantial improvement, especially for sample 1. The main contribution to the residual is the peak at 7.6 Å, indicated with an asterisk in Figure 3a, which does not belong to fluorite ThO_2. A similar feature was previously reported by Magini et al.[31] who investigated hydrolysed Th salts. They assigned it to aggregates of O-centred tetrahedra sharing facets, an early stage of the synthesis of ThO_2 which is made by a network of O-centred tetrahedra sharing edges. In our case, the peak could be the result of surface disorder on 1.0 nm NPs. The disorder could cause a splitting of the peak at 7.75 Å which would correspond to Th at the surface. The assignment of this peak, as well as a deeper insight into the early stages of Th(IV) hydrolysis, require the collection of a bigger set of data which will be the focus of future investigations.

Figure 4 shows Th M_4 edge HERFD data collected on samples 1 and 2 and on samples annealed at 400 °C, 800 °C and 1200 °C. XANES at the M_4 edge of actinides corresponds to the excitation of an electron from the $3d_{3/2}$ to the $5f_{5/2}$ and provides direct access to the f-DOS of the actinide. The spectrum of 1200 °C annealed sample is identical to that of bulk ThO_2 and presents four main features: the main peak A at the absorption edge, two shoulders labelled B and C, and feature D which is well separated by the absorption edge region. Features C and D are absent in sample 1 and only slightly visible in sample 2 and they progressively grow for NPs annealed at high temperatures. We also note that feature B is slightly higher in sample 1. However, the difference is very small and cannot be associated with a trend like for features C and D. Further investigation on larger sets of samples is needed to confirm the effect on feature B.

The progressive growth of features C and D in Th M_4 edge HERFD seems to follow the increase of crystallinity and size of NPs. The results of PDF fitting indicate that the precipitate dried at 40 °C

(sample 1) is predominantly made of small units similar to Th hexamers and 1.0 nm NPs. Drying the precipitate at higher temperature (sample 2) already stimulates the growth of the existing NPs and causes the extinction of the smaller units detected by PDF. From XRD data, we know that the growth continues with annealing at 400 – 1200 °C. The sensitivity to crystallinity and NPs size at the Th M_4 edge is quite a novelty and it may sound surprising. Indeed, 5f states are generally considered strongly localized, not involved in chemical bonding and only mildly sensitive to the crystal field of neighbouring atoms. This description fits better 4f states of lanthanides rather than 5f states of the early actinides. The latter are spatially more extended, more sensitive to the presence of neighbouring atoms and more prone to participate in bonds. The case of actinyl ions, where the actinide forms two very short and strong linear bonds with oxygen atoms, is a well-known case of chemical bond involving 5f orbitals.[54]

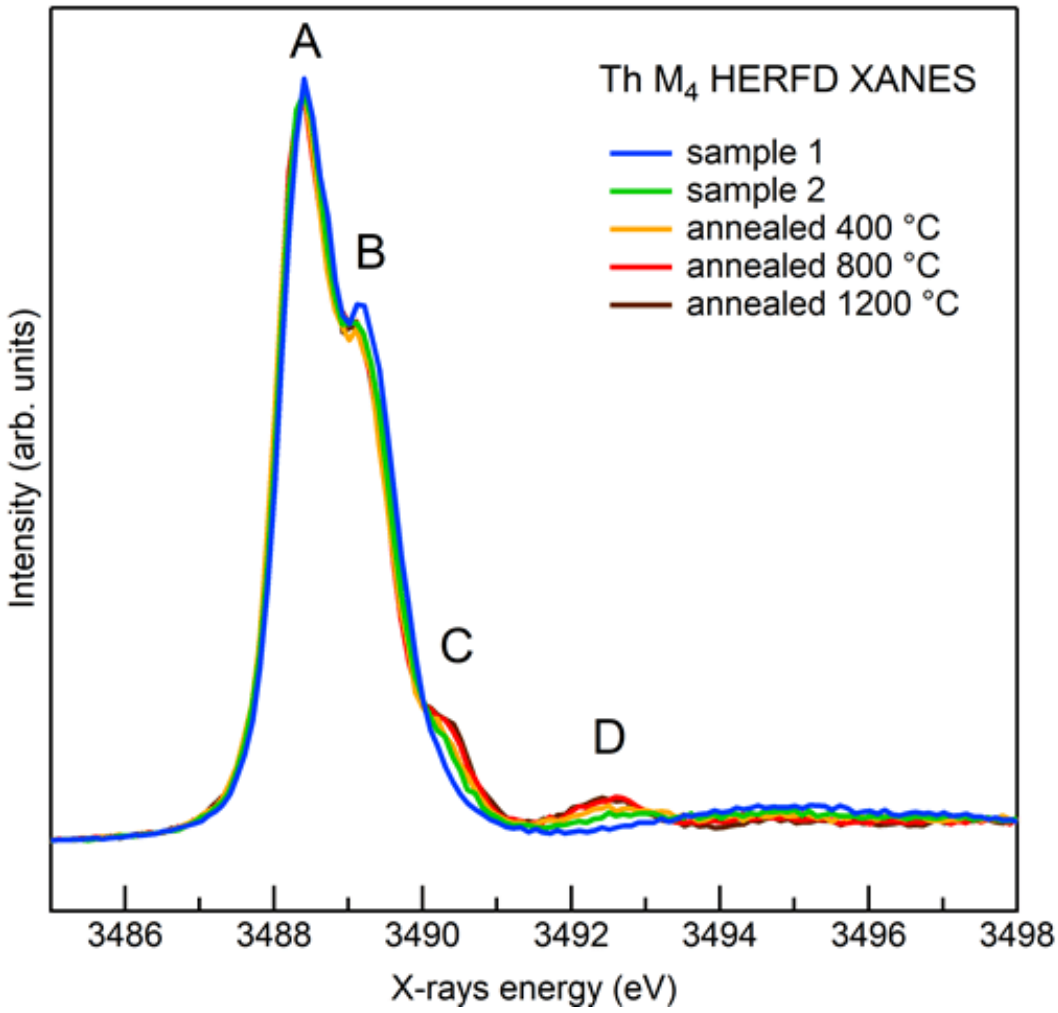

Figure 4. Th M_4 edge HERFD data on sample 1, 2 and samples annealed at 400 °C, 800 °C and 1200 °C. Data were normalized to the total spectral area.

To confirm if the observed effects can correlate with size reduction, we need to understand the nature of each feature in the spectrum and rationalize if the disappearance of peaks C and D is compatible with this hypothesis. In the absence of a large set of well-characterized references, simulations are the only way to shed light on the nature of spectral features. Butorin et al.[55] recently modelled the M_4 HERFD of ThO_2 within the Single Impurity Anderson Model, which fully accounts for electron correlations and treats the inter-atomic interactions as a perturbation.

Features A and B were well reproduced by the O_h crystal field effect on 5f orbitals of Th, while feature D is obtained by adding the ligand-to-metal charge transfer driven by Th 6d – Th 5f – O 2p hybridization. Even if some multiplet poles arise in correspondence of feature C, they are too weak to generate a shoulder and the assignment of feature C remains open. Within the approach used by the authors, based on atomic physics, it is difficult to implement effects due to size and of complex local distortions because the influence of neighbouring atoms is included as a perturbation whose strength is regulated by empirical parameters. The number of parameters increases very fast with the lowering of local symmetry, like that expected for surface atoms or small clusters. Approaches that naturally account for the surrounding atoms, like those based on density functional theory (DFT), have the advantage of avoiding empirical parameters to account for local symmetry and redistribution of valence change. These approaches include electron correlations only partially, making them not suited to treat strongly correlated f-systems. Indeed, this theory fails to reproduce the $M_{4,5}$ edges of 4f elements (lanthanides). The 5f states are less localized and the calculations done following this scheme are less questionable if the purpose is to reproduce observed trends and to deduce valuable information. Moreover, for actinide materials as ThO_2, uranyl-type or U(VI) compounds which have empty 5f orbitals in the ground state, the DFT approaches are well-suited. To our knowledge, only a few attempts have been made to simulate XANES at $M_{4,5}$ edges of early actinides using DFT-based codes.[56-58] The outcomes were promising, even if the implications of disregarding electron correlations in systems with f-electrons have not been discussed explicitly and a comparative study on $M_{4,5}$ edges of early actinides simulated with the two approaches is still missing.

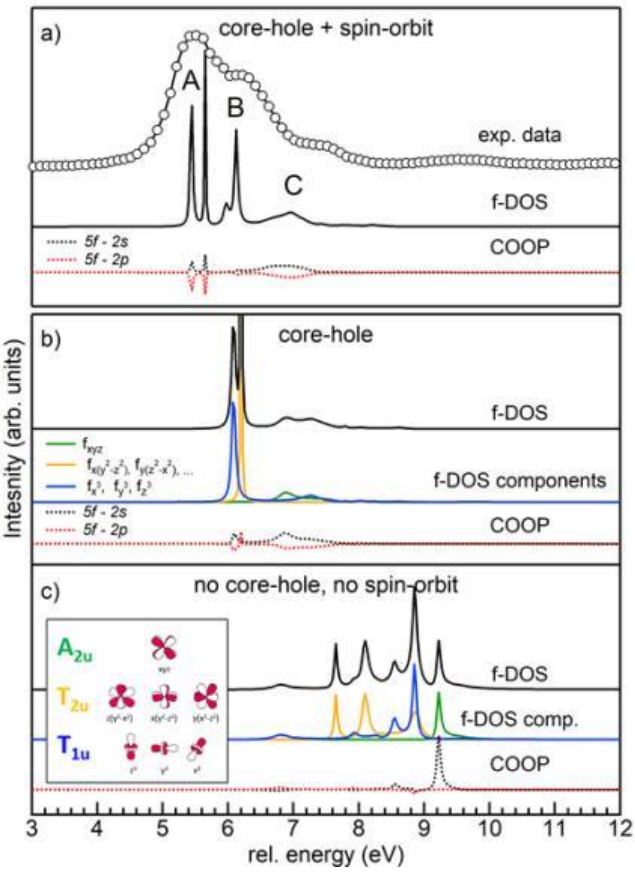

Figure 5. FDMNES simulations of bulk ThO_2 compared with experimental data on 1200 °C annealed sample (panel a – black circles). Panel a) shows the simulation obtained with core-

hole and spin-orbit included: the total f-DOS (black line) and the COOP of Th 5f with O 2s (black dot line) and 2p (red dot line). Panel b) and c) report the results obtained without spin-orbit and with (b) or without (c) core-hole. The total f-DOS and the COOP are reported with the same colour code of panel a). In addition, in panel b) and c) the decomposition on the f-DOS on the cubic set is shown (A_{2u} in green, T_{2u} in yellow and T_{1u} in blue). A sketch of the f-orbital cubic set in O_h symmetry is drawn in panel c.

We simulated the f-DOS and the M_4 edge XANES of bulk ThO_2 with FDMNES[59,60] to elucidate the nature of spectral features. Figure 5 reports the f-DOS with both core-hole and spin-orbit effects included (panel a), with only the core-hole (panel b) and without both (panel c). Each panel reports the total f-DOS (black curve) and the Crystal Overlap Orbital Populations (COOP) between the 5f orbitals of Th and the 2s (black dot line) and 2p (red dot line) orbitals of neighbouring O. COOP quantify the covalency of the Th – O bond by integrating the product of their atomic orbitals inside a sphere centred on the bond axis.[61] Positive/negative COOP indicate bonding/anti-bonding character. Panel b and c of Figure 5 report also the decomposition of the total f-DOS on the cubic set of f-orbitals, which in O_h symmetry splits into three groups, sketched in panel c. We first notice by comparing panel c and b that the core-hole has a strong impact on the f-DOS. It pulls it down in energy and it increases its sharpness and intensity close to the edge. Comparison of panel a and b shows that the effect of spin-orbit is to introduce additional splitting to that originating from local geometry. The final f-DOS resulting from the inclusion of the core-hole and the spin-orbit effects (panel a, black curve) has three groups of features whose energy separation and relative intensity are in good agreement with the experimental data. For further insight into the nature of each group of features, we can look at the decomposition of the total f-DOS on the cubic set for simulations without spin-orbit (panel b and c). ThO_2 crystallizes in the fluorite structure (Fm-3m space group) where Th has eight neighbouring oxygen atoms placed in the vertices of a regular cube. Under this local symmetry, the f-orbitals expressed in the cubic set split in three groups: T_{1u} (f_{x3}, f_{y3}, f_{z3}), T_{2u} ($f_{x(y2-z2)}$, $f_{y(z2-x2)}$, $f_{z(x2-y2)}$) and A_{2u} (f_{xyz}). This is indeed what we observe in Figure 5, panel b and c. The ordering in absence of a core-hole is in agreement with expectations and with previously published results for UO_2:[62] the contribution at lowest energy is of T_{1u} symmetry (small blue peak at ~6.8 eV) while the single orbital A_{2u} (f_{xyz}) is the more destabilized and highest in energy. Indeed, f_{xyz} points towards the vertices of the cube where the O atoms are and it interacts more strongly with them. This is also seen in the COOP, which find strong bonding interaction with O 2s in correspondence of A_{2u}. It is interesting to notice that the core-hole (panel b) pulls all orbitals down and confers T_{1u} and T_{2u} extreme sharpness and high intensity, suggesting an increased localization of these orbitals in presence of the core-hole potential, while A_{2u} remains isolated at higher energy and is broadened. The bonding character of Th 5f A_{2u} – O 2s is maintained with the addition of significant anti-bonding interaction with O 2p. Unfortunately, we cannot decompose the f-DOS of panel a, obtained with spin-orbit, on a basis set symmetrized for the double group O_h*. However, we know from group theory that T_{1u} and T_{2u} are further split in two subgroups and A_{2u} remains unaffected. The parallel with the results of panel b suggests the assignment of peak A and B of the experimental M_4 HERFD to f-orbitals of T_{1u} and T_{2u} symmetry and peak C to the single A_{2u} orbital. COOP shown in panel a are also very similar to those of panel b and further support our assignment. Despite the observation that the f-DOSs calculated by FDMNES are in good agreement with experimental data, the simulated XANES (see Figure 6d) calculated once spin-orbit is added completely disregard part of the f-DOS and peak B is not reproduced. The difference between the f-DOS and the simulated

XANES stems from selection rules, which allow transitions only to states with j=5/2 for M_4 while transitions to both j=5/2 and j=7/2 states are allowed for M_5.[63] Figure S6 in ESI shows the comparison between simulations of M_4 and M_5. The collection of M_5 data would help clarifying the absence of peak B in the simulations.

Unfortunately, with the spectrometer used in this experiment, a Johan-type spectrometer operating at 65 – 90°, the emission energy needed for Th M_5 HERFD is not covered. Measurements of Th M_4 spectra are only feasible with spectrometers having a different design.[64]

The total f-DOS splitting grasps the physics behind spectral features since the energy separation and relative intensity of the f-DOS agree fairly well with experimental data. We can then conclude that peaks A, B and C arise from the combined splitting of the crystal field and the spin-orbit effect on Th 5f orbitals. Peak C, in particular, is the most affected by the interaction with oxygen nearest neighbours. As expected, we do not reproduce peak D, which arises from ligand to metal charge transfer,[55] an effect that the current approach disregards.

We know from PDF that the principal constituents of sample 1 are small units similar to Th hexamer clusters and ThO_2 NPs of 1.0 nm. Both structures have few Th atoms (6 and 13) that, except for the central Th in the 1.0 nm NP, are on the surface and most probably experience a variation of their local environment. The disappearance of peak C in the XANES of sample 1 can then reflect this change. To confirm this hypothesis, we simulated Th M_4 XANES of two Th hexamers whose structure are reported in literature[18,20] and of the 0.56 nm ThO_2 NP that we used in PDF fitting. Both Th hexamers are made of 6 Th atoms linked together as in ThO_2. We added 6 H_2O molecules to the 0.56 nm unit similar to what is found in Th hexamers. Figure 6 shows schematics of all the structures and compares the f-DOS and the XANES simulations of Th clusters and bulk ThO_2. All simulations were shifted in energy to have the first feature aligned. Interestingly, the total f-DOS of the 0.56 nm NP maintains the three features observed in the bulk, while Th hexamers only have the first two intense features and lost the last, corresponding to peak C. The XANES simulations follow the f-DOS results, exception made for the systematic absence of the second peak, which confirms that selection rules are the origin of the discrepancy. While Th hexamers (Figure 6a and b) reproduce the observed disappearance of peak C, the very similar 0.56 nm NP does not (Figure 6c).The reason is the orientation of the four external O bound to each Th: in the 0.56 nm NP they sit on the corner of the cube centred on Th, as in bulk ThO_2. In Th hexamers, the same O atoms are rotated of ~45° around the axis connecting two opposite Th. This rotation breaks the O_h symmetry around Th and stabilizes more the anti-bonding A_{2u} orbital whose superposition with O is lowered. We additionally remark that the relative intensity of the f-DOS peaks of Th hexamer differs from that of bulk ThO_2. In particular, the features corresponding to peak B are more intense in Th hexamer, a hint that the relative intensity of peak A and B can also be sensitive to changes of the local environment and that the slight increase of peak B observed for sample 1 may be relevant.

HEXS and HERFD data when thoroughly analysed as we did in this work, demonstrate to be a very powerful tool to unravel the complexity of ThO_2 NPs structure. PDF reveals that samples are a mixture of particles of different sizes and that a large percentage of subnano NPs is initially formed, which then disappears to favour bigger NPs when Th(IV) precipitate is dried at 150 °C. This finding suggests a formation mechanism where small units, which we found to be similar to Th hexamers, are incorporated into bigger NPs or aggregate with each other. The strongest evidence of the presence of subnano units comes from PDF sensitivity to both short- and

medium-range order: the drop of intensity of Th – Th peaks above 5 Å can only be reproduced by units with only two Th – Th distances. We notice that at these distances the presence of additional Th atoms whose position deviates from those of crystalline ThO_2, would still contribute to the PDF signal, differently from what would happen for EXAFS. The latter has a higher resolution and is only sensitive to short-range order. As a result, a spread of bond distances that do not suppress the coherence needed to observe PDF peaks is sufficient to flatten the signal from higher shells in EXAFS. Figure 7 shows the simulated PDF signal for the 0.56 nm unit cut from ThO_2 and for the Th hexamer from[20]. On the bottom of Figure 7, all Th-centred distances are reported as sticks and show the local disorder present in Th hexamer. Despite for Th hexamer the spread of Th – O distances covers a range between 2.37 – 2.62 Å, the first peak of the simulated PDF is not affected dramatically, while a similar spread has a strong impact on EXAFS as reported by Rothe et al.[28] The few structural information on amorphous hydrous ThO_2 come indeed from EXAFS measurements and are limited to the first Th – O shell, which can only be fitted with multiple Th – O distances differing from those of crystalline ThO_2.

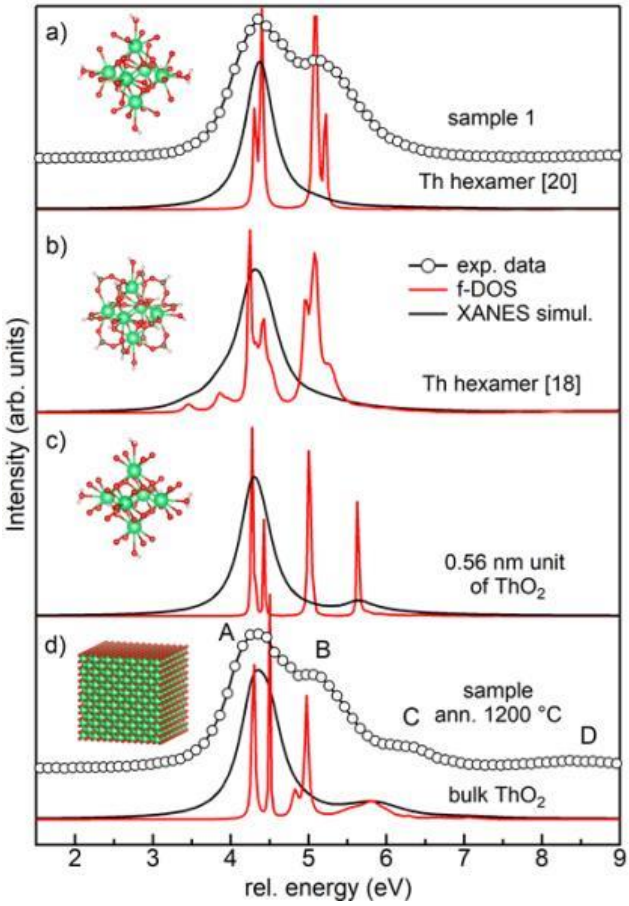

Figure 6. Simulations of the total f-DOSs (black lines) and XANES simulations (red lines) for Th hexamers from [20] (a) and [18] (b), the 0.56 unit from ThO_2 (c) and bulk ThO_2 (d). Experimental data on sample 1 and on 1200 °C annealed sample are shown on top of simulations in a) and d), respectively. Each panel reports a scheme of the simulated structure.

The signal from higher shells is typically very low making impossible to disentangle and quantify static disorder and coordination numbers. The sensitivity of HEXS to short- and medium-range order allows to characterize the sample on all the relevant length scale and reveals the presence of subnano units mixed with bigger NPs. NPs below 1.5 nm have significant local disorder, but

they still preserve the ThO_2 structure at short- and medium-range. Our study suggests that subnano units similar to Th hexamer clusters rather than an amorphous phase are the intermediate step leading to ThO_2 NPs formation. This picture is in line with the findings by Hu et al.[44] and with the more general emerging understanding that tetravalent-cations hydrolysis can result in well-defined metal oxide/hydroxide aggregates.[11,23]

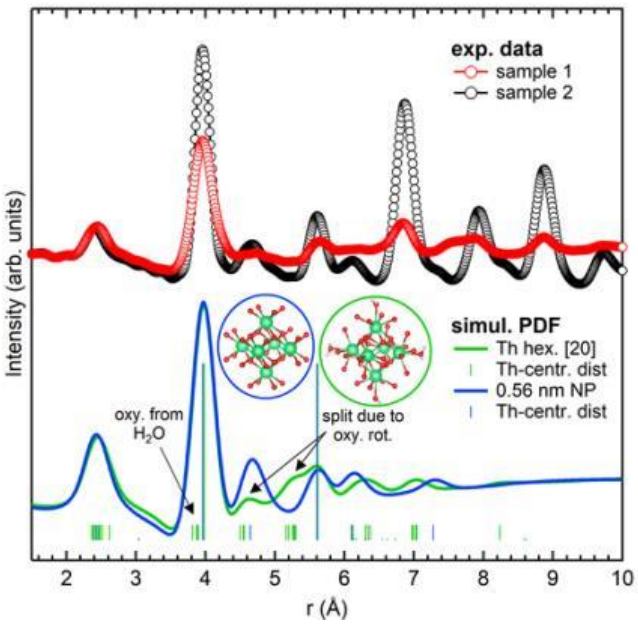

Figure 7. PDF experimental data of sample 1 (red circles) and 2 (black circles) are shown together with the calculated PDF for the structure of the 0.56 small unit cut from bulk ThO_2 (blues line) and Th hexamer from [20]. Vertical sticks on the bottom indicate the Th-centred pair distances in the two structures. The height of the sticks is proportional to the atomic number (Th = 90, O = 8, H = 1) and not to the frequency of the relative distance.

Differently from HEXS, XANES is sensitive to the short-range order and to the stereochemistry around the absorber. More details about the local coordination of the absorber can be extracted. The complexity of XANES analysis is often a bottleneck to extract the information. However, theoretical simulations available today can greatly help their interpretation and knowledge of the structure of the sample can guide the attempts to theoretically reproduce the spectral changes. In this regards, the coupling of HEXS and XANES provides more structural information and when applied to small objects can be an invaluable tool to investigate surface modifications. In the present study, we demonstrated that the trend observed in Th M_4 HERFD XANES can be rationalized as a change of local symmetry around Th atoms as the one found in Th hexamer clusters, where the rupture of the O_h symmetry is caused by the rotation of O ligands. Such break of local symmetry is likely to affect in particular surface atoms, where dangling bonds will leave more freedom for rearrangement.

The predominance of surface atoms in sample 1, whose main constituent are NPs < 1.5 nm, results in the disappearance of feature C and D of M_4 HERFD, which are specifically sensitive to oxygen neighbours and to Th 6d – O 2p hybridization,[55] respectively.

Compared to our previous results on analogous samples,[9,17] this investigation determines with more accuracy the characteristic sizes composing the samples. In particular, the presence of NPs < 1.5 nm is in agreement with the very low Th – Th coordination number found by EXAFS and

with the effect previously observed at Th L_3 edge XANES and ascribed to low coordinated Th atoms at the surface and disorder at the surface.[17]

By illustrating the opportunities of using HEXS and HERFD XANES to investigate ThO_2 NPs, our work opens the way to a thorough investigation of the mechanism of NP formation for ThO_2 and more generally for actinide oxides. The effects of initial chemical conditions, polymerization of the initial Th(IV) precipitates and the stability over time of the NPs can be addressed with this methodology. The latter is of particular interest since ThO_2 NPs, differently from NPs of other actinide dioxides synthesized with the same chemistry route, change with time (ageing effect), increasing size and crystallinity depending on the conditions. Our findings on ThO_2, compared with recent results on CeO_2[65] and PuO_2[15,16] NPs synthesized under similar conditions, already show differences on systems which are often indicated as very similar. The fact that Th can take only one oxidation state, while Ce and Pu not, prevent the accommodation of charge unbalance with oxidation or reduction at selected sites. This limitation may be compensated by increased disorder.[9,14,17] Comparative studies of the structural properties of AnO_2 NPs can help to assess similarities and differences and shed light on the different nucleation mechanisms.

Altogether, the data and the analysis presented demonstrate that investigating very small NPs with HEXS and HERFD provides important insight into the structure of NPs and the local environment at their surface. Combining the two techniques is particularly important when samples are far from being ideal, i.e. with very narrow size distribution and a uniform shape. Being able to extract structural information on such samples is of paramount importance because it sheds light on mechanisms of NPs formation that may be acting in the environment.

Conclusion

We investigated the structure of ThO_2 NPs in two samples representing the initial and a more advanced step of their synthesis via chemical precipitation. We did it by combining HEXS and HERFD XANES at the M_4 edge of Th. The analysis of the PDF with semi-empirical methods and with fits based on real NPs structures revealed that samples dried at mild temperature (40 °C – sample 1) contain mainly ThO_2 NPs < 1.5 nm. Drying at higher temperature (150 °C – sample 2) results in bigger NPs and no subnano units. HEXS reveals that Th(IV) initial precipitates contains a large number of seeds for ThO_2 NPs growth. Moreover, increasing the drying temperature to 150 °C promotes recrystallization into the more thermodynamically stable ThO_2 phase. HERFD at Th M_4 edge shows unexpectedly a remarkable effect on two spectral features, i.e. peak C and D, which progressively grow with the increased crystallinity and particles size. FDMNES simulations shed light on the nature of feature C and revealed its marked sensitivity to the break of O_h symmetry around Th ions, which considered the morphology of our samples is most likely caused by the modified arrangement of O ligands at the surface. Th M_4 edge HERFD demonstrates a high sensitivity to the local structure at the surface when applied to small NPs, a piece of information very difficult to obtain and of fundamental importance for the understanding of interaction mechanisms of NPs. HEXS and HERFD supported by a suitable analysis and theoretical simulations are a powerful tool to investigate actinide nanomaterials, especially when non-homogeneous samples like those obtained in solution chemistry are the focus of the investigation.

Experimental Section

ThO_2 samples were synthesized by sequential heat treatment of freshly precipitated Th(IV) samples. We first mixed aqueous solutions of 0.1 M thorium nitrate pentahydrate and 3 M

sodium hydroxide, which results in the formation of a Th(IV) precipitates. Portions of the freshly precipitated Th(IV) sample were dried in air at 40 °C (sample 1) and at 150 °C (sample 2). To obtain ThO_2 nanoparticles of various sizes, the freshly precipitated Th(IV) was annealed at 400 °C, 800 °C and 1200 °C in air in a muffle furnace. A summary of sample synthesis and their structural characterization by XRD and HRTEM can be found in Electronic Supplementary Information (ESI) (Table S1 and Figure S1).

We collected HEXS on sample 1 and sample 2 at the ID15A[66] beamline of the European Synchrotron Radiation Facility (ESRF, Grenoble). The data were collected at room temperature, the incident energy was set to 120 keV and we measured up to 30 $Å^{-1}$ using a Dectris CdTe 2M pixel detector. Samples were sealed in kapton capillaries (double confinement) and the signal from an empty capillary was used for background subtraction. Patterns were corrected for detector geometry, response and transparency, and integrated using a locally modified version of pyFAI[67] with outlier filtering.

The PDF was calculated from the resulting powder diffraction patterns using modules from PDFgetX3[68] and The data were corrected for electronic noise and weak spurious signal by fitting the high angle part of the calculated F(q) to a weighted spline in order to remove outliers, in a procedure similar to that described in reference.[69] The PDF Gaussian dampening envelope due to limited Q-resolution and the Q-broadening were obtained from the fit of a reference sample and fixed at these values for NPs. The maximum scattering vector Q of the data used for the generation of PDF was 26 $Å^{-1}$. We fit NP data with diffpy-CMI[53] using three different models: periodic models using a single spherical or the lognormal distribution of nanoparticle sizes[70] and a model based on a set of discrete NP structures. The number of refined parameters was kept as low as possible, visual inspection and the residual R_w were used to evaluate the goodness of the fit. The refined parameters for the first two models were the lattice parameter a, the U_{iso} of Th and O, the mean particle size (P_{size}) and the variance of the lognormal distribution (P_{sig}^2). For the model implementing a set of NP structures two parameters were common to all structures, the U_{iso} of Th and O, and two additional parameters were specific to each NP in the set, a scale factor and a lattice expansion parameter. To limit the number of parameters, □$_2$, which takes into account the first neighbour interaction, was fixed to 2.0 Å for all fits.

XANES spectra of Th M_4 edge were collected in the HERFD mode at the ID26 beamline[71] of the ESRF. The incident energy was selected with a Si(111) double crystal monochromator. Rejection of higher harmonics was achieved with three Si mirrors at 3.0, 3.5 and 4.0 mrad angles relative to the incident beam. The X-ray emission spectrometer[72,73] was equipped with 3 Ge(220) spherically bent crystal analysers (1 m radius) at a Bragg angle of 80° to collect the maximum of the M□ emission line of Th (~3148.6 eV – tabulated value). The energy resolution estimated by the FWHM of the elastic peak was 0.4 eV. Samples were measured as dried powders sealed with double kapton confinement in the sample-holder.

We simulated Th M_4 edge XANES with the FDMNES code.[59,60] The scattering potential around the Th absorber was calculated self-consistently within a radius of 5 Å. The best agreement was obtained with the inclusion of a fully screened core-hole and with the Finite Difference Method (FDM). Relativistic effects and spin-orbit interaction were included. An example of the input file used for simulations is provided in ESI.

Acknowledgements

We acknowledge support from the European Research Council (ERC) under grant agreement N° 759696. T.V.P. acknowledge Russian Science Foundation (grant N° 20-73-00130) for supporting synthesis oand primary characterization of ThO_2 nanoparticles. E.G. S.N.K. and K.O.K. acknowledge support by the Russian Ministry of Science and Education under grant N° 075-15-2019-1891. The authors would like to acknowledge the ESRF for providing beamtime. L. A. thanks S. Bauters for fruitful discussions on data analysis.

Keywords: actinides • HERFD • HEXS • nanoparticles • ThO_2

References

[1] S. N. Kalmykov, M. A. Denecke, Eds. , Actinide Nanoparticle Research, Springer, Berlin ; London, 2010.

[2] C. Walther, M. A. Denecke, Chemical Reviews 2013, 113, 995–1015.

[3] J. Spino, H. Santa Cruz, R. Jovani-Abril, R. Birtcher, C. Ferrero, Journal of Nuclear Materials 2012, 422, 27–44.

[4] P. C. Burns, K.-A. Kubatko, G. Sigmon, B. J. Fryer, J. E. Gagnon, M. R. Antonio, L. Soderholm, Angew. Chem. Int. Ed. 2005, 44, 2135–2139.

[5] D. Hudry, C. Apostolidis, O. Walter, T. Gouder, E. Courtois, C. Kübel, D. Meyer, Chem. Eur. J. 2012, 18, 8283–8287.

[6] E. Dalodière, M. Virot, V. Morosini, T. Chave, T. Dumas, C. Hennig, T. Wiss, O. Dieste Blanco, D. K. Shuh, T. Tyliszcak, L. Venault, P. Moisy, S. I. Nikitenko, Sci Rep 2017, 7, 43514.

[7] O. Walter, K. Popa, O. D. Blanco, Open Chemistry 2016, 14, 170–174.

[8] K. Popa, O. Walter, O. D. Blanco, A. Guiot, D. Bouëxière, J.-Y. Colle, L. Martel, M. Naji, D. Manara, CrystEngComm 2018, 20, 4614–4622.

[9] T. V. Plakhova, A. Yu. Romanchuk, D. V. Likhosherstova, A. E. Baranchikov, P. V. Dorovatovskii, R. D. Svetogorov, T. B. Shatalova, T. B. Egorova, A. L. Trigub, K. O. Kvashnina, V. K. Ivanov, S. N. Kalmykov, J. Phys. Chem. C 2019, 123, 23167–23176.

[10] L. Wang, R. Zhao, X. Wang, L. Mei, L. Yuan, S. Wang, Z. Chai, W. Shi, CrystEngComm 2014, 16, 10469–10475.

[11] G. E. Sigmon, A. E. Hixon, Chem. Eur. J. 2019, 25, 2463–2466.

[12] A. Yu. Romanchuk, T. V. Plakhova, A. V. Egorov, T. B. Egorova, P. V. Dorovatovskii, Y. V. Zubavichus, A. A. Shiryaev, S. N. Kalmykov, Dalton Trans. 2018, 47, 11239–11244.

[13] L. Bonato, M. Virot, T. Dumas, A. Mesbah, E. Dalodière, O. Dieste Blanco, T. Wiss, X. Le Goff, M. Odorico, D. Prieur, A. Rossberg, L. Venault, N. Dacheux, P. Moisy, S. I. Nikitenko, Nanoscale Adv. 2020, 2, 214–224.

[14] L. M. Moreau, A. Herve, M. D. Straub, D. R. Russo, R. J. Abergel, S. Alayoglu, J. Arnold, A. Braun, G. J. P. Deblonde, Y. Liu, T. D. Lohrey, D. T. Olive, Y. Qiao, J. A. Rees, D. K. Shuh, S. J. Teat, C. H. Booth, S. G. Minasian, Chem. Sci. 2020, 10.1039.C9SC06117G.

[15] K. O. Kvashnina, A. Yu. Romanchuk, I. Pidchenko, L. Amidani, E. Gerber, A. Trigub, A. Rossberg, S. Weiss, K. Popa, O. Walter, R. Caciuffo, A. C. Scheinost, S. M. Butorin, S. N. Kalmykov, Angew. Chem. Int. Ed. 2019, 58, 17558–17562.

[16] E. Gerber, A. Yu. Romanchuk, I. Pidchenko, L. Amidani, A. Rossberg, C. Hennig, G. B. M. Vaughan, A. Trigub, T. Egorova, S. Bauters, T. Plakhova, M. O. J. Y. Hunault, S. Weiss, S. M. Butorin, A. C. Scheinost, S. N. Kalmykov, K. O. Kvashnina, Nanoscale 2020, 10.1039.D0NR03767B.

[17] L. Amidani, T. V. Plakhova, A. Yu. Romanchuk, E. Gerber, S. Weiss, A. Efimenko, C. J. Sahle, S. M. Butorin, S. N. Kalmykov, K. O. Kvashnina, Phys. Chem. Chem. Phys. 2019, 21, 10635–10643.

[18] S. Takao, K. Takao, W. Kraus, F. Emmerling, A. C. Scheinost, G. Bernhard, C. Hennig, Eur. J. Inorg. Chem. 2009, 2009, 4771–4775.

[19] C. Hennig, S. Takao, K. Takao, S. Weiss, W. Kraus, F. Emmerling, A. C. Scheinost, Dalton Trans. 2012, 41, 12818.

[20] K. E. Knope, R. E. Wilson, M. Vasiliu, D. A. Dixon, L. Soderholm, Inorg. Chem. 2011, 50, 9696–9704.

[21] N. Torapava, I. Persson, L. Eriksson, D. Lundberg, Inorg. Chem. 2009, 48, 11712–11723.

[22] C. Walther, J. Rothe, B. Schimmelpfennig, M. Fuss, Dalton Trans. 2012, 41, 10941.

[23] K. E. Knope, L. Soderholm, Chem. Rev. 2013, 113, 944–994.

[24] S. Higashi, Bull. Inst. Chem. Research, Kyoto Univ. 1959, 37, 200–206.

[25] Nishikawa Shogo, Kobayashi Taishi, Sasaki Takayuki, Takagi Ikuji, ract 2018, 106, 655.

[26] T. Kobayashi, T. Sasaki, I. Takagi, H. Moriyama, Journal of Nuclear Science and Technology 2016, 53, 1787–1793.

[27] C. Bitea, R. Müller, V. Neck, C. Walther, J. I. Kim, Colloids and Surfaces A: Physicochemical and Engineering Aspects 2003, 217, 63–70.

[28] J. Rothe, M. A. Denecke, V. Neck, R. Müller, J. I. Kim, Inorganic Chemistry 2002, 41, 249–258.

[29] S. Dash, R. Krishnan, M. Kamruddin, A. K. Tyagi, B. Raj, Journal of Nuclear Materials 2001, 295, 281–289.

[30] M. Moeini, A. Malekzadeh, S. J. Ahmadi, M. Hosseinpour, Materials Letters 2012, 81, 99–101.

[31] M. Magini, A. Cabrini, G. Scibona, G. Johansson, M. Sandström, Acta Chemica Scandinavica A 1976, 30, 437–447.

[32] D. J. Dzimitrowicz, P. J. Wiseman, D. Cherns, Journal of Colloid and Interface Science 1985, 103, 8.

[33] D. Hudry, J.-C. Griveau, C. Apostolidis, O. Walter, E. Colineau, G. Rasmussen, D. Wang, V. S. K. Chakravadhaluna, E. Courtois, C. Kübel, D. Meyer, Nano Research 2014, 7, 119–131.

[34] D. Hudry, C. Apostolidis, O. Walter, T. Gouder, E. Courtois, C. Kübel, D. Meyer, Chemistry - A European Journal 2013, 19, 5297–5305.

[35] D. Hudry, C. Apostolidis, O. Walter, A. Janßen, D. Manara, J.-C. Griveau, E. Colineau, T. Vitova, T. Prüßmann, D. Wang, C. Kübel, D. Meyer, Chemistry - A European Journal 2014, 20, 10431–10438.

[36] G. Wang, E. R. Batista, P. Yang, Physical Chemistry Chemical Physics 2018, 20, 17563–17573.

[37] L. Soderholm, S. Skanthakumar, J. Neuefeind, Anal Bioanal Chem 2005, 383, 48–55.

[38] W.-Q. Shi, L.-Y. Yuan, C.-Z. Wang, L. Wang, L. Mei, C.-L. Xiao, L. Zhang, Z.-J. Li, Y.-L. Zhao, Z.-F. Chai, Adv. Mater. 2014, 26, 7807–7848.

[39] S. J. L. Billinge, I. Levin, Science 2007, 316, 561–565.

[40] B. Gilbert, Science 2004, 305, 651–654.

[41] K. M. Ø. Jensen, A. B. Blichfeld, S. R. Bauers, S. R. Wood, E. Dooryhée, D. C. Johnson, B. B. Iversen, S. J. L. Billinge, IUCrJ 2015, 2, 481–489.

[42] L. Soderholm, P. M. Almond, S. Skanthakumar, R. E. Wilson, P. C. Burns, Angew. Chem. 2008, 120, 304–308.

[43] R. E. Wilson, S. Skanthakumar, L. Soderholm, Angew. Chem. Int. Ed. 2011, 50, 11234–11237.

[44] Y.-J. Hu, K. E. Knope, S. Skanthakumar, L. Soderholm, Eur. J. Inorg. Chem. 2013, 2013, 4159–4163.

[45] A. Kuzmin, J. Chaboy, IUCrJ 2014, 1, 571–589.

[46] J. Timoshenko, D. Lu, Y. Lin, A. I. Frenkel, The Journal of Physical Chemistry Letters 2017, 8, 5091–5098.

[47] K. O. Kvashnina, Y. O. Kvashnin, S. M. Butorin, Journal of Electron Spectroscopy and Related Phenomena 2014, 194, 27–36.

[48] K. O. Kvashnina, F. M. F. de Groot, Journal of Electron Spectroscopy and Related Phenomena 2014, 194, 88–93.

[49] K. O. Kvashnina, S. M. Butorin, P. Martin, P. Glatzel, Phys. Rev. Lett. 2013, 111, 253002.

[50] G. Leinders, R. Bes, J. Pakarinen, K. Kvashnina, M. Verwerft, Inorg. Chem. 2017, 56, 6784–6787.

[51] S. M. Butorin, K. O. Kvashnina, A. L. Smith, K. Popa, P. M. Martin, Chem. Eur. J. 2016, 22, 9693–9698.

[52] T. Vitova, I. Pidchenko, D. Fellhauer, T. Pruessmann, S. Bahl, K. Dardenne, T. Yokosawa, B. Schimmelpfennig, M. Altmaier, M. Denecke, J. Rothe, H. Geckeis, Chem. Commun. 2018, 54, 12824–12827.

[53] P. Juhás, C. L. Farrow, X. Yang, K. R. Knox, S. J. L. Billinge, Acta Crystallogr A Found Adv 2015, 71, 562–568.

[54] R. G. Denning, J. Phys. Chem. A 2007, 111, 4125–4143.

[55] S. M. Butorin, K. O. Kvashnina, J. R. Vegelius, D. Meyer, D. K. Shuh, Proceedings of the National Academy of Sciences 2016, 113, 8093–8097.

[56] C. Fillaux, J.-C. Berthet, S. D. Conradson, P. Guilbaud, D. Guillaumont, C. Hennig, P. Moisy, J. Roques, E. Simoni, D. K. Shuh, T. Tyliszczak, I. Castro-Rodriguez, C. Den Auwer, Comptes Rendus Chimie 2007, 10, 859–871.

[57] Y. Podkovyrina, I. Pidchenko, T. Prüßmann, S. Bahl, J. Göttlicher, A. Soldatov, T. Vitova, J. Phys.: Conf. Ser. 2016, 712, 012092.

[58] J. Kolorenč, K. O. Kvashnina, MRS Adv. 2018, 3, 3143–3148.

[59] Y. Joly, O. Bunău, J. E. Lorenzo, R. M. Galéra, S. Grenier, B. Thompson, Journal of Physics: Conference Series 2009, 190, 012007.

[60] O. Bunău, Y. Joly, J. Phys.: Condens. Matter 2009, 21, 345501.

[61] R. Dronskowski, P. E. Bloechl, J. Phys. Chem. 1993, 97, 8617–8624.

[62] H. Ramanantoanina, G. Kuri, C. Daul, J. Bertsch, Phys. Chem. Chem. Phys. 2016, 18, 19020–19031.

[63] K. O. Kvashnina, H. C. Walker, N. Magnani, G. H. Lander, R. Caciuffo, Phys. Rev. B 2017, 95, 245103.

[64] M. Rovezzi, A. Harris, B. Detlefs, T. Bohdan, A. Svyazhin, A. Santambrogio, D. Degler, R. Baran, B. Reynier, P. Noguera Crespo, C. Heyman, H.-P. Van Der Kleij, P. Van Vaerenbergh, P. Marion, H. Vitoux, C. Lapras, R. Verbeni, M. M. Kocsis, A. Manceau, P. Glatzel, J Synchrotron Rad 2020, 27, 813–826.

[65] T. V. Plakhova, A. Yu. Romanchuk, S. M. Butorin, A. D. Konyukhova, A. V. Egorov, A. A. Shiryaev, A. E. Baranchikov, P. V. Dorovatovskii, T. Huthwelker, E. Gerber, S. Bauters, M. M. Sozarukova, A. C. Scheinost, V. K. Ivanov, S. N. Kalmykov, K. O. Kvashnina, Nanoscale 2019, 11, 18142–18149.

[66] G. B. M. Vaughan, R. Baker, R. Barret, J. Bonnefoy, T. Buslaps, S. Checchia, D. Duran, F. Fihman, P. Got, J. Kieffer, S. A. J. Kimber, K. Martel, C. Morawe, D. Mottin, E. Papillon, S. Petitdemange, A. Vamvakeros, J.-P. Vieux, M. Di Michiel, J Synchrotron Rad 2020, 27, 515–528.

[67] J. Kieffer, S. Petitdemange, T. Vincent, J Synchrotron Rad 2018, 25, 612–617.

[68] P. Juhás, T. Davis, C. L. Farrow, S. J. L. Billinge, J Appl Crystallogr 2013, 46, 560–566.

[69] L. B. Skinner, C. J. Benmore, J. B. Parise, Nuclear Instruments and Methods in Physics Research Section A: Accelerators, Spectrometers, Detectors and Associated Equipment 2012, 662, 61–70.

[70] L. Gamez-Mendoza, M. W. Terban, S. J. L. Billinge, M. Martinez-Inesta, J Appl Crystallogr 2017, 50, 741–748.

[71] C. Gauthier, V. A. Solé, R. Signorato, J. Goulon, E. Moguiline, Journal of synchrotron radiation 1999, 6, 164–166.

[72] P. Glatzel, U. Bergmann, Coordination Chemistry Reviews 2005, 249, 65–95.

[73] K. O. Kvashnina, A. C. Scheinost, Journal of Synchrotron Radiation 2016, 23, 836–841.